



An Investigation into the Surface, Friction and Wear Properties of Laser Sintered Polyamide-12 Components

Kieran Nar

A thesis submitted for the degree of

Doctor of Philosophy

University of Sheffield

Department of Mechanical Engineering

June 2024

Polymer Laser Sintering

Fact or Friction?

Acknowledgements

I would like to extend my sincerest gratitude to everyone who played a part in this doctoral work. It was a great pleasure working with you all, particularly those named below, whose involvements were fundamental to the success of this project.

Firstly, I would like to thank my supervisors – **Dr Candice Majewski** and **Professor Roger Lewis** for their endless supply of expertise, encouragement and guidance. Moreover, thanks to **Candice** for your shared enthusiasm for puns and kickstarting my passion for pasta-making, and to **Roger**, for always providing the swiftest of feedback, come t(rain) or shine!

Also, thank you to **Esme Graham** for being an all-round champion! I am eternally grateful for all of the support that you have provided during this journey, particularly your unwavering curiosity, ceaseless willingness to listen and inherent ability to always boost morale.

Furthermore, this work would not have been possible without the assistance provided by members of the Advanced Polymer Sintering Lab, specifically **Wendy Birtwistle**, **Kurt Bonser** and **Ryan Brown**. In addition to your vast technical expertise, thank you for all of the rabbit gravy's, chats and (not so) Secret Santa's. Thanks also to **James Tarver**, with who parts of the work discussed in **Chapter 6** were carried out in collaboration with.

Lastly, the time spent with family and friends over these past few years has been filled with countless happy memories. Accordingly, I would like to thank **Dipti Ross**; **Mukesh Nar**; **Emily Nar**; **Philip Ross**; **Louise Nar**; **Connor Worthington**; and **Daniel Hudson** for all of the laughs shared during this time.

Abstract

Polymer Laser Sintering (LS) is an Additive Manufacturing process that is well-established due to its ability to produce functional components with highly complex geometries. However, the adoption of these components for end-use applications remains hindered due to concerns regarding their in-service behaviours, particularly when subject to dynamic contact. Therefore, the scope of this investigation was to characterise the surface, friction and wear properties of polymer laser sintered components to help address these issues. More specifically, Polyamide-12 was selected to be the principal polymer of interest for this investigation as it currently dominates the LS materials market.

Laser sintered Polyamide-12 surfaces were first studied in detail. Results showed that their topographies were dependent on their build orientation, particularly top surfaces, which were found to be asperity peak dominated due to the mechanism of finish layer powder particle adhesion. Moreover, it was demonstrated that it was possible to reduce the top surface heights of laser sintered Polyamide-12 components by as much as 68% when alternative build actions were employed.

Dry sliding tests were then performed to ascertain insight into the friction and wear properties of laser sintered Polyamide-12 components. This included investigating how varying operating conditions, specifically normal load, sliding speed and contact configuration, influenced both their transient and steady-state sliding behaviours. Additionally, incorporating solid lubricants within Polyamide-12 matrices was explored as a potential means of modifying the tribological properties of components manufactured by LS. Ultimately, it was demonstrated that the individual additions of Polytetrafluoroethylene and Molybdenum disulphide reduced the magnitudes of friction and wear incurred during testing by as much as 50% and 78%, respectively.

This was the first time knowledge between tribology and polymer Laser Sintering was comprehensively consolidated. Consequently, new correlations between material, process and resultant surface and sliding phenomena were established.

Declaration

I, the author, confirm that this thesis is my own work. I am aware of the University's Guidance on the Use of Unfair Means (www.sheffield.ac.uk/ssid/unfair-means). This work has not previously been presented for an award at this, or any other, university.

Table of Contents

1. Introduction	1
1.1 The Focus of this Thesis	2
1.2 Research Motivation	2
1.3 Aims and Objectives.....	3
1.4 Thesis Structure	4
2. Background	7
2.1 Additive Manufacturing.....	8
2.1.1 Definition	8
2.1.2 Additive Manufacturing Technologies.....	8
2.2 Polymer Powder Bed Fusion.....	9
2.3 Polymer Laser Sintering.....	10
2.3.1 Laser Sintering Build Process.....	11
2.3.2 Polymers for Laser Sintering.....	16
2.4 Tribology	29
2.4.1 Definition	29
2.5 Polymer Tribology.....	29
2.5.1 Surface Topography	30
2.5.2 Friction.....	36
2.5.3 Wear	39
3. Literature Review	46
3.1 Laser Sintered PA12 Surfaces	47
3.1.1 PA12 Powder Effects on Roughness	47
3.1.2 LS Processing Effects on Roughness	48
3.1.3 Surface Orientation Effects on Roughness.....	49
3.1.4 Comparisons Between PA12 Surfaces Produced by LS and other Leading Polymer-PBF Processes	50
3.1.5 A Summary of the Key Insights Gained from Related Literature on the Surface Topographies of Laser Sintered PA12 Components	54
3.2 Laser Sintered PA12 Friction Related Phenomena	55
3.2.1 COF Results from Laser Sintered PA12 Literature	55
3.2.2 Comparisons Between Laser Sintered PA12 and General Polymer COF Data	56

3.2.3	The Key Factors that Influence the Frictional Behaviours of Laser Sintered PA12 Components	57
3.2.4	A Summary of the Key Insights Gained from Related Literature on the Frictional Behaviours of Laser Sintered PA12 Components	60
3.3	Laser Sintered PA12 Wear Related Phenomena	60
3.3.1	Wear Rate Data from Laser Sintered PA12 Literature	60
3.3.2	Comparisons Between Polyamides and other Engineering Polymers.....	64
3.3.3	The Inclusions of Fillers to Modify the Wear Properties of Laser Sintered PA12 Components.....	66
3.3.4	A Summary of the Key Insights Gained from Related Literature on the Wear Behaviours of Laser Sintered PA12 Components	67
3.4	Literature Review Conclusions	67
4.	Materials and Methods	68
4.1	Materials	69
4.1.1	Polyamide-12.....	69
4.2	Methods.....	73
4.2.1	Laser Sintering.....	73
4.2.2	Characterisation Techniques.....	76
4.3	Auxiliary and Alternative Experimental Practices.....	90
5.	Laser Sintered Polyamide-12 Surfaces	91
5.1	Introduction	92
5.2	Materials and Methods.....	92
5.2.1	Materials	92
5.2.2	Methods	93
5.3	Results and Discussion.....	97
5.3.1	Laser Sintered Side Surfaces.....	97
5.3.2	Laser Sintered Top and Bottom Surfaces.....	101
5.4	Conclusions	115
6.	The Mechanisms that Influence Laser Sintered Polyamide-12 Top Surfaces	117
6.1	Introduction	118
6.1.1	Motivation.....	118
6.1.2	Polymer Melt Viscous Flow.....	119
6.1.3	Finish Layer Powder Particle Adhesion	120
6.2	Materials and Methods.....	120
6.2.1	Materials	120

6.2.2	Specimens	121
6.2.3	Experimental Procedure	121
6.2.4	Surface Analysis.....	126
6.2.5	Tensile Testing.....	127
6.3	Results and Discussion.....	127
6.3.1	The Influence of Laser Parameters on Laser Sintered PA12 Top Surfaces.....	127
6.3.2	The Influence of Finish Layer Deposition on Laser Sintered Polymer Top Surfaces .	139
6.4	Conclusions	149
7.	The Transient Sliding Behaviours of Laser Sintered Polyamide-12 Components	151
7.1	Introduction	152
7.2	Materials and Methods.....	152
7.2.1	Materials	152
7.2.2	Methods	153
7.3	Results and Discussion.....	156
7.3.1	Friction.....	156
7.3.2	Wear	159
7.4	Conclusions	166
8.	The Influence of Normal Load, Sliding Speed and Contact Configuration on the Friction and Wear Properties of Laser Sintered Polyamide-12 Components	168
8.1	Introduction	169
8.2	Materials and Methods.....	169
8.2.1	Materials	169
8.2.2	Specimens	170
8.2.3	Experimental Procedure	171
8.2.4	Surface Analysis.....	173
8.2.5	Friction and Wear Testing	174
8.3	Results and Discussion.....	175
8.3.1	Friction.....	175
8.3.2	Wear	194
8.4	Conclusions	215
9.	The Use of Solid Lubricants to Modify the Properties of Laser Sintered Polyamide-12 Components	218
9.1	Introduction	219
9.1.1	Solid Lubricants.....	219

9.2	Materials and Methods.....	220
9.2.1	Materials	220
9.2.2	Specimens	221
9.2.3	Characterisation	222
9.3	Results and Discussion.....	225
9.3.1	Filler Dispersion	225
9.3.2	Part Warpage	228
9.3.3	Surface Topographies	230
9.3.4	Tensile Properties.....	233
9.3.5	Friction	234
9.3.6	Wear	241
9.4	Conclusions	245
10.	Conclusions and Further Work	247
10.1	Conclusions	248
10.2	Further Work.....	250
	References	252
	Appendices.....	265
A.	Additive Manufacturing Technologies	265
B.	Transient Sliding Microscopy Scan Images.....	268
C.	Auxiliary Friction and Wear Results	273
D.	Auxiliary SEM Filler Inclusion Analysis.....	290

List of Figures

Figure 1.1 – A schematic illustrating both the structure of this thesis and sequence in which it was executed.	6
Figure 2.1 – Conventional pre-, in- and post- processing considerations pertinent to polymer-PBF.	10
Figure 2.2 – An illustration outlining the general Laser Sintering build process.	11
Figure 2.3 – The morphological structures of amorphous, semi-crystalline and crystalline polymers.	12
Figure 2.4 – The mechanism of polymer powder particle coalescence. Adapted from Asgarpour et al. [10].	13
Figure 2.5 – The growth in the annual spend on polymer powders for PBF processes over the last 13 years [2].	17
Figure 2.6 – Polymers that have been reported as being processable by LS, categorised by crystallinity, cost, performance and availability. Adapted from Wingham [12], Tan et al. [26] and Yuan et al. [27]. Thermoplastic abbreviations are as follows (ordered alphabetically): ABS (Acrylonitrile butadiene styrene) [28]; HDPE (High-density polyethylene) [29,30]; PHBV (Poly(3-hydroxybutyrate-co-3-hydroxyvalerate)) [31]; PA11 (Polyamide-11) [32]; PA12 (Polyamide-12) [33]; PA6 (Polyamide-6) [34]; PC (Polycarbonate) [35]; PCL (Polycaprolactone) [36]; PEEK (Polyether-ether-ketone) [37]; PEK (Polyether-ketone) [38], PEKK (Polyether-ketone-ketone) [39]; PI* (Polyimide) [40]; PLA (Polylactic acid) [41]; PLGA (poly(lactic-co-glycolic acid)) [42]; PLLA (poly(L-lactide)) [43]; PMMA (Poly(methyl-methacrylate)) [44]; POM (Polyoxymethylene) [45]; PP [46]; PS (Polystyrene) [47]; PU (Polyurethane) [48]; PVA (Polyvinyl alcohol) [49]; PVDF (Polyvinylidene (di)fluoride) [50]; SAN (Styrene-acrylonitrile resin) [51]; TPE (Thermoplastic elastomers) [52]; TPU (Thermoplastic polyurethane) [52]; UHMWPE [24]. *PI is a thermoset polymer.	18
Figure 2.7 – An illustration of the chain structure of a PA12 molecule. Adapted from Pham et al. [48].	19
Figure 2.8 – An SEM image of a commercially available PA12 powder, specifically PA2200 supplied by EOS GmbH.	21
Figure 2.9 – An example of a part with surfaces that exhibit the ‘Orange Peel’ effect.	22
Figure 2.10 – An illustration highlighting the effect that contrasting powder particle morphologies and size distributions have on their powder packing efficiencies during LS.	24
Figure 2.11 – An illustration highlighting the different optical interactions (absorbance, reflectance and transmission) that occur between the laser beam and powder bed during LS. Adapted from Laumer et al. [51].	25
Figure 2.12 – An illustrative DSC thermograph showing the typical thermal behaviours of feedstock and laser sintered PA12.	26
Figure 2.13 – Example profiles with identical S_a and S_q roughnesses but contrasting (a) Skewness and (b) Kurtosis distributions. Adapted from Gadelmawla et al. [85].	32
Figure 2.14 – An illustrative example of a surface which includes re-entrant / undercut features.	35
Figure 2.15 – An illustration highlighting the difference between the (a) apparent area of contact and (b) real area of contact of a surface.	37

Figure 2.16 – The typical wear trend a component will sustain over its lifetime. Adapted from Williams [116].	40
Figure 2.17 – An illustration highlighting the mechanism of adhesive wear. Adapted from Adelbary [126].	41
Figure 2.18 – Contrasting abrasive wear mechanisms, specifically (a) the plastic grooving of POM and (b) the cutting of Epoxy [128].	43
Figure 2.19 – Lancaster’s correlation between the abrasive wear rate of a variety of polymers and the inverse product of their σb and ϵb values. Adapted from Lancaster [176]. Polymer abbreviations that have not been previously defined include (ordered alphabetically): LDPE (Low-density polyethylene); PA6.6 (Polyamide 6.6); PPO (Polyphenylene oxide); PTFCE (Polychlorotrifluoroethylene); PTFE (Polytetrafluoroethylene); PVC (Polyvinyl chloride); and PVDC (Polyvinylidene chloride).	43
Figure 3.1 – An illustration outlining the general High Speed Sintering build process.	51
Figure 3.2 – An illustration highlighting the selective jetting of detailing fusion agents during the MJF process.	52
Figure 3.3 – A comparison between general polymer COF data collated by Myshkin et al. [108] and the laser sintered PA12 mean COF results summarised in Table 3.3 .	57
Figure 3.4 – Ashby plot displaying the relative variation between different polymer types with respect to their strength and ductility.	65
Figure 4.1 – SEM images highlighting the typical morphologies of the (a) virgin – PA12 and (b) 50/50 – PA12 powders used throughout this investigation.	70
Figure 4.2 – DSC obtained heating and cooling curves of virgin – PA12 and 50/50 – PA12 powders.	71
Figure 4.3 – (a) A schematical illustration of an EOS P100 system (adapted from Goodridge et al. [19]), as well as (b) the system itself and (c) a snapshot of it partway through building.	74
Figure 4.4 – A tensile specimen mounted between the grips of the Tinius Olsen H5KS tensometer used throughout this doctoral work.	76
Figure 4.5 – The specific geometry of an ASTM D638-14 Type 1 tensile specimen. Adapted from ASTM D638-14 [175].	77
Figure 4.6 – The specific (a) FV and (b) SEM microscopy systems used throughout this doctoral work.	78
Figure 4.7 – Example jigs that were used to (a) position and (b) secure samples during FV microscopy analysis.	79
Figure 4.8 – The specific pin-on-disk, ball-on-flat, rotating, uni-directional test set-up adopted throughout this doctoral work.	82
Figure 4.9 – (a) Tribological test specimen geometries and (b) the configurations in which they were subject to dynamic contact relative to one another.	83
Figure 4.10 – Example normal load and sliding speed data recorded by the UMT during the early stages of a 15N – 0.35ms ⁻¹ sliding test.	84
Figure 4.11 – Example roughness profiles illustrating the height and lay of the scratches produced when preparing steel disk samples by surface grinding.	86
Figure 5.1 – A schematic illustrating the quantity, geometry and positioning of samples produced in this study (Chapter 5).	93
Figure 5.2 – The surfaces that were evaluated on each of the different specimen geometries.	94
Figure 5.3 – Micro-CT obtained binarised scan images highlighting the side surface morphologies of samples produced at varying laser powers, specifically (a) 18W, (b) 21W and (c) 24W. The	

central regions of each cross-sectional slice have been concealed to focus the reader's attention to the contour of each sample.	99
Figure 5.4 – A schematic highlighting the mechanism of secondary sintering, which characteristically occurs at the interface between pre-defined part perimeters and surrounding powder.....	100
Figure 5.5 – Typical FV microscopy obtained scan images of a (a) top and (b) bottom laser sintered PA12 surface. Both scan areas are 3.7 mm × 3.7 mm in size and were captured from the same randomly selected 21W sample designated for FV microscopy analysis.	101
Figure 5.6 – The distribution in S_q roughness of top and bottom surfaces (built at varying applied energy densities) across the powder bed.	103
Figure 5.7 – The distribution in S_z roughness of top and bottom surfaces (built at varying applied energy densities) across the powder bed.	106
Figure 5.8 – The distribution in S_{sk} roughness of top and bottom surfaces (built at varying applied energy densities) across the powder bed.	109
Figure 5.9 – A schematic highlighting the ‘Smoothing Effect’ intrinsic to contact profilometry. Adapted from Bhushan [185].	110
Figure 5.10 – An illustration highlighting the proposed mechanism of top surface modification by finish layer powder particle adhesion.	112
Figure 5.11 – The distribution in S_{ku} roughness of top and bottom surfaces (built at varying applied energy densities) across the powder bed. A translucent reference plane at the critical Kurtosis value of three ($S_{ku} = 3$) has also been included.....	113
Figure 6.1 – An illustration of the mechanism of top surface modification by finish layer powder particle adhesion.....	119
Figure 6.2 – The experimental procedure followed in this study to investigate the mechanisms of polymer melt viscous flow and finish layer powder particle adhesion.	121
Figure 6.3 – The layout of each LS build performed as part of this study, including details of which specimens were manufactured with and without finish layers in LS builds (a) 1, (b) 2, (c) 3, and (d) 4.....	122
Figure 6.4 – The top surface S_q and S_{sk} roughness results relative to applied energy density. Corresponding R^2 values show how well each regression curve fitted the roughness data collected.	128
Figure 6.5 – FV microscopy outputs of two laser sintered PA12 top surfaces with contrasting S_q and S_{sk} roughnesses. More specifically, (a) a top surface of a sample built via configuration 7 which recorded the lowest S_q but largest S_{sk} values - corresponding surfaces were peak dominated and comprised of relatively small surface amplitudes; and (b) a top surface of a sample built via configuration 4 which recorded the highest S_q but lowest S_{sk} values - corresponding surfaces were valley dominated and comprised of relatively large surface amplitudes.....	129
Figure 6.6 – A Pareto chart showing the extent to which laser power, scan speed and beam spacing influenced the top surface S_q roughnesses of 50/50 – PA12 parts produced as part of the DoE.....	130
Figure 6.7 – Main effects plot showing the mean S_q responses at low and high laser parameter values.....	130
Figure 6.8 – Contour plots showing the different laser parameter interaction effects on top surface S_q roughness. Dark blue regions represent the laser parameter combinations that should lead to relatively low S_q roughness values, whereas dark green regions indicate the opposite.	131
Figure 6.9 – The effect of beam spacing on powder bed laser exposure for a given spot size diameter of 0.42mm.....	132

Figure 6.10 – A Pareto chart showing the extent to which laser power, scan speed and beam spacing influenced the top surface S_{sk} roughnesses of 50/50 – PA12 parts produced as part of the DoE.....	135
Figure 6.11 – Main effects plot showing the mean S_{sk} responses at low and high laser parameter values.....	135
Figure 6.12 – Contour plots showing the different laser parameter interaction effects on top surface S_{sk} roughness. Dark blue regions represent the laser parameter combinations that should lead to relatively low S_{sk} roughness values, whereas dark green regions indicate the opposite. ..	136
Figure 6.13 – Predicted and measured validation specimen top surface S_q and S_{sk} roughnesses.	138
Figure 6.14 – Top surface S_q and S_{sk} roughness results relative to applied energy density, with the inclusion of validation specimens. Corresponding R^2 values show how well each regression curve fitted the roughness data collected. S_q and S_{sk} curve inflection points occur at 46.5 mJmm^{-2} and 48.4 mJmm^{-2} , respectively.	139
Figure 6.15 – Height maps of laser sintered 50/50 – PA12 top surfaces built using (a) standard and (b) optimised laser parameters (without finish layers). Employing the latter promoted the mechanism of polymer melt viscous flow, resulting in corresponding topographies having comparatively fewer pores.	142
Figure 6.16 – PrimePart top surfaces built (a) with and (b) without finish layers.	145
Figure 6.17 – A comparison between the Young’s Modulus, Ultimate Tensile Strength and Elongation at break of (a) 50/50 – PA12, (b) virgin – PA12 and (c) PrimePart samples built with and without finish layers (as denoted by the abbreviations WFLs and NFLs, respectively).....	147
Figure 7.1 – (a) the geometry of the scratch test specimens, as well as a (b) scratch test in progress.	155
Figure 7.2 – The mean COF responses recorded during 10N, 15N and 20N sliding on the top and bottom surfaces of each of the three laser sintered 50/50-PA12 samples evaluated. The highlighted regions within each mean response plot represents the maximum and minimum values recorded. The areas within each dashed purple sector draw attention to the distances and magnitudes over which COF differed as a result of surface orientation specifically.	156
Figure 7.3 – An illustration highlighting the travel path of the pin during running-in.	157
Figure 7.4 – Scratch coefficient of friction (SCOF) and indenter penetration depth data as a function of scratch distance and applied normal load for each top and bottom laser sintered PA12 surface evaluated. Highlighted regions denote the distances and magnitudes over which top and bottom surface SCOF responses varied.	158
Figure 7.5 – The changes in specific wear rate of top and bottom laser sintered PA12 surfaces during running-in.	160
Figure 7.6 – Empirically determined wear volume data and corresponding $Vabr$ approximations (calculated via the aforementioned modified and original Ratner-Lancaster expressions) for each laser sintered PA12 (a) top and (b) bottom surface evaluated. $Vabr$ approximations are plotted at the same distance intervals as the measured data.	163
Figure 7.7 – Resultant pin and disk top surfaces at each interval during 15N sliding.	164
Figure 7.8 – Resultant pin and disk bottom surfaces at each interval during 15N sliding. Please note that the 25m pin sample surface could not be accurately characterised due to an unfamiliar software-related misalignment error when executing the difference measurement.	165
Figure 8.1 – The variations in polymer sliding intrinsically induced by the different contact configurations employed during testing.....	172
Figure 8.2 – The north, east, south and west locations evaluated on each disk surface post-testing.	174

Figure 8.3 – The four quadrants scanned when polymer pin worn areas were larger than the evaluation region of the SEM (at $\times 50$ magnification).	174
Figure 8.4 – A comparison between the COF results determined within this study with those collated from literature and previously presented in Chapter 3 , specifically Table 3.3	177
Figure 8.5 – The mean (a) COF and (b) friction force responses recorded during $3\text{N} - 0.05\text{ms}^{-1}$ (low load / low speed), metal pin on polymer disk sliding. The highlighted regions within each response plot represents the maximum and minimum values recorded. The distance between dashed vertical lines within the former indicates the period over which mean COF and Ff values were calculated.	178
Figure 8.6 – The mean transient COF response recorded during $3\text{N} - 0.05\text{ms}^{-1}$ (low load / low speed), metal pin on polymer disk sliding.	179
Figure 8.7 – The mean (a) COF and (b) friction force responses recorded during $3\text{N} - 0.5\text{ms}^{-1}$ (low load / high speed), metal pin on polymer disk sliding. The highlighted regions within each response plot represents the maximum and minimum values recorded. The distance between dashed vertical lines within the former indicates the period over which mean COF and Ff values were calculated.	180
Figure 8.8 – The mean (a) COF and (b) friction force responses recorded during $30\text{N} - 0.05\text{ms}^{-1}$ (high load / low speed), metal pin on polymer disk sliding. The highlighted regions within each response plot represents the maximum and minimum values recorded. The distance between dashed vertical lines within the former indicates the period over which mean COF and Ff values were calculated.	181
Figure 8.9 – The mean transient COF response recorded during $30\text{N} - 0.05\text{ms}^{-1}$ (high load / low speed), metal pin on polymer disk sliding.	182
Figure 8.10 – The mean (a) COF and (b) friction force responses recorded during $30\text{N} - 0.5\text{ms}^{-1}$ (high load / high speed), metal pin on polymer disk sliding. The highlighted regions within each response plot represents the maximum and minimum values recorded. The distance between dashed vertical lines within the former indicates the period over which mean COF and Ff values were calculated.	182
Figure 8.11 – The mean (a) COF and (b) friction force responses recorded during $3\text{N} - 0.05\text{ms}^{-1}$ (low load / low speed), polymer pin on metal disk sliding. The highlighted regions within each mean response plot represents the maximum and minimum values recorded. The distance between dashed vertical lines within the former indicates the period over which mean COF and Ff values were calculated.	183
Figure 8.12 – A detailed overview of the main friction-related features that occurred during $3\text{N} - 0.05\text{ms}^{-1}$ (low load / low speed) polymer pin on metal disk sliding.	184
Figure 8.13 – The mean (a) COF and (b) friction force responses recorded during $3\text{N} - 0.5\text{ms}^{-1}$ (low load / high speed), polymer pin on metal disk sliding. The highlighted regions within each mean response plot represents the maximum and minimum values recorded. The distance between dashed vertical lines within the former indicates the period over which mean COF and Ff values were calculated.	185
Figure 8.14 – The mean (a) COF and (b) friction force responses recorded during $30\text{N} - 0.05\text{ms}^{-1}$ (high load / low speed), polymer pin on metal disk sliding. The highlighted regions within each mean response plot represents the maximum and minimum values recorded. The distance between dashed vertical lines within the former indicates the period over which mean COF and Ff values were calculated.	186
Figure 8.15 – The transient COF responses recorded during $30\text{N} - 0.05\text{ms}^{-1}$ (high load / low speed), polymer pin on metal disk sliding.	187

Figure 8.16 – The mean (a) COF and (b) friction force responses recorded during 30N – 0.5ms ⁻¹ (high load / high speed), polymer pin on metal disk sliding. The highlighted regions within each mean response plot represents the maximum and minimum values recorded. The distance between dashed vertical lines within the former indicates the period over which mean COF and <i>F_f</i> values were calculated.....	187
Figure 8.17 – Schematic plots highlighting the typical variations in COF observed when converse contact configurations were employed during testing.	190
Figure 8.18 – A schematic illustrating how the variation in COF values in Figure 8.19 were calculated.	191
Figure 8.19 – The magnitudes by which COF fluctuated during each sliding condition. More specifically, variation in sliding values were determined by calculating the standard deviation of COF results recorded between consecutive 50m increments during each sliding test, as shown in Figure 8.18	191
Figure 8.20 – Contour plots showing the relationship between COF, normal load and sliding speed for both contact configurations evaluated.	193
Figure 8.21 – A Pareto chart showing the extent to which normal load, sliding speed and contact configuration influenced friction force.	193
Figure 8.22 – Microscopy images captured after the second repeat 3N – 0.05ms ⁻¹ (low load / low speed) sliding test. These include wear scars obtained by FV microscopy at (a) north and (b) east locations, as well as SEM images obtained at (c) west and (d) south locations. The orientation of each arrow denotes the instantaneous direction of rotation of each disk region relative to the metal pin, and dashed lines signify the mean wear track width determined for this sliding condition.	197
Figure 8.23 – Microscopy images captured after the second repeat 3N – 0.5ms ⁻¹ (low load / high speed) sliding test. These include wear scars obtained by FV microscopy at (a) north and (b) east locations, as well as SEM images obtained at (c) west and (d) south locations. The orientation of each arrow denotes the instantaneous direction of rotation of each disk region relative to the metal pin, and dashed lines signify the mean wear track width determined for this sliding condition.	199
Figure 8.24 – Microscopy images captured after the second repeat 30N – 0.05ms ⁻¹ (high load / low speed) sliding test. These include wear scars obtained by FV microscopy at (a) north and (b) east locations, as well as SEM images obtained at (c) west and (d) south locations. The orientation of each arrow denotes the instantaneous direction of rotation of each disk region relative to the metal pin. Purple arrows specify the locations in which evidence of plastic flow can be seen.....	200
Figure 8.25 – Microscopy images captured after the second repeat 30N – 0.5ms ⁻¹ (high load / high speed) sliding test. These include wear scars obtained by FV microscopy at (a) north and (b) east locations, as well as SEM images obtained at (c) west and (d) south locations. The orientation of each arrow denotes the instantaneous direction of rotation of each disk region relative to the metal pin. Purple circled regions and arrow icons specify the locations in which evidence of surface melting and plastic flow can be seen, respectively.	202
Figure 8.26 – SEM scan images of a (a) polymer pin worn surface and (b) metal disk sample (east location) captured after 3N – 0.05ms ⁻¹ (low load / low speed) sliding, specifically from test 2.....	203
Figure 8.27 – An example of a worn polymer pin surface that was too reflective to be successfully scanned by FV microscopy.....	204
Figure 8.28 – SEM scan images of a (a) polymer pin worn surface and (b) metal disk sample (east location) captured after 3N – 0.5ms ⁻¹ (low load / high speed) sliding, specifically from test 2. Each circled location highlights a region in which clusters of asperity peaks can be seen.	205

Figure 8.29 – SEM scan images of a (a) polymer pin worn surface and (b) metal disk sample (east location) captured after 30N – 0.05ms ⁻¹ (high load / low speed) sliding, specifically from test 2. ..	206
Figure 8.30 – SEM scan images of a (a) polymer pin worn surface and (b) metal disk sample (east location) captured after 30N – 0.5ms ⁻¹ (high load / high speed) sliding, specifically from test 2. ...	207
Figure 8.31 – Illustrations highlighting the impact lay direction had on the magnitude of polymer wear debris that accumulated within adjacent scratch valleys during sliding.	210
Figure 8.32 – An illustration highlighting the differences in contact geometry induced when converse contact configurations were employed.	211
Figure 8.33 – Contour plots showing the relationship between wear rate, normal load and sliding speed for both contact configurations evaluated.	213
Figure 8.34 – A Pareto chart showing the extent to which normal load, sliding speed and contact configuration influenced wear rate.	214
Figure 9.1 – A schematic illustrating the geometry and positioning of samples produced within this study (Chapter 9).	222
Figure 9.2 – SEM images of each feedstock material, including (a) Virgin – PA12, (b) PTFE – PA12, (c) Graphite – PA12 and (d) MoS ₂ – PA12 powders. Corresponding solid lubricant particles have been circled in orange.	226
Figure 9.3 – Micro-CT rendered volumes of (a) Virgin – PA12, (b) PTFE – PA12, (c) Graphite – PA12 and (d) MoS ₂ – PA12 samples. Brighter voxels represent locations in which more radiation was attenuated, and thus the presence of inclusions and / or contaminants within each laser sintered PA12 matrix.	227
Figure 9.4 – Differential Scanning Calorimetry (DSC) obtained heating and cooling curves of each powdered material evaluated within this study.	230
Figure 9.5 – Top surface topography information, including the mean (a) S _q and (b) S _{sk} roughness values determined for each material evaluated within this study.	232
Figure 9.6 – The resultant tensile curve of each material specimen evaluated within this study.	233
Figure 9.7 – The mean COF responses exhibited during (a) Virgin – PA12, (b) PTFE – PA12, (c) Graphite – PA12 and (d) MoS ₂ – PA12 sliding. The highlighted regions within each mean response plot represents the maximum and minimum values recorded during repeat testing. It should be noted that MoS ₂ – PA12 samples could only be evaluated once during 30N sliding due to them experiencing excessive magnitudes of curl during building.	236
Figure 9.8 – The percentage differences in the mean COF values recorded for each solid lubricant filled polymeric composite relative to Virgin – PA12.	237
Figure 9.9 – The breakdown in lubrication observed during high load (30N) PTFE – PA12 sliding.	239
Figure 9.10 – Resultant (a) Virgin – PA12, (b) PTFE – PA12, (c) Graphite – PA12 and (d) MoS ₂ – PA12 surfaces and corresponding pin counterfaces after 10N and 30N sliding. Orange annotations denote the sliding directions and contacting regions of each pin counterface. The missing information within the Virgin – PA12 wear scars are due to their worn surfaces being highly reflective which inhibited light from being received by the microscope’s detector.	240
Figure 9.11 – The percentage differences in the mean specific wear rate values determined for each solid lubricant filled polymeric composite relative to Virgin – PA12.	242
Figure 9.12 – Resultant (a) Virgin – PA12, (b) PTFE – PA12, (c) Graphite – PA12 and (d) MoS ₂ – PA12 wear scar profiles.	245

List of Tables

Table 2.1 – A summary of the primary powder preparation methods used both industrially and within research. Adapted from Tan et al. [21].	20
Table 2.2 – Melting and crystallisation temperatures of virgin – PA12 in both feedstock and laser sintered form, characterised by Dadbakhsh et al. [49].	27
Table 3.1 – A summary of the findings discerned from related literature in which DoE methodologies were employed to determine the extent to which different processing parameters influenced the Ra / Sa roughnesses of laser sintered Polyamide surfaces.	49
Table 3.2 – Results obtained from several research works in which the Ra roughnesses of top, bottom and side surfaces of PA12 samples produced by LS and MJF were compared. Side surfaces refer to those built perpendicular to the powder bed and standard deviation values have been included where reported.	53
Table 3.3 – A summary of the findings discerned from related literature in the which the frictional performance of laser sintered PA12 samples were experimentally evaluated	55
Table 3.4 – A summary of the findings discerned from related literature in the which the wear behaviours of laser sintered PA12 samples were experimentally characterised	61
Table 3.5 – A selection of research works in which the wear properties of Nylon polymers were qualitatively discussed	64
Table 4.1 – Laser sintered virgin-PA2200 part properties, as determined by the material manufacturer (EOS GmbH) [171]	72
Table 4.2 – The tensile properties of samples produced in-house from virgin – PA12 and 50/50 – PA12	72
Table 4.3 – The standard PA12 LS processing parameters adopted throughout this doctoral work	75
Table 4.4 – The testing procedure adopted during friction and wear testing	84
Table 4.5 – The ranges over which operating conditions were varied throughout this doctoral work	87
Table 4.6 – The methods used to determine laser sintered PA12 wear volumes	89
Table 5.1 – An outline of the metrology methods used to characterise the effects of each of the surface influencing factors investigated within this study.	94
Table 5.2 – Summary of the amplitude roughness parameters used within this study	95
Table 5.3 – A comparison of the Sq and Rq roughness results, and corresponding standard deviations, determined for both the top and bottom surfaces of laser sintered PA12 samples built at varying applied energy densities and evaluated by FV microscopy and contact profilometry.	104
Table 5.4 – A comparison of the Sz and Rz roughness results, and corresponding standard deviations, determined for both the top and bottom surfaces of laser sintered PA12 samples built at varying applied energy densities and evaluated by FV microscopy and contact profilometry.	107

Table 5.5 – A comparison of the Ssk and Rsk roughness results, and corresponding standard deviations, determined for both the top and bottom surfaces of laser sintered PA12 samples built at varying applied energy densities and evaluated by FV microscopy and contact profilometry..	110
Table 5.6 – A comparison of the Sku and Rku roughness results, and corresponding standard deviations, determined for both the top and bottom surfaces of laser sintered PA12 samples built at varying applied energy densities and evaluated by FV microscopy and contact profilometry..	114
Table 5.7 – A summary of the key findings ascertained during Chapter 5	116
Table 6.1 – The LS build parameters employed as part of the DoE (LS build 1)	123
Table 6.2 – The different LS build configurations evaluated as part of the DoE (LS build 1)	123
Table 6.3 – The different build configurations evaluated as part of build 2	125
Table 6.4 – The LS build parameters employed when producing virgin – PA12 and PrimePart samples for finish layer analysis (LS builds 3 and 4, respectively).	126
Table 6.5 – The top surface roughness results, and corresponding standard deviation values, of all the samples evaluated as part of the DoE (build 1)	128
Table 6.6 – A comparison between standard and model optimised laser parameters for minimising top surface Sq roughness. Corresponding coded unit values have also been included	133
Table 6.7 – Predicted and measured validation specimen top surface roughness results	138
Table 6.8 – A qualitative comparison of laser sintered 50/50 – PA12 top surfaces manufactured with and without finish layers using standard and optimised laser parameters	140
Table 6.9 – A quantitative comparison of laser sintered 50/50 – PA12 top surfaces manufactured with and without finish layers using standard and optimised laser parameters. Both mean and corresponding standard deviation values have been included	141
Table 6.10 – A qualitative comparison of laser sintered virgin-PA12 top surfaces manufactured with and without finish layers using standard and optimised laser parameters	143
Table 6.11 – A quantitative comparison of laser sintered virgin-PA12 top surfaces manufactured with and without finish layers using standard and optimised laser parameters. Both mean and corresponding standard deviation values have been included	143
Table 6.12 – The mean tensile properties, and corresponding standard deviation values, of 50/50 – PA12, virgin – PA12 and PrimePart samples built with and without finish layers (as denoted by the abbreviations WFLs and NFLs, respectively).....	146
Table 6.13 – A forecast of annual finish layer material costs incurred when processing PA12 on a variety of LS systems.....	148
Table 7.1 – The mean Sq and Ssk roughnesses, and corresponding standard deviations, of the top and bottom laser sintered disk surfaces used within this study	155
Table 7.2 – The specific values used to compute abrasive wear volume approximations via original and modified Ratner-Lancaster expressions, as well as their sources of ascertainment	162
Table 8.1 – An overview of the pin and disk specimens used within this study.....	170
Table 8.2 – The varying operating conditions employed as part of the DoE	172
Table 8.3 – The different sliding conditions evaluated as part of the DoE.....	173

Table 8.4 – The mean F_f results, and corresponding standard deviation values, determined for each of the sliding conditions evaluated as part of the DoE. Standard deviation values indicate the variation between repeat tests.....	175
Table 8.5 – The mean COF results, and corresponding standard deviation values, determined for each of the sliding conditions evaluated as part of the DoE. Standard deviation values indicate the variation between repeat tests.....	176
Table 8.6 – The increases in COF, as well as their corresponding standard deviation values, measured between sliding distances of 300m and 995m during polymer pin on metal disk sliding. In order to calculate the difference between COF values at 300m and 995m, mean values for each were first computed between 295m – 305m and 990m – 1000m, respectively	189
Table 8.7 – Mean wear rate results, and corresponding standard deviation values, for each of the sliding conditions evaluated as part of the DoE. Standard deviation values indicate the variation between repeat tests	194
Table 8.8 – Mean specific wear rate results, and corresponding standard deviation values, for each of the sliding conditions evaluated as part of the DoE. Standard deviation values indicate the variation between repeat tests.....	195
Table 8.9 – FV microscopy obtained scan images of metal pin surfaces captured before and after each second repeat sliding test. Despite only one set of metal pin surfaces being presented for each sliding condition evaluated, the volume of polymer material that accumulated on each remained consistent between repeat tests. Circled orange regions represent the contact area of each metal pin surface evaluated	209
Table 8.10 – A comparison between initial Hertzian contact area approximations and polymer pin mean worn areas measured post-testing. Corresponding standard deviation values are also given for the latter.....	212
Table 8.11 – A comparison between initial Hertzian contact pressure approximations and the mean resultant contact stresses (p) calculated post-testing. Corresponding standard deviation values are also given for latter	212
Table 8.12 – A summary of the key findings ascertained during Chapter 8	216
Table 9.1 – Solid lubricant particle sizes, as quoted by their suppliers	221
Table 9.2 – The DSC programme employed within this study.....	224
Table 9.3 – A qualitative description of the curl induced during the processing of each material. Resultant part warpages were as follows: $a \sim b < c < d$	229
Table 9.4 – The onset of crystallisation temperatures of each powdered material. Specific values were determined from the DSC obtained cooling curves presented in Figure 9.4	230
Table 9.5 – Qualitative and quantitative descriptions of the top surface topographies of each laser sintered material. The evaluation areas depicted within each scan image are 3.7mm x 3.7mm in size	231
Table 9.6 – The mean tensile properties of each material, as well as their corresponding standard deviation values	233
Table 9.7 – The mean COF values recorded for each material, as well as their corresponding standard deviation values	237
Table 9.8 – The mean specific wear rate values determined for each material, as well as their corresponding standard deviation values	241

Acronyms

AM	Additive Manufacturing
3D	Three Dimensional
PBF	Powder Bed Fusion
LS	Laser Sintering
HSS	High Speed Sintering
MJF	Multi Jet Fusion
2D	Two Dimensional
PA	Polyamide
PA12	Polyamide-12
PSD	Particle Size Distribution
SEM	Scanning Electron Microscopy
AOR	Angle of Repose
DSC	Differential Scanning Calorimetry
DPM	Degree of Particle Melt
UTS	Ultimate Tensile Strength
EaB	Elongation at Break
COF	Coefficient of Friction
YM	Young's Modulus
UTS	Ultimate Tensile Strength
UMT	Universal Mechanical Tester
SD	Standard Deviation
FV	Focus Variation
DoE	Design of Experiments

Nomenclature

T_b	Powder Bed Temperature	°C
T_g	Glass Transition Temperature	°C
T_m	Melting Temperature	°C
x_n	Neck Length Between Adjacent Particles	µm
a_o	Initial Particle Radius	µm
Γ	Coefficient of Surface Tension	
t	Time	S
η_0	Zero-Shear Viscosity	PaS
P	Laser Power	W
x_{scan}	Beam Spacing	mm
v_{scan}	Scan speed	m s ⁻¹
ρ	Density	g cm ⁻³
D_{LB}	Laser Beam Diameter	mm
h	Layer Height	mm
C_{PB}	Specific Heat Capacity of the Powder Bed	J (Kg · °C) ⁻¹
l_f	Enthalpy of Fusion	J Kg ⁻¹
R_r	Fraction of Reflected Radiation	
E_D	Energy Density	mJ mm ⁻²
VE_D	Volumetric Energy Density	mJ mm ⁻³
T_c	Crystallisation Temperature	°C
wt%	Weight Percentage Fraction	
S_a	Arithmetic Mean Height Roughness	µm
S_q	Root Mean Square Roughness	µm
S_z	Maximum Peak-to-Valley Height Roughness	µm
S_{sk}	Skewness	
S_{ku}	Kurtosis	
F_f	Friction Force	N
N	Normal Load	N
μ	Coefficient of Friction	
A_N	Apparent Area of Contact	m ²
v	Sliding Speed / Velocity	m s ⁻¹

A_R	Real Area of Contact	m^2
F_{fA}	Adhesive Component of Friction	N
F_{fD}	Deformation Component of Friction	N
ψ	Plasticity Index	
H	Indentation Hardness	
β	Asperity Peak Tip Radius	μm
E'	Reduced Elastic Modulus	Pa
E	Elastic / Young's Modulus	MPa
ν	Poisson's Ratio	
T	Temperature	$^{\circ}\text{C}$
V	Wear Volume	mm^3
k	Wear Coefficient	
x	Sliding Distance	m
σ_b	Break Stress	MPa
ε_b	Elongation at Break	%
H_s	Scratch Hardness	N mm^{-2}
q	Scratch Hardness Constant	
d	Wear Scar Width	mm
σ_{UTS}	Ultimate Tensile Strength	MPa
R	Wear Scar Radius	mm
r	Pin End Radius	mm
Δm	Mass Loss	g
W	Wear Rate	$\text{mm}^3 \text{m}^{-1}$
W_s	Specific Wear Rate	$\text{Nmm}^3 \text{m}^{-1}$
σ_{yield}	Yield Strength	MPa
$S\emptyset$	Spherical Diameter	mm
A_{\emptyset}	Circular Area Approximation	mm^2
$\phi_{\%}$	Percentage Porosity	%
d_p	Penetration Depth	μm
$\% \Delta COF$	Percentage Change in COF	%

Chapter 1

Introduction

Chapter Summary

This chapter states the focus and motivation of this work, followed by the overall research aim, corresponding list of objectives and an outline of the chapters that comprise this thesis.

1.1 The Focus of this Thesis

This work investigated the surface, friction and wear properties of laser sintered Polyamide-12 components. These three linked themes collectively formed the framework of this thesis, as summarised below:

- a. **Surfaces:** The topographies of laser sintered Polyamide-12 surfaces were comprehensively characterised.
- b. **Friction and wear:** The effects of surface orientation and varying operating conditions were analysed during transient and steady-state sliding.
- c. **Modifying tribological performance:** The inclusion of solid lubricants within laser sintered Polyamide-12 components was explored as a way of modifying their friction and wear properties.

More generally, this research consolidated knowledge between polymer Laser Sintering (LS) and tribology to provide novel insights into the key surface and sliding phenomena pertinent to the vast majority of polymer laser sintered components.

1.2 Research Motivation

Today, Additive Manufacturing (AM) technologies are increasingly being used to manufacture functional end-use components across a range of industries, including aerospace; healthcare and medical; architecture and construction; and consumer goods [1].

In 2021, approximately 33.7% of all AM parts produced were intended for end-use applications [2]. Despite this recent shift in utilising AM for final part production, concerns regarding resultant part quality continue to hinder the further adoption of polymer AM technologies [3–7].

Therefore, greater unification between tribology and polymer AM, particularly LS, is required to better understand the in-service functionality of parts produced and establish their suitability for end-use applications.

1.3 Aims and Objectives

The aim of this research project was to characterise the surface, friction and wear properties of laser sintered Polyamide-12 components.

As previously mentioned in **Section 1.2**, polymer AM technologies are used for a variety of applications across a plethora of different industries. Therefore, this work aimed to holistically investigate the friction and wear behaviours of laser sintered Polyamide-12 components, rather than focus on a single, or limited number of application-specific interactions. In doing so, this work will serve as a benchmark for future studies that will also aim to evaluate the dry sliding behaviours of analogous polymer components.

To achieve the aim of this research project, the following objectives were defined:

- Review existing literature pertaining to both polymer Laser Sintering and tribology.
- Characterise the surface topographies of laser sintered Polyamide-12 components to ascertain how, and the extent by which, they are influenced by key processing parameters.
- Investigate the dry sliding friction and wear responses of laser sintered Polyamide-12 components, particularly when subject to varying operating conditions.
- Assess whether the friction and wear properties of laser sintered Polyamide-12 components can be modified.

1.4 Thesis Structure

This thesis consists of ten chapters, which have been structured in accordance with the aforementioned aims and objectives, as well as the gaps in existing research identified when reviewing related literature in **Chapter 3**. An overview of **Chapters 2 – 10** is given below.

Chapter 2 included background information on aspects related to polymer LS and tribology so that a fundamental understanding of both disciplines could be attained.

Chapter 3 collated and critically reviewed existing literature pertaining to the surface, friction and wear properties of laser sintered Polyamide-12 components, allowing any gaps in existing knowledge to be highlighted.

Chapter 4 outlined the materials and methods fundamental to this doctoral work. These included pertinent material properties, the LS build process followed, and the primary characterisation techniques employed to evaluate the resultant bulk, surface and tribological properties of samples produced.

Chapter 5 characterised laser sintered Polyamide-12 surfaces apropos to amplitude roughness descriptor; applied energy density; XY positioning across the powder bed; part orientation; and metrology method.

Chapter 6 expanded on **Chapter 5** by determining the extent to which the mechanisms of polymer melt viscous flow and finish layer powder particle adhesion influence the top surface topographies of laser sintered polymer components.

Chapter 7 characterised the friction and wear properties of laser sintered Polyamide-12 surfaces during running-in.

Chapter 8 investigated how the sliding behaviours of laser sintered Polyamide-12 components were affected by varying operating conditions. This involved performing different sliding tests in accordance with a Design of Experiments (DoE) to ascertain the extent by which normal load, sliding speed and contact configuration influenced the friction and wear properties of parts produced.

Chapter 9 explored the potential of including solid lubricants within Polyamide-12 feedstock powders (prior to processing via LS) as a means of modifying the friction and wear properties of parts produced.

Chapter 10 discussed how the aim of this project was achieved by summarising the key conclusions attained from each of the experimental studies that comprise this thesis. Additionally, the scope for further work was highlighted, and areas for future research were proposed.

A schematic illustrating the workflow in which this doctoral research has executed can be seen in **Figure 1.1**.

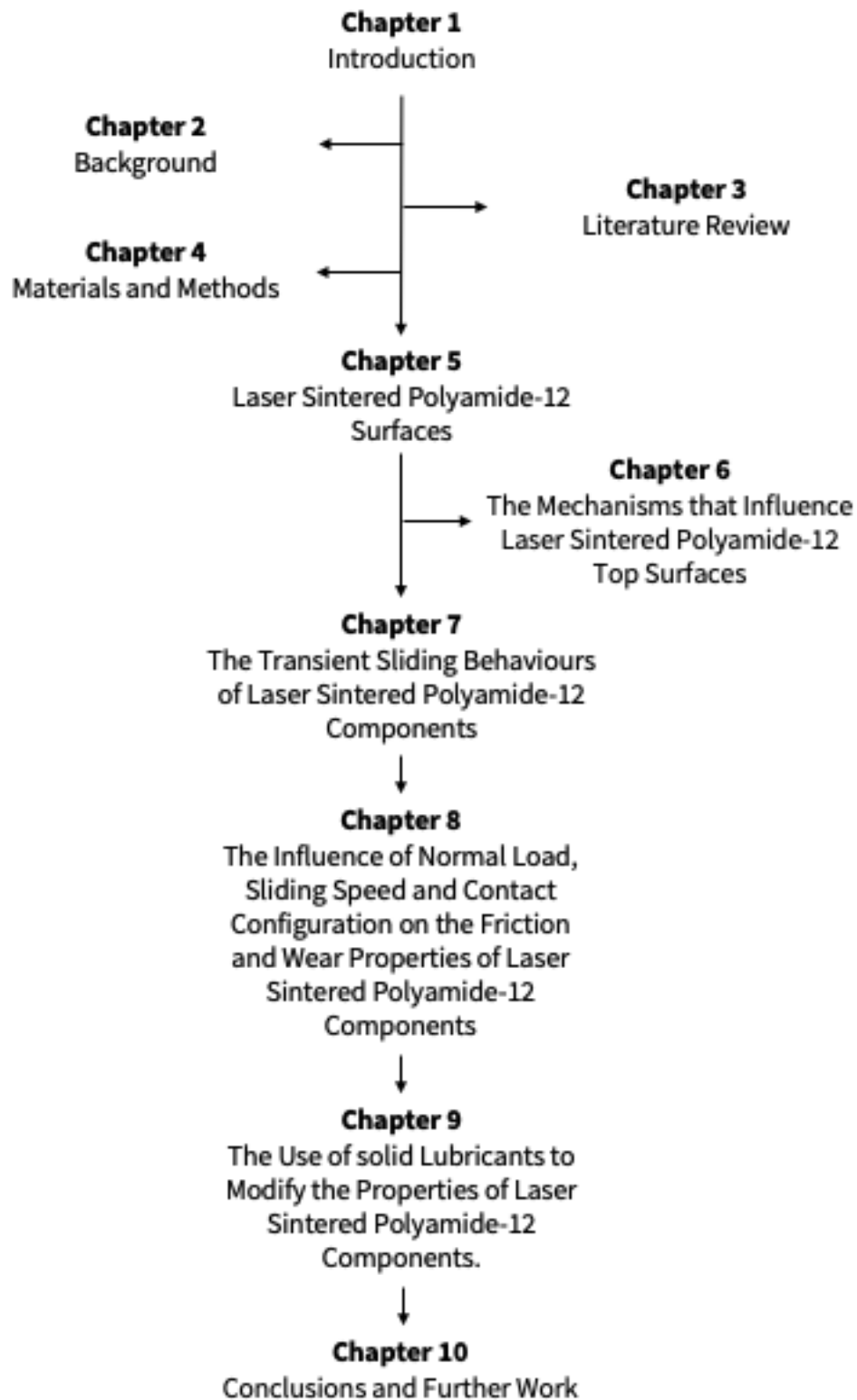


Figure 1.1 – A schematic illustrating both the structure of this thesis and sequence in which it was executed.

Chapter 2

Background

Chapter Summary

This chapter provides background insight into both polymer Laser Sintering and tribology, including relevant theory and associated methodologies. This prerequisite information will serve as reference for work discussed in subsequent chapters.

2.1 Additive Manufacturing

*What is life beyond the extruder?
Far away from the bossy computer.
Out of sight of the glossy build plate,
out of reach of the designer's taste.*

Leon Reid IV

2.1.1 Definition

Additive Manufacturing (AM) is defined within the ISO / ASTM 52900 standard as the process of joining materials to make parts from 3-dimensional (3D) model data, usually layer upon layer, as opposed to subtractive manufacturing and formative manufacturing technologies [8].

Historically, Additive Manufacturing has also been referred to as Additive Layer Manufacturing and Solid Freeform Fabrication. But more recently, the term 3D Printing has become ubiquitous within the public domain. At the time of writing '3D Printing' yielded 1,300,000,000 search results on Google, which was ten times higher than what 'Additive Manufacturing' received.

2.1.2 Additive Manufacturing Technologies

Today, a plethora of AM techniques are commercially available [9], each distinguished by their processing methods and the forms of their compatible feedstock materials [10].

ASTM International [11] have defined the following categories to group these AM technologies, namely: Binder Jetting; Directed Energy Deposition; Material Extrusion; Material Jetting; Sheet Lamination; Vat Photopolymerisation; and Powder Bed Fusion

(PBF). An overview of each of these AM technologies is available in **Appendix A**. The focus of this work is on Powder Bed Fusion, specifically polymer Laser Sintering (LS).

2.2 Polymer Powder Bed Fusion

ASTM International define Powder Bed Fusion (PBF) [11] as an Additive Manufacturing process in which thermal energy selectively fuses regions of a powder bed. Moreover, the term ‘Powder Bed Fusion’ collectively describes a wide variety of AM powder-based technologies capable of processing polymers, metals, composites and ceramics.

Polymer-PBF techniques include Laser Sintering; High Speed Sintering (HSS); Multi Jet Fusion (MJF); Selective Inhibition Sintering; Selective Mask Sintering; Selective Heat Sintering; and proprietary variations of the aforementioned [12].

Despite consolidating material by different methods, polymer-PBF techniques share similar processing considerations. Conventionally, these considerations are categorised chronologically relative to the order in which they are executed, as shown in **Figure 2.1**. Furthermore, these pre-, in- and post- processing considerations are mutually inclusive, as the final quality of polymer-PBF produced parts is determined by the interactions between these factors.

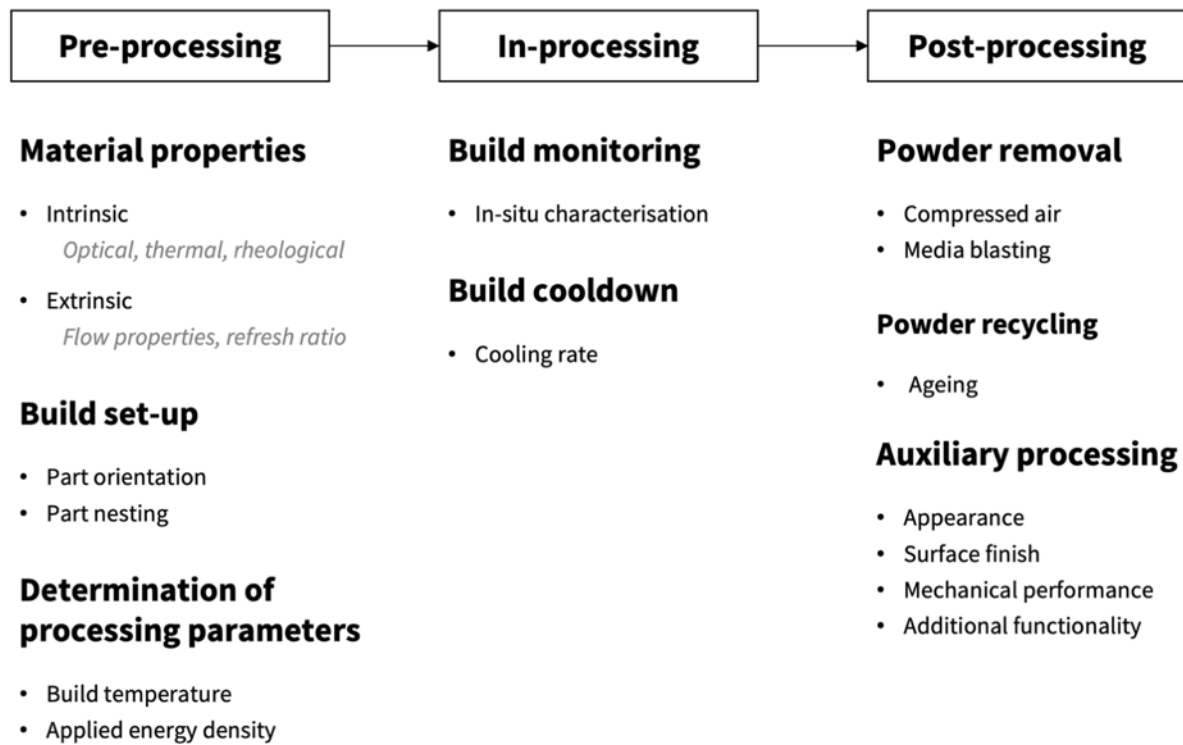


Figure 2.1 – Conventional pre-, in- and post- processing considerations pertinent to polymer-PBF.

Ultimately, polymer powders constitute the largest segment within the AM materials market [2]. This, coupled with AM's shift towards being predominantly used for final part production, provides strong indication that polymer-PBF is currently the AM technology favoured within industry for producing components for end-use applications.

2.3 Polymer Laser Sintering

Polymer Laser Sintering was the first powder-based AM technique to be developed. This took place in 1986, but it was not until 1992 that polymer LS became commercially available; the first system to incorporate this technology was DTM's Sinterstation 2000 [13]. Over the last 30 years, developments in technology and polymer science have enabled LS to advance significantly. Today, many different polymer LS systems and compatible materials are commercially available and its adoption within industry continues to grow [14].

2.3.1 Laser Sintering Build Process

Although the specific details of different systems vary, the LS build process generally consists of the following phases described below and illustrated in **Figure 2.1**:

- 1) A powder recoating device deposits a thin layer of material across the build area.
- 2) A laser (or multiple lasers) selectively fuses together the current cross-section of the part(s) being produced.
- 3) The build platform is lowered by a distance equal to the programmed layer height.
- 4) The process repeats.

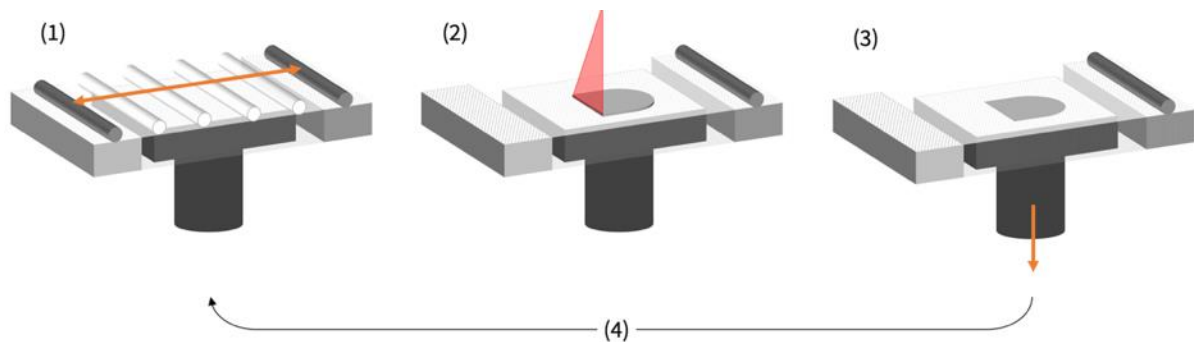


Figure 2.2 – An illustration outlining the general Laser Sintering build process.

2.3.1.1 Powder Pre-Heating

Powder pre-heating involves consecutively depositing and heating layers of powder to form a suitable base on which building can ensue.

More specifically, material is deposited across the build area by a recoating device, often a blade or roller. Initially, these deposition strokes are relatively infrequent to minimise convective heating losses and the volume of powder required to form a suitable base. In between deposition strokes, heaters bring the build chamber up to the programmed bed temperature (T_b). The optimal value for T_b depends on the crystallinity of the

thermoplastic¹ polymer being processed, which intrinsically is a function of its molecular chain arrangements. Furthermore, these can range from amorphous polymers which have entangled molecular chain structures with no long-range order, to crystalline polymers which comprise of organised and tightly packed lamellae [15], as shown in **Figure 2.3**.

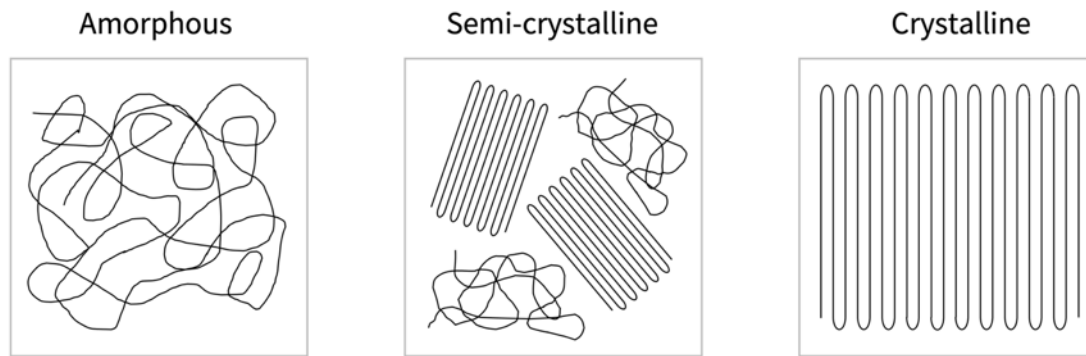


Figure 2.3 – The morphological structures of amorphous, semi-crystalline and crystalline polymers.

Gibson and Shi [16] identified that the powder bed temperatures of amorphous and crystalline polymers should be set as close as possible to, without exceeding, their glass transition temperatures (T_g) or melting temperature (T_m), respectively. The former (T_g) is the temperature at which an amorphous polymer begins to transition from a hard and relatively brittle ‘glassy’ state to a viscous or rubbery state [17]. Whereas the latter (T_m) represents the point at which a physical change in state, from solid particle to viscous polymer melt occurs.

Practically, many engineering polymers (Nylon, Polypropylene (PP), Polyethylene (PE) etc) are semi-crystalline and thus comprise of both amorphous and crystalline regions, as shown in **Figure 2.3**. Therefore, their optimal powder bed temperatures generally range between T_g and T_m [18]. Ultimately, when processing semi-crystalline polymers, the greatest T_b value attainable without inducing adjacent powder particle coalescence (prior to laser exposure) is typically selected. This is to ensure that parts produced are dimensionally accurate, but also to minimise the laser energy required to selectively raise

¹ While several thermoset polymers can be processed via LS, they remain to be significantly less widely adopted than compatible thermoplastic materials.

the temperature of regions of the powder bed to above their T_m . Furthermore, minimising the thermal gradient between sintered and un-sintered powder reduces the potential for curl to occur during building [19].

2.3.1.2 Part Consolidation

Once a suitable powder base has been created, building can take place [20]. As shown in **Figure 2.2**, this involves using a laser (or multiple lasers) to consecutively sinter and consolidate the cross-section of the build layer-by-layer in accordance with the sliced CAD file. More specifically, energy applied by the laser heats specific regions of the powder bed to above its melting point. At these locations, the powdered-polymer material changes state to a highly viscous fluid, the flow of which induces intra- and inter- layer particle sintering.

Polymer Particle Sintering

Mechanistically, the sintering of adjacent polymer powder particles occurs in three non-discrete stages – Initiation, neck growth and densification [21,22], as shown in **Figure 2.4**. During the initial two stages, the contact area at the interface between adjacent particles grows significantly and early onset necking takes place. As sintering ensues, further necking results in greater densification and particle coalescence.

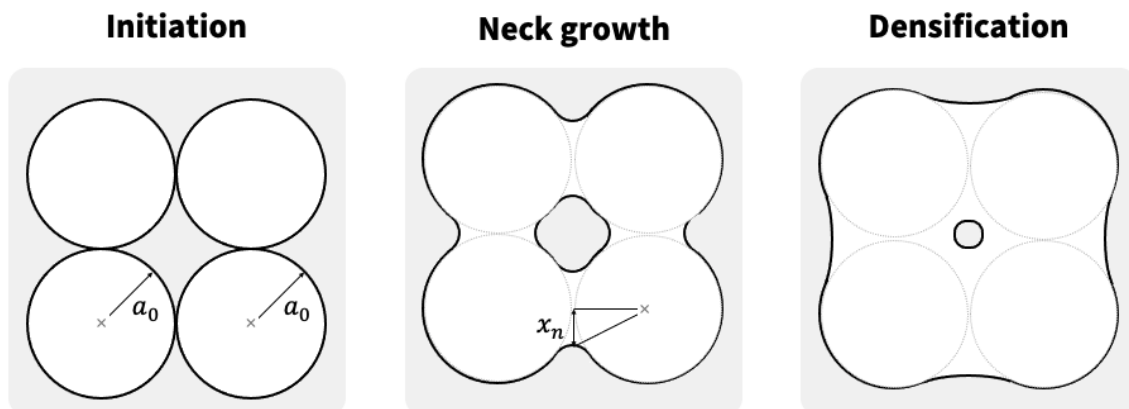


Figure 2.4 – The mechanism of polymer powder particle coalescence. Adapted from Asgarpour et al. [10].

Processing Parameters

Practically, several processing parameters can be controlled when executing a LS build², the primary of which are discussed below.

Influential laser-related processing parameters include laser power (P), beam spacing (x_{scan}) and scan speed (v_{scan}).

Laser power describes the magnitude of energy transferred to the powder bed per unit time and can be approximated by **Equation 2.1** below [16]:

$$P = \frac{v_{scan} \cdot \rho \cdot D_{LB} \cdot h [C_{PB}(T_m - T_b) + l_f]}{(1 - R_r)}$$

Equation 2.1

where ρ is the density of the material being processed, D_{LB} is the diameter of the laser beam, h is the layer height of the build, C_{PB} is the specific heat capacity of the powder bed, l_f is the enthalpy of fusion of the powder material and R_r is the fraction of laser light reflected by the powder bed.

Beam spacing is equal to the distance between parallel laser scans and scan speed is the velocity at which the laser beam traverses across the powder bed [19].

The compound effect of these laser-related processing parameters can be evaluated via the function Energy Density (E_D) [46], also known as Andrews number, using **Equation 2.2** below:

$$E_D = \frac{P}{x_{scan} \cdot v_{scan}}$$

Equation 2.2

² The ability and extent to which these processing parameters can be controlled is often at the system manufacturer's discretion.

Star et al. [23] also considered layer thickness when calculating E_D . Consequently, this gave rise to the term Volumetric Energy Density (VE_D) which can be calculated using **Equation 2.3** below:

$$VE_D = \frac{P}{x_{scan} \cdot v_{scan} \cdot h}$$

Equation 2.3

Conventionally, layer thicknesses of around 0.1mm are considered best practice for LS. However, this height is dependent on the size of the powder being processed and will influence the builds inter-layer sintering dynamics and total duration, as well as the surface roughness of the parts produced.

The number of times a powder bed layer is scanned by the laser (n_{scan}) can also be controlled. Goodridge et al. [24] identified that scanning each layer twice (but with less applied E_D) may facilitate the processing of polymers that crystallise relatively quickly, such as Ultra-High Molecular Weight Polyethylene (UHMWPE). Furthermore, Wegner and Witt [25] demonstrated that double scanning strategies have the potential to promote inter-layer coalescence and consequently reduce vertical anisotropies in the mechanical properties of parts produced.

Troubleshooting / Optimising LS Processing Parameters

A synergistic balance between energy density and powder bed temperature is required to produce geometrically accurate and functional components.

Sufficient energy should be applied to ensure resultant parts are suitably dense. However, surplus energy should be avoided to avert their enlargement and / or distortion during LS. More specifically, excess energy may affect the scale and / or shape of parts produced due to either secondary sintering at the interface between pre-defined part perimeters and exterior powder, or curl induced by excessive shear stresses accumulated during the

scanning of each layer, respectively. The latter also has the potential to prompt a build to fail if the resultant part distortions are significant enough to impede the path of the recoating device during processing.

Practically, fast scanning speeds and low laser powers are desirable when determining the optimal E_D value for a specific LS system / material combination. This is to maximise process throughput as well as the longevity of an LS system's optics, respectively.

Additionally, if the thermal characteristics of the polymer being processed are known, a felicitous value for T_b can be selected prior to building. This is discussed in greater detail in **Section 2.3.2.3**.

2.3.1.3 Build Cooldown

Once the final build layer has been sintered, additional powder layers are then consecutively deposited on top of the parts produced. These 'finish layers' provide insulation to ensure that all of the parts produced cool homogenously. A builds cooldown period is typically equal to its build duration. For example, if a LS build takes 10 hours to complete (including the time taken to deposit insulating finish layers), the build should be left to cool for a further 10 hours. Upon sufficient cooling, parts can then be extracted from the build chamber and post-processed in accordance with **Figure 2.1**.

2.3.2 Polymers for Laser Sintering

As previously mentioned in **Section 2.2**, thermoplastic powders currently constitute the largest segment within the AM materials market (34.7%) [2]. The growth of AM polymer powders, given by their annual total expenditures, over the last 13 years can be seen in **Figure 2.5**.

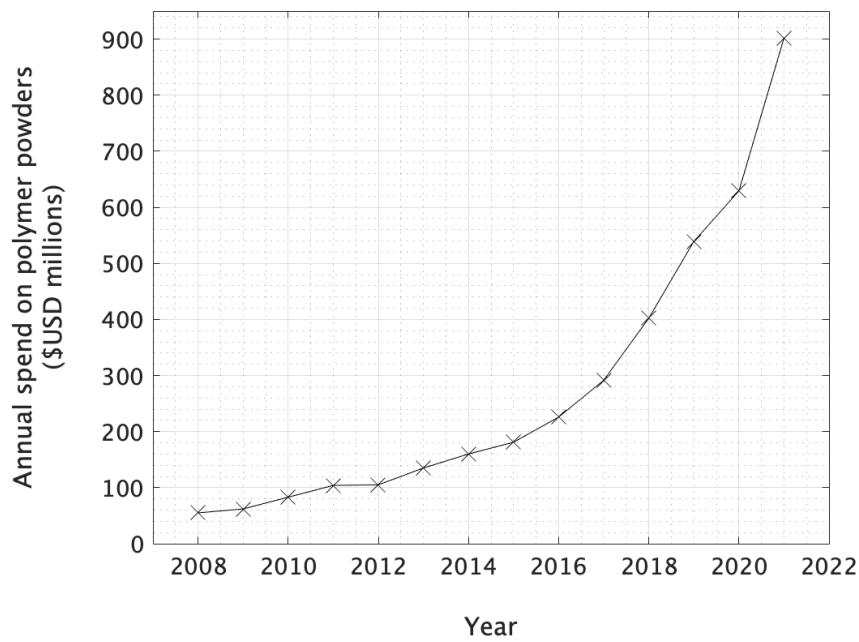


Figure 2.5 – The growth in the annual spend on polymer powders for PBF processes over the last 13 years [2].

Today, a variety of thermoplastic powders are commercially available, with many more also having been demonstrated as being processable by LS within polymer-PBF focussed literature. These polymers in their bulk form, i.e., without the inclusion of any secondary filler materials, are specified in **Figure 2.6**.

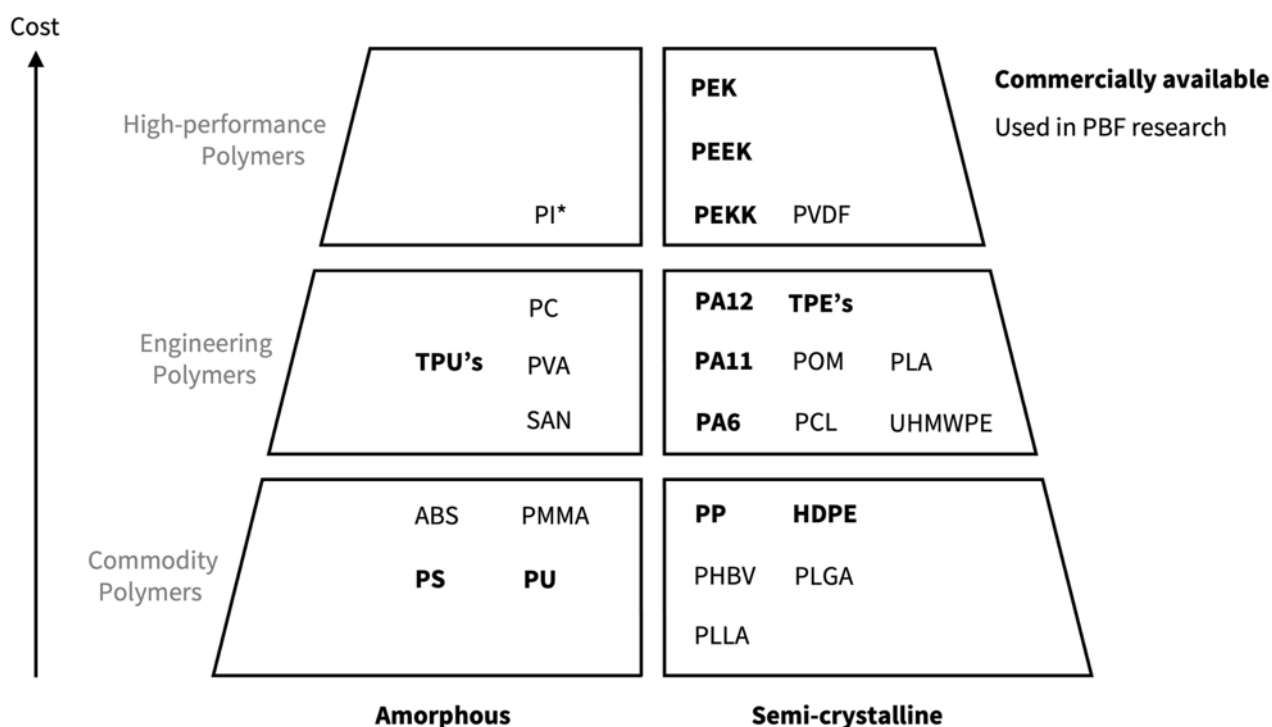


Figure 2.6 – Polymers that have been reported as being processable by LS, categorised by crystallinity, cost, performance and availability. Adapted from Wingham [12], Tan et al. [26] and Yuan et al. [27]. Thermoplastic abbreviations are as follows (ordered alphabetically): ABS (Acrylonitrile butadiene styrene) [28]; HDPE (High-density polyethylene) [29,30]; PHBV (Poly(3-hydroxybutyrate-co-3-hydroxyvalerate)) [31]; PA11 (Polyamide-11) [32]; PA12 (Polyamide-12) [33]; PA6 (Polyamide-6) [34]; PC (Polycarbonate) [35]; PCL (Polycaprolactone) [36]; PEEK (Polyether-ether-ketone) [37]; PEK (Polyether-ketone) [38], PEKK (Polyether-ketone-ketone) [39]; PI* (Polyimide) [40]; PLA (Polylactic acid) [41]; PLGA (poly(lactic-co-glycolic acid)) [42]; PLLA (poly(L-lactide)) [43]; PMMA (Poly(methyl-methacrylate)) [44]; POM (Polyoxymethylene) [45]; PP [46]; PS (Polystyrene) [47]; PU (Polyurethane) [48]; PVA (Polyvinyl alcohol) [49]; PVDF (Polyvinylidene (di)fluoride) [50]; SAN (Styrene-acrylonitrile resin) [51]; TPE (Thermoplastic elastomers) [52]; TPU (Thermoplastic polyurethane) [52]; UHMWPE [24]. *PI is a thermoset polymer.

The most established polymers for LS are variations of Polyamide (PA). Approximately 90% of the LS materials market is dominated by a specific configuration of PA, namely Polyamide-12 (PA12) [26]. Due to its popularity, both within industry and research, PA12 will be the principal polymer of interest throughout the entirety of this thesis.

PA12 (which is often also referred to as Nylon-12) is a semi-crystalline thermoplastic with the chemical formula $(C_{12}H_{23}NO)_n$. Its numerical label is derived from the number of carbon

atoms in the monomers from which it is synthesised from. An illustration highlighting the typical structure of a PA12 molecule can be seen in **Figure 2.7**.

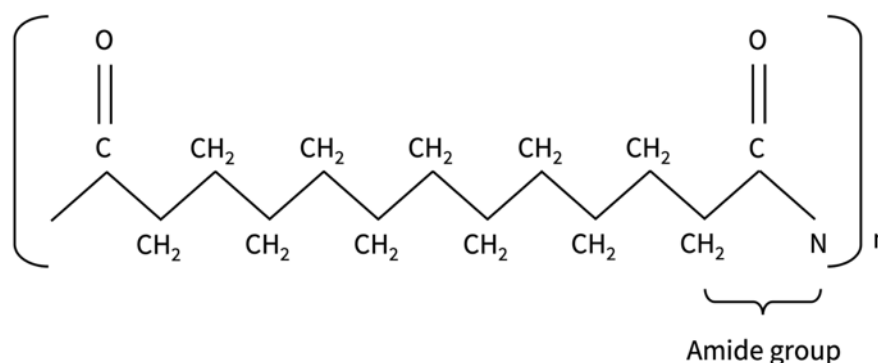


Figure 2.7 – An illustration of the chain structure of a PA12 molecule. Adapted from Pham et al. [48].

Ultimately, PA12's vast adoption is due to its inherent LS processability, which is discussed in greater detail in the following sections.

2.3.2.1 Powder Preparation

Powder is fundamental to the LS build process and the method by which it is produced will influence its size, morphology and composition [27]. A summary of the primary polymer powder preparations methods used both industrially and within research can be seen in **Table 2.1**.

Table 2.1

A summary of the primary powder preparation methods used both industrially and within research. Adapted from Tan et al. [21].

Powder preparation method	
Mechanical	Ball milling
	Wet grinding
	Cryogenic grinding
Solution-based	Dissolution precipitation
	Direct polymerisation
Melt-based	Melt emulsification / coextrusion

Mechanical processes involve reducing the size of feedstock polymers, which typically exist in pellet form, by impacting them until the resultant fractured material conforms to the particle size distribution (PSD) required for a given PBF process. Moreover, it is conventional practice to utilise coolants, specifically organic solvents or cryogenic refrigerants, to reduce the energy required to fracture feedstock polymers. Ultimately, mechanical powder preparation methods are suitable for grinding most polymers, though the particles produced are typically irregular in shape which can lead to flowability issues during building [26,53]. Therefore, subsequent post-processing via a downer reactor is often necessary to improve the roundness and sphericity of mechanically prepared powder particles [27].

Solution based powder preparation methods include dissolution precipitation and direct polymerisation. The former involves dissolving a polymer in a solvent at a high temperature and pressure before cooling the solution at a controlled rate, thus allowing the polymer to precipitate into powder particles [26]. This technique is favoured for producing commercial PA12 powders [54,55], particularly at scale, as it allows for their PSD's to be controlled effectively [26]. A Scanning Electron Microscopy (SEM) obtained image of a commercial PA12 powder, specifically PA2200 supplied by EOS GmbH, can be seen in **Figure 2.8**. Direct polymerisation, on the other hand, first requires micelles to be formed within a monomer dispersed solvent mixture by the addition of a suitable surfactant. An initiator is then added to the mixture to begin the polymerisation reaction

which results in the subsequent materialisation of powder particles that are alike in size and molecular weight [26].

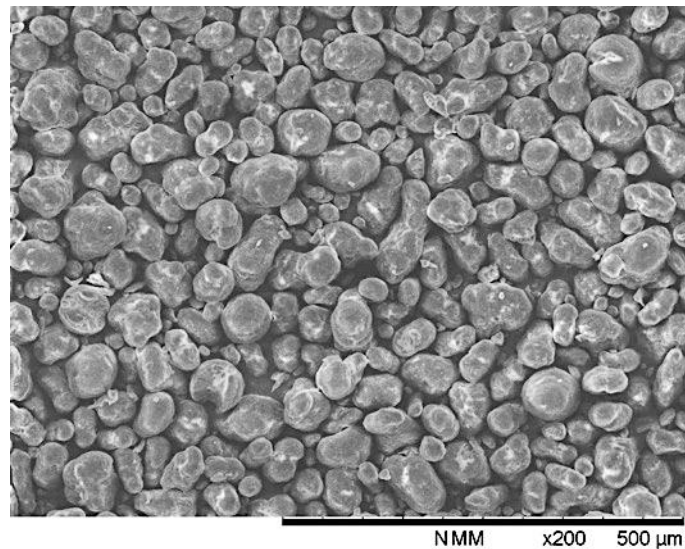


Figure 2.8 – An SEM image of a commercially available PA12 powder, specifically PA2200 supplied by EOS GmbH.

Melt emulsification, otherwise known as coextrusion, is a multi-step process which first involves melting and blending the polymer of interest with another immiscible polymer matrix. The resultant melt blend is then sheared, typically by extrusion, to form a colloid. When sufficiently cool, a solvent is applied to the colloidal suspension to dissolve the matrix material and reveal the insoluble polymer of interest in powder form.

2.3.2.2 Refresh Ratio

Refresh ratio is a measure of a powder's composition, specifically the quantities in which recycled and virgin material are present.

Generally, LS consolidates less than 10% – 15% of the entire build volume and therefore more than 85% – 90% of the material used remains un-sintered and recyclable [56]. Additionally, the high cost of LS virgin polymer powders necessitates their need to be reused. More specifically, LS polymer powders are typically priced between 40 – 250 \$USD / kg, making them between 20 – 100 times more expensive than thermoplastic

feedstock for Injection Moulding [57]. Therefore, refresh ratios of between 30% – 50% virgin-powder and 50% – 70% used-powder are generally adopted [56].

However, most polymer powders can only be recycled a finite number of times. Prolonged exposure to elevated temperatures in a dry nitrogen atmosphere will adversely impact their subsequent processing responses [55]. More specifically, when PA12 powders are subject to these processing conditions, post-condensation and cross-linking reactions induce an increase in their molecular weights. Consequently, the rheological behaviour and future processability of used – PA12 will be of lesser quality than that of virgin – PA12 [58].

Ultimately, the rate of polymer powder degradation depends on its chemistry, the processing parameters employed, the number of build cycles previously experienced and the location of the powder with respect to scan strategy. These degradation effects materialise as porosity and undesirable surface textures. The latter is more commonly referred to as the ‘Orange Peel’ effect [56,59], as shown in **Figure 2.9**.

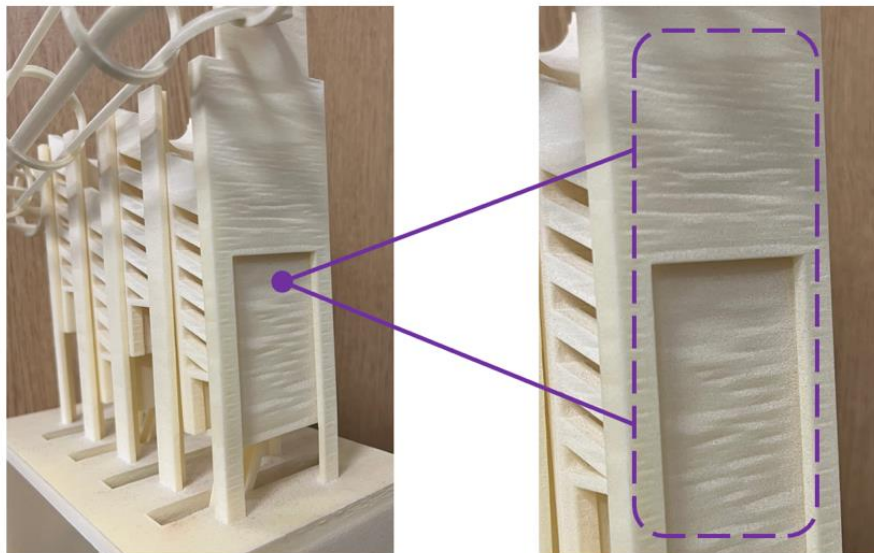


Figure 2.9 – An example of a part with surfaces that exhibit the ‘Orange Peel’ effect.

2.3.2.3 Material Requirements

The following properties must be considered when assessing the processability of polymer powders for LS.

Flow Properties

Particle size, shape and size distribution all impact a powder's ability to flow [60]. Powder flow properties describe bulk material behaviour but arise from the accumulation of forces that act on individual particles, such as Van der Waals, electrostatic, surface tension, friction etc [61]. Flowability expands on flow properties by additionally accounting for how a material is handled. Powders should have good flowability to allow for the consistent deposition of both thin and homogeneous layers [32]. Furthermore, powder flowability correlates to how efficiently a powder bed will pack, which determines how effectively heat is transferred between adjacent powder particles during sintering. Consequently, the magnitude of conduction induced will affect the density and mechanical properties of the parts produced [52].

An SEM obtained image detailing the morphology and size distribution of particles sampled from a commercially available LS PA12 powder, specifically PA2200 supplied by EOS GmbH, can be seen in **Figure 2.8**.

Theoretically, powders with smaller sized particles enable more dimensionally accurate parts with reduced amplitude roughnesses to be produced. However, practically this is only true until a critical particle diameter. Powder particles that are smaller than this critical diameter will be more prone to agglomeration. Resultant aggregates will behave like rougher, larger particles that are unable to tessellate with the same powder packing efficiencies [9]. As can be seen in **Figure 2.8**, commercial PA12 powders typically have an average particle diameter of approximately 50µm.

Vock et al. [62] found that powders with narrower PSD's generally have better flow properties. However, multi-modal particle size distributions allow greater powder packing densities to be achieved. **Figure 2.10** schematically illustrates the effect that contrasting powder particle morphologies and PSD's have on their bulk powder packing efficiencies during LS.

Powder flow properties and packing efficiencies are improved when bulk powders comprise of particles with minimal surface area to volume ratios [19]. Berretta et al. [63] used Angle of Repose (AOR) to characterise the flowability of several LS and non-LS grade polymeric powders. They found that highly spherical powders resulted in lower AOR results and therefore had better flow properties. Moreover, they also determined that particle morphology influences the flow properties of a bulk polymer powder comparatively more so than its PSD.

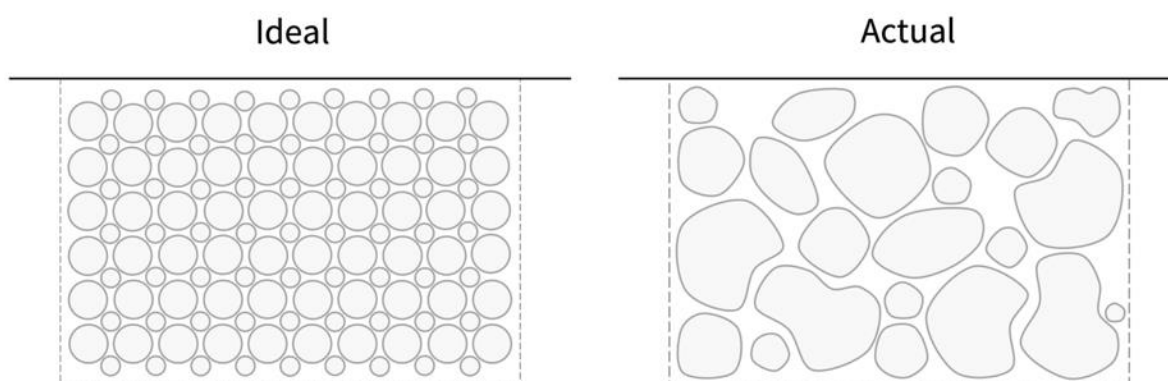


Figure 2.10 – An illustration highlighting the effect that contrasting powder particle morphologies and size distributions have on their powder packing efficiencies during LS.

Often flow agents are added to polymer powders to improve their flow properties [64]. These inorganic additives typically consist of either fumed silica, glassy oxides, metallic stearates, or fluoroplastics [65]. Furthermore, flow agents typically have particle diameters of approximately $1\mu\text{m}$ and are usually added to bulk powders in weight percentage loadings (wt%) of less than 5 wt% [64,66].

Optical Properties

As previously discussed in **Section 2.3.1.2**, particle sintering is initiated upon exposure to a laser. Resultant beam–matter interactions are influenced by the wavelength of the laser, as well as the chemical composition and PSD of the powder bed [18]. An illustration highlighting the different beam–matter interactions that occur between the laser and powder bed during LS can be seen in **Figure 2.11**.

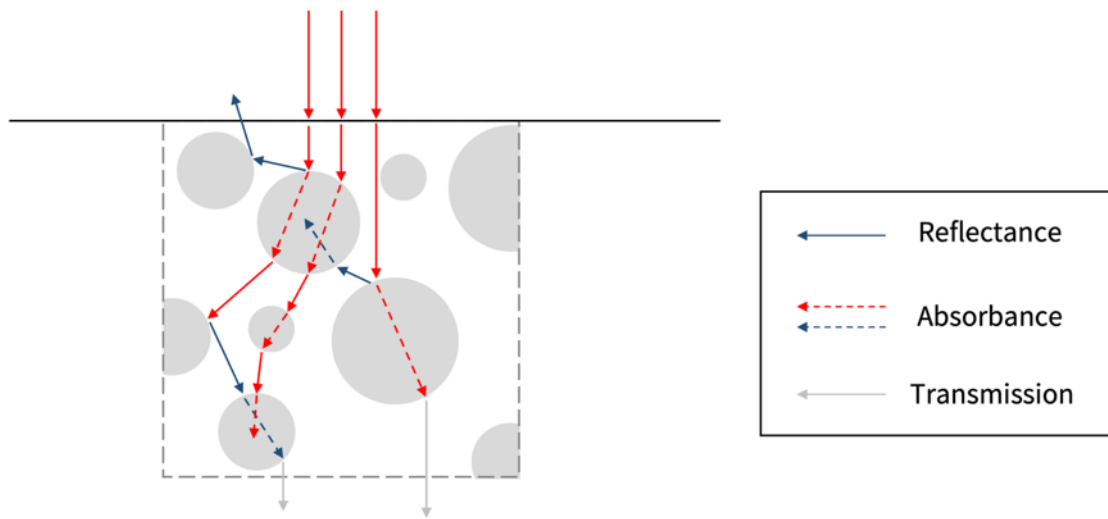


Figure 2.11 – An illustration highlighting the different optical interactions (absorbance, reflectance and transmission) that occur between the laser beam and powder bed during LS. Adapted from Laumer et al. [51].

Typically, industrial LS systems employ CO₂ lasers that have wavelengths of 10.6μm. Laumer et al. [67] demonstrated that when PA12 powder layers (200μm in thickness) were subject to this frequency of photon energy the ratio in which it was absorbed, reflected and transmitted was equal to 0.93, 0.06 and 0.01, respectively. Additionally, Fourier Transform Infrared Spectroscopy analysis conducted by Cui and Yan [68] showed that PA12's excellent energy absorptance was due to the stretching vibrations that occur between carbon and carbonyl groups within its crystalline regions.

Functional fillers can also be added to polymer powders to improve their optical properties. Xi et al. [69] demonstrated that the reflectance of PA12 could be reduced by

the inclusion of carbon black (CB) nanoparticles. More specifically, they found the composite powder (2wt%) CB – PA12 had a reduced optical reflectance of 7% relative to unfilled – PA12.

Thermal Properties

The thermal characteristics of the polymer being sintered, particularly the temperatures at which it melts and crystallises should be comprehensively understood. Differential Scanning Calorimetry (DSC) is often employed to characterise the temperatures at which these endothermic and exothermic phenomena occur. An illustrative DSC thermograph of feedstock and laser sintered PA12 can be seen in **Figure 2.12**.

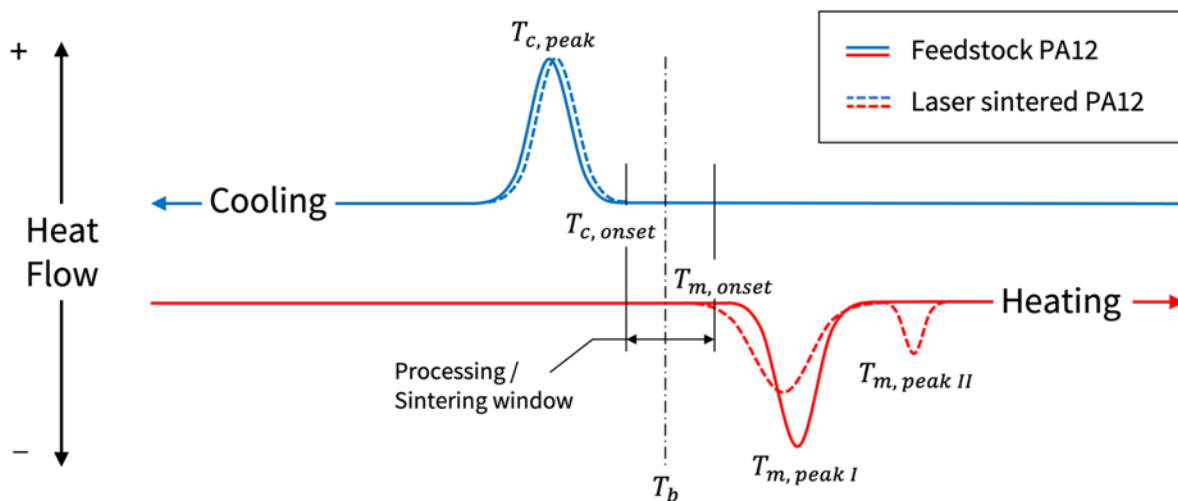


Figure 2.12 – An illustrative DSC thermograph showing the typical thermal behaviours of feedstock and laser sintered PA12.

For semi-crystalline polymers a metastable thermodynamic region, more commonly referred to as the processing or sintering window, exists between the onsets of crystallisation and melting [70]. Dadbakhsh et al. [55] characterised the temperatures at which these thermal behaviours occur for both feedstock and laser sintered PA12. These values can be seen in **Table 2.2**.

Table 2.2

Melting and crystallisation temperatures of virgin – PA12 in both feedstock and laser sintered form, characterised by Dadbakhsh et al. [49].

PA12 sample form	Onset of primary melting peak (°C)	Primary melting peak width (°C)	Onset of crystallisation (°C)	Crystallisation peak width (°C)
Feedstock powder	180.1 ± 0.8	7.9 ± 0.2	154.4 ± 0.4	7.9 ± 1.1
Laser sintered material	172.2 ± 0.2	14.9 ± 0.5	153.4 ± 0.4	7.9 ± 0.3

The size of a material's sintering window will determine its LS processability. Polymers with melting and crystallisation peaks that are close to one another, or superimposed, will crystallise relatively rapidly as they cool post laser exposure, and thus will be more prone to shrinkage and distortion [19,70]. Whereas polymers with relatively large sintering windows allow for powder bed temperatures to be selected that enable them to remain in their liquid state for longer. Consequently, they will be less prone to shrinkage or distortion as they will accumulate fewer stresses due to the retardation of in-process part crystallisation [71].

Furthermore, Zarringhalam et al. [72] identified that the double melt peak phenomenon observable in **Figure 2.12** is due to incomplete particle melting during LS. Whereby the primary and secondary melt peaks (as indicated by descending peak height magnitudes) represent the fully-melted and un-melted proportions of a laser sintered polymer sample, respectively. Additionally, Zarringhalam [73] determined that the degree of particle melt (DPM) of a laser sintered material is best characterised by the magnitude of its secondary melt peak height. Moreover, Majewski et al. [74] demonstrated that PA12 specimens with greater DPM values were stronger and more ductile (as indicated by their Ultimate Tensile Strength (UTS) and Elongation at Break (EaB) values) than samples of alike material comprising of a greater number of un-melted particle cores.

Ultimately, powder bed temperatures should be selected at an optimal location within the sintering window that will enable relatively good DPM values to be achieved, whilst also preventing early onset particle coalescence (prior to laser exposure) and the occurrence of part distortion.

Rheological Properties

In accordance with the Frenkel–Eshelby model (outlined in **Equation 2.4** below), optimal particle coalescence is achieved when surface tension is high and zero-shear viscosity is low [58].

$$\left(\frac{x}{a_0}\right)^2 = \frac{\Gamma \cdot t}{a_0 \cdot \eta_0}$$

Equation 2.4

where x is the length of the growing neck between adjacent particles, a_0 is the initial radii of the particles, Γ is the coefficient of surface tension, t is time and η_0 is zero-shear viscosity.

Haworth et al. [75] quantified the zero-shear viscosities of different grades of PA12 using rotational rheometry. They found used – PA12 powders had significantly higher zero-shear viscosities than virgin – PA12 material, thus confirming the correlation between molecular weight, rheological behaviour and resultant laser sintered part properties [55,76,77].

Hot Stage Microscopy and Melt Flow Rate methods are more commonly used to evaluate the melt flow behaviour of polymers. These methods do not explicitly characterise zero-shear viscosity but have been shown to provide insight into the coalescence behaviours of different polymer powders [21,69,78]

2.4 Tribology

*Tribologists have shown an addiction
to seeking the causes for friction;
When pressed, they'd confide,
that watching things slide
created that mental affliction.*

**Adapted from a poem composed by Peter Blau for
the Wear of Materials 2023 conference dinner**

2.4.1 Definition

Tribology is the study of interacting surfaces in relative motion, focusing on friction, wear and lubrication [79].

2.4.1.1 Etymology

The word 'tribology' has Greek origins and is the product of the verb τρίβω (tribo) which translates to 'I rub', and the suffix -logy, from -λογία, meaning 'the science or study of'. Peter Jost formally coined the term in 1966 when producing a government commissioned report titled: "Lubrication (Tribology) – A report on the present position and industry's needs" [80].

2.5 Polymer Tribology

Polymer tribology pertains to the study of polymeric materials specifically when subject to surface-related phenomena, such as friction and wear.

Its recognition as a distinct subfield of tribology first occurred in the mid-20th century [81] (at a similar time to when Peter Jost coined the term 'Tribology'). Initially, related

research was prompted by the automotive industry and focussed on the friction and wear behaviours of elastomers and rubbers to better understand the mechanisms pertinent to brake pad and tyre degradation [82].

2.5.1 Surface Topography

Tribology is the science of interacting surfaces [83], therefore a comprehensive understanding of surface topography is essential. Descriptions of surface topography comprise of roughness, waviness and irregularities [84].

2.5.1.1 Surface Roughness

Gadelmawla et al. [85] reported there to be over 55 different roughness parameters capable of distinctly describing surface roughness. Therefore, it is common practice to categorise these parameters into one of three groups, namely amplitude parameters, spacing parameters or hybrid parameters. Though, despite the multitude of ways to mathematically describe roughness, polymer AM surfaces are predominantly characterised by the distributions of their vertical heights.

Amplitude roughness parameters are defined as either R- or S- descriptors depending on whether the evaluation region being examined is a 2-dimensional (2D) profile or 3D area, respectively.

Arithmetic Mean Height (S_a) is the most commonly observed amplitude roughness descriptor within polymer AM literature. S_a is defined as the average absolute deviation of roughness irregularities from the mean plane of a surface [85], as shown in **Equation 2.5** below:

$$S_a = \frac{1}{A} \iint_A |Z(x, y)| \, dx dy$$

Equation 2.5

Other popular amplitude roughness parameters include Root Mean Square roughness (S_q) and Maximum Peak-to-Valley Height (S_z) [59,86–89]. Both of which are mathematically described in **Equation 2.6** and **Equation 2.7**, respectively.

$$S_q = \sqrt{\frac{1}{A} \iint_A \{Z(x, y)\}^2 \, dx dy}$$

Equation 2.6

S_z quantitatively describes the vertical distance between locations of maxima and minima within a defined evaluation area. Therefore, S_z is very sensitive to anomalous peaks and valleys, which intrinsically are characteristic within LS surfaces.

$$S_z = \max Z - |\min Z|$$

Equation 2.7

Despite their vast adoption, these amplitude height parameters do not provide insight into the symmetry or form of a surface. Therefore, amplitude density functions, such as Skewness (S_{sk}) and / or Kurtosis (S_{ku}) should also be used, particularly when analysing non-Gaussian surfaces. Moreover, S_{sk} and S_{ku} are capable of distinguishing between roughness profiles that have identical S_a and S_q values but contrasting material distributions, as shown in **Figure 2.13**.

Skewness describes the symmetry of a surface about its mean plane and is calculated via **Equation 2.8** below. More specifically, S_{sk} describes whether the distribution of bulk material that comprises a surface exists above or below its mean plane. If a profile has a negative Skewness value, valleys are more of a dominant feature than peaks, and vice versa.

$$S_{sk} = \frac{1}{S_q^3} \frac{1}{A} \iint_A Z^3(x, y) dx dy$$

Equation 2.8

Kurtosis describes the sharpness of a surface height distribution [90] and is calculated via **Equation 2.9** below. Profiles with leptokurtic distributions ($S_{ku} > 3$) are conventionally considered to be relatively spiky, whereas the opposite is typically deemed to be true for platykurtic profiles ($S_{ku} < 3$) [85].

$$S_{ku} = \frac{1}{S_q^4} \frac{1}{A} \iint_A Z^4(x, y) dx dy$$

Equation 2.9

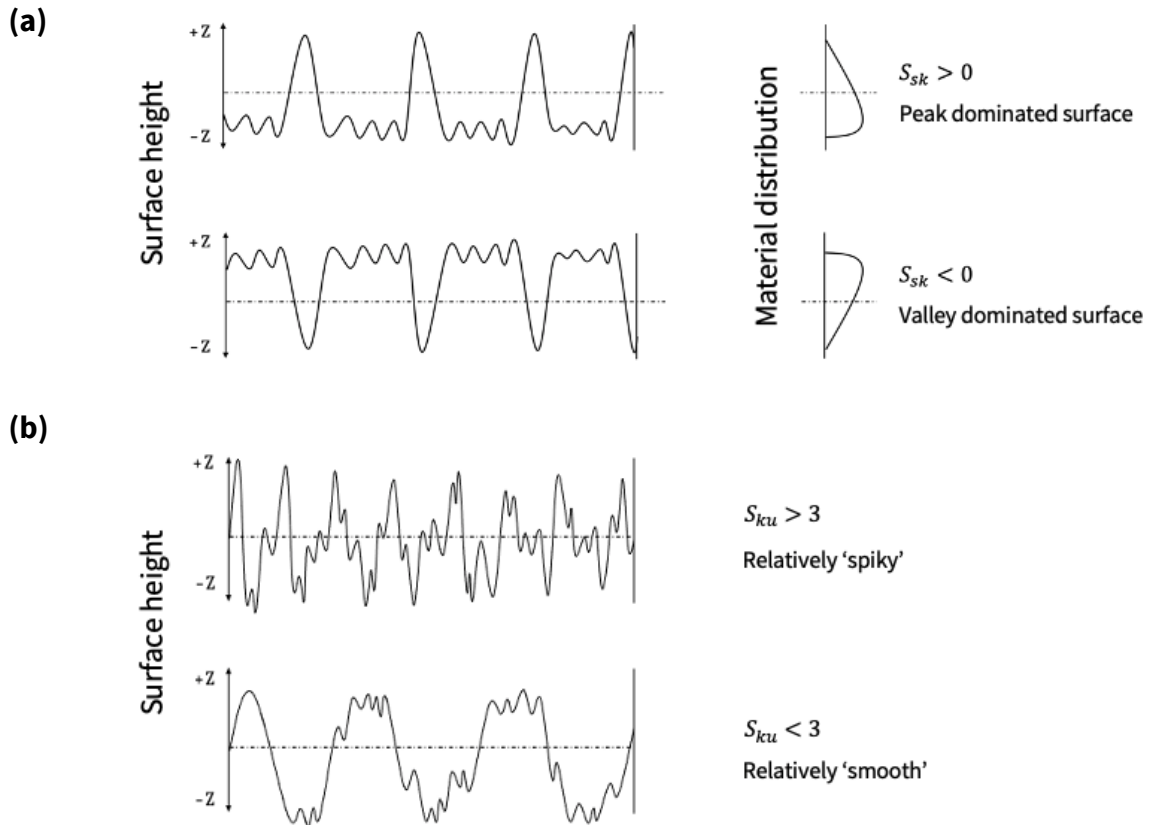


Figure 2.13 – Example profiles with identical S_a and S_q roughnesses but contrasting (a) Skewness and (b) Kurtosis distributions. Adapted from Gadelmawla et al. [85].

2.5.1.2 Surface Metrology Techniques

Empirical measurements determine the accuracy with which polymer AM surfaces can be characterised. Therefore, a fundamental understanding of the principles by which different surface analysis techniques function is essential. The following methods are the most commonly observed within AM related literature.

Contact Metrology Methods

Contact techniques involve analysing the physical interaction between the surface being evaluated and the instrument or sensor executing the measurement. Corresponding methods include, contact profilometry, GelSight and Atomic Force Microscopy, with the first-mentioned technique being the most ubiquitous within related literature.

In general, contact profilometry is well adopted due to its speed [91], simple tractability [91] and abundant regulation by well-established standards [92]. However, the accuracy of a recorded profile intrinsically depends on the form of the stylus tip used during measurement execution, specifically its angle and radius of curvature. Moreover, their finite geometries often result in profiles being characterised as having shallower valley depths and rounder asperity peaks than that is accurate. Additionally, the inherent tactility of contact profilometry has previously been observed to leave scratches, indentations and visible trace paths on polymer surfaces during measurement execution [93,94].

Non-contact Metrology Methods

Non-contact techniques analyse the response of reflected radiation from a surface to compute its changes in height.

Focus Variation (FV) microscopy is the most well-adopted technique for characterising AM surfaces [91–93,95]. FV utilises the small depth of field of an optical system, with vertical

scanning, to capture 3D topographical surface data [96,97]. A more detailed explanation of how FV microscopy operates is provided in **Chapter 4**, specifically **Section 4.2.2.2**.

Confocal microscopy methods are also well adopted for evaluating polymer AM surfaces [92]. Corresponding techniques are either optical or laser based, though both reconstruct 3D surface topographies via a similar process. This involves radiation (reflected from a specimen's surface) being filtered by confocal pin holes, thus only allowing in-focus light to reach the detector. This is then repeated at different focal heights so that an array of axially orientated confocal images can be accumulated to form a replica model of the surface topography being examined [91,98]. Like FV microscopy, large evaluation areas can be quickly evaluated with vertical resolutions in the nanometer range [98].

Several other non-contact surface metrology methods have also been reported as being viable options for examining polymer PBF produced part surfaces. These include Structure Light Scanning [99]; Coherence Scanning Interferometry [100]; Fringe Projection [91]; and Optical Coherence Tomography [101].

Surface Feature Characterisation Techniques

LS produces surfaces that are abundant with different features. To analyse these features in detail, techniques that exploit radiation with wavelengths smaller than that of visible light need to be employed.

Scanning electron microscopy (SEM) is an incredibly versatile tool that is used across a range of industries [102,103]. It can magnify features up to 1 million times their original size [103] and therefore is often used to identify features within LS surfaces [91,101]. A detailed explanation of how SEM operates is provided in **Section 4.2.2.2**. However, despite SEM's effectiveness at gathering qualitative insight into the size and shape of specific surface features, current technologies lack the capability of returning reliable, quantitative dimensional information [90].

X-ray Computed Tomography (XCT) is the only practical and non-destructive method of analysing internal features within polymer AM parts [104]. Additionally, it is also the only technique capable of characterising re-entrant or undercut surface features, which would otherwise be impossible to achieve via contact or optical line-of-sight metrology methods. An illustrative example of a surface which includes re-entrant / undercut features can be seen in **Figure 2.14**. In general, XCT involves penetrating a sample with X-ray radiation and capturing the unattenuated response. Different local sample densities will attenuate X-ray radiation by correspondingly varying degrees, enabling internal vacant features, such as pores, to be distinguished from solid part.

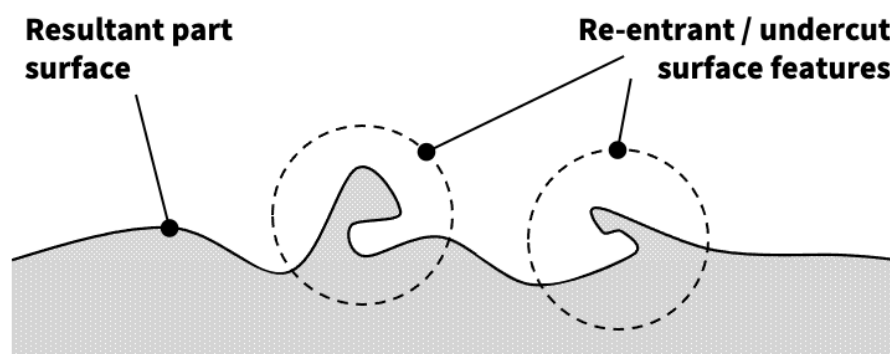


Figure 2.14 – An illustrative example of a surface which includes re-entrant / undercut features.

Relevant Standards

Many ISO specific standards have been created to facilitate the repeatable analysis of specimen surfaces via both contact profilometry and optical methods.

The primary regulatory body of literature that pertains to the analysis of polymer AM surfaces is ISO 25178, titled: '*Geometrical Product Specification (GPS) – Surface texture: areal*'. More specifically, ISO 25178 is a collection of internationally recognised standards that covers a variety of aspects relating to the analysis of 3-dimensional areal surface textures, such as: terms and definitions; specification operators; and the nominal characteristics of various non-contact instruments. At the time of writing, ISO 25178 comprised of 20 individual standards.

Despite this, there remains mixed adoption of ISO 25178 standards in the literature when analysing AM surfaces [92,95,105].

2.5.2 Friction

Friction is the resistance encountered when one body moves tangentially over another with which it is in contact with [106].

The empirically determined Amontons – Coulomb laws can be used to describe dry sliding friction phenomena. These are detailed below:

Amonton's 1st Law: The force of friction (F_f) is directly proportional to the applied normal load (N):

$$F_f = \mu N$$

Equation 2.10

where μ , the constant of proportionality, represents coefficient of friction (COF).

Amonton's 2nd Law: The force of friction is independent of the apparent area of contact (A_N).

Coulomb's Law: Kinematic friction is independent of sliding velocity (v).

2.5.2.1 Real Area of Contact

Seminal work by Bowden and Tabor [107] recognised that the real area of contact (A_R), rather than the apparent area of a surface, determines the frictional properties of the contact. More specifically, the real area of contact is the summation of individual micro-regions, otherwise known as junctions, at which two surfaces meet. An illustration highlighting the difference between A_N and A_R can be seen in **Figure 2.15**.

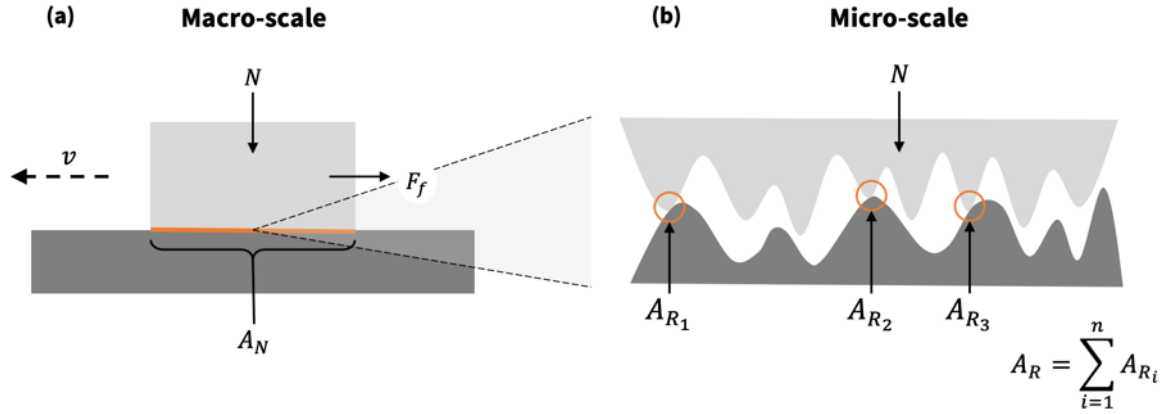


Figure 2.15 – An illustration highlighting the difference between the **(a)** apparent area of contact and **(b)** real area of contact of a surface.

In general, the proportion of asperity contact between interfacing surfaces determines the magnitude of friction incurred during sliding. As discussed in **Section 2.5.1.1**, the size and distribution of asperities that comprise a given surface are typically characterised by their resultant amplitude roughnesses.

2.5.2.2 Coefficient of Friction

As shown in **Equation 2.10**, coefficient of friction is defined as the ratio of friction force to normal load [79]. It is universally recognised as the principal descriptor for quantifying the severity of friction between surfaces during sliding. COF values typically range from $0 < \mu < 1$, where $\mu \rightarrow 0$ is denotative of interactions that incur minimal resistance to sliding. Conversely, the effect of friction is widely considered significant when $\mu > 0.5$, particularly during polymer–steel dry sliding interactions [108].

Ultimately, the COF of a given contact is a function of both surfaces involved. Therefore, the nature of these surfaces, specifically their roughnesses, chemistries and bulk mechanical properties, as well as the conditions they operate within, should also be specified when quoting COF values [106].

2.5.2.3 Types of Friction Interactions

It is well recognised that friction force is primarily governed by two types of interaction, namely adhesion (F_{f_A}) and deformation (F_{f_D}) [109]. The compound effect of these contributions can be evaluated via **Equation 2.11** below:

$$F_f = F_{f_A} + F_{f_D}$$

Equation 2.11

Adhesion

As the size and stiffness of a material decreases, adhesive contact forces become increasingly more influential [110]. Therefore, the adhesion component of friction is generally of greater significance than the deformation component in polymer tribology [111].

Adhesive forces of attraction primarily include Van der Waal and electrostatic forces. Hydrogen bonding may also be significant, but only when certain interfacial contact chemistries appertain.

Deformation

The deformation component of friction within polymer tribology is akin to abrasive wear, therefore the F_{f_D} incurred by a polymer surface during sliding is typically described by its resistance to ploughing.

Polymer surface asperities will experience either elastic or plastic deformation during dynamic contact [111,112]. To determine which will ensue, Greenwood et al. [113] devised the term plasticity index (ψ). As shown in **Equation 2.12**, ψ is a function of the material and topographical properties of both contacting bodies:

$$\psi = \frac{E'}{H} \sqrt{\frac{S_q}{\beta}}$$

Equation 2.12

where H is indentation hardness of the softer surface and β is the average radius of its asperity peak tips. E' represents reduced elastic modulus and is calculated using the Young's Modulus (E) and Poisson's Ratio (ν) of both contacting surfaces, as shown in **Equation 2.13**:

$$\frac{1}{E'} = \frac{1 - \nu_1^2}{E_1} + \frac{1 - \nu_2^2}{E_2}$$

Equation 2.13

This criterion suggests that plastic deformation occurs when ψ exceeds unity ($\psi \geq 1$) [114]. Additionally, **Equation 2.12** indicates that polymer surfaces with greater S_q and S_{ku} roughnesses are more likely to yield [115].

2.5.3 Wear

Wear is broadly defined as the progressive damage, generally involving material loss, that occurs on the surface of a component as a result of its motion relative to other contacting bodies; it is the almost inevitable companion of friction [116,117]. Generally, the surface within a tribo-pair that has the lowest cohesive energy is the one that will wear during sliding [81].

Various standardised wear tests have been established by ASTM International, with the most general being ASTM G190 [118], which primarily serves as a guide for the selection and / or development of existing wear testing procedures. ASTM G190 also includes details of more specific wear testing methods, such as ASTM G99 (pin-on-disk sliding) [119]; ASTM G133 (linear reciprocating ball-on- flat sliding) [120]; and ASTM G77 (block-on-ring sliding) [121]. Therefore, it serves as a useful resource for determining the most suitable standardised wear test methodology for a given objective.

The nature and rate of wear arises from the mechanical stresses, temperatures and chemical reactions incurred during sliding [81]. These wear inducing interactions are complex and concomitant, changing with time as the contact develops [122].

As shown in **Figure 2.16**, wear is typically characterised as occurring in one of three sequential periods, specifically either the transient (also referred to as running-in), steady-state or catastrophic regime, respectively [82].

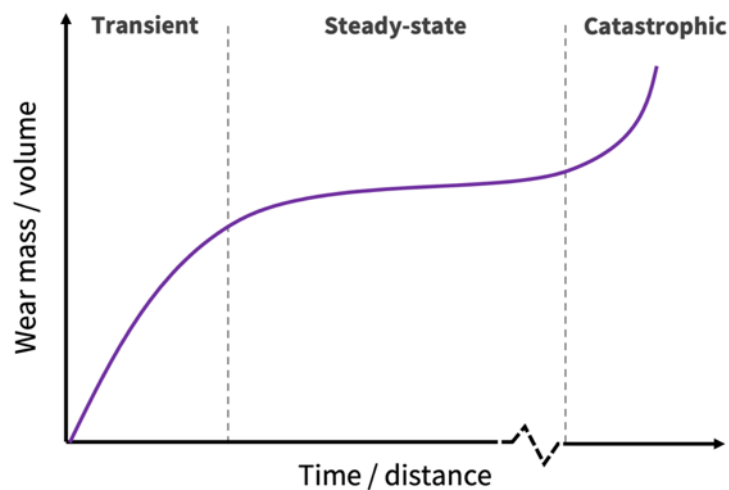


Figure 2.16 – The typical wear trend a component will sustain over its lifetime. Adapted from Williams [116].

During the transient wear regime, surfaces come into contact for the first time. These initial interactions reduce the amplitude roughness of the softer surface within a tribo-pair by fracturing and flattening its extreme asperity peaks [123]. Accordingly, the wear rates determined during running-in are often greater than the wear rates characterised during steady-state polymer sliding.

2.5.3.1 Adhesive Wear

ASTM International [124] define adhesive wear as the localised bonding between contacting solid surfaces leading to material transfer between the two surfaces or loss from either surface.

In polymer tribology, adhesive wear is one of the most characteristic but least understood types of wear [125]. However, it is recognised that adhesive wear occurs when the strengths of the adhesive bonds formed between a polymer and a counterface exceeds the cohesive strength of the polymer surface itself [82]. Therefore, adhesive wear can be described as a cycle of junction formation, growth and rupture [112], as illustrated in **Figure 2.17**. Furthermore, ruptured material may subsequently influence the contact by either acting as a third-body or by adhering to the counterface to form part of a transfer film [82].

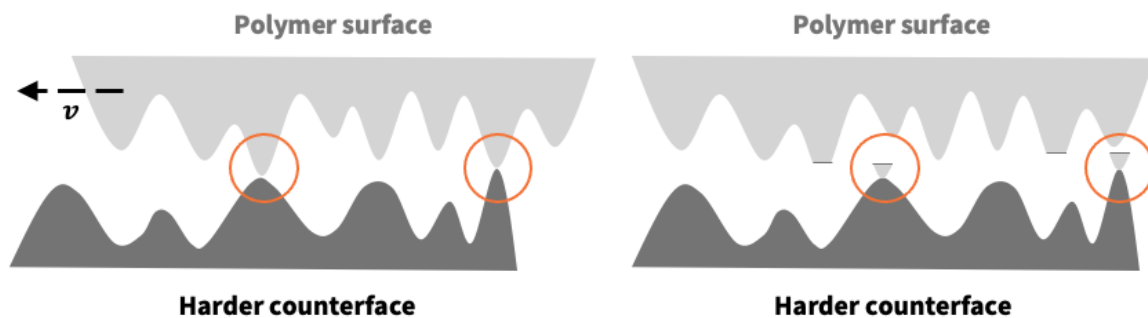


Figure 2.17 – An illustration highlighting the mechanism of adhesive wear. Adapted from Adelbary [126].

The Archard wear model (detailed in **Equation 2.14** below) remains to be the most widely used expression for quantitatively evaluating adhesive wear [126]:

$$V_{adh} = k \frac{Nx}{H_B}$$

Equation 2.14

where V_{adh} is the total volume of material removed from the softer surface due to adhesive wear, H_B is the Brinell hardness of the softer material and k is the adhesive wear coefficient. k is an empirically determined factor that is highly condition sensitive.

Transfer Films

Transfer films are characteristic of adhesive wear and modify a contact such that sliding instead occurs between the substrate and resultant transfer film of alike material, rather than with the harder asperities on the original counterface.

Transfer films are attributed to the self-lubricating property often associated with polymers [127]. Bahadur and Schwartz [127] identified that during polymer – metal sliding the quality of resultant transfer film adhesion is dependent on the attraction of polymer chain ends or free radicals to the metals surface.

2.5.3.2 Abrasive Wear

ASTM International [124] define abrasion as the process by which the relative motion between a surface and hard particles or protuberances on an opposing surface produces abrasive wear of that surface.

There are two distinct modes of deformation incurred during the two-body abrasion of polymers, namely plastic grooving (also referred to as ploughing) and cutting. The former does not remove any material from a polymer's surface during sliding [112], but instead continually displaces material outwards to form ridges adjacent to the developing groove. Contrastingly, the latter is named cutting because it resembles conventional machining, whereby material is removed from a surface in the form microchips or flecks. These abrasive wear mechanisms can be seen in **Figure 2.18**.

(a)

Image redacted for copyright purposes

(b)

Image redacted for copyright purposes

Figure 2.18 – Contrasting abrasive wear mechanisms, specifically (a) the plastic grooving of POM and (b) the cutting of Epoxy [128].

Furthermore, seminal work by Lancaster [129] correlated the bulk mechanical performance of a variety of polymers with their resultant abrasive wear rates. More specifically, he demonstrated the latter to be inversely proportional to the product of a polymer's break stress (σ_b) and Elongation at Break (ε_b), as shown in **Figure 2.19**.

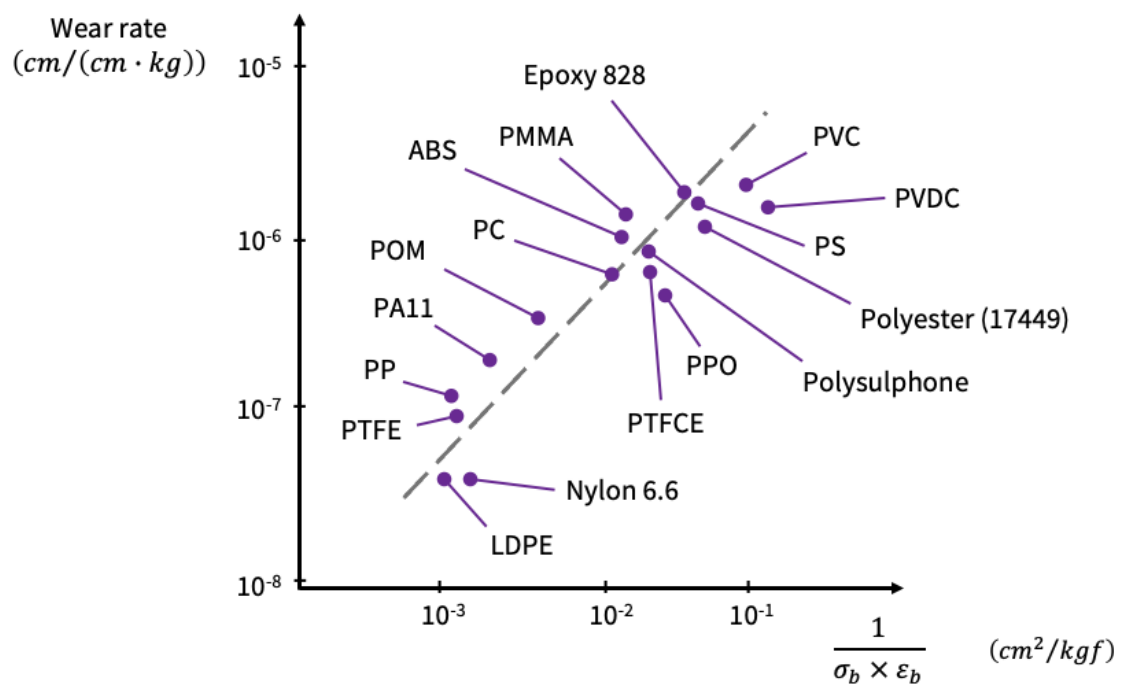


Figure 2.19– Lancaster's correlation between the abrasive wear rate of a variety of polymers and the inverse product of their σ_b and ε_b values. Adapted from Lancaster [176]. Polymer abbreviations that have not been previously defined include (ordered alphabetically): LDPE (Low-density polyethylene); PA6.6 (Polyamide 6.6); PPO (Polyphenylene oxide); PTFCE (Polychlorotrifluoroethylene); PTFE (Polytetrafluoroethylene); PVC (Polyvinyl chloride); and PVDC (Polyvinylidene chloride).

Recognising the relationship between the mechanical and wear properties of different polymers subsequently led to the derivation of the Ratner–Lancaster expression, detailed in **Equation 2.15** below:

$$V_{abr} = \frac{\mu \cdot N \cdot x}{H (\sigma_b \cdot \varepsilon_b)}$$

Equation 2.15

where, V_{abr} is the worn volume due to abrasive wear and x is sliding distance. Additionally, the compound product $(\sigma_b \cdot \varepsilon_b)$ of a material is related to the area under its stress–strain curve.

Hardness

The hardness of a polymers surface will determine its resistance to deformation [130]. Though, it is important to note that hardness is not an intrinsic material property; it is the result of a defined measurement technique and can be determined by either indentation or scratching methods. Conventional indentation techniques include, but are not limited to, Vickers, Brinell, Shore and Rockwell measurement methods. Scratch hardness testing on the other hand is a dynamic process in which a rigid indenter traverses across a surface under an applied normal load to produce a scratch. The resultant deformation is then analysed to ascertain information regarding the hardness of the scratched surface. Briscoe et al. [131] identified scratch hardness methods to be better suited than quasistatic indentation techniques for characterising the surfaces of time and strain dependent materials, such as polymers [131]. The scratch hardness of viscoelastic-plastic surfaces (by traversing conical indentation) can be calculated using **Equation 2.16** below [132]:

$$H_s = q \frac{4N}{\pi d^2}$$

Equation 2.16

where, d is the recovered width of the scratch and q is a constant that depends on the deformation of the material tested. For elastic materials $q \cong 1$, whereas for plastic materials $q \cong 2$.

However, despite the recurrent inclusion of hardness within wear models, its explicit correlation with the wear properties of polymers has yet to be observed within the literature [128,133].

Three-body Abrasive Wear

Particles interposed between two surfaces are known as third bodies [134]. These particles primarily exist as wear debris generated directly within the contact, particularly during running-in, but may also comprise of foreign matter inadvertently brought into the contact at any point during sliding.

If the presence of third bodies increases wear rate, it may be due to three-body abrasion. This occurs when free particles readily penetrate, and lead to the wear of a surface, in an alike manner to that of two-body abrasion [126].

Chapter 3

Literature Review

Chapter Summary

Literature pertaining to the surface, friction and wear properties of laser sintered PA12 components was reviewed. Each topic was discussed in detail and compared with other polymers or analogous AM processes wherever felicitous. This allowed any gaps in existing knowledge to be identified and prompted the formulation of several related research themes for further investigation.

3.1 Laser Sintered PA12 Surfaces

LS characteristically produces components with anisotropic and often less-than desirable surface roughnesses; the latter of which, when described by S_a , have been reported to range from 10 μ m to 20 μ m in PA12 specific literature [89,91,135]. Furthermore, the resultant ‘grainy’ surface textures characteristic of parts produced by LS predominantly exist due to there being no physical boundaries to inhibit particle coalescence, specifically necking, between pre-defined part perimeters and exterior powder.

Ultimately, laser sintered surfaces are a function of the powder feedstock used and the manner by which it is consolidated [93,136]. Therefore, LS surface modification strategies primarily involve optimising either the powder or the processing parameters employed³.

3.1.1 PA12 Powder Effects on Roughness

Schmid et al. [136] compared the resultant part properties of two different industrially available PA12 powders, namely Duraform (produced by dissolution precipitation) and Orgasol Invent Smooth (produced by direct polymerisation). They found Orgasol Invent Smooth powder particles to be comparatively smaller, more spherical and have a narrower size distribution than Duraform powder particles. Consequently, parts manufactured from Orgasol Invent Smooth had comparatively smaller S_a roughnesses (ranging from 16%–58%), for every surface orientation evaluated.

Furthermore, Petzold et al. [93] found that smaller S_a roughness values were attainable when virgin – PA12 was used in choice of recycled – material. This confirmed similar qualitative findings reported by Pham et al. [15] and Kruth et al. [71].

³ Excluding any post-processing related strategies.

3.1.2 LS Processing Effects on Roughness

Sachdeva et al. [89]; Mavoori et al. [137]; Bacchewar et al. [138]; and Petzold et al. [93] all used Design of Experiment (DoE) methodologies to determine the extent to which different processing parameters influenced the R_a / S_a roughnesses of resultant laser sintered Polyamide surfaces. The main and interaction effects that were found to be statistically significant have been summarised in **Table 3.1**.

Table 3.1

A summary of the findings discerned from related literature in which DoE methodologies were employed to determine the extent to which different processing parameters influenced the R_a / S_a roughnesses of laser sintered Polyamide surfaces.

Research details	Parameters considered	Main and interaction effects parameters that were found to be statistically significant (in descending order of influence)
Sachdeva et al. [89]	Laser power Scan spacing Powder bed temperature Hatch length Scan count	Laser power × Hatch length Hatch length Laser power Powder bed temperature Scan spacing
Bacchewar et al. [138]	Laser power Scan speed Build orientation Layer thickness Hatch spacing	Top surfaces: Build orientation Layer thickness Bottom surfaces: Build orientation Build orientation × Layer thickness Layer thickness Laser power
Petzold et al. [93]	Laser power Roller speed Powder type Scan spacing	Powder type Powder type × Scan spacing Roller speed Scan spacing Roller speed × Powder type Roller speed × Powder type × Scan spacing Roller speed × Scan spacing Laser power × Roller speed × Powder type Laser power × Powder type × Scan spacing
Mavoori et al. [137]	Laser power Layer thickness Powder bed temperature	Layer thickness × Powder bed temperature Laser power × Powder bed temperature Powder bed temperature

3.1.3 Surface Orientation Effects on Roughness

Part orientation is defined by the user during the pre-processing stage of an LS build, as detailed in **Figure 2.1**.

Schmidt et al. [136], Silani et al. [139] and De Pastre et al. [100] all found that laser sintered PA12 top and bottom surfaces (built parallel to the powder bed) had smaller S_a and S_q values than the side surfaces (built perpendicular to the powder bed) of the same samples. Furthermore, Schmidt et al. [136] and Silani et al. [139] also discerned that top surfaces had greater resultant S_q values than bottom surfaces, despite them having the same surface orientation with respect to the powder bed.

Ultimately, surfaces orientated non-parallel to the powder bed will contain layer-wise discontinuities intrinsic to the LS build process. This ‘stair-stepping’ effect [138] is a function of both processing parameters and powder properties and is exacerbated by the presence of re-entrant or undercut features, such as partially sintered powder particles. Accordingly, both Launhardt et al. [91] and Zhu et al. [95] prescribed that surfaces containing re-entrant or undercut features are unable of being accurately characterised by contact profilometry and /or optical line-of-sight surface metrology methods.

3.1.4 Comparisons Between PA12 Surfaces Produced by LS and other Leading Polymer–PBF Processes

Other well-established and industrially adopted polymer–PBF techniques include High Speed Sintering (HSS) and Multi Jet Fusion (MJF). These processes are typically utilised for similar applications but consolidate powdered-polymer materials by different methods to LS [140].

High Speed Sintering was developed at Loughborough University in 2006 [141]. HSS employs digital inkjet printing to improve the throughput of PBF by increasing the rate at which individual layers can be sintered. A generalised overview of the HSS build process is described below and illustrated in **Figure 3.1**.

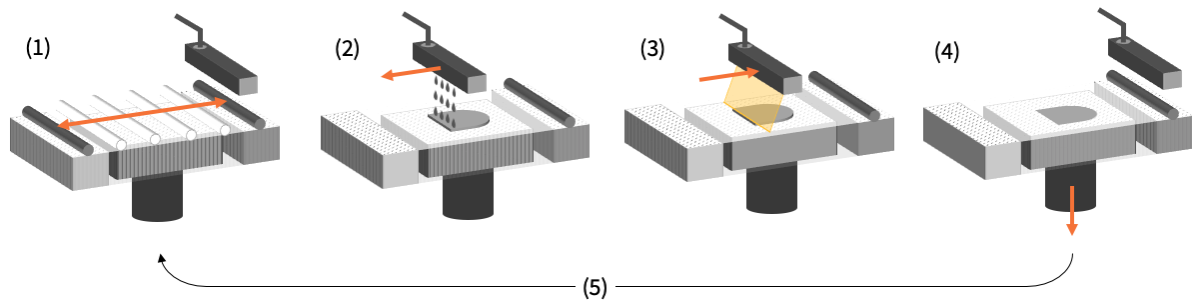


Figure 3.1 – An illustration outlining the general High Speed Sintering build process.

- 1) A powder recoating device deposits a thin layer of material across the build area.
- 2) An inkjet printhead selectively jets radiation absorbing ink in accordance with the current cross-section of the part(s) being produced.
- 3) An infrared lamp radiates the build area which induces sintering between adjacent ink covered powder particles.
- 4) The build platform is lowered by a distance equal to the programmed layer height.
- 5) The process repeats.

Multi Jet Fusion is a proprietary technology owned by Hewlett-Packard (HP) that was only relatively recently introduced to the AM market in 2016.

Like HSS, MJF utilises digital inkjet printing to produce functional components quickly. However, unlike HSS, MJF printheads are multifunctional and selectively jet both radiation absorbing and inhibiting inks, otherwise known as fusing and detailing agents, respectively. The latter is applied at the contours of parts being produced, to prevent the occurrence of undesirable sintering at the interface between part surfaces and surrounding powder, as illustrated in **Figure 3.2**.

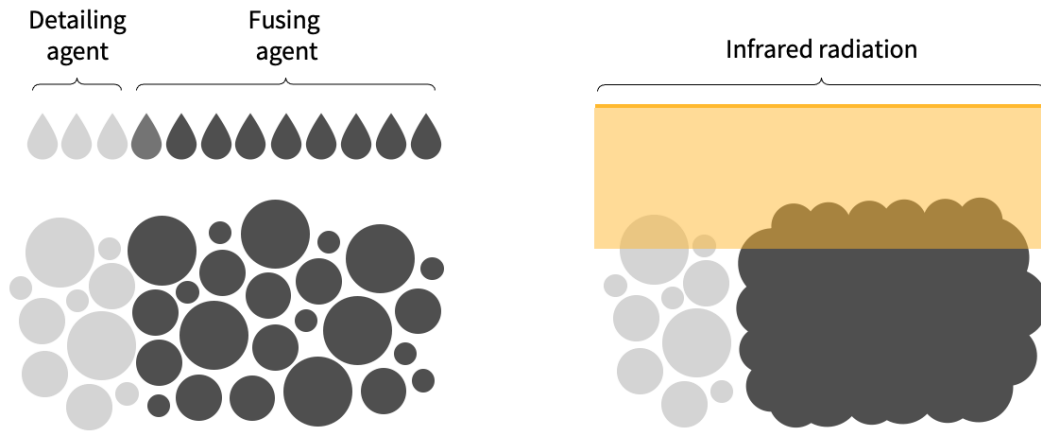


Figure 3.2 – An illustration highlighting the selective jetting of detailing fusion agents during the MJF process.

The following sections compare laser sintered PA12 surfaces to those produced by HSS and MJF.

3.1.4.1 Comparisons Between PA12 Surfaces Produced by LS and HSS

Zhu et al. [142] and Ellis et al. [130] both characterised the surfaces of PA12 samples produced by HSS. However, these studies did not extend to comparing the results obtained with those of analogous LS surfaces.

Zhu et al. [142] found the Arithmetic Mean Heights of HSS surfaces to range from $5\mu\text{m}$ – $20\mu\text{m}$, in congruency with findings reported in LS focussed literature. Additionally, they ascertained that parts produced with higher levels of porosity (due to lower energy inputs) had greater resultant S_a , S_q and S_v ⁴ roughness values.

Zhu et al. [142] also demonstrated that amplitude density functions, specifically Skewness and Kurtosis, could be used to distinguish between the top and bottom surfaces of parts built by HSS. To the best of the authors knowledge, a similar correlation for polymer laser sintered surfaces has not yet been recognised in the literature.

⁴ S_v describes the maximum valley depth of a selected area.

Ellis et al. [130] investigated the effect of build orientation on the resultant R_a roughnesses of top and bottom surfaces of PA12 parts produced by HSS. They found that as the build angle of specimens increased, specifically their orientations relative to the powder bed (from 0° to 90°), their resultant top and bottom R_a roughnesses also increased. This relationship was discerned to be linear for both top and bottom surfaces, with the former ranging from approximately $30\mu\text{m}$ – $45\mu\text{m}$. The influence of build orientation was more pronounced for bottom surfaces, as evidenced by their comparatively larger increases in R_a ($\sim 7.5\mu\text{m}$ – $32.5\mu\text{m}$). This phenomenon was attributed to the ‘stair-stepping’ effect, which, as discussed in **Section 3.1.3**, will have led to the formation of more layer-wise discontinuities as the build angle of the parts produced was increased.

3.1.4.2 Comparisons Between PA12 Surfaces Produced by LS and MJF

Table 3.2 includes results obtained from literature in which the roughnesses of PA12 samples produced by LS and MJF were compared.

Table 3.2

Results obtained from several research works in which the R_a roughnesses of top, bottom and side surfaces of PA12 samples produced by LS and MJF were compared. Side surfaces refer to those built perpendicular to the powder bed and standard deviation values have been included where reported.

Research Works	PBF process	R_a Roughness (μm)		
		Top surfaces	Bottom surfaces	Side surfaces
Cai et al. [143]	LS	17	-	30
	MJF	21	-	16
Xu et al. [144]	LS	14.62 ± 0.45	14.40 ± 1.06	-
	MJF	15.58 ± 0.59	6.31 ± 0.43	-
Rosso et al. [145]	LS	10.4 ± 1.6	15.0 ± 2.3	10.8 ± 0.8
	MJF	8.7 ± 0.9	13.3 ± 1.0	11.2 ± 1.2

As shown in **Table 3.2**, Cai et al. [143] found that laser sintered top surfaces had smaller resultant R_a values compared to MJF top surfaces. However, they also ascertained that their side surface heights were nearly twice as large as those produced by MJF. This was attributed to the overlap between hatching and contour laser scanning during LS, resulting in increased energy exposure at the perimeters of each part during processing, thereby prompting the adhesion of surrounding powder to their side surfaces. These results also demonstrated the effectiveness of the detailing agent in minimising the occurrence of surrounding powder particle adhesion during MJF.

Similarly, when qualitatively characterising LS and MJF side surfaces by SEM analysis, Xu et al. [144] discerned that the former comprised of many sintering necks and voids, whereas the latter were observed to be much denser in comparison. Additionally, they also suggested that the differences in the R_a results collected for MJF top and bottom surfaces stemmed from the detailing agent only being applied to the first, and not the final, build layer during processing. This is likely why MJF top surfaces were found to have a similar mean R_a roughness value to LS top surfaces.

Rosso et al. [145] observed different trends to the previously discussed studies. However, they employed different refresh ratios when conducting LS and MJF builds (1:1 and 1:4 measures of virgin and used PA12 powder, respectively), which may explain why these results were comparatively discordant.

3.1.5 A Summary of the Key Insights Gained from Related Literature on the Surface Topographies of Laser Sintered PA12 Components

Upon reviewing the literature, it was ascertained that laser sintered PA12 surfaces have relatively large resultant amplitude roughnesses, ranging from $10\mu\text{m} < S_a < 20\mu\text{m}$. These roughness values were discerned to be primarily influenced by the feedstock and processing parameters employed, with surface orientation being particularly significant. Additionally, it was made evident that laser sintered PA12 surfaces are highly susceptible

to secondary sintering, or undesirable powder particle adhesion, which is why they are often described as having ‘grainy’ surface textures.

3.2 Laser Sintered PA12 Friction Related Phenomena

3.2.1 COF Results from Laser Sintered PA12 Literature

Table 3.3 includes COF data collated from existing literature that investigated the frictional performance of laser sintered PA12, detailing the testing conditions under which these results were obtained.

Table 3.3

A summary of the findings discerned from related literature in the which the frictional performance of laser sintered PA12 samples were experimentally evaluated.

Research work	COF value	Testing configuration	Pertinent contact details	Load / pressure	Speed / frequency
Guo et al. [88]	0.33	Linear, reciprocating, ball-on-flat	Stainless steel ball ($\varnothing = 6\text{mm}$)	2N	10Hz
Bai et al. [146]	0.30	Linear, reciprocating, ball-on-flat	Stainless steel ball ($\varnothing = 9.525\text{mm}$)	35N	0.33ms^{-1}
Bai et al. [135]	0.18	Linear, reciprocating, ball-on-flat	Stainless steel ball ($\varnothing = 8\text{mm}$)	35N	—
Ziegler et al. [147]	0.06 – 0.28	—	—	10N	0.03mms^{-1} – 300mms^{-1}
Rajendran and Ganesan [148]	0.14 – 0.18	Rotating, pin-on-disk, flat-on-flat	PA12 pin ($\varnothing = 8\text{mm}$), Medium carbon steel disk	10N – 40N	0.50ms^{-1} – 1ms^{-1}
Yu et al. [149]	0.3 – 0.4	Rotating, pin-on-disk, ball-on-flat	304 stainless steel ball ($\varnothing = 8\text{mm}$)	20N	360 rpm
Wörz and Drummer [150]	~0.50	Rotating, pin-on-disk, flat-on-flat	PA12 pin ($\boxplus = 4 \times 4\text{mm}$), EN31 steel disk	4Nmm^{-2}	0.5ms^{-1}
Gadelmoula and Aldahash [151]	0.15 – 0.42	Rotating, pin-on-disk, flat-on-flat	PA12 pin ($\varnothing = 4\text{mm}$), Stainless steel disk	50N	0.25ms^{-1}

As can be seen in **Table 3.3**, a wide range of test procedures have previously been employed in the literature to characterise the frictional properties of laser sintered PA12 samples. Consequently, the COF results recorded varied significantly across these studies.

The effects of normal load, sliding speed, temperature and build orientation on the frictional responses, as reported in the studies outlined in **Table 3.3**, are discussed in **Section 3.2.3**.

3.2.2 Comparisons Between Laser Sintered PA12 and General Polymer COF Data

More generally, Myshkin et al. [108] collated COF information for a range of different polymer groups. An overview of which can be seen in **Figure 3.3**. Additionally, the results from **Table 3.3** have also presented in **Figure 3.3** to elucidate the consensus between the aforementioned laser sintered PA12 frictional responses and general polymer COF data reported in the literature.

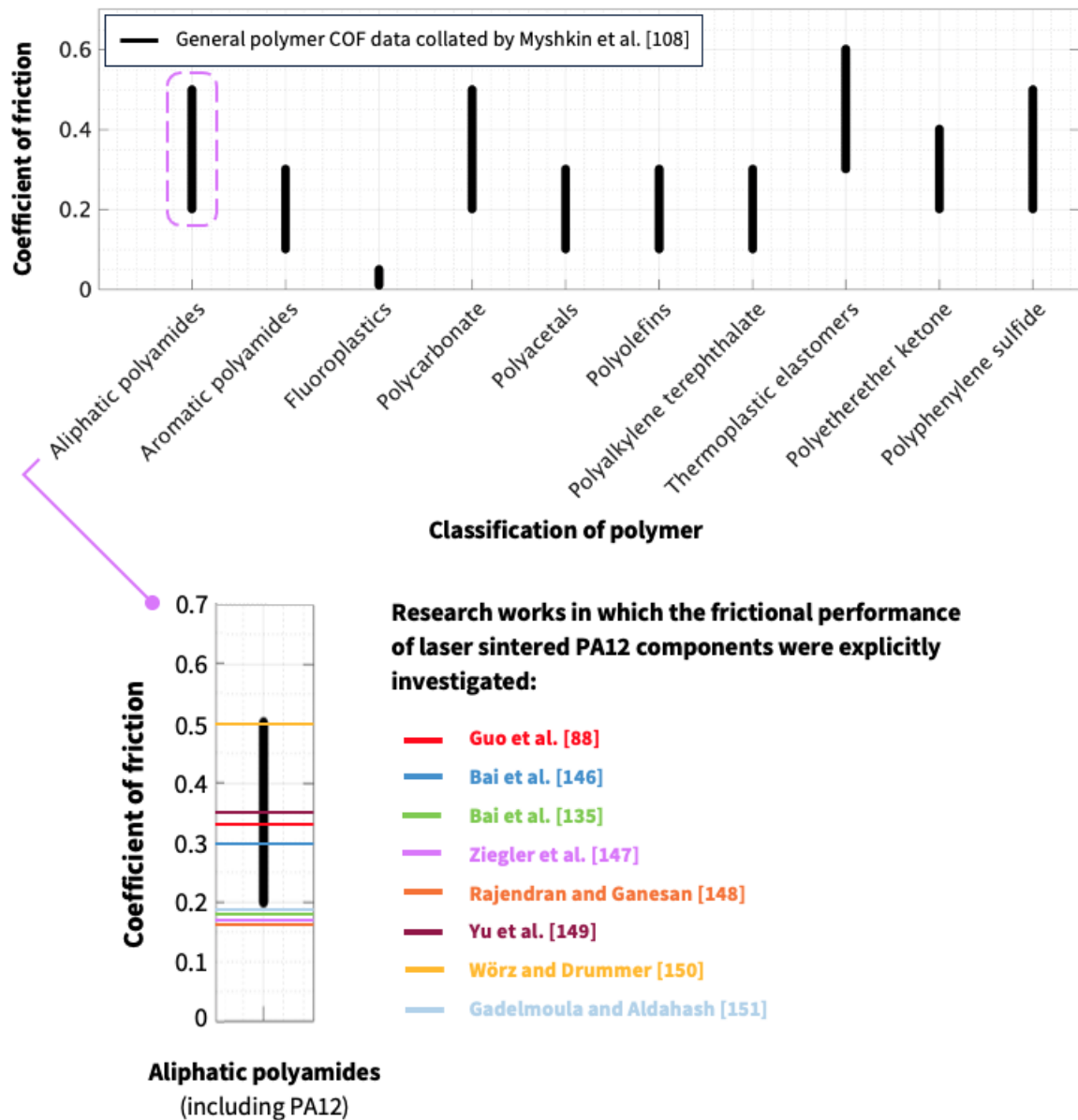


Figure 3.3 – A comparison between general polymer COF data collated by Myshkin et al. [108] and the laser sintered PA12 mean COF results summarised in **Table 3.3**.

3.2.3 The Key Factors that Influence the Frictional Behaviours of Laser Sintered PA12 Components

Friedrich [152] prescribed that polymer tribology does not comply with the traditional laws of friction due to COF being unconventionally influenced by normal load, sliding speed and temperature.

3.2.3.1 The Influence of Normal Load on the Frictional Behaviours of Laser Sintered PA12

Kragelski [153] discerned that the mechanism by which a polymer surface supports a normal load is dependent on whether its asperities deform elastically or plastically during sliding. Elastic contacts involve supporting normal loads at the tips of surface asperities (typically when $N < 1\text{N}$), whereas plastic contacts support normal loads by yielded asperities and bulk surface material (typically when $N > 5\text{N}$).

Shooter and Tabor [154] validated Amonton's 1st Law for a variety of polymers when subject to a range of applied normal loads, specifically between 10N and 100N. Though, in concurrence with Kragelski [153], they also identified that proportionality between N and F_f becomes skewed at applied normal loads outside of this range, particularly when $N < 1\text{N}$ [81].

Rajendran and Ganesan [148] carried out a DoE to determine the extent to which normal load, sliding speed and build orientation influenced the frictional properties of laser sintered PA12 samples (when subject to rotating, pin-on-disk, flat-on-flat, dry sliding against steel). Ultimately, they ascertained that both normal load and sliding speed had statistically significant impacts on COF, in descending order of influence, respectively.

3.2.3.2 The Influence of Sliding Speed on the Frictional Behaviours of Laser Sintered PA12

As stated in **Section 2.5.2**, Coulomb's Law specifies that kinematic friction is independent of sliding velocity. However, this is only true if the effects of frictional heating are deemed insignificant.

Supplementary to the previously discussed work performed by Rajendran and Ganesan [148], Ziegler et al. [147] also found sliding speed to be significant when investigating the dry sliding behaviours of laser sintered PA12 samples against steel. More specifically, they

varied sliding speed from 0.03mms^{-1} – 300mms^{-1} and discerned that COF was correspondingly affected when $v > 3\text{mms}^{-1}$.

3.2.3.3 The Influence of Temperature on the Frictional Behaviours of Laser Sintered PA12

The frictional mechanisms that induce heat during dynamic contact include, adhesion, deformation, hysteresis, dispersion and viscous flow [81,126].

Hooreweder et al. [155] found that the molecular chains within the amorphous regions of laser sintered PA12 samples stretched and elongated when their glass transition temperatures were exceeded, leading to larger deformations at the same stress levels. Therefore, when $T > (T_g = 48.8^\circ)$ [156], the F_{fA} component of F_f is expected to increase during polymer sliding.

Gadelmoula and Aldahash [151] used an infrared laser sensor to measure the magnitude of frictional heat induced during laser sintered PA12 – stainless steel sliding. They recorded linear increases in temperature from approximately 30°C to 60°C , with the actual interfacial contact temperatures (T_c) expected to be even higher. Consequently, the stiffness of PA12 will have likely decreased during testing, which was evidenced by the occurrence of adhesion observed during SEM analysis post-testing.

3.2.3.4 The Influence of Build Orientation on the Frictional Behaviours of Laser Sintered PA12

As discussed in **Section 3.1.3**, build orientation impacts the resultant surface topography of parts produced by LS.

In contrast to what was observed by Rajendran and Ganesan [148], both Bai et al. [135] and Ziegler et al. [147] found that the orientation in which laser sintered PA12 part surfaces were built affected their resultant frictional properties.

Ziegler et al. [147] discerned that at sliding speeds greater than 3mms^{-1} , part surfaces built parallel (0°) to the powder bed had reduced resultant COF values relative those built perpendicular (90°) to the powder bed. Moreover, Bai et al. [135] found that the frictional responses of top surfaces (built parallel to the powder bed) were 64% greater than the COF values measured when evaluating the side surfaces (built perpendicular to the powder bed) of the same samples. They suggested that upon becoming dislodged, the partially adhered powder particles on the side surface of samples may have acted as roller elements, facilitating sliding during testing.

Similarly, Guo et al. [88] performed sliding tests on laser sintered PA12 samples that were subjected to varying levels of post-processing, including as-built, precision grinding and magnetic field-assisted finishing. Resultant sample surfaces had R_a roughnesses of $15\mu\text{m}$, $2.85\mu\text{m}$ and $0.89\mu\text{m}$, and corresponding COF values of 0.329, 0.397 and 0.315, respectively. Therefore, no correlations between surface topography and friction properties could be discerned.

3.2.4 A Summary of the Key Insights Gained from Related Literature on the Frictional Behaviours of Laser Sintered PA12 Components

When collating the information presented in **Table 3.3**, it became evident that there are no established test procedures for assessing the frictional performance of laser sintered PA12 components. Consequently, the results collected varied significantly, indicating that an in-depth understanding of how different operating conditions affect COF has yet to be attained.

3.3 Laser Sintered PA12 Wear Related Phenomena

3.3.1 Wear Rate Data from Laser Sintered PA12 Literature

Table 3.4 includes specific wear rate data collated from existing literature that investigated the wear performance of laser sintered PA12, detailing the testing conditions

under which these results were obtained, as well as the wear mechanisms that dominated during sliding.

Table 3.4

A summary of the findings discerned from related literature in the which the wear behaviours of laser sintered PA12 samples were experimentally characterised.

Research work	Specific wear rate (mm ³ / Nmm)	Key contact details	Wear mechanisms
Guo et al. [88]	4.91 ± 0.58 ($\times 10^{-7}$)	Test configuration: Linear, reciprocating, ball-on-flat Contact geometry: <i>Stainless steel ball ($\phi = 6\text{mm}$)</i> Load / pressure: <i>2N</i> Speed / frequency: <i>10Hz</i>	No discussion of the wear mechanisms induced during the analysis of as-built samples
Bai et al. [146]	2.28 ± 0.26 ($\times 10^{-7}$)	Test configuration: <i>Linear, reciprocating, ball-on-flat</i> Contact geometry: <i>Stainless steel ball ($\phi = 9.525\text{mm}$)</i> Load / pressure: <i>35N</i> Speed / frequency: <i>0.33\text{ms}^{-1}</i>	Worn surfaces were observed to be very rough and discontinuous, with resultant wear debris taking the form of lumps. Additionally, ploughing marks and pits were evident. The latter was indicative of severe abrasive wear.
Bai et al. [135]	Top surfaces: 6.61 Side Surfaces: 6.22	Test configuration: <i>Linear, reciprocating, ball-on-flat</i> Contact geometry: <i>Stainless steel ball ($\phi = 8\text{mm}$)</i> Load / pressure: <i>35N</i> Speed / frequency: -	It was suggested that voids formed due to partial powder particle adhesion acted as crack initiators, leading to wear. Though, the wear debris produced was hypothesised to reduce the stresses transmitted to the 'first bodies', thus decreasing the amount of deformation incurred.
Ziegler et al. [147]	Volume loss measurements provided in choice of wear rate data.	Several different wear tests performed.	Scratch marks within the resultant wear scars indicated that abrasive wear by plastic deformation was the primary wear mechanism.

Rajendran and Ganesan [148]	Not quantified	<p>Test configuration: <i>Rotating, pin-on-disk, flat-on-flat</i></p> <p>Contact geometry: <i>PA12 pin ($\varnothing = 8\text{mm}$), Medium carbon steel disk</i></p> <p>Load / pressure: <i>10N – 40N</i></p> <p>Speed / frequency: <i>0.50ms^{-1} – 1ms^{-1}</i></p>	<p>Initial contact resulted in abrasive wear, specifically microcutting and the shearing of PA12 asperities, which subsequently prompted the formation of a transfer film.</p> <p>Upon being removed, resultant wear debris acted as rolling elements between contacting surfaces, as evidenced by the needle-, fibre-, and spheroidal-shaped wear debris identified post-testing.</p>
Yu et al. [149]	1.88 ($\times 10^{-7}$)	<p>Test configuration: <i>Rotating, pin-on-disk, ball-on-flat</i></p> <p>Contact geometry: <i>304 stainless steel pin ($\varnothing = 8\text{mm}$)</i></p> <p>Load / pressure: <i>20N</i></p> <p>Speed / frequency: <i>360 rpm</i></p>	<p>Relatively smooth wear scars indicated that abrasive wear, specifically plastic shear flow, dominated during testing.</p>
Wörz and Drummer [150]	20 – 40 ($\times 10^{-9}$)	<p>Test configuration: <i>Rotating, pin-on-disk, flat-on-flat</i></p> <p>Contact geometry: <i>PA12 pin ($\boxplus = 4 \times 4\text{mm}$), EN31 hardened steel disk</i></p> <p>Load / pressure: <i>4Nmm^{-2}</i></p> <p>Speed / frequency: <i>0.5ms^{-1}</i></p>	<p>Wear was not attributed to any specific mechanisms.</p>
Gadelmoula and Aldahash [151]	3 – 12 ($\times 10^{-8}$)	<p>Test configuration: <i>Rotating, pin-on-disk, flat-on-flat</i></p> <p>Contact geometry: <i>PA12 pin ($\varnothing = 4\text{mm}$), Stainless steel disk</i></p> <p>Load / pressure: <i>50N</i></p> <p>Speed / frequency: <i>0.25ms^{-1}</i></p>	<p>SEM analysis showed the occurrence of tearing in line with the direction of sliding, with the wear debris produced being flake-like in shape. This indicated that adhesive wear dominated during testing.</p>

3.3.2 Comparisons Between Polyamides and other Engineering Polymers

To the best of the author's knowledge, comparisons between the wear properties of PA12 components prepared by LS and other manufacturing methods, including other polymer-PBF techniques, have yet to be reported within the literature.

More generally, Nylon polymers, including PA12, are regarded as having a relatively good resistance to wear, as outlined in **Table 3.5**.

Table 3.5

A selection of research works in which the wear properties of Nylon polymers were qualitatively discussed.

Research work	Comment
Myshkin et al. [108]	<i>"Low wear and high fatigue resistance"</i>
Unal et al. [157]	<i>"Polyamide has been reported to have a superior wear resistance sliding against a steel counterface relative to other polymers"</i>
Steinbuch [158]	<i>"High wear resistance with relatively low coefficient of friction when sliding on metals is the principal ground for its application"</i>
Weimin et al. [159]	<i>"Nylon is a good bearing material because of its high strength and good wear resistance"</i>
Ma et al. [160]	<i>"Nylon 12 (PA12) is an important material with excellent physical properties such as toughness, abrasion resistance"</i>
Bijwe et al. [161]	<i>"Polyamide (PA) 12 is a versatile engineering thermoplastic ... It possesses high strength, modulus, toughness, resistance to creep, abrasion and fatigue"</i>
Rouholamin and Hopkinson [162]	<i>"Polyamide 12 or nylon 12 is a thermoplastic polymer ... Good abrasion resistance, high elongation at break, specific strength ..."</i>

Furthermore, according to the Ratner–Lancaster expression detailed in **Equation 2.15**, the polymers in the upper right quadrant of the Ashby plot presented in **Figure 3.4**, which includes Polyamides, are expected to be more resistant to abrasive wear.

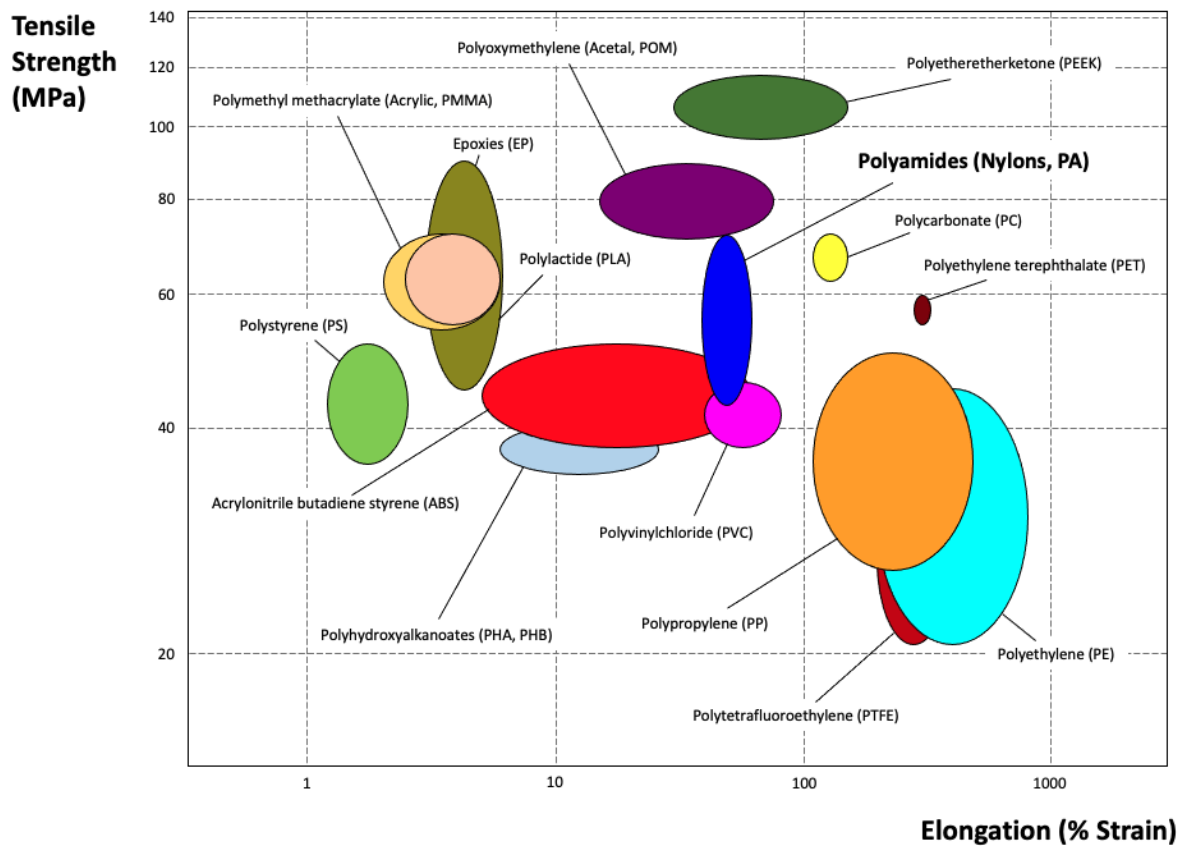


Figure 3.4 – Ashby plot displaying the relative variation between different polymer types with respect to their strength and ductility.

In two different studies, Unal et al. [163,164] investigated the wear performance of polyamide 66, aliphatic polyketone (APK), polyoxymethylene, ultrahigh molecular weight polyethylene and glass fibre reinforced polyphenylenesulfide (PPS + 30% GFR). They found the wear rate of PA66 ($\times 10^{-6} \text{ mm}^3/\text{Nm}$) to be an order of magnitude lower than APK, UHMWPE and PPS + 30% GFR ($\times 10^{-5} \text{ mm}^3/\text{Nm}$), which were all significantly more resistant to wear than POM ($\times 10^{-3} \text{ mm}^3/\text{Nm}$), when subject to varying normal loads and sliding speeds [164]. Similarly, they found that PA66 had the second lowest wear rate, with respect to the other aforementioned polymers, when subject to dynamic contact against different abrasive papers of varying grit sizes [163].

3.3.3 The Inclusions of Fillers to Modify the Wear Properties of Laser Sintered PA12 Components.

Several of the studies outlined in **Table 3.4** explored the inclusion of different filler materials within PA12 powders prior to LS as a method of improving the wear resistance of parts produced.

Yu et al. [149] incorporated a 10% mass fraction of Silicon Carbide (SiC) into a batch of PA12 powder prior to LS. Resultant composite samples were found to be 20% more resistant to wear compared to neat-PA12 specimens processed identically. This difference was attributed to the 6% increase in indentation hardness achieved by the inclusion of SiC particles.

Gadelmoula and Aldahash [151] compared the friction and wear properties of laser sintered parts produced from commercially available PA12 and Carbon Fibre (CF) reinforced PA12 powders, namely PA2200 and CarbonMide supplied by EOS GmbH, respectively. The specific wear rates of CF – PA12 samples were 15% to 40% lower than PA12 samples, depending on the build orientation evaluated.

Bai et al. [146] modified the tribological performance of laser sintered PA12 samples by including 1 wt% Molybdenum disulfide. (MoS_2). The addition of this solid lubricant was found to induce transfer film formation, which consequently reduced both COF and wear rate by 56.7% and 41.7%, respectively (during linear reciprocating, ball-on-flat sliding). Other filler materials have also been reported to improve the wear resistance of bulk Nylon polymers by promoting transfer film formation during sliding. These include Copper Monosulphide (CuS) [165,166]; Cupric Oxide (CuO) [166]; Copper Fluoride (CuF_2) [166]; Glass Fibres [167]; PTFE [167]; Lead Sulphide (PbS) [168,169]; and Aluminium Oxide (Al_2O_3) [170]. However, it should be noted that the morphologies and weight percentage inclusions of these filler materials varied between studies.

3.3.4 A Summary of the Key Insights Gained from Related Literature on the Wear Behaviours of Laser Sintered PA12 Components

The use of different test procedures in previous related literature made it difficult to once again compare findings, as different wear mechanisms dominated depending on the contact conditions employed. Nonetheless, this review highlighted the potential to characterise both transient and steady-state sliding (rather than just the latter), as well as better establish the effects of different surface orientations and varying operating conditions on the wear responses of laser sintered PA12 components. Moreover, the inclusion of filler materials within PA12 powders prior to processing via LS should be investigated further, as their impacts on wear have been shown to be significant.

3.4 Literature Review Conclusions

This literature review comprehensively collated insights reported within related literature regarding the surface, friction and wear properties of laser sintered PA12 components.

Based on this information, the following gaps in research have been identified as topics for further study:

- Further characterisation of laser sintered PA12 surfaces, with a particular focus on identifying any recurring surface features that may affect their sliding behaviours.
- Investigating the friction and wear behaviours of laser sintered PA12 components during both transient and steady-state wear regimes, including the effects of different surface orientations and varying operating conditions.
- Exploring whether the COF and / or wear rate of laser sintered PA12 surfaces can be reduced by including solid lubricant fillers within PA12 powders prior to LS.

Accordingly, the following chapters of this thesis will focus on investigating the above.

Chapter 4

Materials and Methods

Chapter Summary

This chapter details the PA12 powder properties and experimental methods pertinent to this doctoral work. Moreover, the latter includes a detailed description of the LS build process followed, as well as a delineated outline of the primary characterisation techniques employed to evaluate the resultant bulk, surface and tribological properties of samples produced.

Recapitulate descriptions of the following experimental details are also provided within subsequent chapters of this thesis.

4.1 Materials

4.1.1 Polyamide-12

Commercial grade Polyamide-12, specifically PA2200 supplied by EOS GmbH, was used throughout this doctoral work. As mentioned in **Section 2.3.2**, Polyamide powders are typically very reliable when processed via LS, which is primarily why approximately 90% of the LS materials market is dominated by PA12 [26]. Due to its widespread adoption, PA12 was the principal polymer of focus throughout the entirety of this thesis.

As discussed in **Section 2.3.2.2**, it is conventional practice to implement a refresh ratio when laser sintering PA12. Therefore, a refresh ratio of 50% virgin – material and 50% once – used – material ⁵ (hereinafter referred to as 50/50 – PA12) was predominantly adopted throughout this investigation. Though, when entirely virgin – PA12 was employed, it was done so to eliminate the possibility of used-powder potentially influencing the resultant surface, friction and wear properties of parts produced. The specific PA12 powder compositions adopted within each experimental study are stated within the ‘Materials’ section of each corresponding thesis chapter.

4.1.1.1 Powder Morphology

Figure 4.1 includes SEM obtained micrographs that provide a qualitative description of the particle morphologies that comprise the virgin – PA12 and 50/50 – PA12 powders used throughout this investigation.

⁵ Once – used – material refers to PA12 powder recycled from a single previous LS build in which only virgin – PA12 was processed.

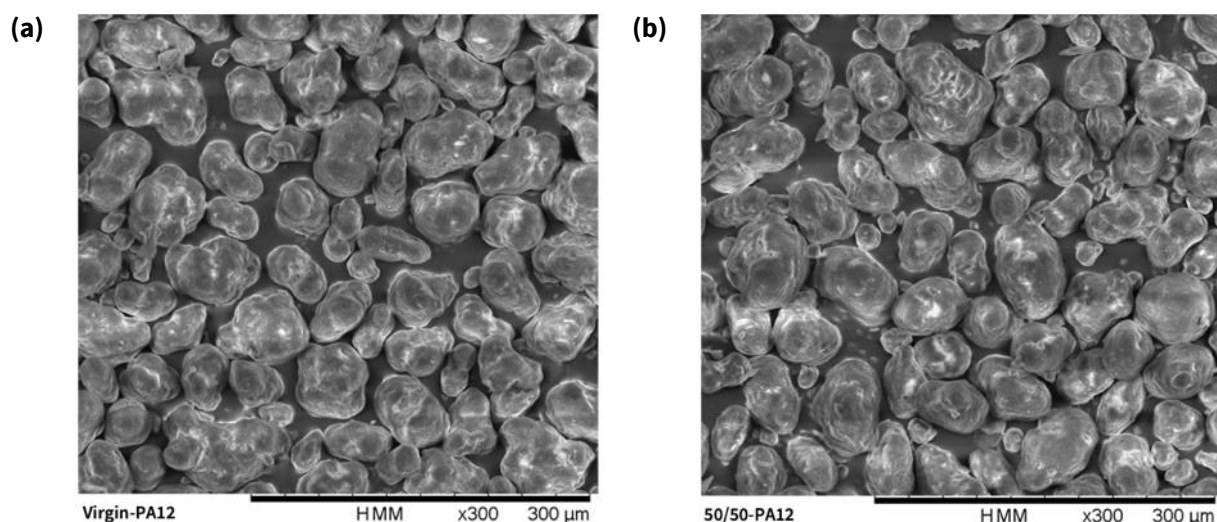


Figure 4.1 – SEM images highlighting the typical morphologies of the **(a)** virgin – PA12 and **(b)** 50/50 – PA12 powders used throughout this investigation.

As elucidated in **Figure 4.1**, the virgin – PA12 and 50/50 – PA12 powders used within this investigation comprised of particles that were similar in size and morphology. Additionally, these SEM micrographs are congruous with the powder information provided by the material manufacturer – EOS GmbH, who report the average particle size of virgin – PA2200 to be 56μm [171].

4.1.1.2 Thermal Properties

Figure 4.2 includes the heating and cooling curves for both virgin – PA12 and 50/50 – PA12 powders. The key features of this DSC obtained thermograph were previously discussed in **Section 2.3.2.2**.

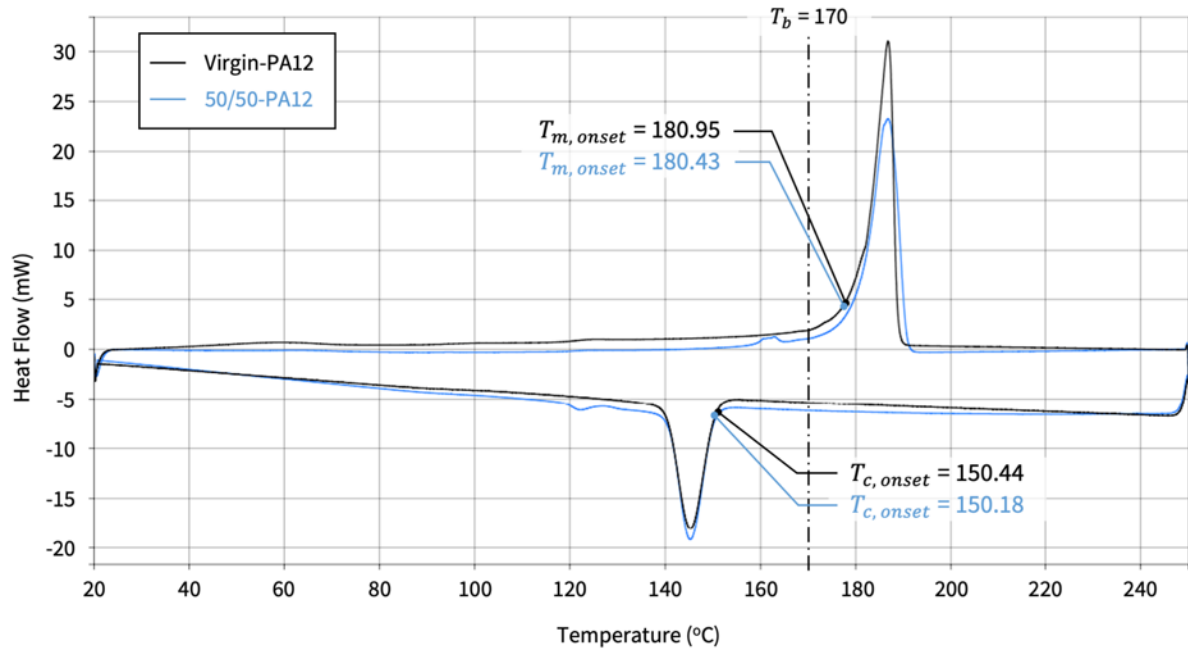


Figure 4.2 – DSC obtained heating and cooling curves of virgin – PA12 and 50/50 – PA12 powders.

Practically, the most significant insight to be drawn from the heating and cooling curves presented in **Figure 4.2** is the correspondence between the processing windows of virgin – PA12 and 50/50 – PA12. More specifically, both PA12 configurations have alike onsets of melting and crystallisation (180°C and 150°C, respectively). Therefore, the same powder bed temperatures were employed when processing both materials.

4.1.1.3 Material Properties

Table 4.1 includes details of the laser sintered virgin – PA2200 material properties deemed attainable by the material manufacturer (EOS GmbH) [171].

Table 4.1

Laser sintered virgin-PA2200 part properties, as determined by the material manufacturer (EOS GmbH) [171].

Material property	Standardised test method followed	Value
Density (g/cm ³)	–	0.93
Young's Modulus (MPa)	ISO 527	1700
Ultimate Tensile Strength (MPa)	ISO 527	48
Elongation at Break (%)	ISO 527	24
Ball Indentation Hardness (N/mm ²)	ISO2039	78
Shore D Hardness	ISO 868	75
Melting point (°C)	ISO 11357-1	172-180

Additionally, the resultant tensile properties of virgin – PA12 and 50/50 – PA12 samples manufactured in-house (using the processing parameters detailed in **Table 4.3**) are given in **Table 4.2**. A comprehensive overview of the test methodology followed to obtain these mechanical properties is provided in **Section 4.2.2.1**.

Table 4.2

The tensile properties of samples produced in-house from virgin – PA12 and 50/50 – PA12.

Mechanical property	Standardised test method followed	Virgin – PA12	50/50 – PA12
Young's Modulus (MPa)	ASTM D638-14	1402	1547
Ultimate Tensile Strength (MPa)	ASTM D638-14	43.0	45.2
Elongation at Break (%)	ASTM D638-14	23.3	27.6

Despite PA12 samples produced in-house having reduced tensile properties relative to those deemed attainable by the material manufacturer (EOS GmbH), they are in good agreement with results reported in the literature [77,208,209]. Though, it is generally expected that different LS systems and adopted build parameters will result in parts produced having different mechanical properties.

Moreover, the slight differences between the tensile properties of in-house produced virgin – PA12 and 50/50 – PA12 samples should also be noted. However, these variations, in particular those observed when analysing Elongation at Break, are also congruent with results reported in the literature [77, 93, 210].

4.2 Methods

4.2.1 Laser Sintering

All samples were designed using Autodesk Fusion 360, before being arranged within a virtual build envelope using Magics 23.0. Proprietary software developed by EOS GmbH (compatible with the LS system used) was then utilised to slice and assign specific processing parameters to specimens within each LS build.

An EOS Formiga P100 system was employed to execute each LS build. An image of the specific machine used, as well as a schematical diagram of its key components and snapshot of it partway through building can be seen in **Figure 4.3**.

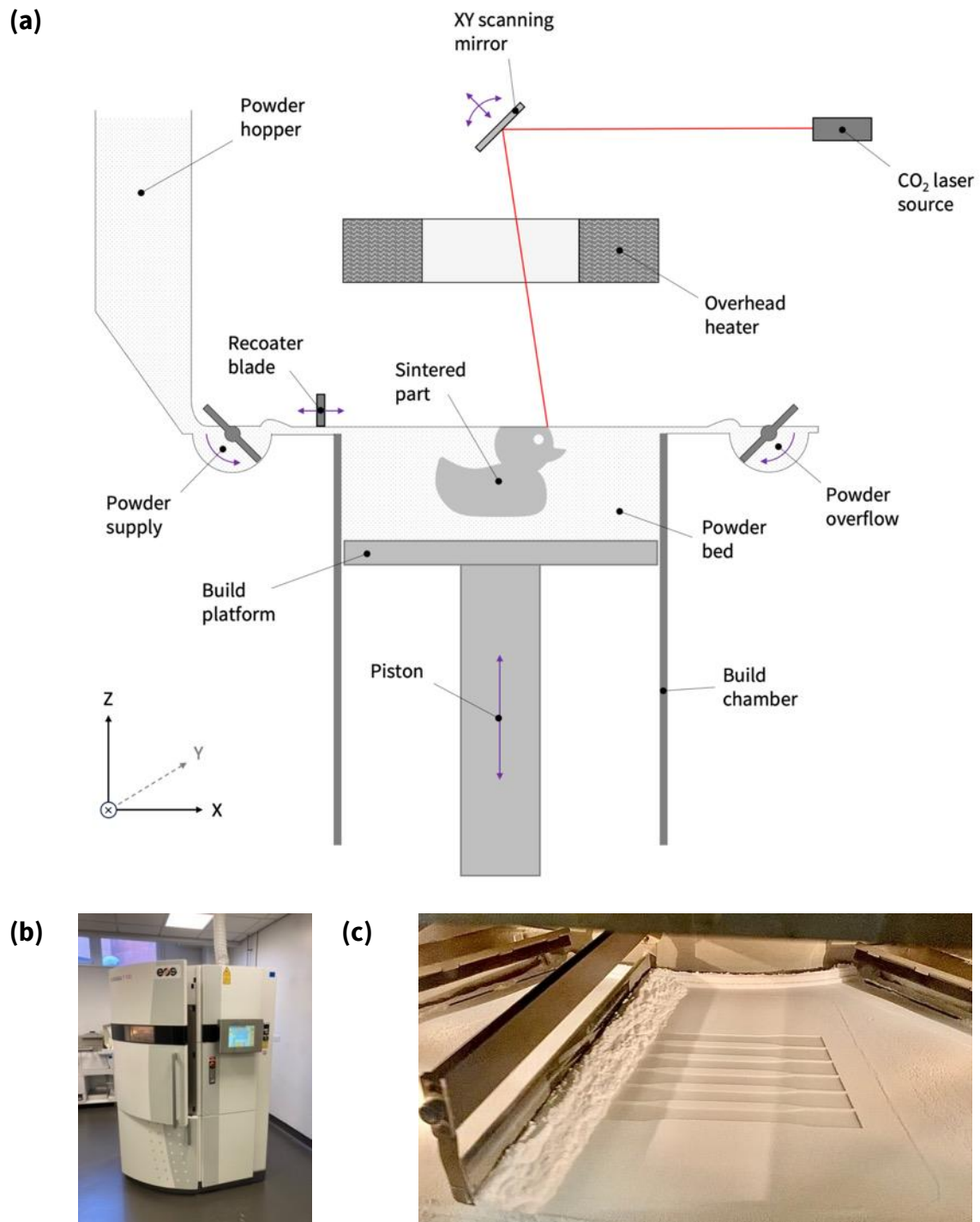


Figure 4.3 – (a) A schematical illustration of an EOS P100 system (adapted from Goodridge et al. [19]), as well as (b) the system itself and (c) a snapshot of it partway through building.

Unless explicitly stated otherwise, the LS processing parameters outlined **Table 4.3** (hereinafter referred to as standard PA12 parameters) were used throughout this

investigation. These build parameters were previously developed by both past and present members of the Advanced Polymer Sintering Laboratory at the University of Sheffield to maximise the tensile properties of PA12 parts produced in-house. Correspondingly, these processing parameters have a resultant energy density value of 33.6 mJ(mm⁻²).

Table 4.3

The standard PA12 LS processing parameters adopted throughout this doctoral work.

Processing parameter	Value
Laser power (W)	21
Beam spacing (mm)	0.25
Scan speed (mm s ⁻¹)	2500
Bed temperature (°C)	170
Scan count	1
Contour scan	Off
Layer thickness (mm)	0.1
Number of blank powder layers that directly preceded and followed particle sintering.	40

Prior to building, all PA12 powders were sieved to remove any agglomerates that may have subsequently impeded their ability to flow. Additionally, if powder blends were used, such as 50/50 – PA12, composite constituents were homogenised by rotary tumbling at a speed of 12.5 rpm for durations ranging from 20 minutes to 120 minutes, depending on the composition of the mixture used. The exact rotary tumbling durations employed in each experimental study are detailed within each corresponding thesis chapter.

Samples were arranged with at least 5mm margins in every direction to minimise any thermal interactions that may have occurred between neighbouring parts during building.

Upon completion of each LS build (including their respective cooldown periods), compressed air was used to remove loose powder particles from the surfaces of each

sample produced. When required, glass bead blasting was also utilised to separate parts from their relatively ‘harder’ powder cakes, as stated in each corresponding thesis chapter.

4.2.2 Characterisation Techniques

4.2.2.1 Tensile Testing

As shown in **Figure 4.4**, a Tinius Olsen H5KS tensometer with a H500L laser extensometer was used to measure the Young’s Modulus (YM), Ultimate Tensile Strength (UTS) and Elongation at Break (EaB) of resultant samples in accordance with ASTM D638-14 [175].

The cross-sectional area of each tensile specimen was calculated from width and thickness measurements taken at three locations between their grips, and tensile loads were applied parallel to their gauge lengths at a speed of 5 mm(min⁻¹).



Figure 4.4 – A tensile specimen mounted between the grips of the Tinius Olsen H5KS tensometer used throughout this doctoral work.

All tensile specimens were oriented in the XY plane of the LS machine, as defined in **Figure 4.3**. The major dimensions of an ASTM D638-14 Type 1 tensile specimen can be seen in **Figure 4.5**.

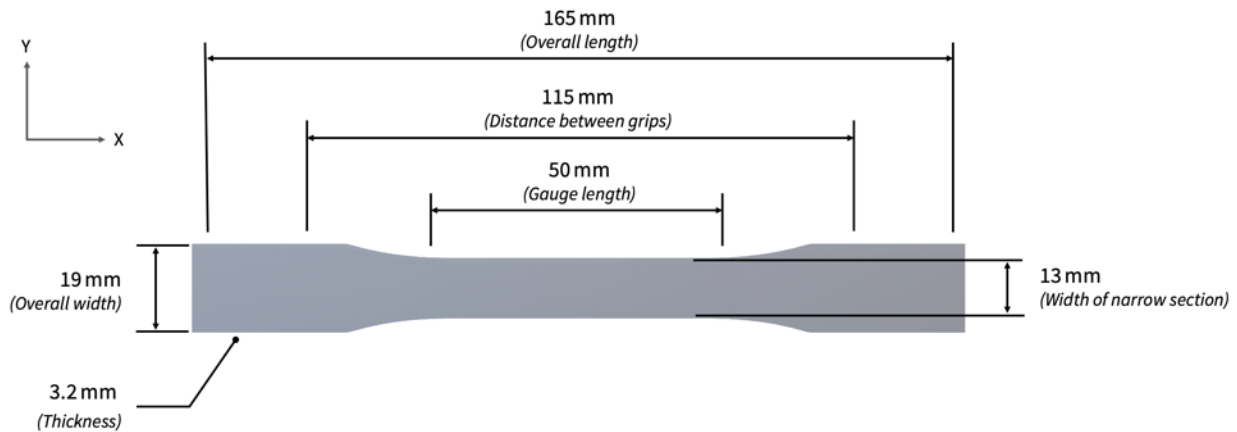


Figure 4.5 – The specific geometry of an ASTM D638-14 Type 1 tensile specimen. Adapted from ASTM D638-14 [175].

4.2.2.2 Microscopy Analysis

Focus Variation (FV) and Scanning Electron Microscopy (SEM) were both frequently utilised for a range of different characterisation activities, including those pertaining to the analysis of powder morphologies, surface topographies, wear scars and material transfer. The specific FV and SEM microscopy systems used throughout this investigation can be seen in **Figure 4.6**.

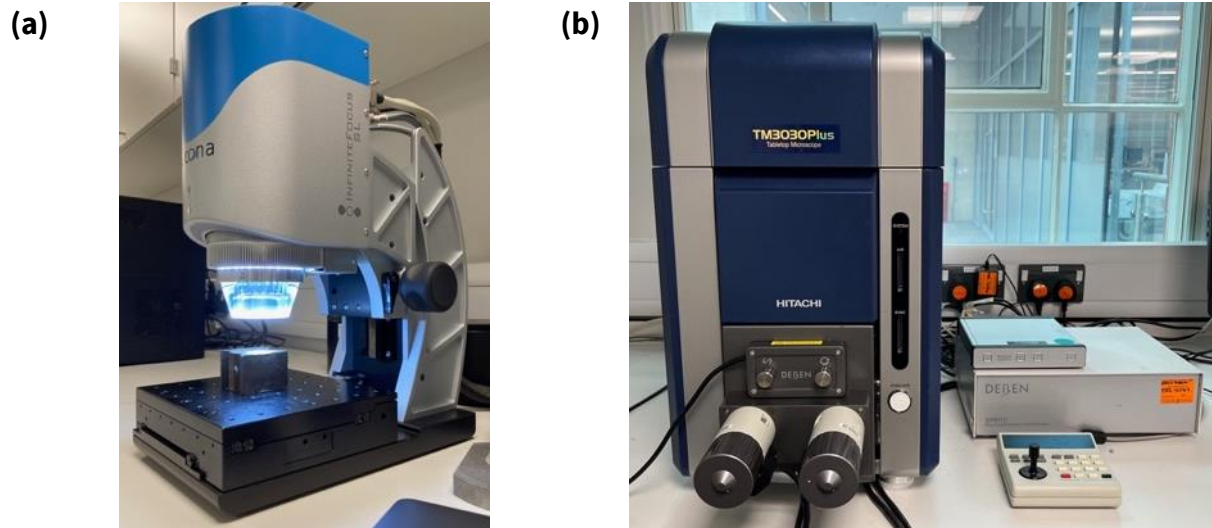


Figure 4.6 – The specific (a) FV and (b) SEM microscopy systems used throughout this doctoral work.

Focus Variation Microscopy

During the FV process, a vertical array of images is captured, where the distance between each image is equal to the vertical resolution of the scan. To extract depth information (Z-heights) from the image array, each pixel within each image is compared with neighbouring pixels to gain a measure of relative contrast [97]. The size of the XY region selected to evaluate the relative contrast of each individual pixel is more commonly referred to as the lateral resolution of the scan. The relative contrast of each pixel within each image is then compared with the relative contrasts of all the other pixels throughout the vertical image array that have the same X- and Y- coordinates. Finally, the location of each pixel with the greatest relative contrast with respect to the length of the vertical image array is used to compute its Z-height.

FV microscopy was performed using an Alicona InfiniteFocusSL system. More specifically, a x5 AV objective lens, equipped with a coaxial polarised ring light, was used to capture $3.7\text{mm} \times 3.7\text{mm}$ sampling regions with a vertical resolution of 550nm and the smallest lateral resolution required to generate a complete scan. Jigs were used to position specimens, and wherever necessary, ensure that they remained completely flat during scanning, as shown in **Figure 4.7**.

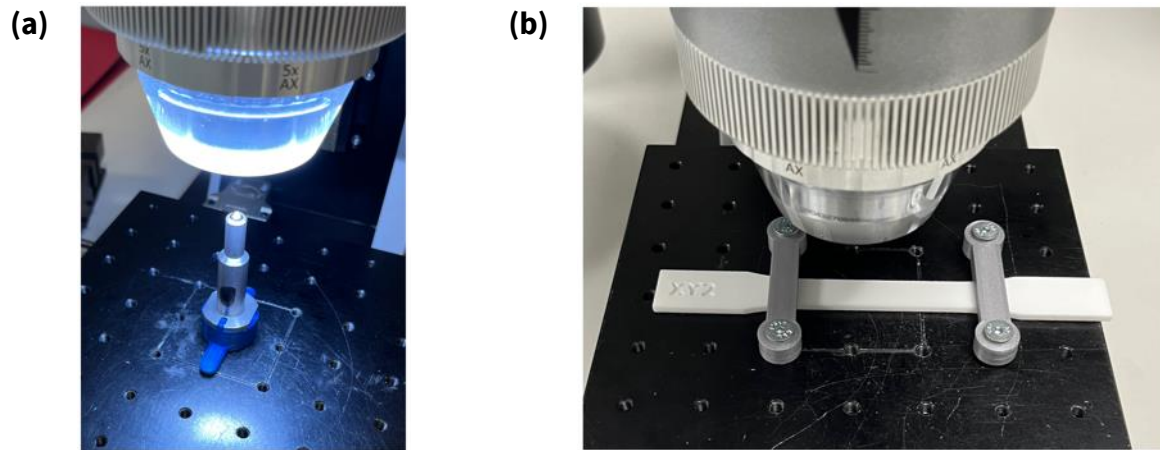


Figure 4.7 – Example jigs that were used to **(a)** position and **(b)** secure samples during FV microscopy analysis.

When FV microscopy was utilised to specifically characterise the amplitude roughnesses of laser sintered polymer surfaces, evaluation areas ($2.5\text{mm} \times 2.5\text{mm}$ in size) were subsequently analysed without the application of any spatial filtering. It should be noted that the latter was discordant with guideline outlined in ISO 25178-3 [176], which suggests that S-, L- and F- filtering should always be applied to remove small-scale, large-scale and form components from optically obtained surface scans, respectively. However, due to ambiguity in ISO 25178-3, it was difficult to discern specific nesting index values for each of these operations. Furthermore, whenever these filtering operations were previously adopted within polymer-PBF related literature, accompanying nesting index values were rarely specified. In fact, the most extensive bodies of research that previously employed FV microscopy to characterise laser sintered polymer surfaces did so without the application of any filtering. The former includes works by Petzold et al. [93,177] and Launhardt et al. [91].

Conversely, when extracting 2D wear scar profiles from 3D areal surface scans, a cut-off length of 0.8mm was applied in accordance with ISO 13565-1 [178].

Scanning Electron Microscopy

During SEM, electrons are accelerated by a potential difference and focussed to a defined location on a sample surface by a series of electromagnetic lenses and apertures [102,103]. This process is conducted within a vacuum so that the electrons can travel through the microscope undisturbed. The interaction between the electron beam and specimen surface produces a variety of different signal responses, including X-rays and secondary and backscattered electrons. Subsequently, these signals are captured by the detector and digitally transformed into an image or a spectrum that either describes the topography or composition of a surface, respectively.

In this doctoral work, SEM analysis was performed using a Hitachi TM3030 system. More specifically, a 15kV accelerating voltage was used to capture mixed secondary and back scattering electron images in either standard or charge-up reduction mode, depending on which produced the most perspicuous output.

4.2.2.3 Contact Profilometry

Contact profilometry was performed using a Mitutoyo Surftest SJ-400. Measurements were recorded over an evaluation length of 4mm at a transverse speed of $0.5\text{mm}(\text{s}^{-1})$, using a stylus that had a tip radius and angle of $2\mu\text{m}$ and 60° , respectively. Gaussian filtering with a cut-off length of 0.8mm was applied in conformity with ISO 13565-1 [178].

4.2.2.4 Micro-CT

Micro-CT analysis was carried out using a Skyscan 1172 system with an accelerating voltage of 40kV; a source current of $148\mu\text{A}$; an exposure time of 295ms; a reconstructed voxel size (or image pixel size) of $4.18\mu\text{m}$; 180° rotation with a step size of 0.7° ; and no filtering. These scanning parameters were selected based on their previous suitability in related research works [162,179]. Post-scanning, the software package NRecon was used to reconstruct the obtained angular radiographs into a series of cross-sectional images.

Furthermore, the binarised scan images presented in **Chapter 5** were created using CTAn. This software programme enabled manual thresholding to be applied so that the presence of sub-surface pores could be identified. Additionally, the volume renderings shown in **Chapter 9** were produced using CTVox, which allowed different local densities to be distinguished, thereby enabling the visualisation of each filler material within their respective PA12 matrix.

4.2.2.5 Scratch Testing

Scratch testing was performed using an Anton Paar Revetest system, equipped with a diamond Rockwell indenter that had a tip radius and cone angle of 200 μ m and 120°, respectively.

During scratching, progressive loads ranging from 0.5N to 50N were applied over an evaluation distance of 30mm at a transverse speed of 0.1mm/s.

4.2.2.6 Friction and Wear Testing

As discussed in **Section 1.3**, the aim of this doctoral work was to holistically investigate the friction and wear properties of polymer laser sintered components. Therefore, when selecting the most appropriate tribological test method, the main criterion was not to replicate a certain interaction, but instead ensure that any data collected could easily be understood and reproduced.

Testing Configuration

Upon extensive consideration, a pin-on-disk, ball-on-flat, rotating, uni-directional test configuration was deemed to be the most suitable. This methodology was chosen due to its wide-recognition, practicability and well-established regulation. A schematic

highlighting the specific test-setup adopted throughout this doctoral work can be seen in **Figure 4.8**.

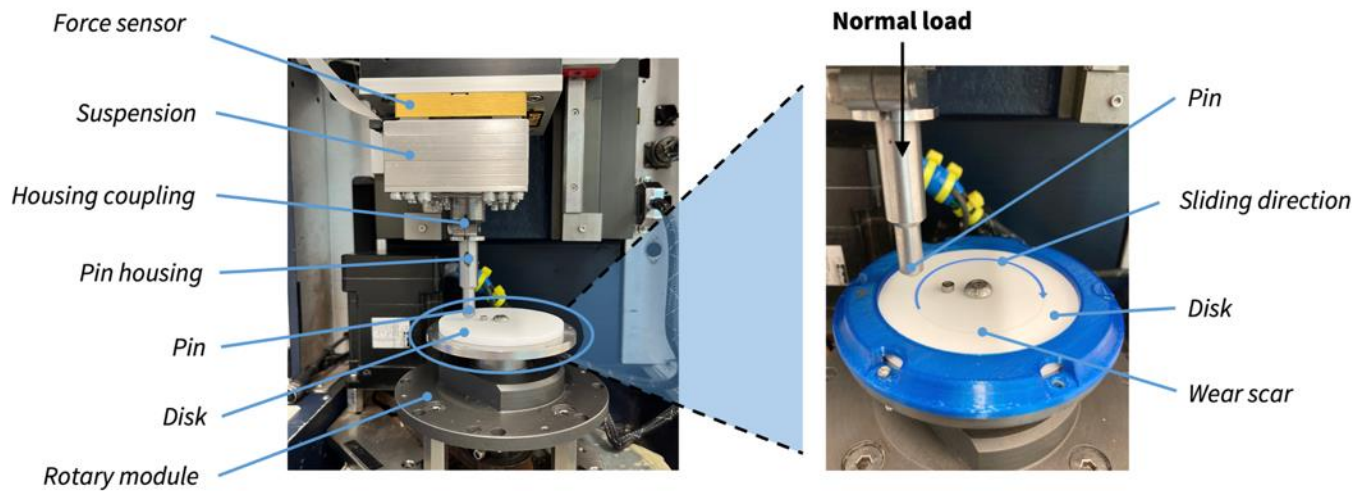
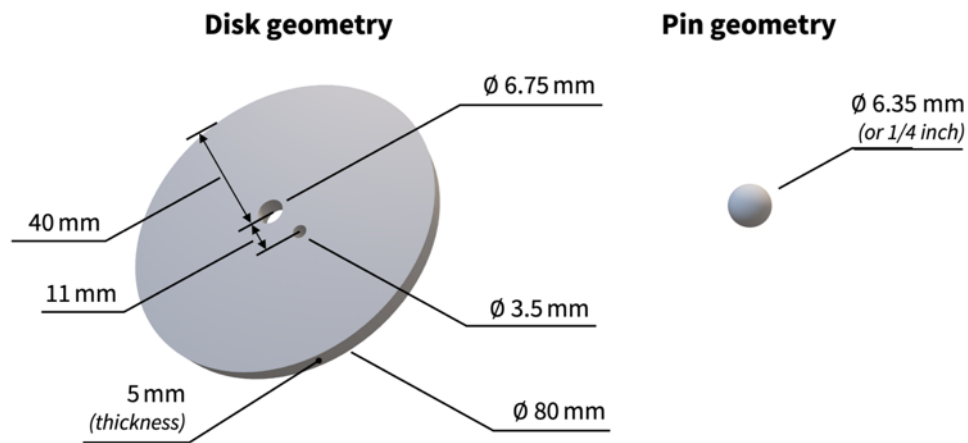


Figure 4.8 – The specific pin-on-disk, ball-on-flat, rotating, uni-directional test set-up adopted throughout this doctoral work.

A ball-on-flat testing configuration was chosen to intrinsically induce point contacts, regardless of the angles at which the pin and disk samples were oriented relative to one another, thereby preventing the occurrence of edge loading. Additionally, rotating, uni-directional sliding was carried out at a constant speed to avoid acceleration / deceleration phenomena, which have previously been shown to induce unsteady sliding motions, such as stick-slip [180,181].

A Bruker Universal Mechanical Tester (UMT) TriboLab was used to execute friction and wear testing in accordance with ASTM G99 [119]. Test samples included pin and disk specimens, whereby the former comprised of a spherical ball secured within a steel housing. As shown in **Figure 4.8**, disk samples were mated to the rotary module using a central screw to ensure concentricity, as well as off-centre and circumferentially to prevent slipping and ensure flatness relative to the rotary module, respectively. The specific geometries of each test sample, as well as a schematical diagram highlighting their sliding configurations relative to one another can be seen in **Figure 4.9**.

(a)



(b)

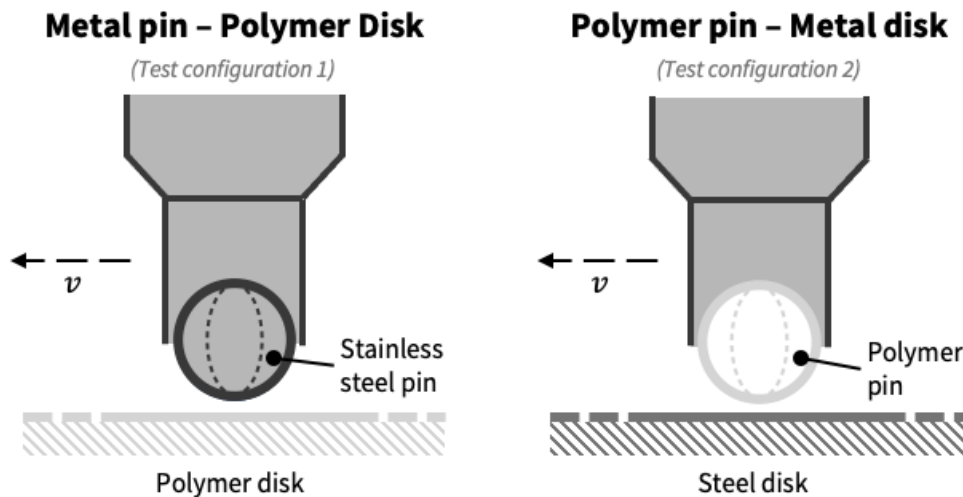


Figure 4.9 – (a) Tribological test specimen geometries and (b) the configurations in which they were subject to dynamic contact relative to one another.

This doctoral work focussed on investigating the sliding interactions between laser sintered PA12 and steel surfaces only. The auxiliary characterisation of other laser sintered PA12 sliding pairs, albeit worthwhile, was beyond the scope of what was possible to complete during the duration of this investigation.

Testing procedure

Each test conducted using the UMT was executed in accordance with the script outlined in **Table 4.4**. More specifically, this testing procedure comprised of three consecutive stages,

namely: (1) initial contact, (2) steady-state test speed attainment and (3) test load application. An initial contact force of 3N was selected, as this was the lowest load that could be accurately applied by the force sensor.

Table 4.4

The testing procedure adopted during friction and wear testing.

Step number	Normal load (N)	Sliding speed (ms^{-1})	Duration (s)
1	3	0	5
2	3	0 \rightarrow Test Speed	5
3	3 \rightarrow Test Load	Test Speed	Test Duration

Example normal load and sliding speed data recorded by the UMT during the early stages of a $15\text{N} - 0.35\text{ms}^{-1}$ sliding test can be seen in **Figure 4.10**.

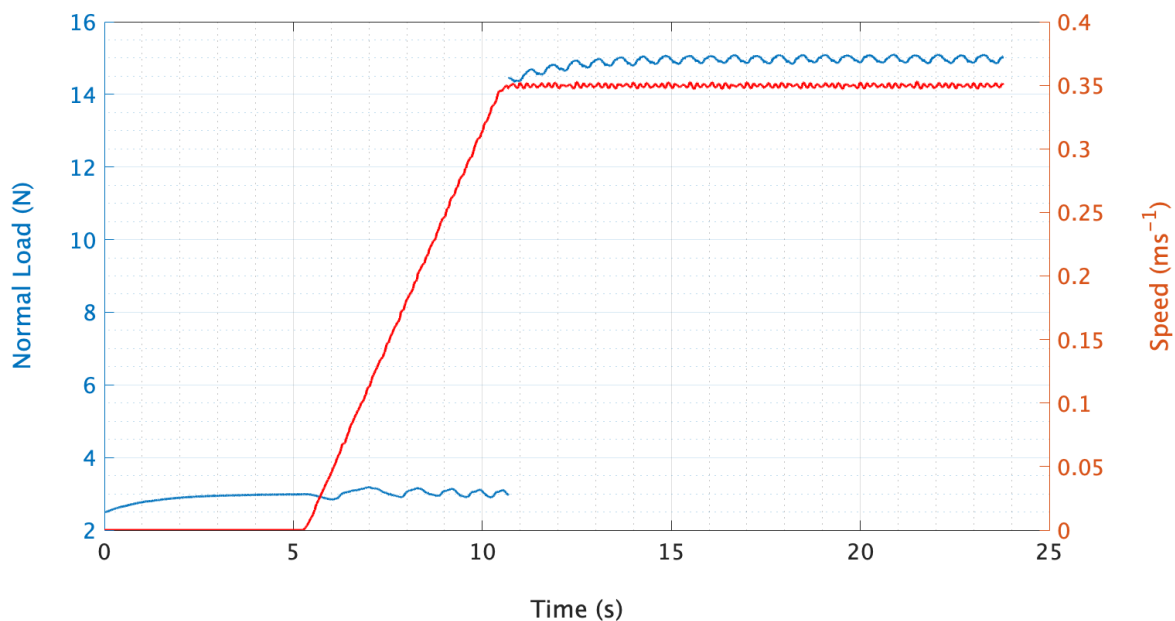


Figure 4.10 – Example normal load and sliding speed data recorded by the UMT during the early stages of a $15\text{N} - 0.35\text{ms}^{-1}$ sliding test.

As shown in **Figure 4.10**, variations in N were likely due to disk samples not being aligned exactly perpendicular to the direction of loading. Despite efforts to minimise the former – such as securing each disk to the rotary module axially, off-centre and circumferentially, slight misalignments between the rotary module and load cell were impossible to avoid.

Accordingly, these fluctuations in loading response, specifically their frequencies and amplitudes, will have corresponded with the positioning of each wear track, as well as the sliding speeds and normal loads employed during testing.

Sample Preparation

Polymeric Samples

Laser sintered polymeric samples were prepared in accordance with the procedures outlined in **Section 4.2.1**.

Auxiliary mechanical and surface properties (more specific than those provided in **Section 4.1.1.3**) are detailed in corresponding thesis chapters, wherever pertinent.

Metallic Samples

Friction and wear testing was predominantly carried out via ‘contact configuration 1’ (stainless steel pin – polymer disk), as shown in **Figure 4.7b**. More specifically, the contacting proportion of each metallic pin specimen comprised of a 6.35mm (1/4 inch) diameter stainless steel sphere, which had an elemental composition of 82.3% Fe, 17.2% Cr, 0.2% Mn, 0.1% V, and 0.2% Ni⁶.

As a part of work discussed in **Chapter 8**, friction and wear testing was also performed via contact configuration 2 (polymer pin – steel disk). In this instance, two steel disks with an elemental composition of 99.2% Fe, 0.6% Mn, and 0.2% Cr⁶ were used. These samples were sliced from the same section of round steel bar and ground⁷ to remove any contaminants, such as oxide formations, prior to testing. Consequently, resultant surfaces

⁶ Determined using a Fisherscope X-Ray XAN analyser.

⁷ Surface grinding was performed via a ‘vertical spindle – reciprocating table’ configuration.

comprised of adjacent scratch marks with lay profiles akin to those outlined in **Figure 4.11**.

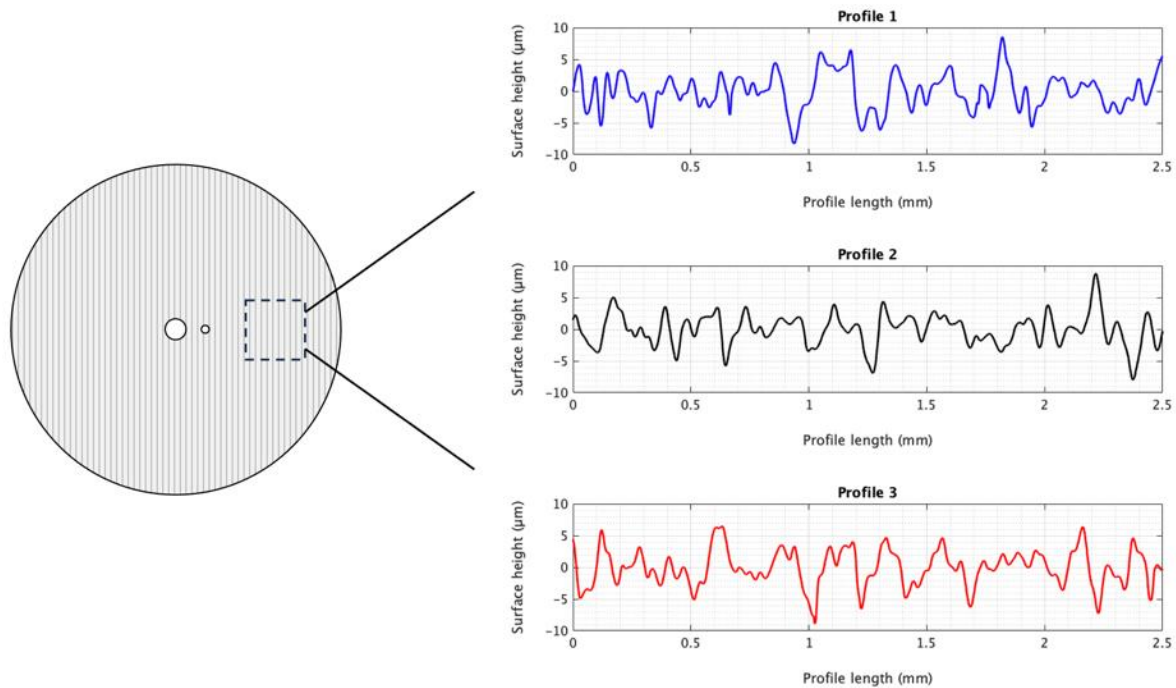


Figure 4.11 – Example roughness profiles illustrating the height and lay of the scratches produced when preparing steel disk samples by surface grinding.

Operating Conditions

User-defined operating conditions included contact configuration, sliding speed, normal load and sliding distance. The ranges over which these operating conditions were varied throughout this doctoral work can be seen in **Table 4.5**. These values were selected based on the upper and lower limits previously employed within existing literature, as outlined in **Table 3.3**.

Normal loads were specified in preference to contact stresses throughout this thesis. This is because calculating corresponding contact stresses via classical Hertzian theory invalidates several of the main assumptions on which this theory is based upon, including [182]:

- Contacting bodies are homogenous, isotropic, and non-conforming.
- Contacting bodies are elastic and the strains are sufficiently small to permit the theory of elasticity to be applied.
- The elastic bodies in contact are assumed to be semi-infinite elastic half-spaces, thus the contact dimensions and extent of deformation incurred are both far smaller than the geometrical dimensions of the contacting bodies.
- Adhesives forces are ignored.
- The roughnesses of both contacting surfaces are negligible.

Additionally, components within industrial tribosystems are typically subject to predetermined normal loads rather than contact stresses, thus further supporting the preference for specifying the former.

Table 4.5

The ranges over which operating conditions were varied throughout this doctoral work.

Test condition	The ranges over which each operating condition was varied throughout this doctoral work
Contact configuration	[Steel pin – Polymer disk] – [Polymer pin – Steel disk]
Sliding speed, v (ms^{-1})	0.05 – 0.5
Normal load, N (N)	3 – 30
Sliding distance, x (m)	5 – 1000

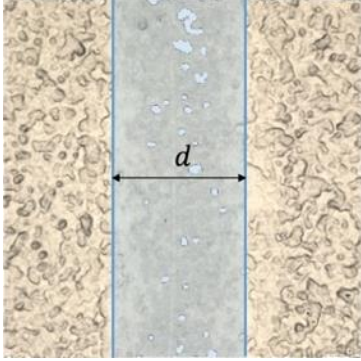
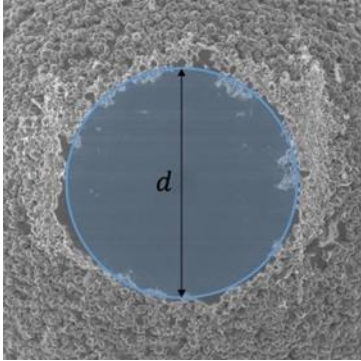
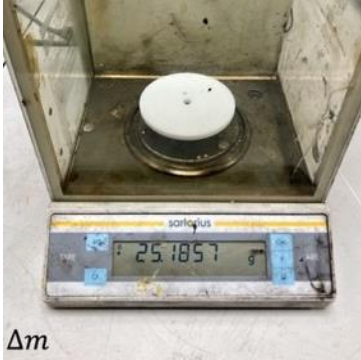
Determining Friction and Wear Properties

COF was the principal friction-related parameter of interest. Corresponding values were outputted directly from the UMT, which was programmed to record experimental data at a rate of 100Hz. Though, for the purposes of graph plotting this was downsampled such that COF data was reported every 0.5m to facilitate the visual comprehension of the results presented.

Laser sintered PA12 wear volumes (V) were characterised by either wear scar geometry analysis or mass loss; a more detailed description of each is provided in **Table 4.6**. Though, in conformity with ASTM G99 [119], the former method was predominantly adopted throughout this doctoral work. Only in **Chapter 7** were wear volumes determined from mass loss measurements, though this was due to ambiguity arising when attempting to discern the resultant widths of the wear scars produced.

Table 4.6

The methods used to determine laser sintered PA12 wear volumes.

Wear volume characterisation method	Visual description of wear volume characterisation method	Corresponding wear volume equation, with definitions of constituent terms
Disk analysis via FV microscopy		$V = 2\pi R \left[r^2 \sin^{-1} \left(\frac{d}{2r} \right) - \left(\frac{d}{4} \right) (4r^2 - d^2)^{1/2} \right]$ <p>where:</p> <p>R = wear track radius</p> <p>d = wear scar width</p> <p>r = pin end radius (3.175mm)</p>
Pin analysis via SEM		$V = \left(\frac{\pi h}{6} \right) \left[\frac{3d^2}{4} + h^2 \right]$ <p>where:</p> $h = r - \left[r^2 - \frac{d^2}{4} \right]^{1/2}$ <p>d = wear scar diameter</p> <p>r = pin end radius (3.175mm)</p>
Mass loss		$V = \frac{\Delta m}{\rho}$ <p>where:</p> <p>Δm = mass loss</p> <p>ρ = density</p>

Subsequently, wear rate (W) and / or specific wear rate (W_s) values were then calculated using **Equation 4.1** and / or **Equation 4.2**, respectively:

$$W = \frac{V}{x}$$

Equation 4.1

$$W_s = \frac{V}{N \times x}$$

Equation 4.2

4.3 Auxiliary and Alternative Experimental Practices

In the several instances in which auxiliary and / or alternative experimental practices were adopted, the rationale for doing so, as well as their specific operational details have been provided within the ‘Materials and Methods’ section of each corresponding thesis chapter.

Chapter 5

Laser Sintered Polyamide-12 Surfaces

Chapter Summary

The work presented in this chapter utilised contact profilometry, FV microscopy and micro-CT to characterise the surfaces of laser sintered PA12 samples apropos to amplitude roughness descriptor; applied energy density; XY positioning across the powder bed; part orientation; and metrology method.

This chapter includes published work, available via the following citation:

K. Nar, C. Majewski and R. Lewis, A Comprehensive Characterisation of Laser Sintered Polyamide-12 Surfaces, *Polymer Testing*. Vol. 106, (2021).
<https://doi.org/10.1016/j.polymertesting.2021.107450>.

5.1 Introduction

An incomplete understanding of part quality continues to hinder the further adoption of laser sintered polymer components for end-use applications [3–7]. Therefore, the aim of this experimental study was to supplementarily characterise laser sintered PA12 surfaces in order to address this lack of insight and establish whether they comprise of any features that may affect their sliding behaviours.

As discussed in **Section 3.1**, laser sintered polymer surfaces are influenced by a range of factors, including those related to powder properties; processing parameters; part positioning; roughness descriptor; and metrology method. Though, despite there being existing literature pertaining to each of the former, a holistic grasp of their compound influence remains to be seen.

5.2 Materials and Methods

5.2.1 Materials

A 50/50 – PA12 powder configuration (50% virgin-material and 50% once-used-material) was used in this study. All samples were produced from the same batch of powder and constituents were blended by rotary tumbling for 20 minutes.

5.2.1.1 Specimens

All specimens were manufactured within a single build to best ensure they were subjected to alike processing conditions, thereby minimising variability and reducing powder wastage. Though, as shown in **Figure 5.1**, different laser powers (18W, 21W and 24W) were selected to vary the energy density applied to each tier of the build to $28.8 \text{ mJ}(\text{mm}^{-2})$, $33.6 \text{ mJ}(\text{mm}^{-2})$ and $38.4 \text{ mJ}(\text{mm}^{-2})$, respectively. Standard PA12 processing parameters were otherwise employed, as outlined in **Table 4.3**.

As shown in the LS build layout presented in **Figure 5.1**, different specimen geometries were designed depending on their intended analyses. More specifically, 16mm × 16mm × 16mm cube-shaped specimens were produced for contact profilometry; 8mm × 8mm × 8mm cube-shaped specimens were produced for Focus Variation microscopy; and 5mm × 6mm (diameter × length) cylindrical-shaped specimens were produced for micro-CT.

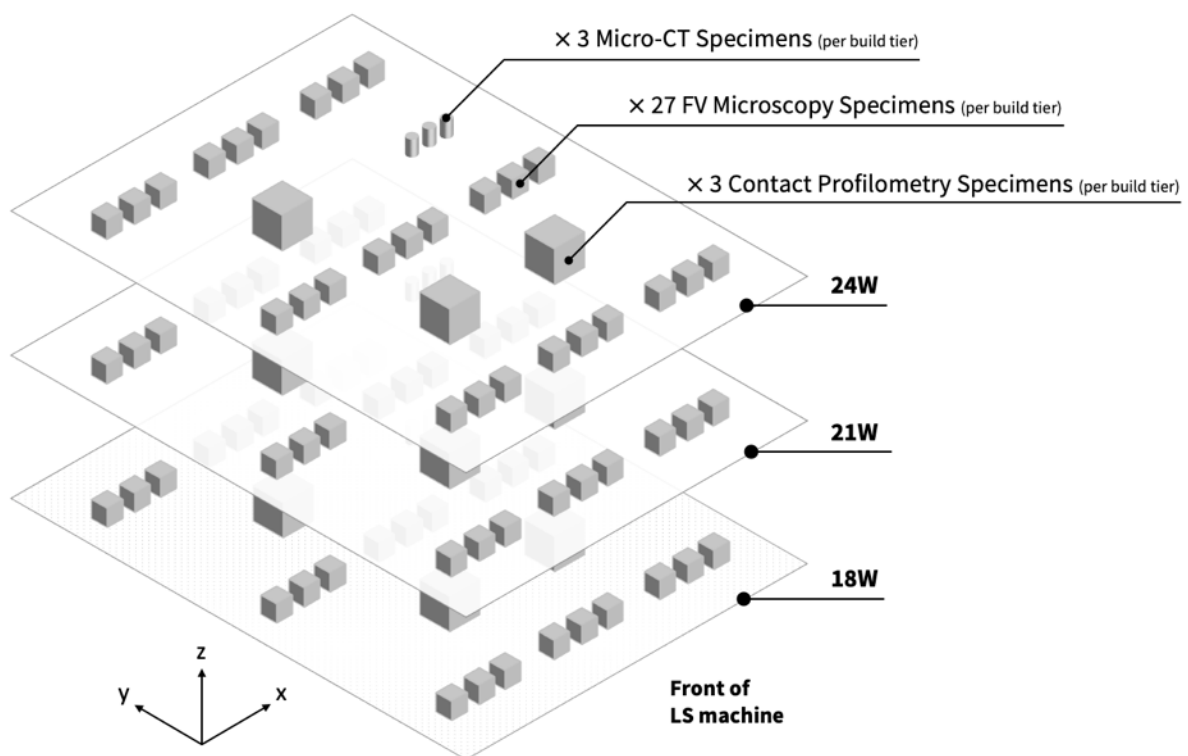


Figure 5.1 – A schematic illustrating the quantity, geometry and positioning of samples produced in this study (**Chapter 5**).

Upon build completion, compressed air was used to remove loose powder particles from all of the surfaces of parts produced.

5.2.2 Methods

Specimens were characterised using metrology techniques of varying geometrical dimensional capability, ranging from 2D profile (contact profilometry) to 3D areal (FV microscopy) and volume based (micro-CT) analysis methods.

Table 5.1 outlines the metrology techniques that were used to characterise the effects of each of the surface influencing factors investigated within this study.

Table 5.1

An outline of the metrology methods used to characterise the effects of each of the surface influencing factors investigated within this study.

Factor of interest	Contact profilometry	Focus Variation microscopy	Micro-CT
Amplitude roughness descriptor	✓	✓	✗
Applied energy density	✓	✓	✓
XY positioning across the powder bed	✗	✓	✗
Part orientation	✓	✓	✓
Measurement technique	✓	✓	✓

Additionally, **Figure 5.2** shows the surfaces that were evaluated on each of the different specimen geometries.

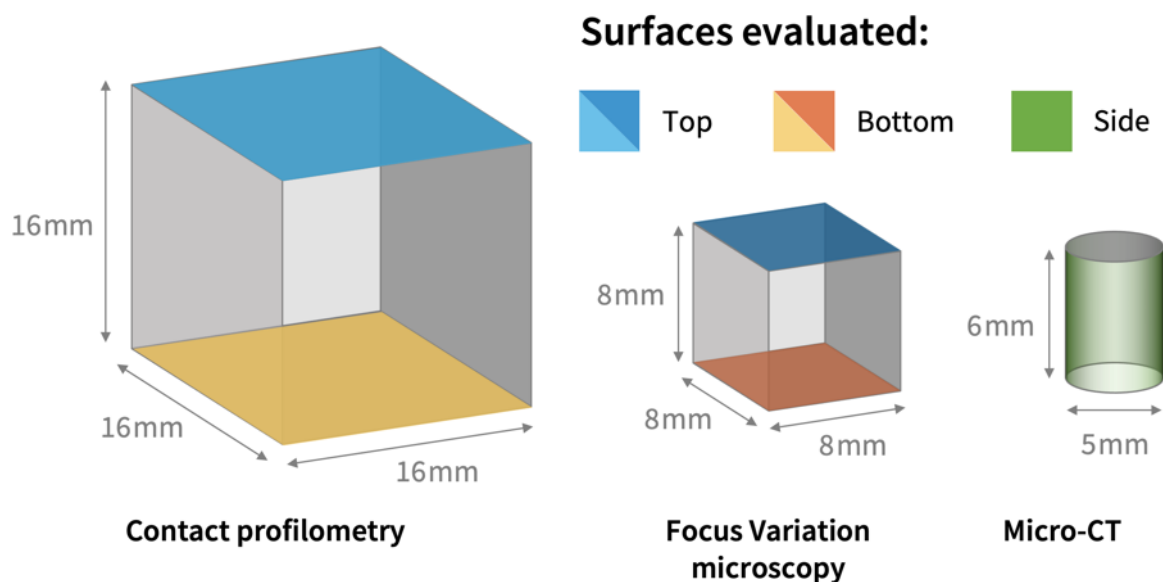


Figure 5.2 – The surfaces that were evaluated on each of the different specimen geometries.

As previously mentioned in **Section 5.2.1.1** and illustrated in **Figure 5.2**, cube-shaped specimens were manufactured for contact profilometry and FV microscopy analysis. These samples were designed at different scales to accommodate their respective evaluation lengths / regions, as specified in **Section 5.2.2.1**. Contrastingly, samples designated for Micro-CT analysis were cylindrical to ensure consistent X-ray penetration at equal distances for all rotational steps, thereby enabling the acquisition of high quality radiographs.

5.2.2.1 Characterisation

Roughness Parameters

The descriptors S_q , S_z , S_{sk} , S_{ku} , and equivalent R-parameters, were used to characterise the size and form of captured roughness profiles. A summary of each is given in **Table 5.2**.

Table 5.2

Summary of the amplitude roughness parameters used within this study.

Surface roughness parameter	Abbreviation	Description
Root Mean Square (RMS)	S_q / R_q	The standard deviation of the distribution of surface heights [85] within a given evaluation region.
Maximum Peak-to-Valley Height	S_z / R_z	The sum of the maximum peak height and maximum valley depth within a given evaluation region.
Skewness	S_{sk} / R_{sk}	Describes whether the distribution of bulk material that comprises a surface profile is above or below its mean plane. If a profile has a negative Skewness roughness value, valleys will be a more dominant feature than asperity peaks, and vice versa.
Kurtosis	S_{ku} / R_{ku}	Describes the sharpness of a surface height distribution [90]. If a profile has a Kurtosis value greater than three ($S_{ku} > 3$), it will comprise of a relatively large number of high peaks and low valleys, and vice versa [85].

Contact Profilometry

As shown in **Figure 5.1**, nine specimens were produced for contact profilometry analysis. More specifically, three specimens were manufactured at each applied laser power and three repeat profile measurements were performed on each specimens top and bottom surface.

Focus Variation Microscopy

Areal surface analysis was carried out using FV microscopy in accordance with the process specified in **Section 4.2.2.2**.

Three repeat scans were performed on the top and bottom surfaces of each of the 81 specimens produced for FV microscopy analysis specifically. Additionally, specimens were distributed across the powder bed to assess whether any potential non-uniformities in bed temperature affected the resultant roughnesses of parts produced.

Micro-CT

It is well agreed upon that re-entrant and / or undercut features are unable of being captured by contact and / or optical line-of-sight surface metrology techniques [91,95]. Therefore, micro-CT was employed to elucidate the extent to which these features comprised the side surfaces of laser sintered PA12 specimens.

As shown in **Figure 5.1**, three cylindrical specimens were manufactured at each laser power (18W, 21W and 24W) to ensure redundancy in case of loss or damage due to their small size, though only one of each was subsequently characterised by micro-CT.

Evaluation regions with annuli widths of 0.5mm were selected when computing percentage porosity results. This included material within a depth of between 2 – 3 times the measured S_z of each sample cross-section.

5.3 Results and Discussion

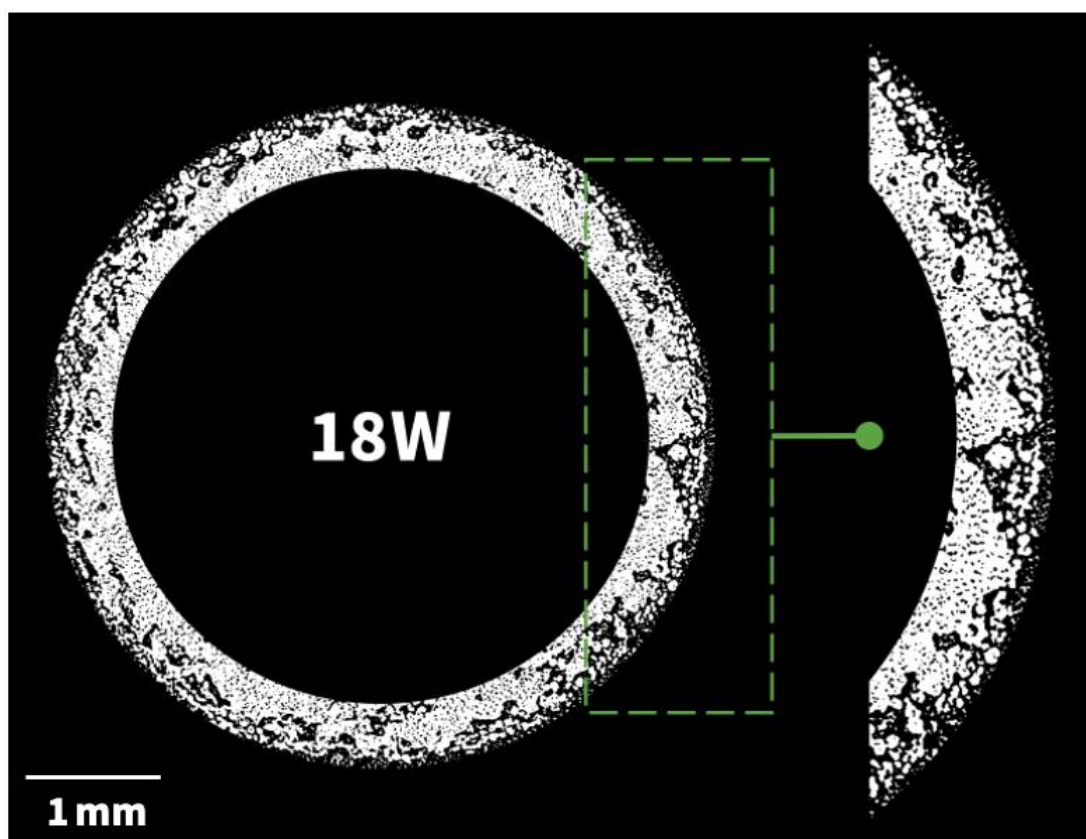
The following analysis was carried out in relation to part surface orientation as it best elucidated the effects of the other factors of interest.

5.3.1 Laser Sintered Side Surfaces

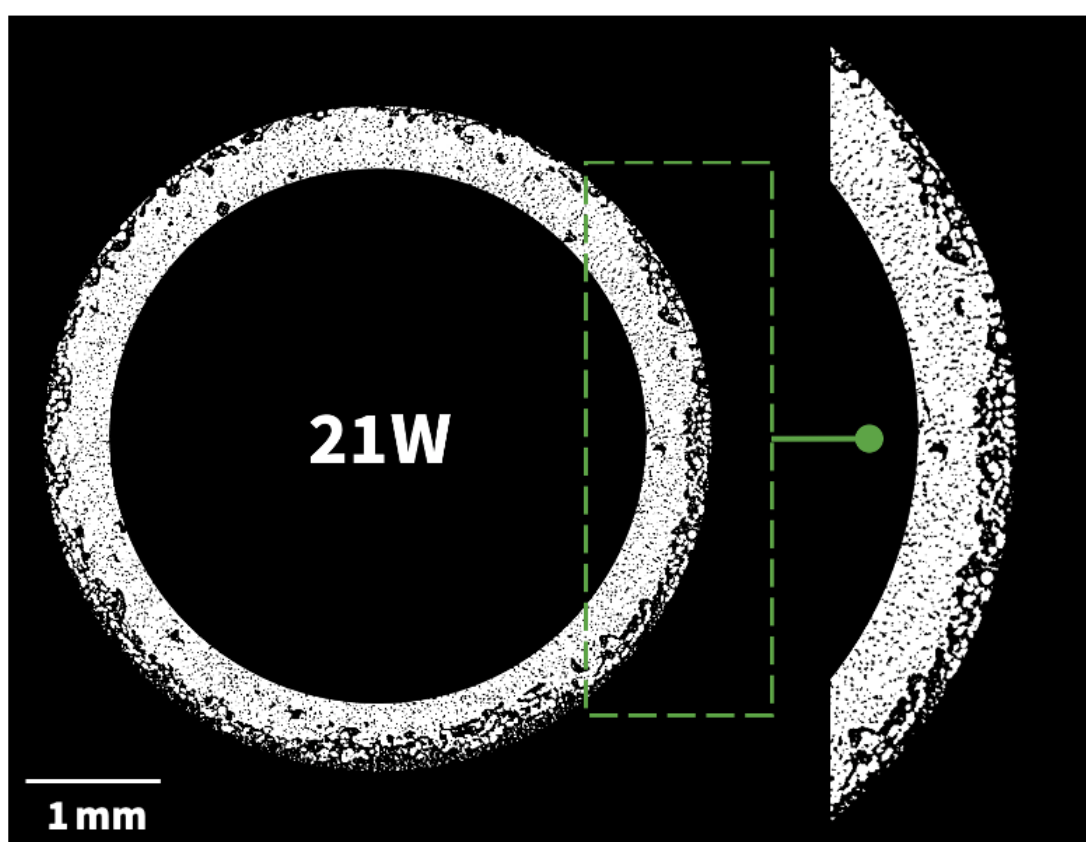
Laser sintered side surfaces conventionally refer to the contours of parts which are oriented non-parallel to the powder bed.

The side surface morphologies of the samples analysed by micro-CT are presented in **Figure 5.3**. Corresponding binarised cross-sectional slices are presented from the middle of each cylindrical specimen in their axial directions.

(a)



(b)



(c)

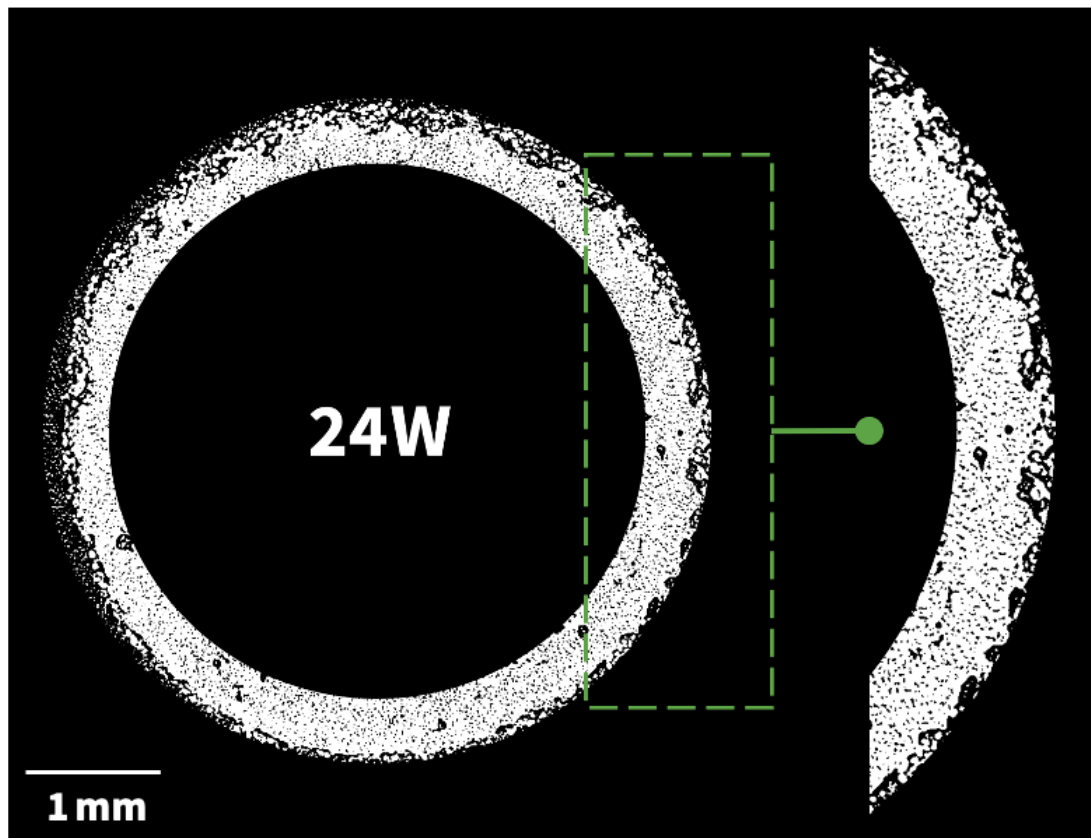


Figure 5.3 – Micro-CT obtained binarised scan images highlighting the side surface morphologies of samples produced at varying laser powers, specifically **(a)** 18W, **(b)** 21W and **(c)** 24W. The central regions of each cross-sectional slice have been concealed to focus the reader’s attention to the contour of each sample.

In agreement with Launhardt et al. [91] and Zhu et al. [95], the laser sintered PA12 side surfaces presented in **Figure 5.3** comprised of many undercut and re-entrant features.

As mentioned in **Chapter 3**, specifically **Section 3.1.3**, laser sintered side surfaces are particularly prone to secondary sintering, specifically necking, between pre-defined part perimeters and surrounding powder particles during building. A schematic highlighting this phenomenon can be seen in **Figure 5.4**.

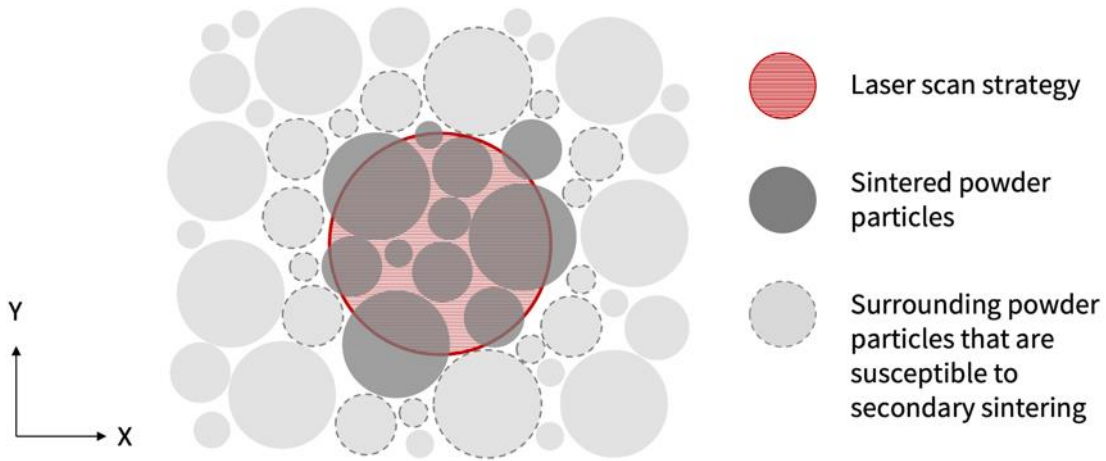


Figure 5.4 – A schematic highlighting the mechanism of secondary sintering, which characteristically occurs at the interface between pre-defined part perimeters and surrounding powder.

Conventionally, contour scan strategies are implemented to reduce the prevalence of undercut and re-entrant features. More specifically, this involves exposing part perimeters to lower laser powers and scan speeds than those typically employed for bulk hatching [183]. However, without the presence of a physical boundary to inhibit secondary sintering, the formation of undercut and re-entrant features will be inevitable during LS. Therefore, metrology methods with greater capabilities than those of contact and / or optical line-of-sight techniques should be employed when characterising laser sintered surfaces orientated non-parallel to the powder bed.

Supplementarily, percentage porosity values ($\phi_{\%}$) were computed to indicate the impact that applied energy density had on the prevalence of secondary sintering induced features. More specifically, percentage porosity values were calculated from four cross-sectional annuli that were evenly distributed along the axial direction of each specimen using **Equation 5.1** below:

$$\phi_{\%} = \left(1 - \frac{n_{\text{white pixels within a cross-sectional annulus of interest}}}{n_{\text{white pixels within a corresponding fully dense annulus of interest}}} \right) \times 100$$

Equation 5.1

Correspondingly, 18W, 21W and 24W samples had mean percentage porosity values of 32.0%, 24.6% and 28.2%, respectively. This confirmed that the mechanisms of incomplete powder consolidation and pronounced secondary sintering dominated when laser powers lower (18W) and greater (24W) than standard PA12 parameters (21W) were applied, respectively.

5.3.2 Laser Sintered Top and Bottom Surfaces

Laser sintered top and bottom surfaces conventionally refer to the first and final build layers orientated parallel to the powder bed, as shown in **Figure 5.2**.

Figure 5.5 shows a typical top and bottom laser sintered PA12 surface scan obtained by FV microscopy.

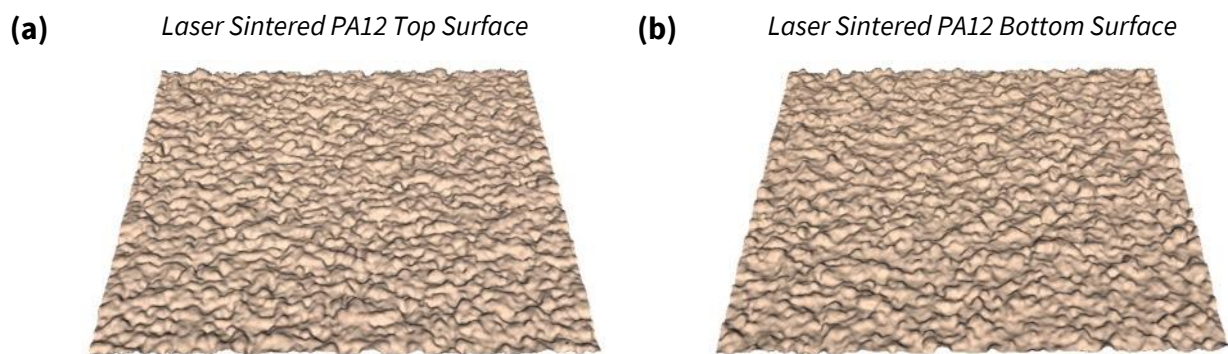


Figure 5.5 – Typical FV microscopy obtained scan images of a **(a)** top and **(b)** bottom laser sintered PA12 surface. Both scan areas are 3.7 mm × 3.7 mm in size and were captured from the same randomly selected 21W sample designated for FV microscopy analysis.

Upon qualitative inspection of the top and bottom surfaces presented in **Figure 5.5**, no discernible differences between their topographies can be seen.

Accordingly, **Figure 5.6**, **Figure 5.7**, **Figure 5.8** and **Figure 5.11** provide quantitative insight into the resultant roughnesses of top and bottom specimen surfaces built at varying laser powers and evaluated by contact profilometry and FV microscopy metrology methods. More specifically, mean profile roughness results are represented by a reference

plane within each subfigure, whereas individual sample surface roughness magnitudes are given by the heights of their vertical bars. The latter also elucidates the extent to which each amplitude roughness response varied across the powder bed. Though, it should be noted that the layouts of these figures are partly illustrative with respect to the exact XY positioning of samples across the powder bed. Corresponding mean S- and R- roughness results are detailed in **Table 5.3**, **Table 5.4**, **Table 5.5** and **Table 5.6**, respectively.

5.3.2.1 Root Mean Square Roughness (S_q / R_q)

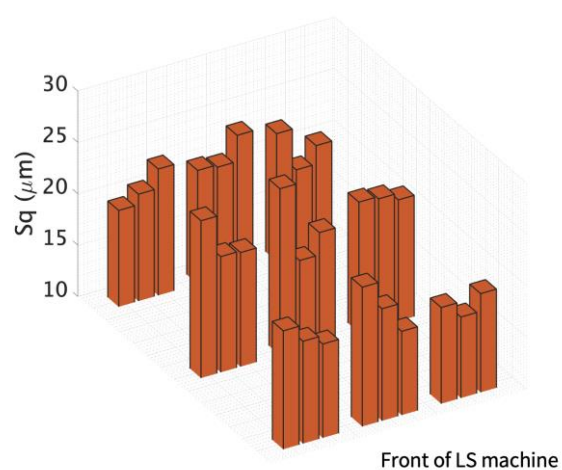
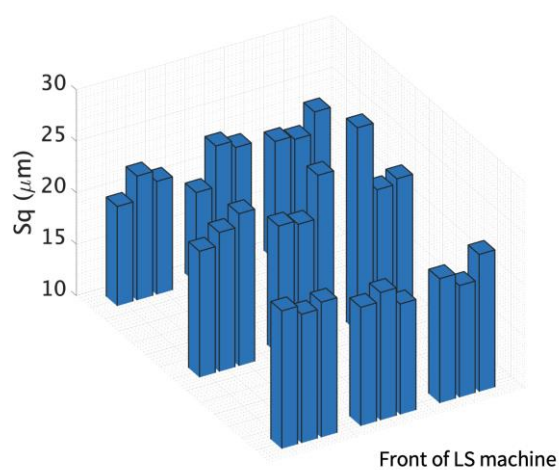
S_q and R_q roughness results are shown in **Figure 5.6** and **Table 5.3**.

S_q/R_q

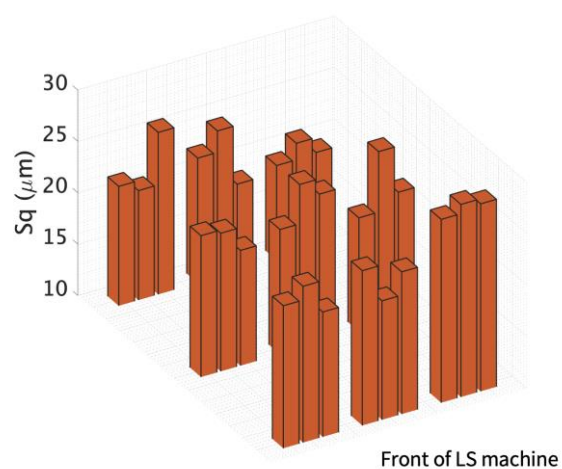
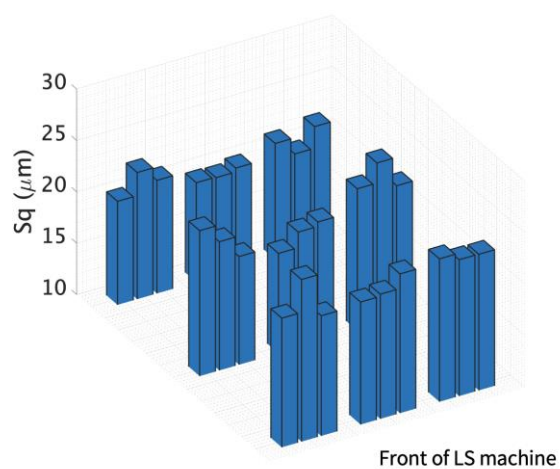
Top Surfaces

Bottom Surfaces

18W



21W



24W

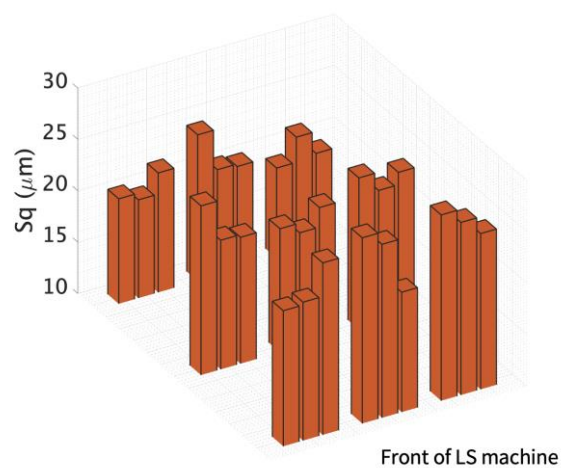
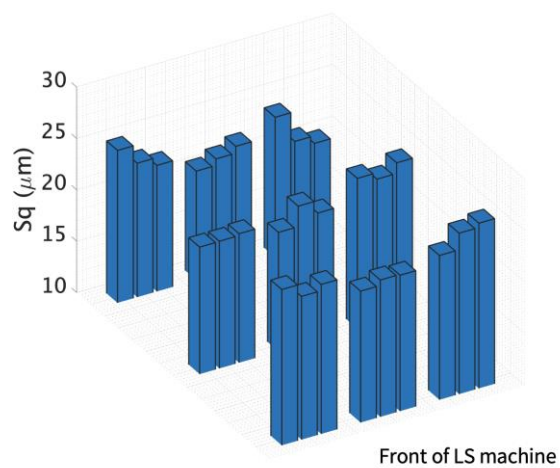


Figure 5.6 – The distribution in S_q roughness of top and bottom surfaces (built at varying applied energy densities) across the powder bed.

Table 5.3

A comparison of the S_q and R_q roughness results, and corresponding standard deviations, determined for both the top and bottom surfaces of laser sintered PA12 samples built at varying applied energy densities and evaluated by FV microscopy and contact profilometry.

S_q / R_q roughness	Metrology technique	Applied laser power		
		18W	21W	24W
Top surfaces	FV microscopy	22.61 (± 2.08) μm	22.07 (± 1.76) μm	23.61 (± 1.58) μm
	Contact profilometry	17.57 (± 1.40) μm	17.38 (± 0.80) μm	17.25 (± 1.05) μm
Bottom surfaces	FV microscopy	21.06 (± 2.06) μm	23.35 (± 2.77) μm	23.13 (± 2.76) μm
	Contact profilometry	14.45 (± 1.11) μm	14.22 (± 1.55) μm	15.16 (± 1.29) μm

As can be seen in **Table 5.3**, there was a significant difference between the top and bottom RMS profile roughnesses evaluated by contact profilometry. In agreement with Schmidt et al. [136] and Silani et al. [139], resultant top surfaces R_q roughness magnitudes were greater than those of bottom surfaces. Furthermore, this relationship between part surface orientation and resultant R_q was independent of applied laser power.

Contrastingly, no significant variations between the top and bottom S_q roughnesses of samples evaluated by FV microscopy could be discerned. Though, the resultant S_q roughnesses of parts produced were also found to be independent of applied energy density and their build locations across the powder bed, as shown in **Figure 5.6**.

It is expected that these differences in profile and areal surface height magnitudes were partly due to the contact and optical characterisation methods employed having different technique-specific constraints. As previously discussed in **Section 2.5.1.2** and **Section 4.2.2.2**, contact profilometry is typically constrained by tip geometry and scan area, whereas FV microscopy tends to be limited by its ability to detect reflected radiation, respectively. Therefore, variations in bandwidth filtering will have resulted in measured values being described on different length scales [184].

5.3.2.2 Maximum Peak-to-Valley Height (S_z / R_z)

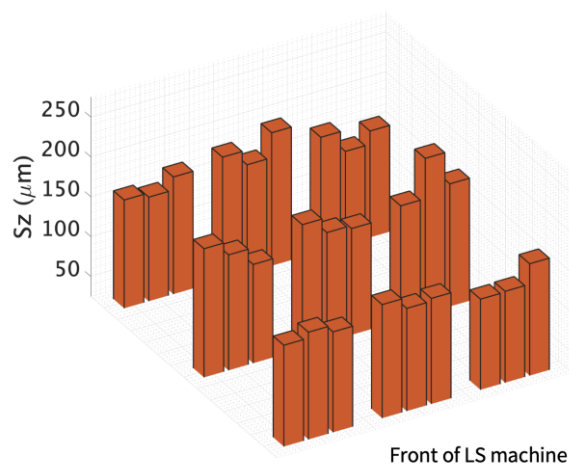
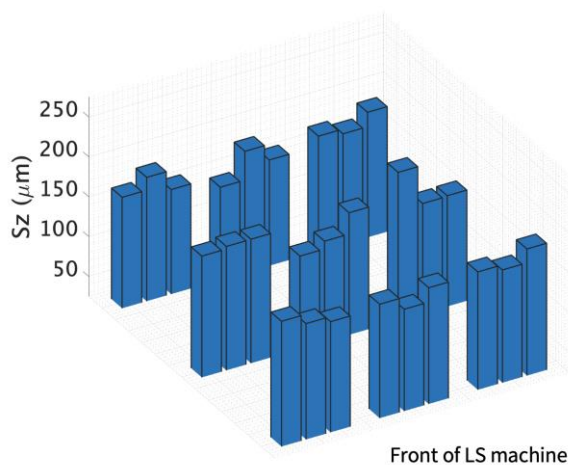
S_z and R_z roughness results are shown in **Figure 5.7** and **Table 5.4**.

S_z/R_z

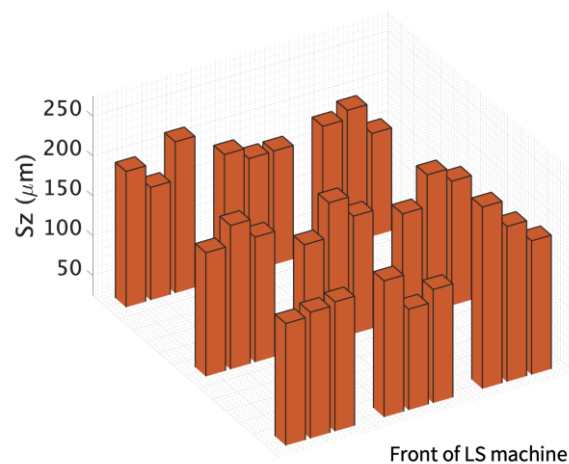
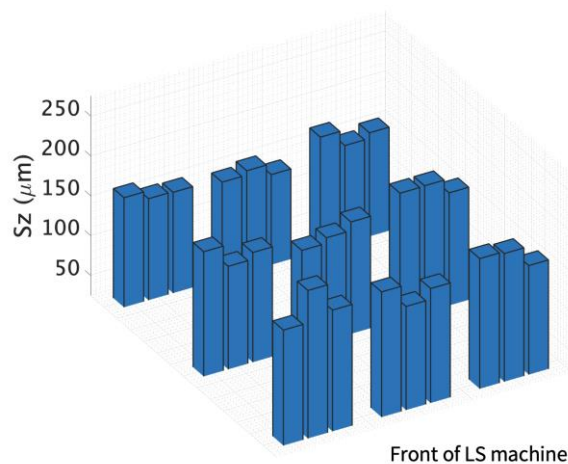
Top Surfaces

Bottom Surfaces

18W



21W



24W

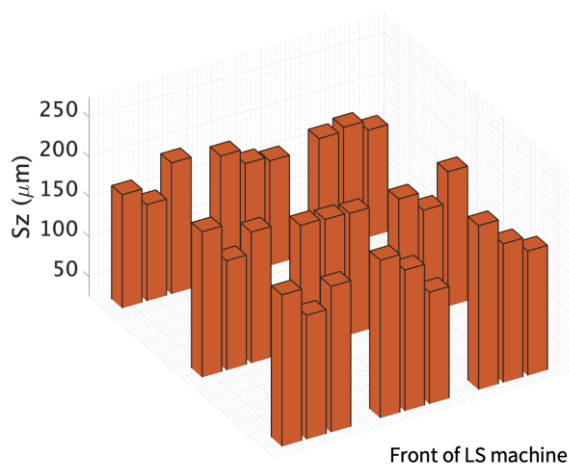
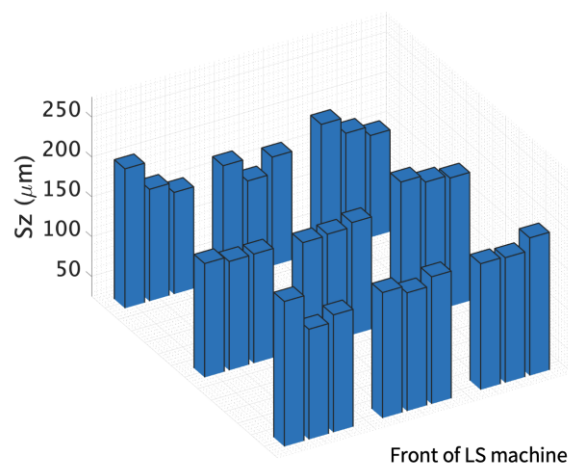


Figure 5.7 – The distribution in S_z roughness of top and bottom surfaces (built at varying applied energy densities) across the powder bed.

Table 5.4

A comparison of the S_z and R_z roughness results, and corresponding standard deviations, determined for both the top and bottom surfaces of laser sintered PA12 samples built at varying applied energy densities and evaluated by FV microscopy and contact profilometry.

S_z/R_z roughness	Metrology technique	Applied laser power		
		18W	21W	24W
Top surfaces	FV microscopy	169.2 (\pm 14.5) μm	165.5 (\pm 16.6) μm	173.4 (\pm 16.6) μm
	Contact profilometry	75.9 (\pm 4.4) μm	74.2 (\pm 3.8) μm	73.2 (\pm 5.4) μm
Bottom surfaces	FV microscopy	164.6 (\pm 17.4) μm	184.3 (\pm 22.4) μm	182.4 (\pm 21.8) μm
	Contact profilometry	65.8 (\pm 4.6) μm	65.1 (\pm 4.8) μm	67.3 (\pm 5.9) μm

Both profile and areal results were in good agreement with data collected by Laundhardt et al. [91], who reported mean contact profilometry and FV microscopy results of approximately 80 μm and 200 μm , respectively.

In concurrence with the previously discussed R_q and S_q results, mean top surface R_z roughnesses were again found to be greater than those measured for bottom surfaces, whereas no correlation between S_z and surface orientation could be discerned. Additionally, the R_z and S_z roughnesses of all samples produced were found to be independent of their build locations across the powder bed and the magnitudes of energy density applied during building, as shown in **Table 5.4** and **Figure 5.7**.

Generally, R_z and S_z values are determined by the single largest irregularity within each of their respective evaluation regions. Therefore, maximum peak-to-valley height parameters intrinsically do not provide insight into entire surface distributions, and thus in most cases are less apt than R_q or S_q at describing the amplitude profiles of laser sintered polymer surfaces, independent of their part orientation.

5.3.2.3 Skewness (S_{sk} / R_{sk})

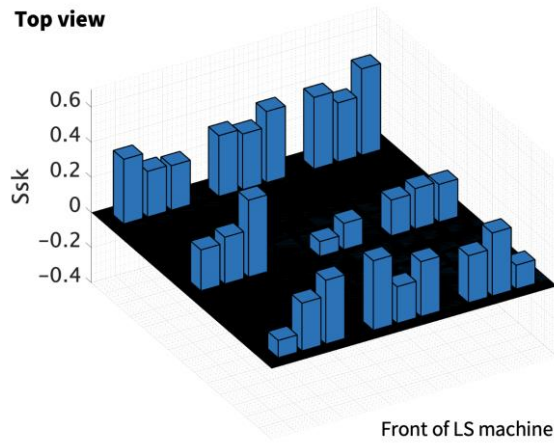
S_{sk} and R_{sk} roughness results are shown in **Figure 5.8** and **Table 5.5**.

S_{sk}/R_{sk}

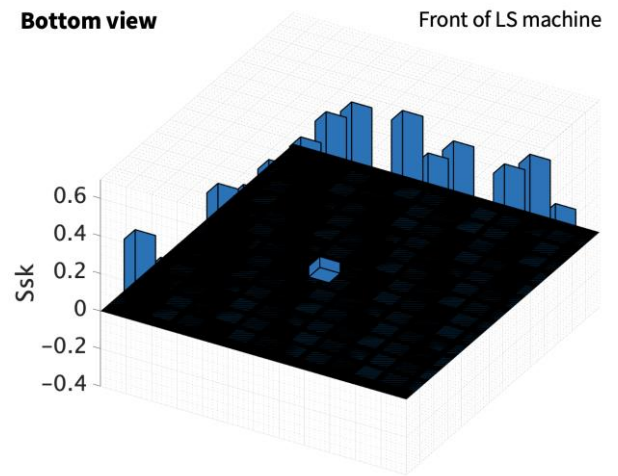
Top Surfaces

18W

Top view

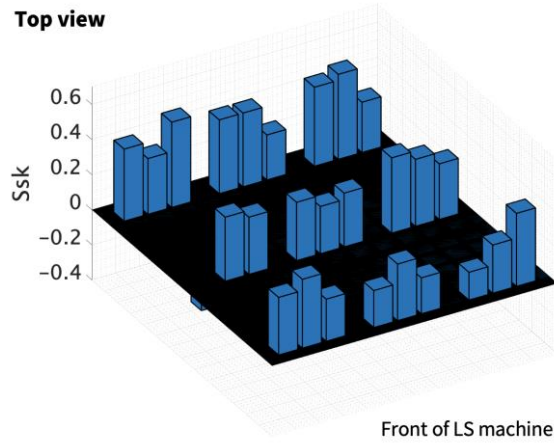


Bottom view

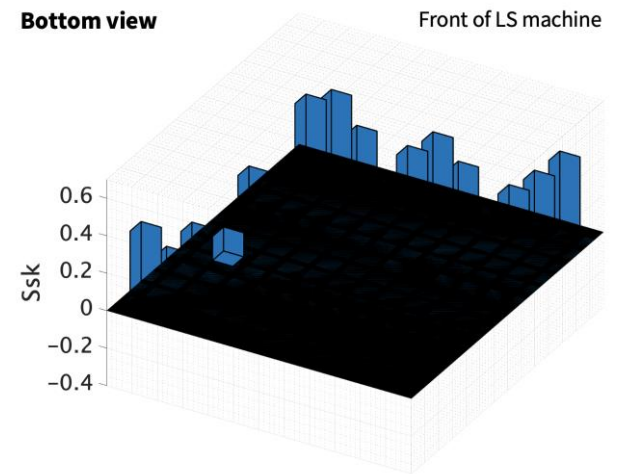


21W

Top view

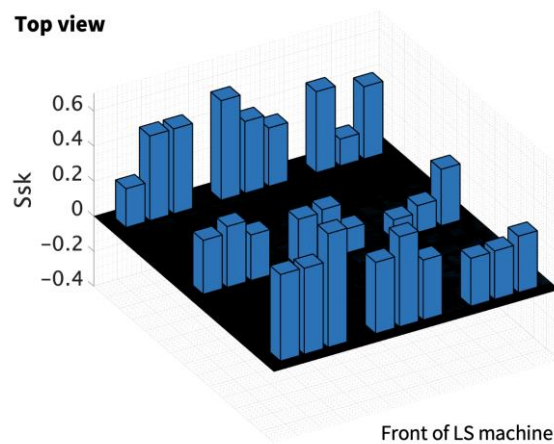


Bottom view

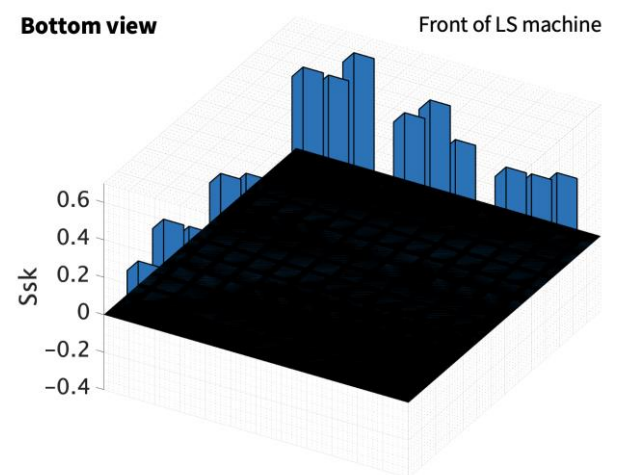


24W

Top view

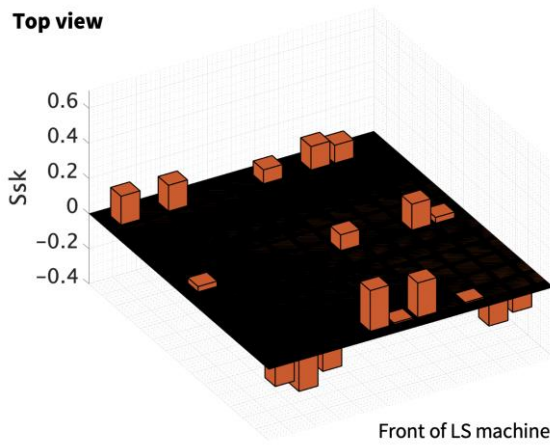


Bottom view

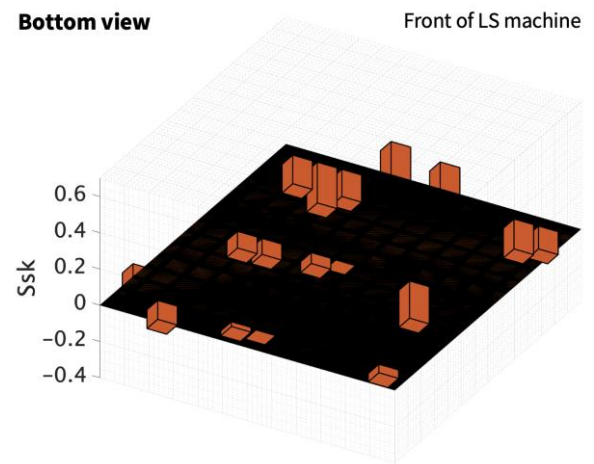


Bottom Surfaces

18W

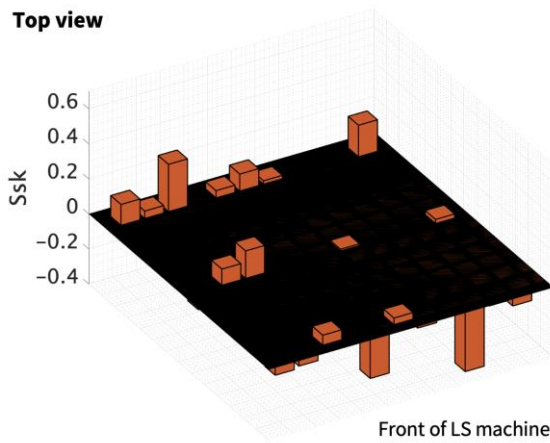
Top view

Front of LS machine

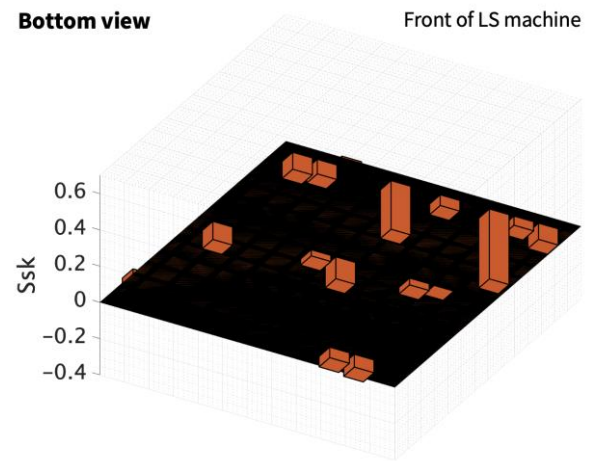
Bottom view

Front of LS machine

21W

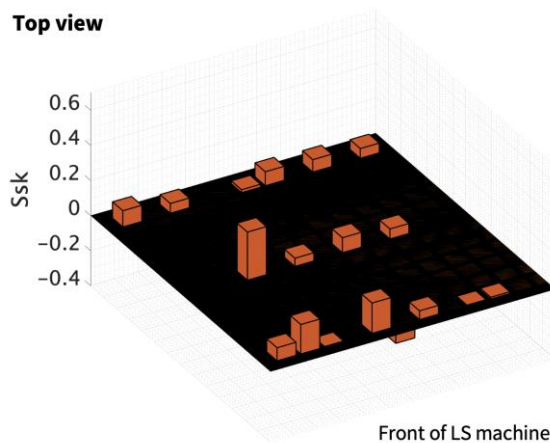
Top view

Front of LS machine

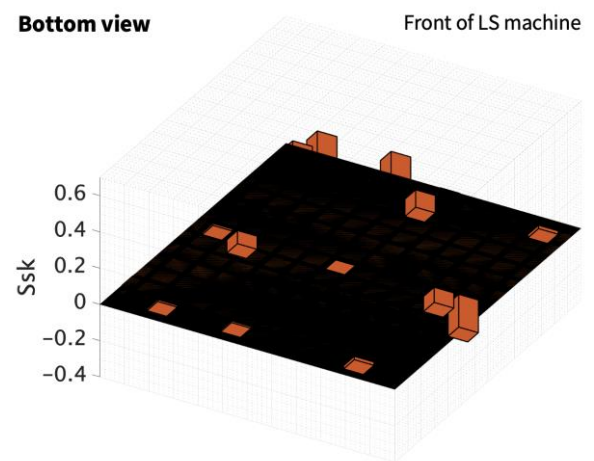
Bottom view

Front of LS machine

24W

Top view

Front of LS machine

Bottom view

Front of LS machine

Figure 5.8 – The distribution in S_{sk} roughness of top and bottom surfaces (built at varying applied energy densities) across the powder bed.

Table 5.5

A comparison of the S_{sk} and R_{sk} roughness results, and corresponding standard deviations, determined for both the top and bottom surfaces of laser sintered PA12 samples built at varying applied energy densities and evaluated by FV microscopy and contact profilometry.

S_{sk}/R_{sk} roughness	Metrology technique	Applied laser power		
		18W	21W	24W
Top surfaces	FV microscopy	0.27 (± 0.12)	0.32 (± 0.12)	0.35 (± 0.14)
	Contact profilometry	0.09 (± 0.11)	0.13 (± 0.14)	0.02 (± 0.06)
Bottom surfaces	FV microscopy	0.00 (± 0.13)	-0.01 (± 0.13)	0.03 (± 0.09)
	Contact profilometry	-0.04 (± 0.14)	-0.09 (± 0.12)	-0.03 (± 0.18)

As can be seen in **Table 5.5**, the Skewness results obtained by contact profilometry were all centred around zero. This indicated that both top and bottom surfaces were relatively Gaussian, and thus comprised of a symmetrical balance of peaks and valleys.

However, the ‘Smoothing Effect’ intrinsic to contact profilometry will have likely impacted the R_{sk} results collected. As mentioned in **Section 2.5.1.2**, the finite geometry of the stylus tip will have resulted in profiles being characterised as having shallower valley depths and rounder asperity peaks than that is accurate. This phenomenon is illustrated in **Figure 5.9**. Consequently, the material distributions of surfaces evaluated by contact profilometry will have effectively been shifted towards their asperity tips, resulting in peak dominated surfaces ($S_{sk} > 0$) appearing to be relatively Gaussian ($S_{sk} \sim 0$).

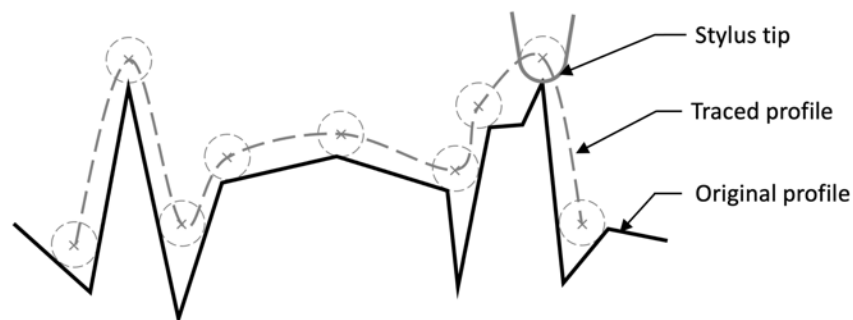


Figure 5.9 – A schematic highlighting the ‘Smoothing Effect’ intrinsic to contact profilometry. Adapted from Bhushan [185].

As shown in **Figure 5.8**, almost all top surfaces evaluated by FV microscopy were ascertained as having a positive Skewness value (p-value = 0.025). Moreover, when compared with a significance level (α) of 0.05, the former phenomenon was deemed to be statistically true for all laser sintered PA12 top surfaces evaluated. De Pastre et al. [100] also found that laser sintered PA12 top surfaces had consistently positive Skewness roughness responses when evaluated by FV microscopy, as well as when measured by Coherence Scanning Interferometry and XCT.

Furthermore, increasing applied laser power from 18W to 21W and 24W increased the mean top surface Skewness of each tier of samples from 0.27 to 0.32 and 0.35, respectively.

The mechanism of finish layer powder particle adhesion serves as a potential explanation as to why laser sintered PA12 top surfaces were ascertained as being asperity peak dominated (as indicated by their resultant positive Skewness values). It is expected that the subsequent adhesion that takes place between the final build layer and powder particles within the following deposition of finish layer material modifies the top surfaces of parts produced such that their topographies comprise primarily of asperity peaks. This mechanism is illustrated in **Figure 5.10** and explored in significantly more detail in **Chapter 6**.

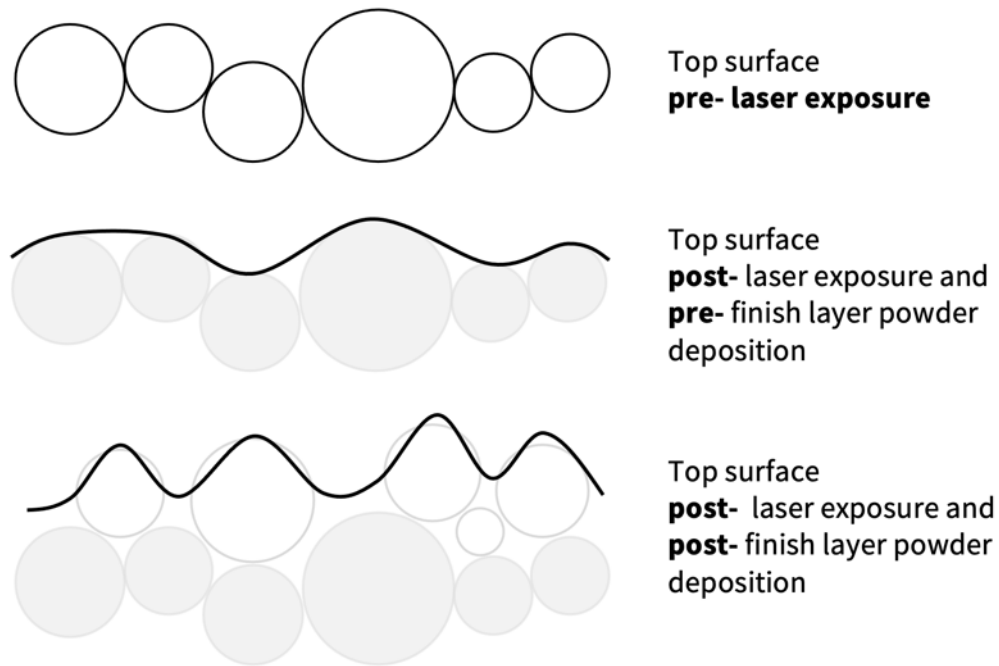


Figure 5.10 – An illustration highlighting the proposed mechanism of top surface modification by finish layer powder particle adhesion.

Bottom surface Skewness results obtained by FV microscopy were neither predominantly positive nor negative. Ultimately, no correlations between bottom surface Skewness, specimen positioning across the powder bed and applied energy density could be discerned.

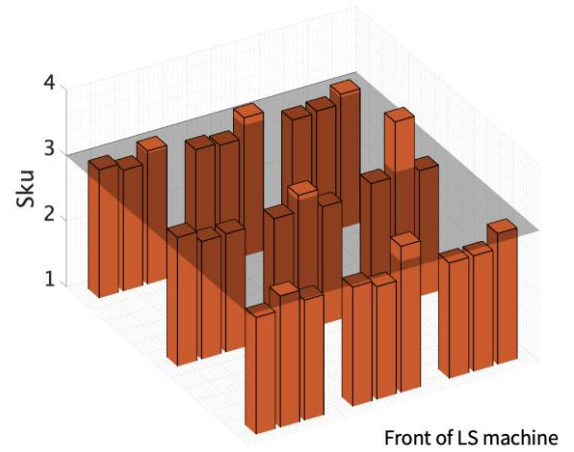
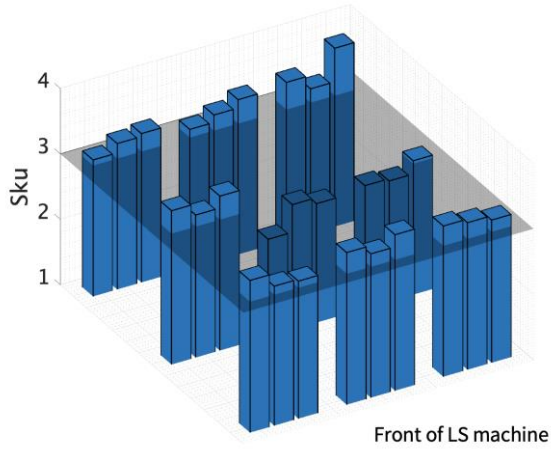
5.3.2.4 Kurtosis (S_{ku} / R_{ku})

S_{ku} and R_{ku} roughness results are shown in **Figure 5.11** and **Table 5.6**.

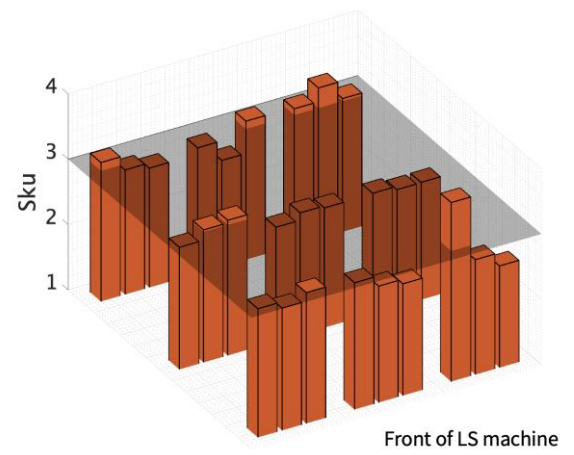
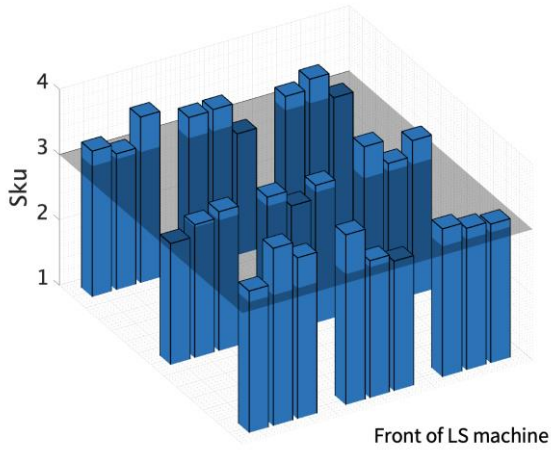
Top Surfaces

Bottom Surfaces

18W



21W



24W

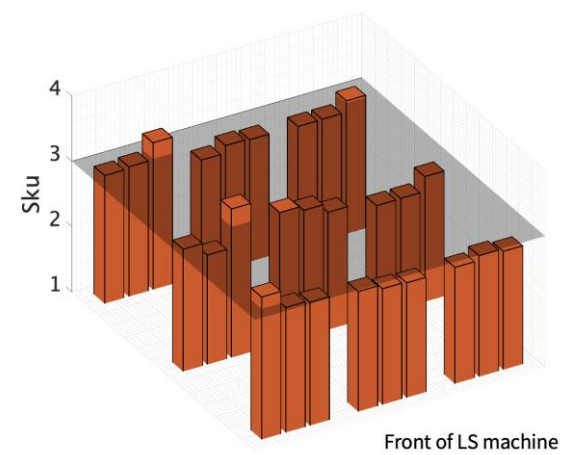
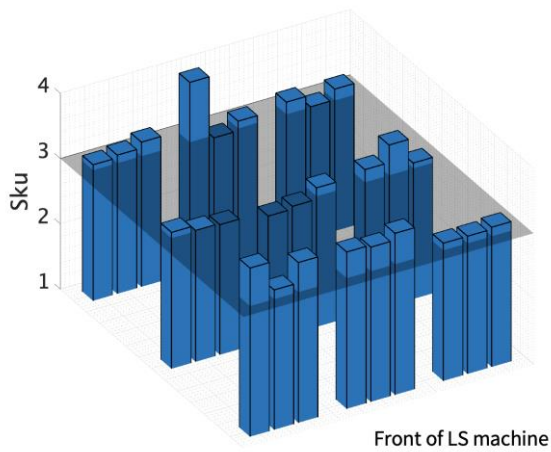


Figure 5.11 – The distribution in S_{ku} roughness of top and bottom surfaces (built at varying applied energy densities) across the powder bed. A translucent reference plane at the critical Kurtosis value of three ($S_{ku} = 3$) has also been included.

Table 5.6

A comparison of the S_{ku} and R_{ku} roughness results, and corresponding standard deviations, determined for both the top and bottom surfaces of laser sintered PA12 samples built at varying applied energy densities and evaluated by FV microscopy and contact profilometry.

S_{ku}/R_{ku} roughness	Metrology technique	Applied laser power		
		18W	21W	24W
Top surfaces	FV microscopy	3.17 (± 0.24)	3.21 (± 0.22)	3.20 (± 0.23)
	Contact profilometry	2.50 (± 0.09)	2.48 (± 0.16)	2.45 (± 0.18)
Bottom surfaces	FV microscopy	2.94 (± 0.21)	2.93 (± 0.23)	2.89 (± 0.15)
	Contact profilometry	2.58 (± 0.11)	2.66 (± 0.13)	2.61 (± 0.30)

Mean R_{ku} results were all less than the critical value of three ($R_{ku} < 3$). This suggests that both top and bottom surfaces evaluated by contact profilometry were platykurtic (relatively ‘non-spiky’). Moreover, this is congruent with theory discussed in **Section 5.3.2.3**, which highlighted that surfaces characterised by contact profilometry will intrinsically be subject to the ‘Smoothing Effect’, as illustrated in **Figure 5.9**.

Similarly, laser sintered PA12 bottom surfaces were also measured to have mean Kurtosis values of less than three when evaluated by FV microscopy ($S_{ku-bottom} < 3$). Ultimately, this validated that the laser sintered PA12 bottom surfaces evaluated within this study were indeed platykurtic (relatively ‘non-spiky’).

Contrastingly, mean top surface S_{ku} results obtained by FV microscopy were greater than three ($S_{ku-top} > 3$), independent of applied laser power. This was concordant with data collected by De Pastre et al. [100]. Therefore, it is expected the mechanism of finish layer powder particle adhesion also ensued the formation of leptokurtic (relatively ‘spiky’) top surface topographies.

5.4 Conclusions

This work holistically characterised laser sintered PA12 surfaces with respect to the factors previously shown to influence their description. More specifically, contact profilometry, FV microscopy and micro-CT were employed to better understand how laser sintered PA12 surfaces are a function of amplitude roughness descriptor; applied energy density; XY positioning across the powder bed; part orientation; and measurement technique. A summary of the key findings ascertained apropos to each of these factors is outlined in **Table 5.7**.

Table 5.7

A summary of the key findings ascertained during **Chapter 5**.

Factor of interest	Key findings ascertained
Measurement technique	<ul style="list-style-type: none"> - Roughness profiles measured by contact profilometry are intrinsically subject to the 'Smoothing Effect' due to the finite geometry of the stylus tip. - Areal surface scans captured by FV microscopy are significantly more representative of entire part surfaces than 2D profile results obtained by contact profilometry. - Generally, contact and / or optical line-of-sight metrology methods are incapable of characterising surfaces abundant with re-entrant and undercut features, such as laser sintered surfaces oriented non-parallel to the powder bed.
Part orientation	<ul style="list-style-type: none"> - Side surfaces are prone to secondary sintering during LS. - Top and bottom surfaces were found to have similar roughness amplitudes when evaluated by FV microscopy. However, results obtained by contact profilometry showed that top surfaces had greater R_q and R_z roughnesses than bottom surfaces. - Top surface topographies were found to be relatively sharp and also asperity peak dominated, whereas bottom surfaces were characterised as being relatively Gaussian and comparatively smooth.
Amplitude roughness descriptor	<ul style="list-style-type: none"> - S_q was determined as being the most apt amplitude roughness parameter for describing the surface heights of laser sintered PA12 components. - S_{sk} was also deemed important to consider. The mechanism of finish layer powder particle adhesion was attributed to why top surfaces were discerned to be dominated by asperity peaks.
Applied energy density	<ul style="list-style-type: none"> - Over the LS parameter range investigated, varying the magnitude of laser power, and consequently energy density, applied during building was not found to affect the top or bottom surface heights of parts produced. Though, this was discordant with work carried out by Sachdeva et al. [89], thus is studied in more detail in Chapter 6.
XY positioning across the powder bed	<ul style="list-style-type: none"> - Build positioning across the powder bed had no notable effect on the top or bottom surface topographies of samples evaluated.

Chapter 6

The Mechanisms that Influence Laser Sintered Polyamide-12 Top Surfaces

Chapter Summary

This chapter expands on **Chapter 5** by specifically characterising the extent to which the mechanisms of polymer melt viscous flow and finish layer powder particle adhesion influence the top surface topographies of laser sintered PA12 components.

This chapter includes published work, available via the following citation:

J. Tarver, K. Nar and C. Majewski, An Investigation into the Mechanisms that Influence Laser Sintered Polyamide-12 Top Surfaces, *Rapid Prototyping Journal*. Vol. 30, (2024).

<https://doi.org/10.1108/RPJ-09-2023-0317>

6.1 Introduction

It is well established that laser sintered surfaces are a function of the powder feedstock used [15,93,136], processing parameters employed [89,93,137] and orientation in which parts are digitally placed within the build envelope [100,138]. It is also widely agreed upon that the mechanisms that drive the formation of different laser sintered surface topographies vary depending on these considerations.

6.1.1 Motivation

This work builds on research that was carried out in **Chapter 5**, by specifically characterising the processing parameter related mechanisms that principally influence the top surface topographies of laser sintered PA12 components. These include the mechanisms of polymer melt viscous flow (illustrated in **Figure 6.1**) and finish layer powder particle adhesion – which was proposed for the first time in **Section 5.3.2.3** (illustrated in **Figure 5.10**).

More generally, this study demonstrates the scope to which laser sintered PA12 top surfaces can be modified without performing any auxiliary post-processing.

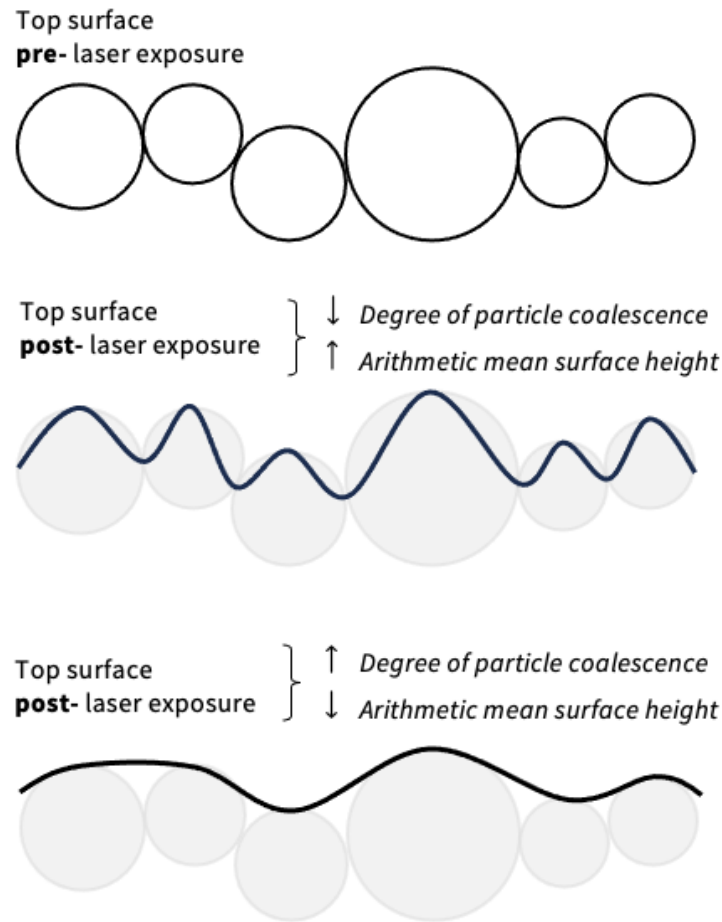


Figure 6.1 – An illustration of the mechanism of top surface modification by finish layer powder particle adhesion.

6.1.2 Polymer Melt Viscous Flow

As illustrated in **Figure 6.1**, the magnitude of polymer melt dispersion incurred during building determines the top surface topographies of parts produced. Sachdeva et al. [89] found that increasing applied laser power from 28W to 32W induced greater particle sintering, which as a result reduced the top surface R_a , R_q and R_z roughnesses of samples evaluated.

Similar studies have also been documented within the literature, specifically works by Bacchewar et al. [138], Petzold et al. [93] and Mavoori et al. [137]. However, these studies all holistically evaluated the effect of several different processing parameter types, rather

than the compound effect of multiple associated parameters, such as those exclusively related to powder properties (e.g., state of reuse, morphology, layer thickness) or laser properties (e.g. laser power, beam spacing, scan speed). Consequently, there remains to be little agreement on which processing parameters preponderantly effect the top surface topographies of laser sintered components.

6.1.3 Finish Layer Powder Particle Adhesion

As previously mentioned in **Section 2.3.1.3**, it is conventional practice to consecutively deposit numerous blank layers of material, more commonly referred to as finish layers, on top of newly sintered parts.

Though, it was proposed in **Chapter 5** that as well as providing insulation during build cooldown, the deposition of finish layers modify the top surface topographies of laser sintered PA12 components such that they consequently primarily comprise of asperity peaks. More specifically, it is thought that this is due to the subsequent adhesion that takes place between the final sintered build layer and powder particles within the following deposition of finish layer material, as illustrated in **Figure 5.10**.

6.2 Materials and Methods

6.2.1 Materials

In addition to 50/50 – PA12, virgin – PA12 and PrimePart (a thermoplastic elastomer produced by EOS GmbH) were also employed so that refresh ratio and polymer-type could be evaluated, respectively, when investigating the impact of finish layer deposition on the top surface topographies of laser sintered components.

Each powder was sieved to remove any agglomerates, and 50/50 – PA12 powder batches were blended by rotary tumbling for 20 minutes prior to building.

6.2.2 Specimens

ASTM D638-14 type 1 tensile specimens were produced so that both surface analysis and subsequent tensile testing could be performed. The specific geometry of these specimens can be seen in **Figure 4.5**. The samples used within this study were manufactured over multiple builds in accordance with the experimental procedure outlined in **Section 6.2.3**.

Upon build completion, compressed air was used to remove loose powder particles from all resultant specimen surfaces.

6.2.3 Experimental Procedure

The experimental procedure outlined in **Figure 6.2** was followed to specifically examine the influence of polymer melt viscous flow and finish layer powder particle adhesion of laser sintered PA12 top surfaces.

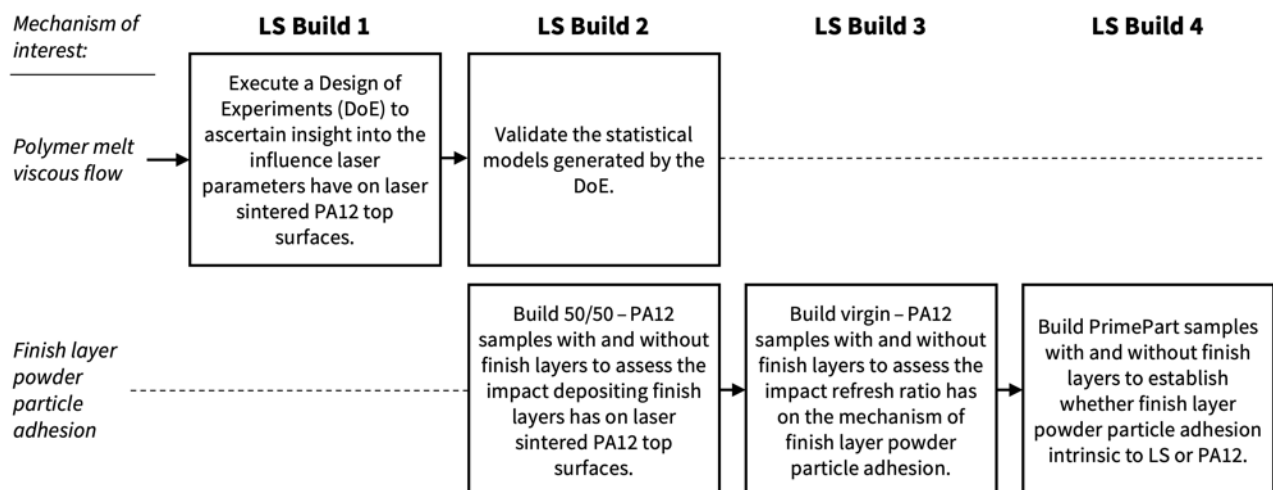


Figure 6.2 – The experimental procedure followed in this study to investigate the mechanisms of polymer melt viscous flow and finish layer powder particle adhesion.

Additionally, **Figure 6.3** shows the layout of each LS build performed as part of this study, including details of which specimens were manufactured with and without finish layers.

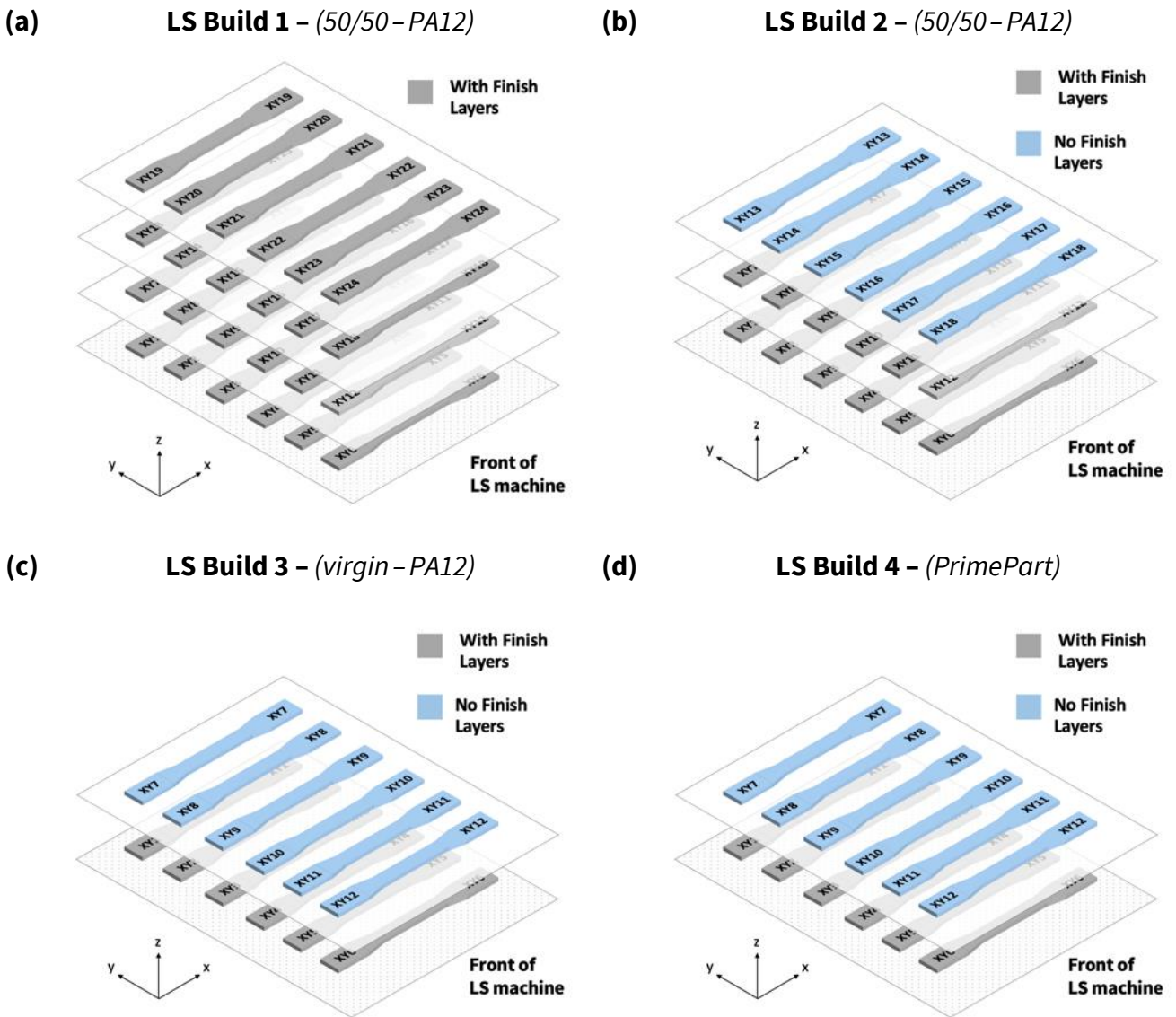


Figure 6.3 – The layout of each LS build performed as part of this study, including details of which specimens were manufactured with and without finish layers in LS builds (a) 1, (b) 2, (c) 3, and (d) 4.

6.2.3.1 LS Build 1

Firstly, a full factorial Design of Experiments (DoE) was carried out to evaluate the extent to which laser sintered PA12 top surfaces were affected by varying laser parameter combinations. This design methodology was chosen due to its efficiency when analysing multiple interacting factors [186]. More specifically, a two-level design was adopted, whereby laser power, scan speed and beam spacing were tested at low and high values

relative to standard PA12 parameters, as shown in **Table 6.1**. These low and high values were selected based on the lower and upper PA12 processing limits (specific to the LS machine used throughout this doctoral work) previously determined by members of the Advanced Polymer Sintering Laboratory. A total of 24 specimens were produced as part of the DoE, which included eight different sets of samples (each comprising of three repeat specimens), manufactured in accordance with the build configurations outlined in. **Table 6.2**.

Table 6.1

The LS build parameters employed as part of the DoE (LS build 1).

Parameter	Fixed / variable	Standard value (0)	Low value (-1)	High value (1)
Laser power (W)	Variable	21	17	25
Scan speed ((mm)s ⁻¹)	Variable	2500	2000	3000
Beam spacing (mm)	Variable	0.25	0.2	0.3
Bed temperature (°C)	Fixed	170		
Scan count	Fixed	1		
Contour scan	Fixed	Off		
Layer thickness (mm)	Fixed	0.1		

Table 6.2

The different LS build configurations evaluated as part of the DoE (LS build 1).

Build configuration	A – Laser power	B – Scan speed	C – Beam spacing	Energy density ((mJ)mm ⁻²)	Percentage difference from the E_D value for standard PA12 parameters (33.6 (mJ)mm ⁻²)
1	-1	-1	-1	42.50	+ 26.9
2	-1	-1	1	28.30	- 15.8
3	-1	1	-1	28.30	- 15.8
4	-1	1	1	18.89	- 43.8
5	1	-1	-1	62.50	+ 86.0
6	1	-1	1	41.67	+ 24.0
7	1	1	-1	41.67	+ 24.0
8	1	1	1	27.78	- 17.3

The statistical software package ‘Minitab’ was utilised to analyse the full factorial DoE. Probability values (p-values) were computed to evaluate the extent to which individual and interaction laser parameters effected the top surface topographies of laser sintered PA12 components. Results were deemed statistically significant when their corresponding p-values were less than the adopted 0.05 standard significance level (α). Regression expressions were generated to model the relationships between applied laser parameters and measured roughness responses. Terms with p-values greater than α were removed from all statistical models. Both coefficient of determination values (R^2) and residual plot responses were analysed to determine how well each model fitted the data collected. Additionally, R^2 -pred values were computed to indicate how well each regression model was expected to predict new roughness responses.

6.2.3.2 LS Build 2

As mentioned in **Figure 6.2**, validation specimens were manufactured so that the accuracy of the roughness predictions generated from each regression model could be evaluated (build configurations: 9 – 12). Different laser parameters to those previously selected for the DoE were employed, as detailed in **Table 6.3**.

This build also included samples manufactured without finish layers to ascertain the extent to which finish layer deposition affected the top surface topographies of parts produced (build configurations 13 and 14), as shown in **Figure 6.3**. In practice, this was achieved by manually stopping the build immediately after the final build layer had been sintered. Details of the laser parameters employed when manufacturing these no finish layer 50/50 – PA12 specimens can be seen in **Table 6.3**.

A total of 18 specimens were produced in build 2, including six different sample sets (each comprising of three repeat specimens), manufactured in accordance with the build configurations outlined in **Table 6.3**.

Table 6.3

The different build configurations evaluated as part of build 2.

Build configuration	Finish layers	Laser power (W)	Scan speed ((mm)s ⁻¹)	Beam spacing (mm)	Energy density ((mJ)mm ⁻²)	Percentage difference from the E_D value for standard PA12 parameters (33.6(mJ)mm ⁻²)
9	Yes	21.6	3000	0.20	36.0	+ 6.7
10	Yes	24.8	2280	0.20	54.4	+ 61.2
11	Yes	22.0	2400	0.20	45.8	+ 36.3
12	Yes	21.0	2500	0.25	33.6	0 (standard PA12 parameters)
13	No	21.0	2500	0.25	33.6	0 (standard PA12 parameters)
14	No	25.0	3000	0.20	41.7	+ 24.0 (optimised parameters) ^a

^a ‘Optimised parameters’ refers to the laser parameter configuration that was found to most significantly minimise the top surface heights of resultant laser sintered 50/50 – PA12 samples. This is discussed in detail in **Section 6.3.1.1**.

6.2.3.3 LS Builds 3 and 4

As outlined in **Figure 6.2**, auxiliary LS builds were performed to determine whether the mechanism of finish layer powder particle adhesion was intrinsic to PA12 or LS. Accordingly, virgin – PA12 and PrimePart samples were manufactured in separate builds (specifically LS builds 3 and 4, respectively), using the processing parameters outlined in **Table 6.4**. The PrimePart processing parameters employed were previously developed by members of the Advanced Polymer Sintering Laboratory to maximise the tensile properties of parts produced. Correspondingly, these processing parameters had a resultant energy density value of 27.2mJ(mm⁻²).

Since both the virgin – PA12 and PrimePart LS builds only comprised of samples designated for finish layer analysis, it was possible to accommodate the production of six repeat specimens of each material in each of their respective builds.

Table 6.4

The LS build parameters employed when producing virgin – PA12 and PrimePart samples for finish layer analysis (LS builds 3 and 4, respectively).

Processing parameter	Virgin – PA12		PrimePart	
	Standard	Optimised ^a	Standard	Optimised ^a
Laser power (W)	21	25	17	–
Beam spacing (mm)	0.25	0.20	0.25	–
Scan speed ((mm) s ⁻¹)	2500	3000	2500	–
Bed temperature (°C)	170	170	130	–
Scan count	1	1	1	–
Contour scan	Off	Off	Off	–
Layer thickness (mm)	0.1	0.1	0.1	–

^a Optimised virgin – PA12 processing parameters refer to those that were found to most significantly minimise the top surface heights of laser sintered 50/50 – PA12 samples. This is discussed in detail in **Section 6.3.1.1**.

6.2.4 Surface Analysis

This study utilised the roughness descriptors Root Mean Square (S_q) and Skewness (S_{sk}) in concurrence with work carried out in **Chapter 5**, in which these parameters were deemed apt at characterising the height and symmetry of laser sintered PA12 top surfaces, respectively.

To recapitulate, S_q represents the standard deviation of ordinate amplitudes within a defined evaluation area and S_{sk} describes whether the distribution of bulk material that comprises a surface exists above or below its mean plane. As illustrated in **Figure 2.13**, when $S_{sk} > 0$, asperity peaks will be more characteristic than valleys / pores within a surface, and vice versa.

In accordance with the process specified in **Section 4.2.2.2**, an Alicona InfiniteFocus SL system, which operates on the principle of Focus Variation (FV), was used to characterise

S_q and S_{sk} roughness at three evenly distributed locations across the top surfaces of parts produced.

6.2.5 Tensile Testing

Tensile testing was performed to identify whether building without finish layers induced any changes in the mechanical properties of samples produced – due to different cooling rates for example.

An outline of the general testing procedure followed is given in **Section 4.2.2.1**. Though, due to the intrinsic elasticity of PrimePart samples, crosshead speeds of 50 (mm)min^{-1} were correspondingly employed in accordance with ASTM D638-14.

6.3 Results and Discussion

6.3.1 The Influence of Laser Parameters on Laser Sintered PA12 Top Surfaces

Table 6.5 shows the mean S_q and S_{sk} values of all the top surfaces of samples produced as part of the DoE (build 1). Additionally, a graphical comparison between these resultant top surface roughness values and their corresponding applied energy densities can be seen in **Figure 6.4**. Strong quadratic relationships were produced, as evidenced by their high coefficient of determination (R^2) values. Furthermore, an inverse trend can be seen when comparing Root Mean Square and Skewness roughness. More specifically, the laser sintered top surfaces that recorded the smallest S_q roughnesses were also the most asperity peak dominated (highest S_{sk} values), as shown in **Figure 6.5**. This relationship suggests that minimum and maximum S_q and S_{sk} values should theoretically be attained at applied energy densities of 45.7 (mJ)mm^{-2} and 50.2 (mJ)mm^{-2} , respectively.

Table 6.5

The top surface roughness results, and corresponding standard deviation values, of all the samples evaluated as part of the DoE (build 1).

Build configuration	Laser power (W)	Scanning speed ((mm)s ⁻¹)	Beam spacing (mm)	Energy density ((mJ)mm ⁻²)	S _q (μm)	S _{sk}
1	17	2000	0.2	42.50	15.77 (±2.28)	0.468 (±0.083)
2	17	2000	0.3	28.30	18.71 (±0.71)	0.167 (±0.020)
3	17	3000	0.2	28.30	19.43 (±1.13)	0.036 (±0.107)
4	17	3000	0.3	18.89	25.70 (±2.27)	-0.234 (±0.081)
5	25	2000	0.2	62.50	19.45 (±0.44)	0.337 (±0.048)
6	25	2000	0.3	41.67	17.56 (±1.05)	0.283 (±0.117)
7	25	3000	0.2	41.67	15.30 (±1.35)	0.492 (±0.151)
8	25	3000	0.3	27.78	20.79 (±2.88)	0.060 (±0.081)

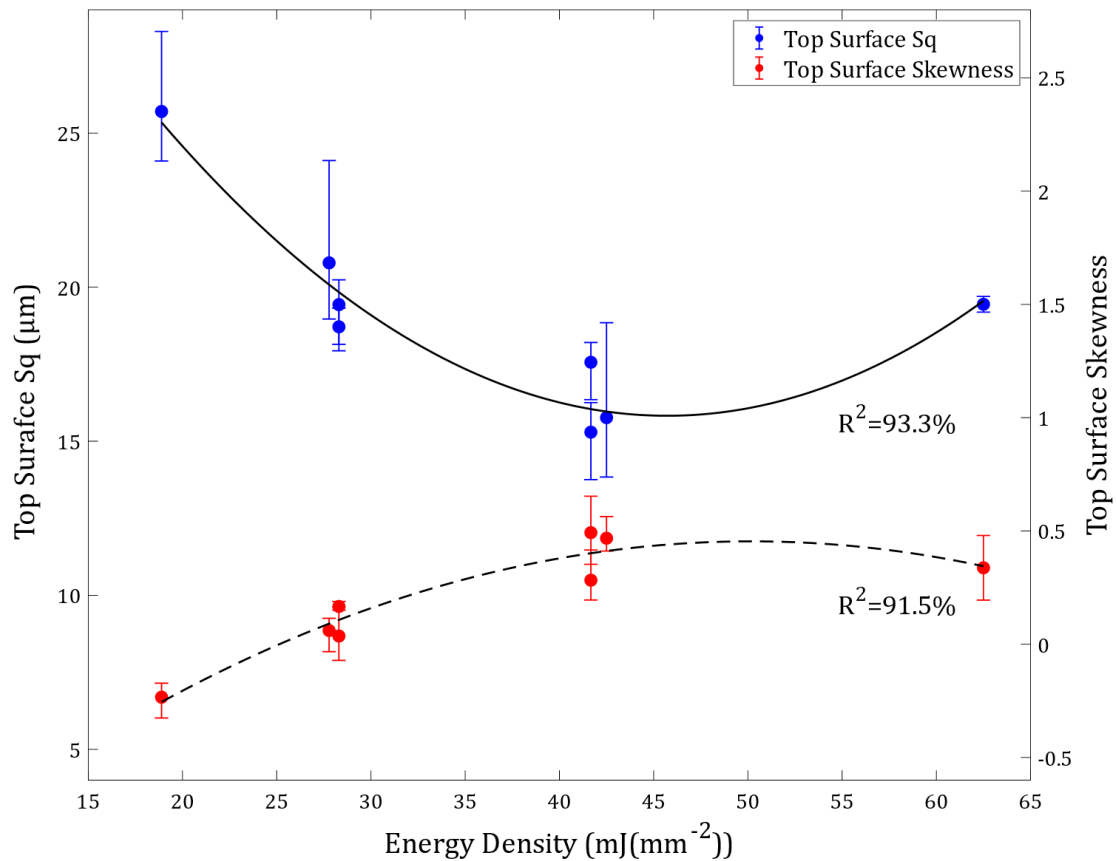


Figure 6.4 – The top surface S_q and S_{sk} roughness results relative to applied energy density. Corresponding R² values show how well each regression curve fitted the roughness data collected.

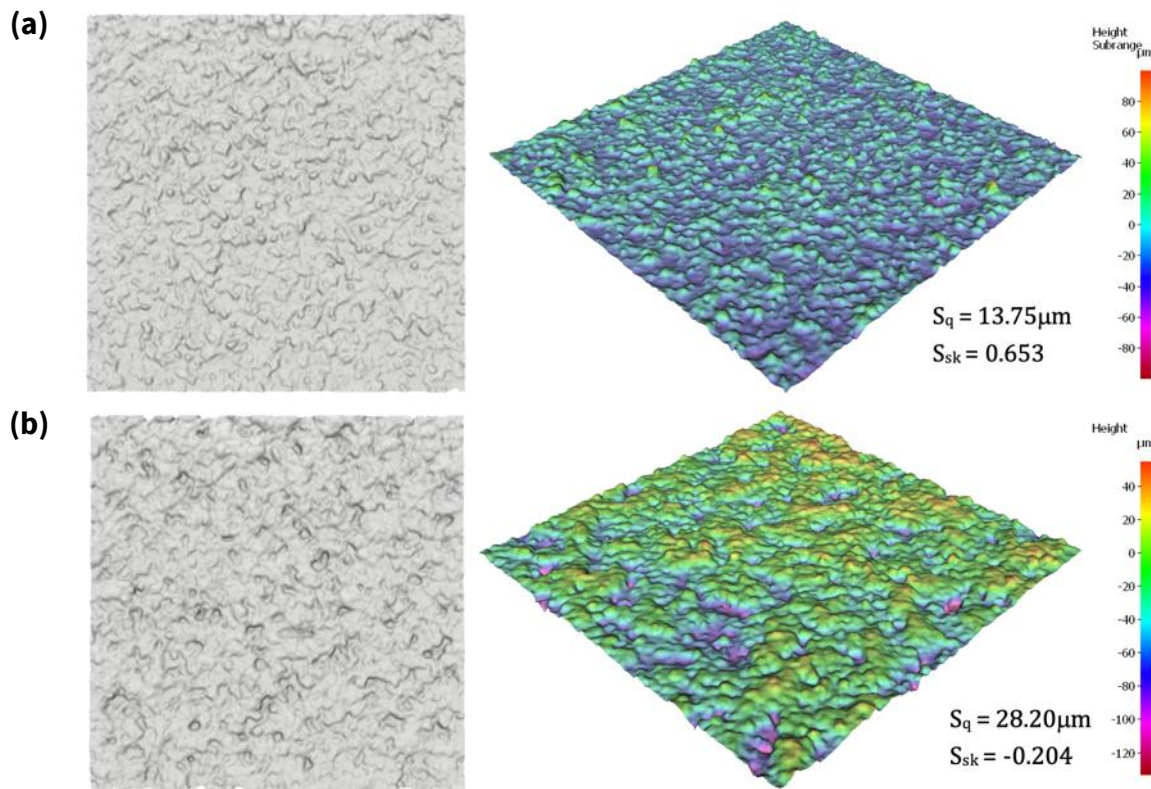


Figure 6.5 – FV microscopy outputs of two laser sintered PA12 top surfaces with contrasting S_q and S_{sk} roughnesses. More specifically, **(a)** a top surface of a sample built via configuration 7 which recorded the lowest S_q but largest S_{sk} values - corresponding surfaces were peak dominated and comprised of relatively small surface amplitudes; and **(b)** a top surface of a sample built via configuration 4 which recorded the highest S_q but lowest S_{sk} values - corresponding surfaces were valley dominated and comprised of relatively large surface amplitudes.

6.3.1.1 Resultant Top Surface Heights (S_q)

Figure 6.6 outlines the laser parameters that were found to influence the top surface S_q roughnesses of parts produced. Terms that had a standardised effect greater than 2.120 were deemed statistically significant. This reference value for statistical significance is displayed at point t , where t is the $(1 - \alpha/2)$ quantile of the resultant t-distribution in which its degrees of freedom are equal to the degrees of freedom of its error term [187].

The laser parameters that were found to be statistically significant included beam spacing (C), scan speed (B) and laser power (A), as well as the interaction effect between [laser power x scan speed (AB)] and [scan speed x beam spacing (BC)]. The main effect and contour plots presented in **Figure 6.7** and **Figure 6.8** show the individual and interactive

effects that each laser parameter had on the top surface S_q roughnesses of samples produced, respectively.

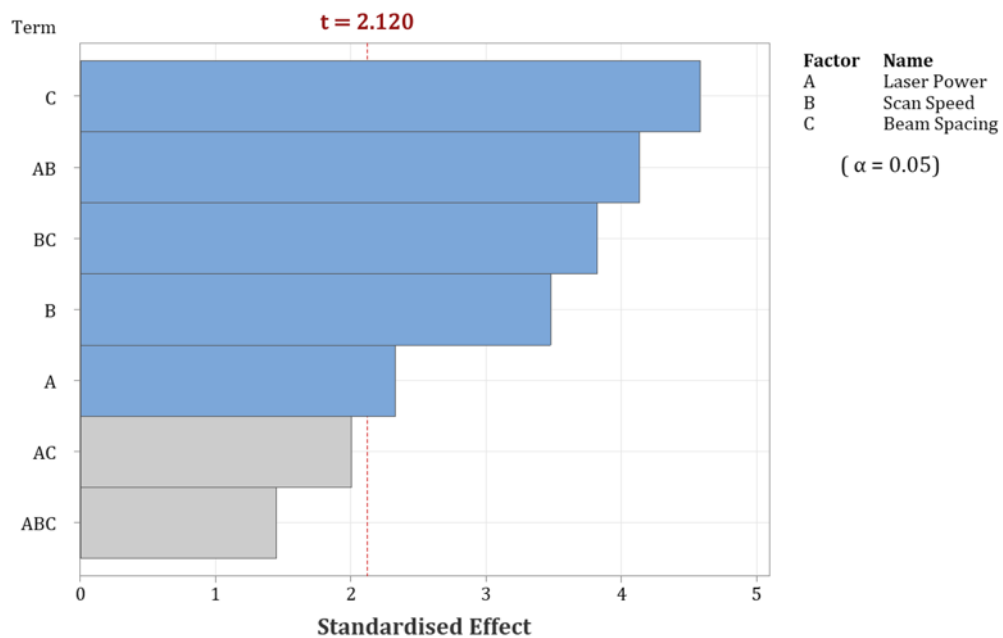


Figure 6.6 – A Pareto chart showing the extent to which laser power, scan speed and beam spacing influenced the top surface S_q roughnesses of 50/50 – PA12 parts produced as part of the DoE.

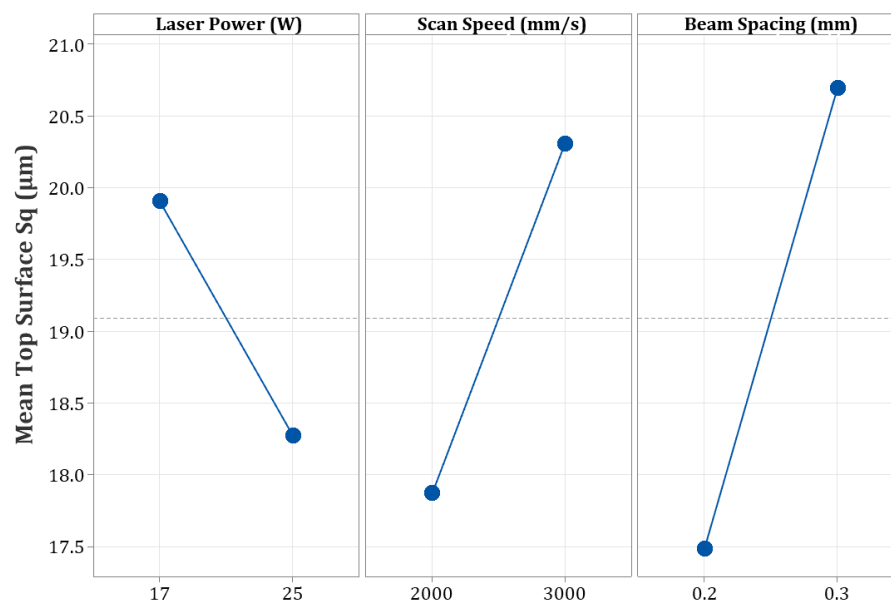


Figure 6.7 – Main effects plot showing the mean S_q responses at low and high laser parameter values.

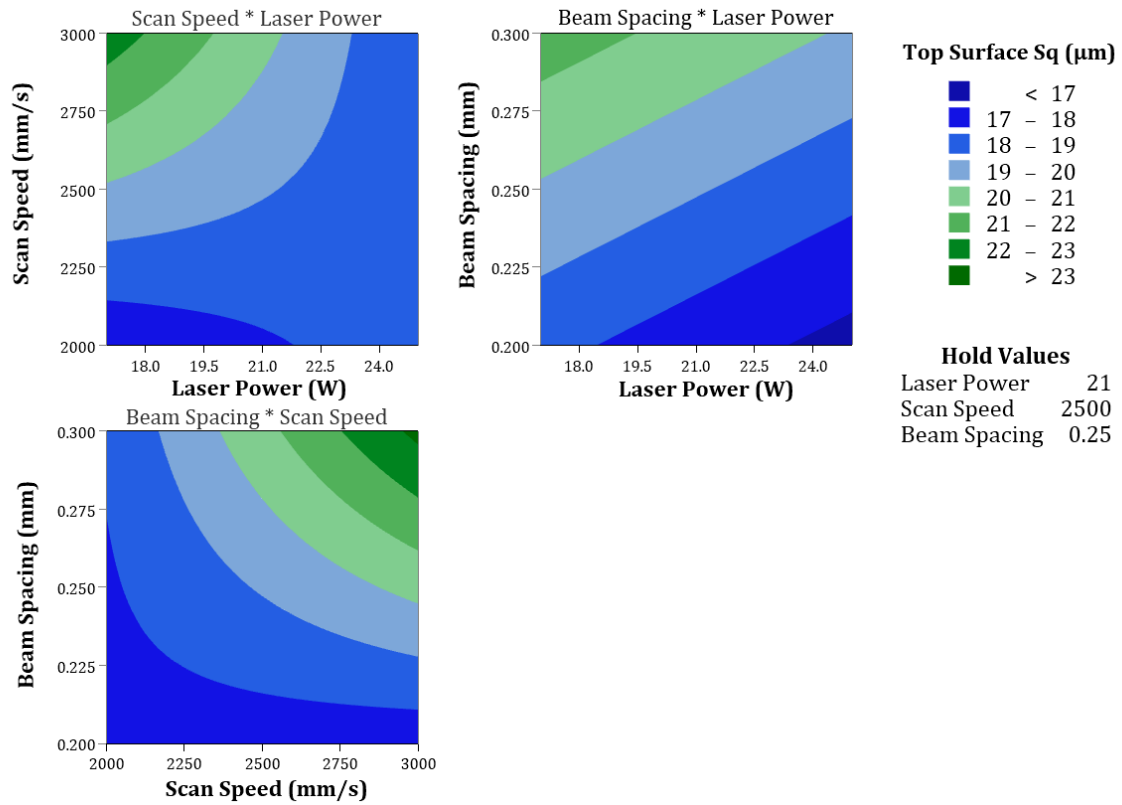


Figure 6.8 – Contour plots showing the different laser parameter interaction effects on top surface S_q roughness. Dark blue regions represent the laser parameter combinations that should lead to relatively low S_q roughness values, whereas dark green regions indicate the opposite.

As shown in **Figure 6.6**, the laser parameter configuration [ABC] was found to have a statistically insignificant influence on the top surface heights of parts produced. This suggests that it is not always apt to utilise the term energy density to characterise the relationship between applied laser parameters and resultant top surface S_q roughness. Furthermore, E_D lacks the ability to account for scan strategy and delay time. Analysing degree of particle melt by DSC (post-building) is expected to provide a better indication into the levels of particle coalesce incurred during processing.

Furthermore, **Figure 6.7** shows that the action of decreasing beam spacing had the greatest effect on reducing top surface S_q roughness. In practice, increasing the overlap between adjacent hatch lengths will have consequently increased the amount of laser scanning each layer received during building, as shown in **Figure 6.9**. More specifically, the LS machine used within this study generated a laser beam with an approximate spot

size diameter of 0.42mm. Therefore, when beam spacings of 0.2mm were employed, each hatch length will have been fully scanned at least twice. This is in good agreement with Sachdeva et al. [89], who also determined that relatively reduced Root Mean Square roughnesses were achieved when beam spacings less than the laser spot size radius were employed. Ultimately, increased laser exposure will have promoted the mechanism of polymer melt viscous flow.

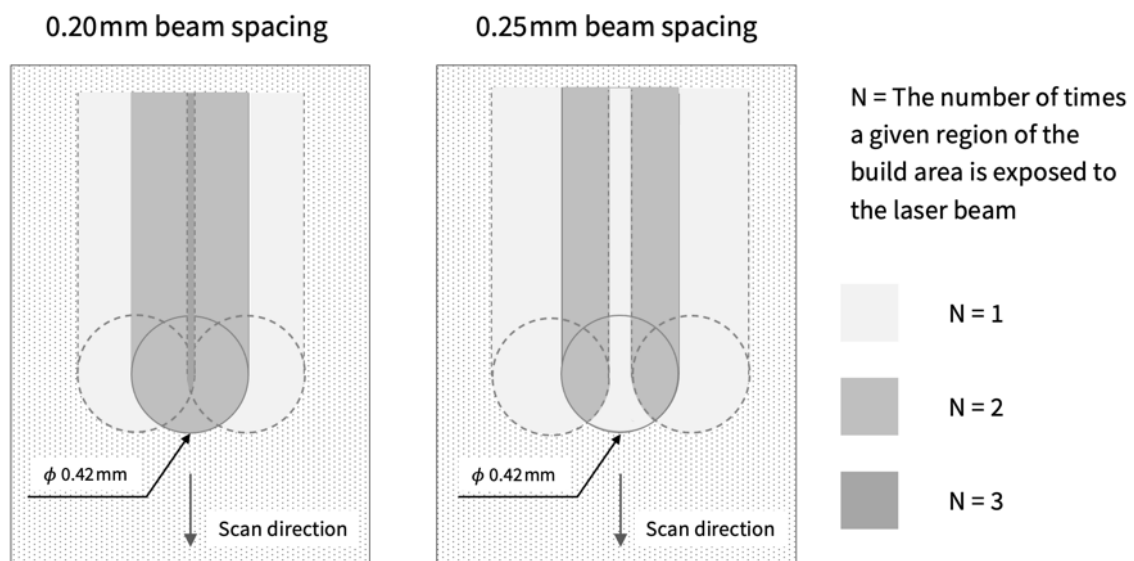


Figure 6.9 – The effect of beam spacing on powder bed laser exposure for a given spot size diameter of 0.42mm.

Additionally, **Figure 6.6** shows that the interaction between laser power and scan speed ($P \times v_{scan}$) had a greater influence on S_q than their individual effects. This compound term represents the magnitude and duration of laser energy applied to the powder bed during LS. Though, as shown in **Figure 6.8**, ($P \times v_{scan}$) was not discerned to linearly effect top surface S_q . Moreover, it can also be seen in **Figure 6.8**, that reducing scan speed and beam spacing resulted in lower S_q values across all of the interaction pairs evaluated. This suggests that laser exposure, rather than intensity, had the greatest impact on the top surface heights of parts produced.

For the laser parameter range investigated, the regression expression detailed in **Equation 6.1** was generated to model the resultant S_q roughnesses of laser sintered 50/50 – PA12 top surfaces:

$$S_q = 19.089 - 0.815A + 1.217B + 1.604C - 1.448AB + 1.337BC$$

Equation 6.1

where laser power (A), scan speed (B) and beam spacing (C) terms are given in coded unit form, which are proportional to their corresponding magnitudes and range between -1 and 1.

This model had an R^2 value of 76% and both normally distributed and independent residuals, which suggests that it provided a relatively adequate fit to the results collected. Though, its ability to predict new top surface S_q roughness responses was expected to be limited, as indicated by its corresponding R^2 –pred value of 57%.

Based on **Equation 6.1**, the laser parameter configuration detailed in **Table 6.6** was determined to be optimal for minimising the top surface heights of parts produced. To avert confusion, all future mention of optimised laser parameters within this chapter will be in reference to the former.

Table 6.6

A comparison between standard and model optimised laser parameters for minimising top surface S_q roughness. Corresponding coded unit values have also been included.

Parameter type	Laser Power (W)	Scan Speed ((mm)s ⁻¹)	Beam Spacing (mm)	Energy density ((mJ)mm ⁻²)	Predicted top surface S_q (μm) \pm 95% confidence interval	Actual top surface S_q (μm) \pm 95% confidence interval
Standard	21 (0)	2500 (0)	0.25 (0)	33.60	19.09 \pm 0.82	22.11 \pm 1.23
Optimised	25 (1)	3000 (1)	0.20 (-1)	41.70	15.10 \pm 2.00	15.30 \pm 1.53

As shown in **Table 6.8**, notably different surface topographies were obtained when optimised laser parameters were employed in place of standard values. More specifically, optimised top surface S_q roughnesses were 30.8% lower on average than those recorded when evaluating standard top surface topographies. Additionally, predicted and actual top surface S_q values differed by 15.8% and 1.3% when standard and optimised laser parameters were employed, respectively. Optimised laser sintered 50/50 – PA12 top surfaces were also found to be comparatively more asperity peak dominated, in congruency with the relationship outlined in **Figure 6.4**.

6.3.1.2 Resultant Top Surface Symmetries (S_{sk})

Top surfaces were almost all asperity peak dominated in accordance with the results obtained in **Chapter 5** and by De Pastre et al. [100].

Build configuration 4 was the only applied laser parameter set to deviate from this finding. However, as shown in **Table 6.5**, this build configuration was subject to the lowest applied energy density. Consequently, resultant top surfaces will have incurred relatively little polymer melt viscous flow resulting in valley formation, particularly at locations of minimum powder packing efficiency. This can be seen in **Figure 6.5**, which shows a corresponding FV microscopy obtained surface scan in which valleys are prevalent throughout.

Figure 6.10 shows the degree to which the investigated laser parameters affected top surface S_{sk} roughness. Statistically significant terms included, beam spacing (C), scan speed (B), laser power (A), as well as the interaction between [laser power x scan speed (AB)], [laser power x scan speed x beam spacing (ABC)] and [scan speed x beam spacing (BC)]. The only laser parameter interaction that was determined to be statistically insignificant was [laser power x beam spacing (AC)].

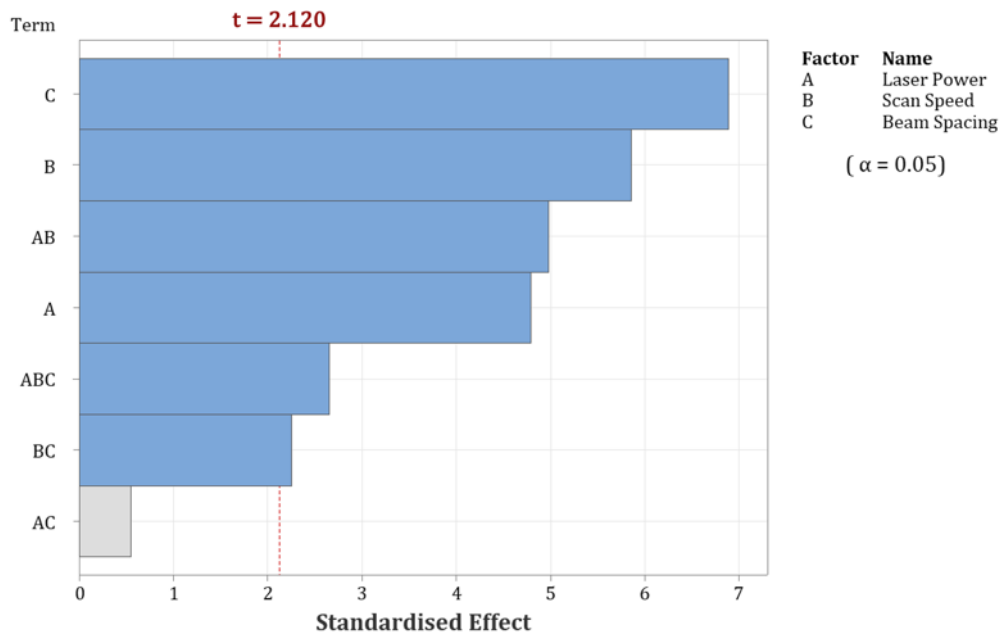


Figure 6.10 – A Pareto chart showing the extent to which laser power, scan speed and beam spacing influenced the top surface S_{sk} roughnesses of 50/50 – PA12 parts produced as part of the DoE.

The effects of individual laser parameters and their interactions are shown in **Figure 6.11** and **Figure 6.12**, respectively. It can be seen that greater top surface Skewness values are expected in the same regions at which relatively low S_q values were previously predicted in **Figure 6.7** and **Figure 6.8**.

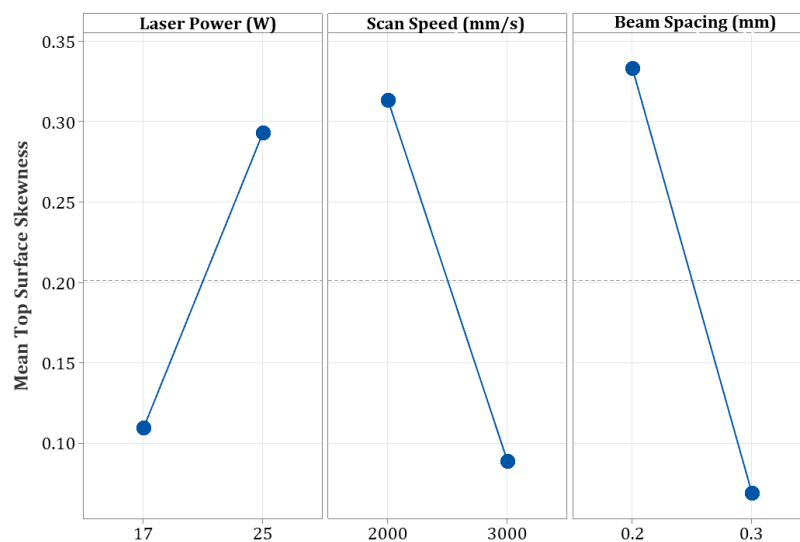


Figure 6.11 – Main effects plot showing the mean S_{sk} responses at low and high laser parameter values.

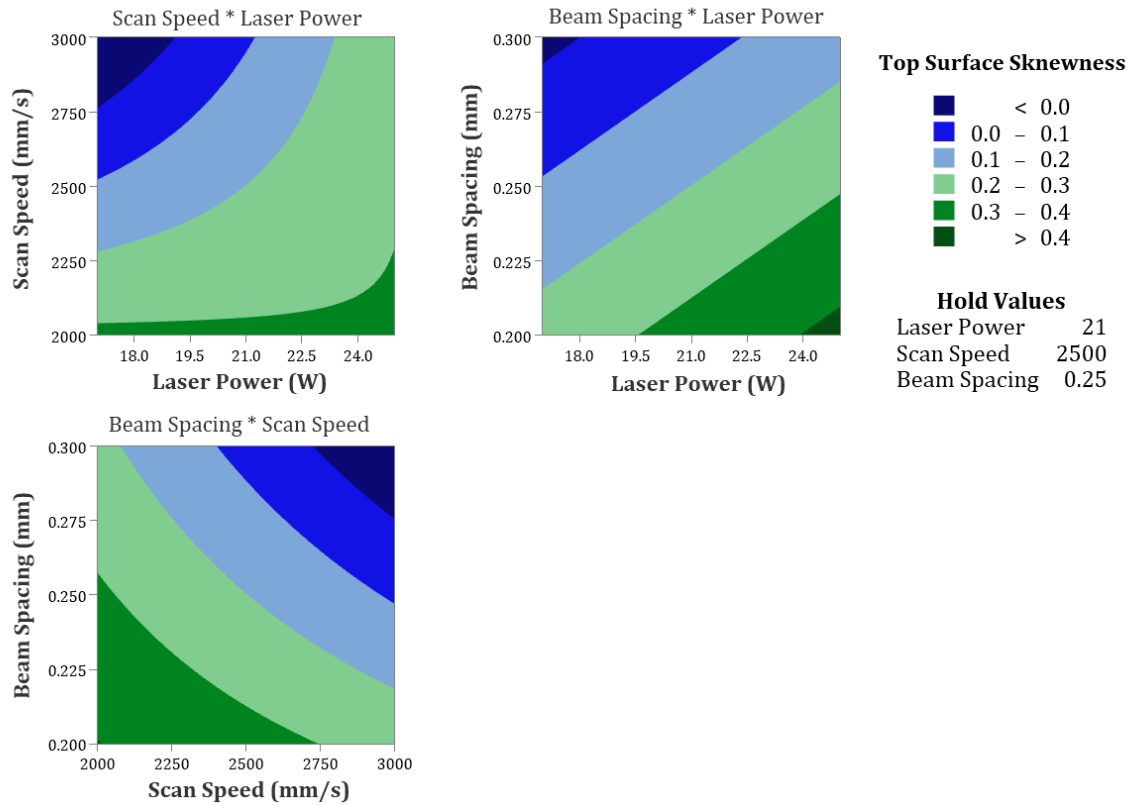


Figure 6.12 – Contour plots showing the different laser parameter interaction effects on top surface S_{sk} roughness. Dark blue regions represent the laser parameter combinations that should lead to relatively low S_{sk} roughness values, whereas dark green regions indicate the opposite.

Furthermore, results presented in **Figure 6.4** and **Figure 6.14** support the findings previously discerned in **Section 5.3.2.3**, where increasing applied energy densities were found to induce greater asperity peak formation within laser sintered PA12 top surfaces. Accordingly, upon being exposed to these increased quanta of laser energy, more heat will have accumulated within part top surfaces, consequently prompting more powder particle adhesion to ensue during the subsequent deposition of finish layer material. In praxis, corresponding increases in S_{sk} roughness were observed up until approximately $50 \text{ (mJ/mm}^2\text{)}$, as shown in **Figure 6.4** and **Figure 6.14**.

In a similar manner to S_q , the regression expression detailed in **Equation 6.2** was produced to model the resultant S_{sk} roughnesses of laser sintered 50/50 – PA12 top surfaces:

$$S_{sk} = 0.2012 + 0.0920A - 0.1124B - 0.1322C + 0.0956AB - 0.0433BC - 0.0510ABC$$

Equation 6.2

where laser power (A), scan speed (B) and beam spacing (C) terms are given in coded unit form, which are proportional to their corresponding magnitudes and range between -1 and 1.

This model had an R^2 value of 90% and both normally distributed and independent residuals, which suggests that it provided a good fit to the results collected. Additionally, **Equation 6.2** was expected to predict new S_{sk} roughness responses reasonably well, as indicated by its corresponding R^2 -pred value of 79%.

6.3.1.3 Validation of Statistical Models

To improve the comprehensiveness of the energy density range analysed within this study, validation specimens were manufactured (build 2) using different laser parameters to those previously selected for the DoE (build 1), as outlined in **Table 6.3**. A comparison between predicted and measured roughness results can be seen in **Table 6.7**.

Despite both statistical models being apt at providing insight into the general topographical features expected to comprise the top surfaces of parts produced, their accuracy at predicting specific mean S_q and S_{sk} roughness values was found to be limited. Measured roughness results were mostly found to be outside the upper and lower confidence bounds of model predicted estimates, as shown in **Figure 6.13**. However, it should be noted that these predictions were generated from laser power, scan speed and beam spacing alone.

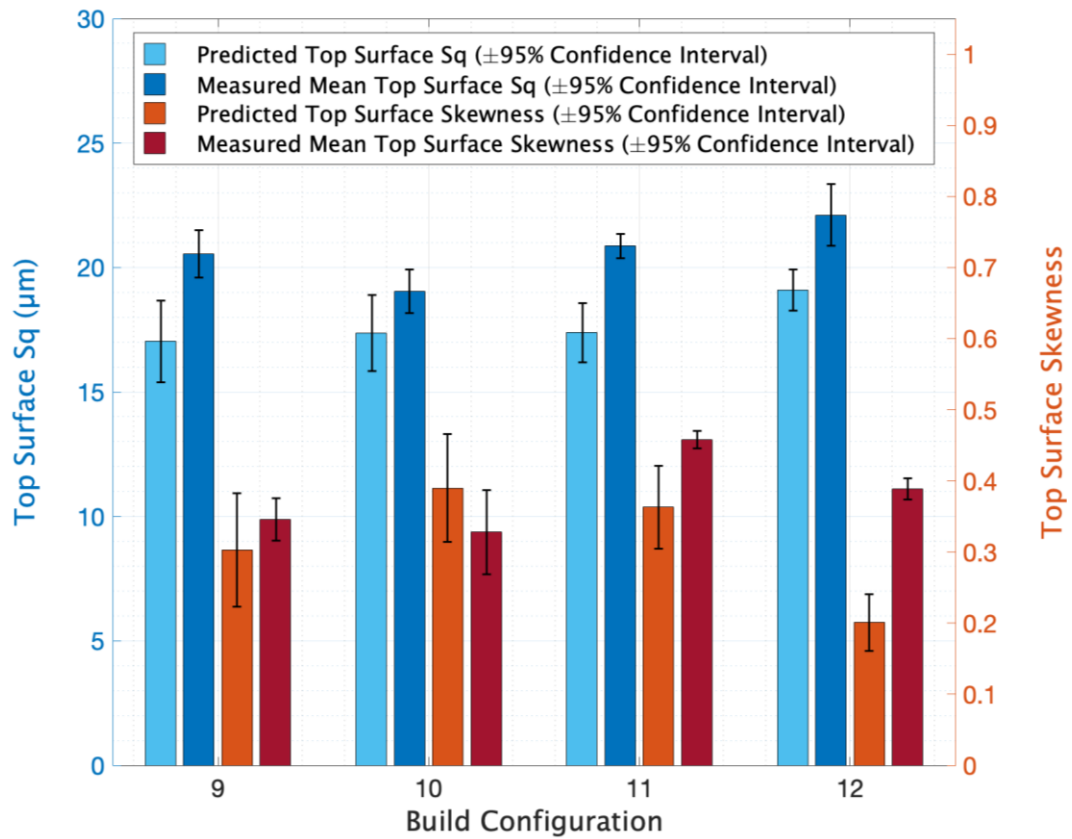


Figure 6.13 – Predicted and measured validation specimen top surface S_q and S_{sk} roughnesses.

Table 6.7

Predicted and measured validation specimen top surface roughness results.

Build Configuration	S_q			S_{sk}		
	Predicted	Measured	% difference	Predicted	Measured	% difference
9	17.03 (± 1.64)	20.55 (± 0.95)	+ 17.1%	0.303 (± 0.080)	0.346 (± 0.030)	+ 12.4%
10	17.37 (± 1.52)	19.04 (± 0.88)	+ 8.8%	0.390 (± 0.760)	0.328 (± 0.059)	- 18.9%
11	17.38 (± 1.19)	20.86 (± 0.50)	+ 16.7%	0.363 (± 0.058)	0.458 (± 0.012)	+ 20.7%
12	19.09 (± 0.82)	22.11 (± 1.23)	+ 13.7 %	0.201 (± 0.040)	0.389 (± 0.015)	+ 48.3%

Furthermore, a weak correlation was discerned when recreating the relationship between top surface S_q roughness and applied energy density with data collected from the validation specimens. As detailed in **Figure 6.14**, this relationship yielded a R^2 value of 52.6%. However, this is congruous with the previous observation discussed in **Section 6.3.1.1**, which highlighted that over the laser parameter range investigated,

energy density had a statistically insignificant effect on the top surface S_q roughness of samples produced.

Conversely, measured top surface S_{sk} results were still found to correlate well with applied energy density when data from the validation build was included, as indicated by its corresponding R^2 value of 87.9%.

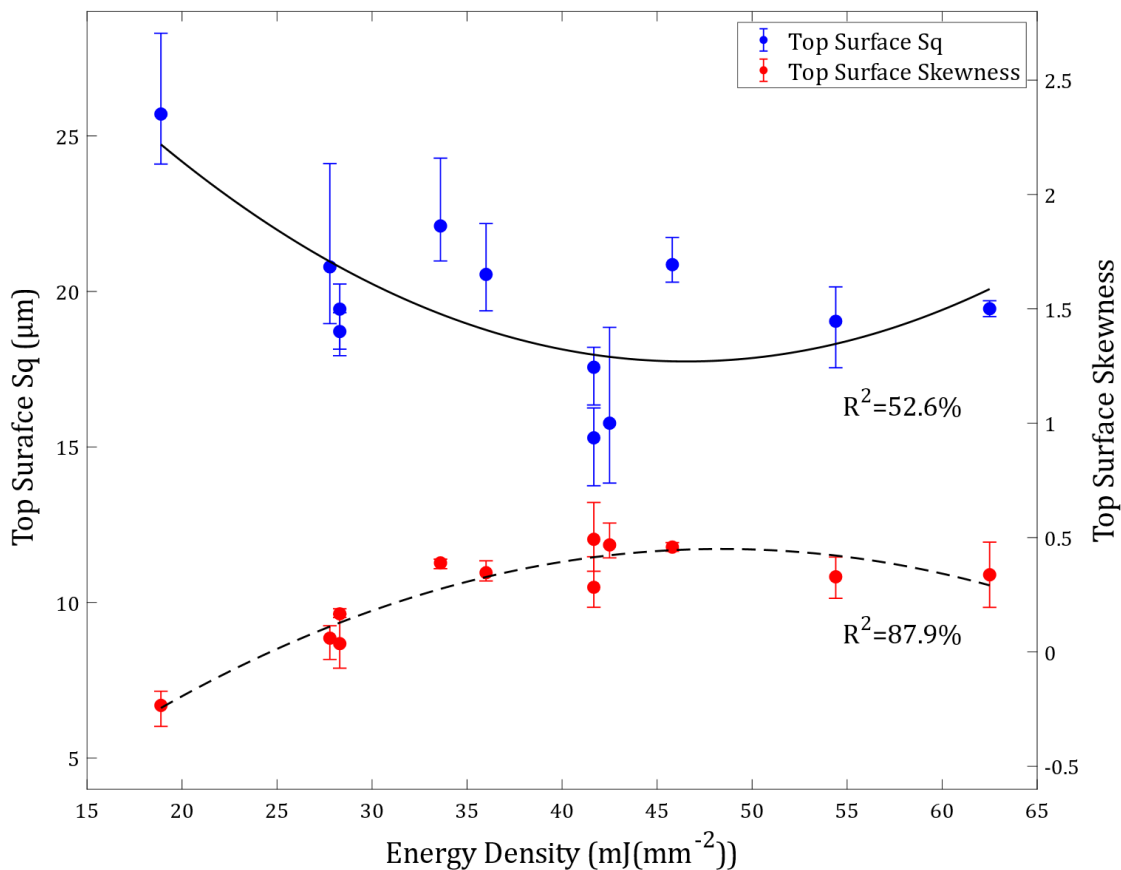


Figure 6.14 – Top surface S_q and S_{sk} roughness results relative to applied energy density, with the inclusion of validation specimens. Corresponding R^2 values show how well each regression curve fitted the roughness data collected. S_q and S_{sk} curve inflection points occur at 46.5 mJmm⁻² and 48.4 mJmm⁻², respectively.

6.3.2 The Influence of Finish Layer Deposition on Laser Sintered Polymer Top Surfaces

As previously mentioned in **Section 6.2.3**, 50/50 – PA12, virgin – PA12 and PrimePart samples (manufactured in builds 2, 3 and 4, respectively) were analysed to ascertain the

extent to which the mechanism of finish layer powder particle adhesion influenced their top surface topographies.

6.3.2.1 Resultant Top Surface Topographies

Ultimately, it was demonstrated that finish layer powder deposition had a transformative effect on the top surface topographies of every laser sintered component evaluated within this study.

50/50 – PA12 Samples

Table 6.8 and **Table 6.9** qualitatively and quantitatively elucidate the impact finish layer deposition had on the top surface topographies of 50/50 – PA12 samples, respectively.

Table 6.8

A qualitative comparison of laser sintered 50/50 – PA12 top surfaces manufactured with and without finish layers using standard and optimised laser parameters.





Laser parameters employed	With Finish Layers	No Finish Layers
Standard		
Optimised		

Table 6.9

A quantitative comparison of laser sintered 50/50 – PA12 top surfaces manufactured with and without finish layers using standard and optimised laser parameters. Both mean and corresponding standard deviation values have been included.

Laser parameters employed	With Finish Layers		No Finish Layers	
	S_q (μm)	S_{sk}	S_q (μm)	S_{sk}
Standard	22.11 (\pm 1.89)	0.389 (\pm 0.022)	11.52 (\pm 0.50)	-0.579 (\pm 0.136)
Optimised	15.30 (\pm 1.35)	0.492 (\pm 0.151)	9.69 (\pm 0.28)	-0.306 (\pm 0.149)

In this study, building without finish layers reduced the mean top surface heights of 50/50 – PA12 samples by 47.9% and 36.7%, relative to specimens manufactured conventionally using standard and optimised laser parameters, respectively.

Additionally, it can be seen in **Table 6.8** that pores were the most dominant feature within 50/50 – PA12 top surfaces built without finish layers. As previously mentioned in **Section 6.3.1.2**, these pore-like formations are likely to have existed at locations of minimum powder packing efficiency, where viscous flow leading to the coalescence of adjacent powder particles was not achieved. Furthermore, this apparent contrast in surface symmetry, pre- and post- finish layer deposition further validates that asperity peaks are formed due to the adhesion between newly sintered part top surfaces and powder particles within the following deposition of finish layer material.

Supplementarily, building without finish layers also allowed for the relationship between polymer melt viscous flow and applied laser parameters to be analysed. As shown in **Figure 6.15**, employing optimised laser parameters promoted the mechanism of polymer melt viscous flow, resulting in corresponding top surface topographies having comparatively fewer pores than top surfaces built using standard laser parameters.

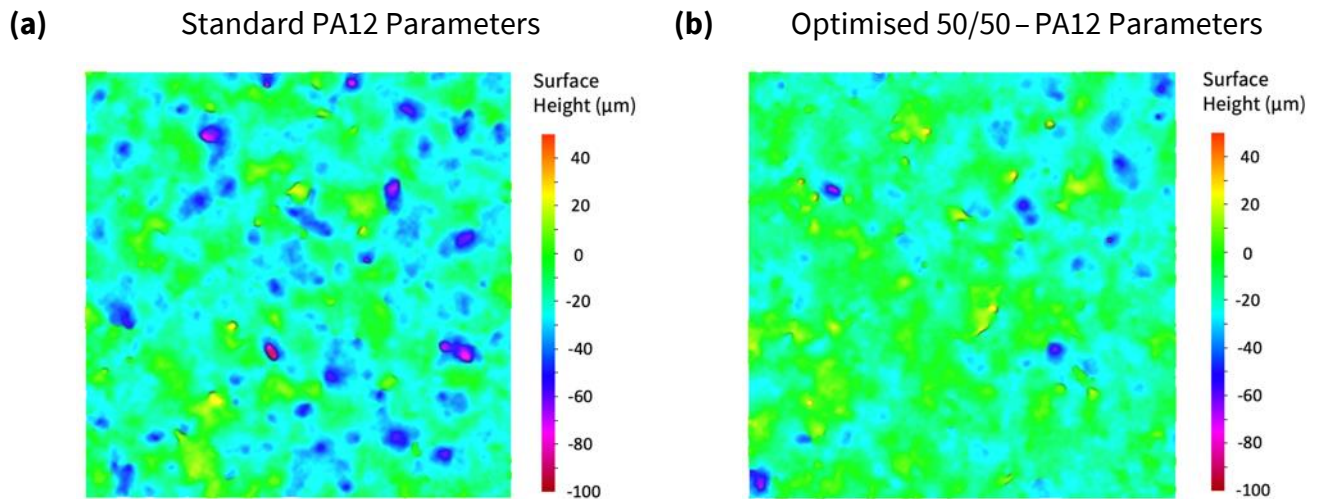


Figure 6.15 – Height maps of laser sintered 50/50 – PA12 top surfaces built using **(a)** standard and **(b)** optimised laser parameters (without finish layers). Employing the latter promoted the mechanism of polymer melt viscous flow, resulting in corresponding topographies having comparatively fewer pores.

Virgin – PA12 Samples

Table 6.10 and **Table 6.11** qualitatively and quantitatively elucidate the impact finish layer deposition had on the top surface topographies of virgin – PA12 samples, respectively.

Table 6.10

A qualitative comparison of laser sintered virgin-PA12 top surfaces manufactured with and without finish layers using standard and optimised laser parameters.

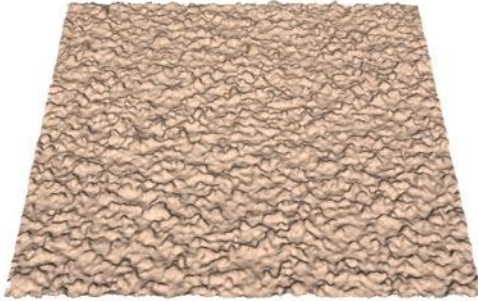


Laser parameters employed	With Finish Layers	No Finish Layers
Standard		
Optimised	—	

Table 6.11

A quantitative comparison of laser sintered virgin-PA12 top surfaces manufactured with and without finish layers using standard and optimised laser parameters. Both mean and corresponding standard deviation values have been included.

Laser parameters employed	With Finish Layers		No Finish Layers	
	S_q (μm)	S_{sk}	S_q (μm)	S_{sk}
Standard	14.58 (± 0.96)	0.667 (± 0.126)	4.52 (± 0.52)	-0.508 (± 0.223)
Optimised	—	—	4.96 (± 1.77) ^a	-0.500 (± 0.290) ^a

^a Results from tensile specimen six, specifically from the sample set built without finish layers and optimised laser parameters, were determined to be anomalous and therefore were not included when calculating mean roughness results and corresponding standard deviation values.

Virgin – PA12 samples manufactured without finish layers were measured to have top surface S_q roughnesses that were 69.0% lower on average than conventionally built laser sintered top surfaces.

Furthermore, employing entirely virgin – PA12 material induced greater transformations in top surface symmetry, pre- and post- finish layer deposition, than the differences measured when characterising 50/50 – PA12 top surfaces. Correspondingly, virgin – PA12 and 50/50 – PA12 samples built with and without finish layers had mean top surface S_{sk} differences ($|S_{sk(\text{with finish layer})} - S_{sk(\text{no finish layer})}|$) of 1.175 and 0.968, respectively. Ultimately, this suggests that the mechanism of finish layer powder particle adhesion has a more pronounced impact on laser sintered PA12 top surfaces when powder configurations comprising of entirely virgin material are employed.

Contrary to expectation, employing optimised laser parameters did not further reduce the mean top surface S_q roughness of virgin – PA12 samples built without finish layers. However, it should be noted that the optimised laser parameters employed in build 3 were originally developed to minimise the top surface heights of conventionally manufactured 50/50 – PA12 top surfaces. This suggests that individual optimisation studies should be carried out when wanting to tailor the specific surface roughnesses of different PA12 configurations.

PrimePart Samples

The mechanism of finish layer powder particle adhesion was also found to impact the top surfaces of PrimePart samples. FV microscopy obtained scan images of PrimePart top surfaces pre- and post- finish layer deposition are presented in **Figure 6.16**.

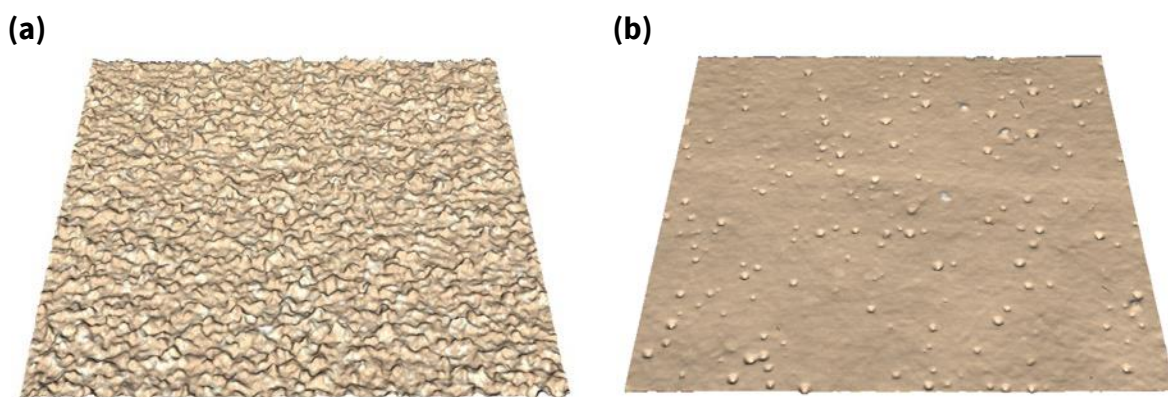


Figure 6.16 – PrimePart top surfaces built **(a)** with and **(b)** without finish layers.

It was not possible to quantitatively characterise the topographies of PrimePart samples built without finish layers. This was due to their translucency, which inhibited light from being reflected and received by the microscope's detector. However, upon visually analysing the top surfaces presented in **Figure 6.16**, a strong resemblance with the FV microscopy obtained scan images shown in **Table 6.8** and **Table 6.10** can be seen.

Therefore, it can be asserted with a reasonable degree of confidence that LS polymers, other than PA12, will also be susceptible to the mechanism of finish layer powder particle adhesion.

6.3.2.2 Resultant Part Tensile Properties

As previously mentioned in **Section 6.2.5**, tensile testing was performed to assess whether the action of building without finish layers induced any significant changes in the mechanical properties of samples produced. The results of which can be seen in **Table 6.12** and **Figure 6.17**.

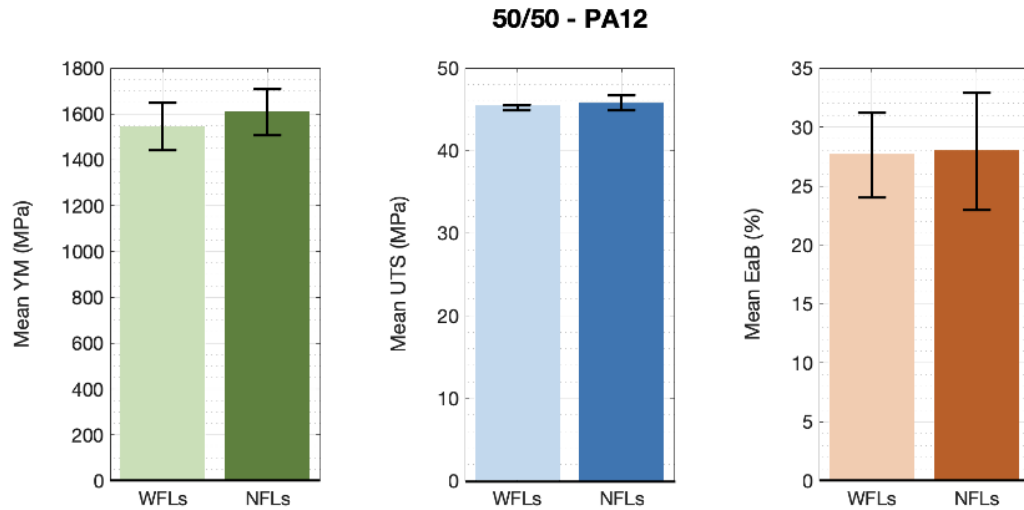
Ultimately, no statistical difference between the Young's Modulus (YM), Ultimate Tensile Strength (UTS) and Elongation at Break (EaB) of samples built with and without finish layers could be discerned, as indicated by their overlapping standard deviations.

Table 6.12

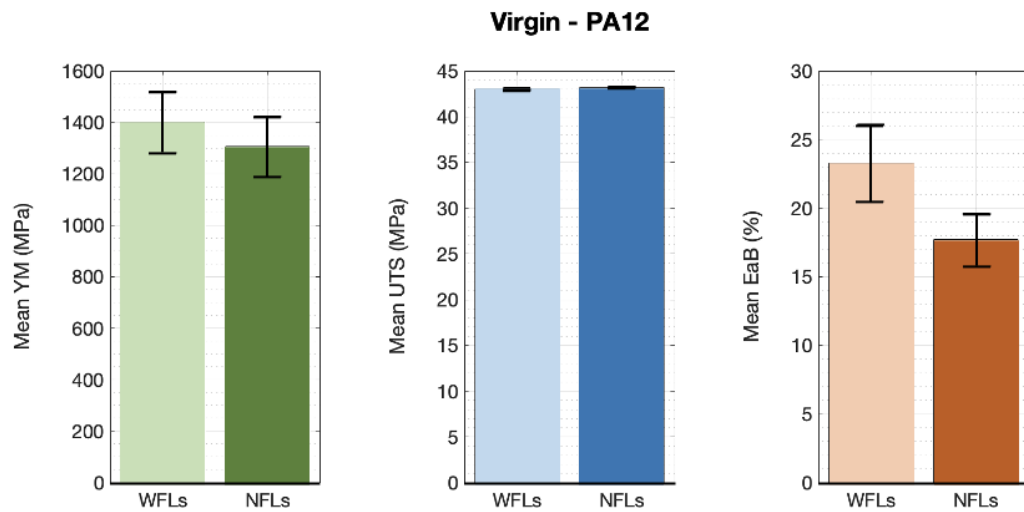
The mean tensile properties, and corresponding standard deviation values, of 50/50 – PA12, virgin – PA12 and PrimePart samples built with and without finish layers (as denoted by the abbreviations WFLs and NFLs, respectively).

Sample Material	YM (MPa)		UTS (MPa)		EaB (%)	
	WFLs	NFLs	WFLs	NFLs	WFLs	NFLs
50/50 – PA12	1547 (± 102)	1607 (± 104)	45.2 (± 0.29)	45.8 (± 0.93)	27.6 (± 3.6)	27.9 (± 5.0)
Virgin – PA12	1402 (± 118)	1307 (± 117)	43.0 (± 0.14)	43.2 (± 0.08)	23.3 (± 2.8)	17.7 (± 1.9)
PrimePart	101 (± 29)	87 (± 15)	9.2 (± 0.23)	9.5 (± 0.07)	197.0 (± 19.0)	217.3 (± 18.6)

(a)



(b)



(c)

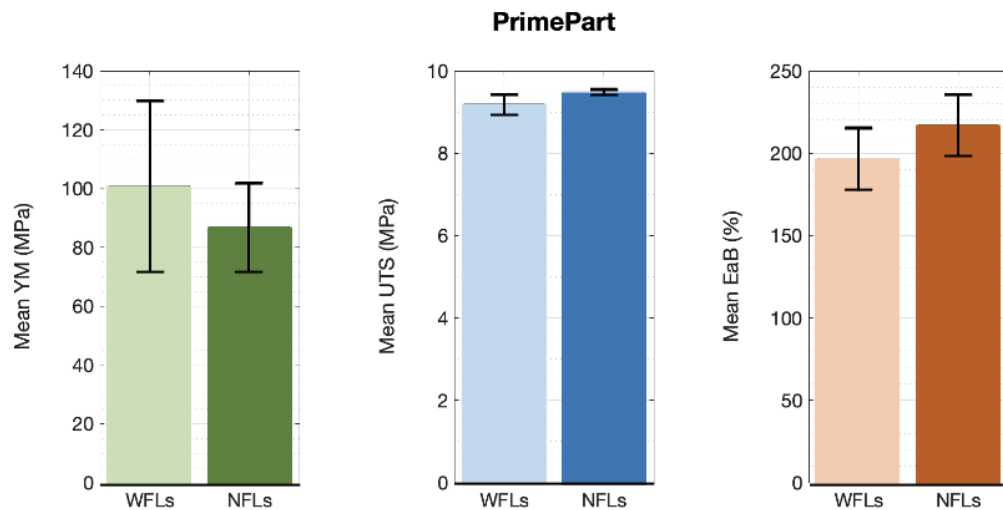


Figure 6.17 – A comparison between the Young’s Modulus, Ultimate Tensile Strength and Elongation at break of (a) 50/50 – PA12, (b) virgin – PA12 and (c) PrimePart samples built with and without finish layers (as denoted by the abbreviations WFLs and NFLs, respectively).

6.3.2.3 Industrial Significance

In addition to significantly reducing the top surface heights of parts produced, building without finish layers could also increase LS process profitability by reducing energy usage, material requirements and build times.

An estimated breakdown of the material costs incurred when depositing PA12 finish layers on a variety of LS systems is provided in **Table 6.13**. The following assumptions were made when performing this analysis:

- Finish layer powder bed densities of 0.432 gcm^{-3} are attained, in agreement with Ruesenberg and Schmid [188].
- The cost of PA12 supplied by EOS GmbH and Formlabs [189] (excl. VAT) is equal to 45.50 £GBP/kg and 81.60 £GBP/kg, respectively. Though, in practice these material costs will vary depending on a range of factors.
- Material refresh ratios of 50% are implemented.
- 40 finish layers are deposited on top of the final build layer, with layer thicknesses of $100\mu\text{m}$ and $110\mu\text{m}$ selected for EOS and Formlabs systems, respectively.
- LS systems are operational 5 days a week, 52 weeks per annum.

Table 6.13

A forecast of annual finish layer material costs incurred when processing PA12 on a variety of LS systems.

LS System	LS System build volume, (W × D × H), (mm × mm × mm)	Finish layer material mass (g)	Finish layer material cost (£GBP)	Annual finish layer material cost for 1, 2 and 3 builds a day (£GBP)		
				1	2	3
Formlabs Fuse 1	165 x 165 x 300	51.75	2.11	549	1097	1646
EOS P100	170 x 220 x 290	64.63	1.47	382	764	1146
EOS P770	700 x 380 x 580	459.65	10.46	2720	5440	8160

As outlined in **Table 6.13**, the annual cost of depositing finish layers is relatively insignificant, particularly when compared to the initial cost of each LS system.

However, when the time taken to deposit finish layers is instead considered, their impact on LS process productivity is evidently more considerable. More specifically, the LS machine used throughout this doctoral work took 19 minutes to deposit 40 finish layers. Therefore, if the afore assumptions are again followed, the total time taken to deposit finish layers on an industrial EOS P100 system with a production rate of 1, 2 and 3 builds per day would equate to 82, 165 and 247 hours annually (approximately 2, 4 and 6 standard works per year), respectively.

6.4 Conclusions

The work presented in this chapter investigated the extent to which the mechanisms of polymer melt viscous flow and finish layer powder particle adhesion determine the top surface topographies of laser sintered PA12 components.

From the DoE, it was ascertained that top surface S_q and S_{sk} roughness results were inversely related to one another, and both principally influenced by beam spacing. Furthermore, the laser parameter configuration [ABC], akin to the term energy density, was found to have a statistically insignificant effect on the top surface S_q roughness of samples produced. Regression expressions were generated to model the top surface heights and peak / valley distributions of the samples produced. Model optimised laser parameters reduced the mean S_q roughness of resultant topographies by 30.8% relative to standard 50/50 – PA12 top surfaces. However, validation results highlighted the limited accuracy of each regression model in predicting new responses.

In conformity with the hypothesis proposed in **Chapter 5**, finish layer deposition had a significant effect on the top surface topographies of 50/50 – PA12, virgin – PA12 and PrimePart samples evaluated. More specifically, when standard laser parameters were employed, building without finish layers reduced the mean top surface heights of

50/50-PA12 and virgin – PA12 samples by 47.9% and 69.0%, respectively, and transformed their top surface symmetries such that they were instead dominated by pore-like features ($S_{sk} < 0$).

Additionally, tensile testing demonstrated that there were no apparent differences in the mechanical properties of alike material samples built with and without finish layers. This prompted consideration of the applied gains in LS process productivity attainable if the action of depositing finish layers was made redundant.

Chapter 7

The Transient Sliding Behaviours of Laser Sintered Polyamide-12 Components

Chapter Summary

Work presented in this chapter aimed to characterise the friction and wear properties of laser sintered PA12 surfaces during running-in. Accordingly, sliding and scratch tests were performed on both the top and bottom surfaces of 50/50 – PA12 samples to determine whether any of the previously discerned differences in surface topography, specifically Skewness, affected their transient sliding behaviours. Additionally, resultant wear data was compared with Ratner-Lancaster approximations, and Focus Variation microscopy was employed to identify any transfer film formation during testing.

7.1 Introduction

Upon initial dynamic contact, interfacing surfaces undergo a process of running-in. During this regime, the friction and wear behaviours incurred typically differ from those experienced during steady-state sliding [157]. Despite only occurring for a finite period, it is important to characterise these transient sliding behaviours as they have been shown to affect the long-term performance of a range of mechanical contacts [123,190], particularly those which involve polymers [191].

Furthermore, it is well documented that polymer surfaces experience augmented levels of wear during running-in [192]. Consequently, greater magnitudes of material transfer and subsequent film formation are likely to ensue within polymer-metal contacts [193]. However, despite transient wear phenomena being relatively well understood, to the best of the author's knowledge, there remains to be limited literature pertaining to the frictional running-in behaviours of polymer surfaces.

Additionally, it was previously highlighted in **Chapter 5** that laser sintered PA12 components have anisotropic surface symmetries and pronounced surface heights, particularly when compared with moulded part surfaces. Therefore, a dedicated program of work was carried out to characterise the specific friction and wear behaviours exhibited by top and bottom laser sintered PA12 surfaces during running-in.

7.2 Materials and Methods

7.2.1 Materials

Prior to LS processing, 50/50 – PA12 powder batches were blended for approximately 20 minutes by rotary tumbling.

7.2.1.1 Specimens

Laser sintered specimens included those designated for sliding and scratch testing. The specific geometries of each are detailed in **Figure 4.9** and **Figure 7.1a**, respectively.

7.2.2 Methods

7.2.2.1 Laser Sintering

Standard PA12 parameters were employed during LS, as outlined in **Table 4.3**. After build completion and subsequent cooling, compressed air was used to remove loose powder particles from all sample surfaces.

7.2.2.2 Surface Analysis

In accordance with the procedure specified in **Section 4.2.2.2**, FV microscopy was employed to determine surface roughness, as well as characterise pin and disk surfaces during sliding. More specifically, the latter involved capturing any incremental changes in wear scar geometry and transferred polymer material during wear focussed testing.

7.2.2.3 Friction and Wear Testing

Ball-on-flat, pin-on-disk, uni-directional sliding tests were performed, specifically via ‘configuration 1’ (stainless steel pin on polymer disk), in accordance with the process detailed in **Section 4.2.2.3**. More specifically, these sliding tests were performed at a constant speed of 0.35ms^{-1} , over a distance of 100m, and at three different applied normal loads of 10N, 15N and 20N. These sliding speed and normal load values were chosen because they fell within the mid-range of the operating conditions previously employed within the literature, as outlined in **Table 3.3**.

Friction

During friction focussed testing, friction force (F_f) was captured by load sensors within the UMT and then normalised by normal load (N) to obtain coefficient of friction (COF) data. To ensure that the findings discerned were reliable, each sliding test was repeated on three different samples for every normal load and surface orientation evaluated.

Wear

Interrupted sliding tests were also carried out to characterise the changes in wear rate encountered during running-in. More specifically, mass loss measurements were performed every 5m, from commencement to 75m, as well as upon test completion. At each interval, a Sartorius Basic Plus BP210D analytical balance with a 0.1mg readability was used to weigh each polymer disk to establish mean mass loss measurements from three repeat readings. Ultimately, volume loss values were then obtained by dividing each Δm_{mean} measurement by a ρ value of 0.97 g/cm³ (the mean density of the laser sintered 50/50 – PA12 samples produced for this work). Specific wear rate results were then computed using **Equation 4.2**.

Laser Sintered PA12 Top and Bottom Surface Topographies

Both top and bottom laser sintered PA12 disk surfaces were evaluated to elucidate whether any differences in surface topography, specifically [Skewness](#), affected their friction and wear behaviours during running-in.

Table 7.1 details the mean S_q and S_{sk} roughnesses of the top and bottom disk surfaces used within this study.

Table 7.1

The mean S_q and S_{sk} roughnesses, and corresponding standard deviations, of the top and bottom laser sintered disk surfaces used within this study.

Surface orientation	S_q (μm)	S_{sk}
Top	14.99 ± 0.57	0.41 ± 0.09
Bottom	16.46 ± 1.01	-0.08 ± 0.13

7.2.2.4 Scratch Testing

Scratch testing was carried out to primarily determine whether laser sintered PA12 components exhibit any orientation dependent sub-surface microstructural differences. This was achieved by comparing the relationships between applied normal load and penetration depth (d_p) during the scratching of top and bottom surfaces.

Two repeat scratches were carried out on the top and bottom surfaces of different block-type samples, as shown in **Figure 7.1b**.

Due to limited resources and the restrictions of the machine, it was not possible to adhere to specific scratch testing related guideline outlined in ISO or ASTM standards. Therefore, this test procedure was instead followed as it best enabled the fundamental theory pertinent to this study to be investigated.

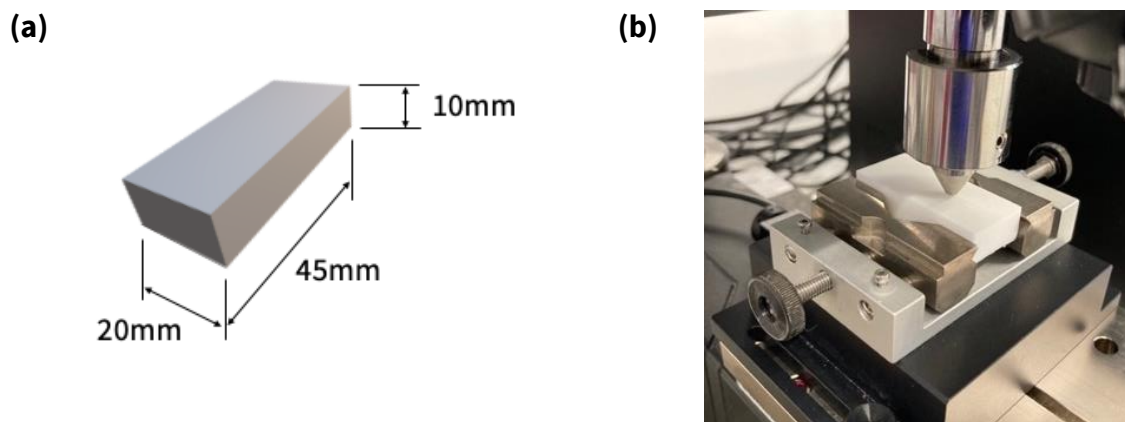


Figure 7.1 – (a) the geometry of the scratch test specimens, as well as a (b) scratch test in progress.

7.3 Results and Discussion

7.3.1 Friction

The mean COF response recorded during each friction-focussed sliding test can be seen in **Figure 7.2**.

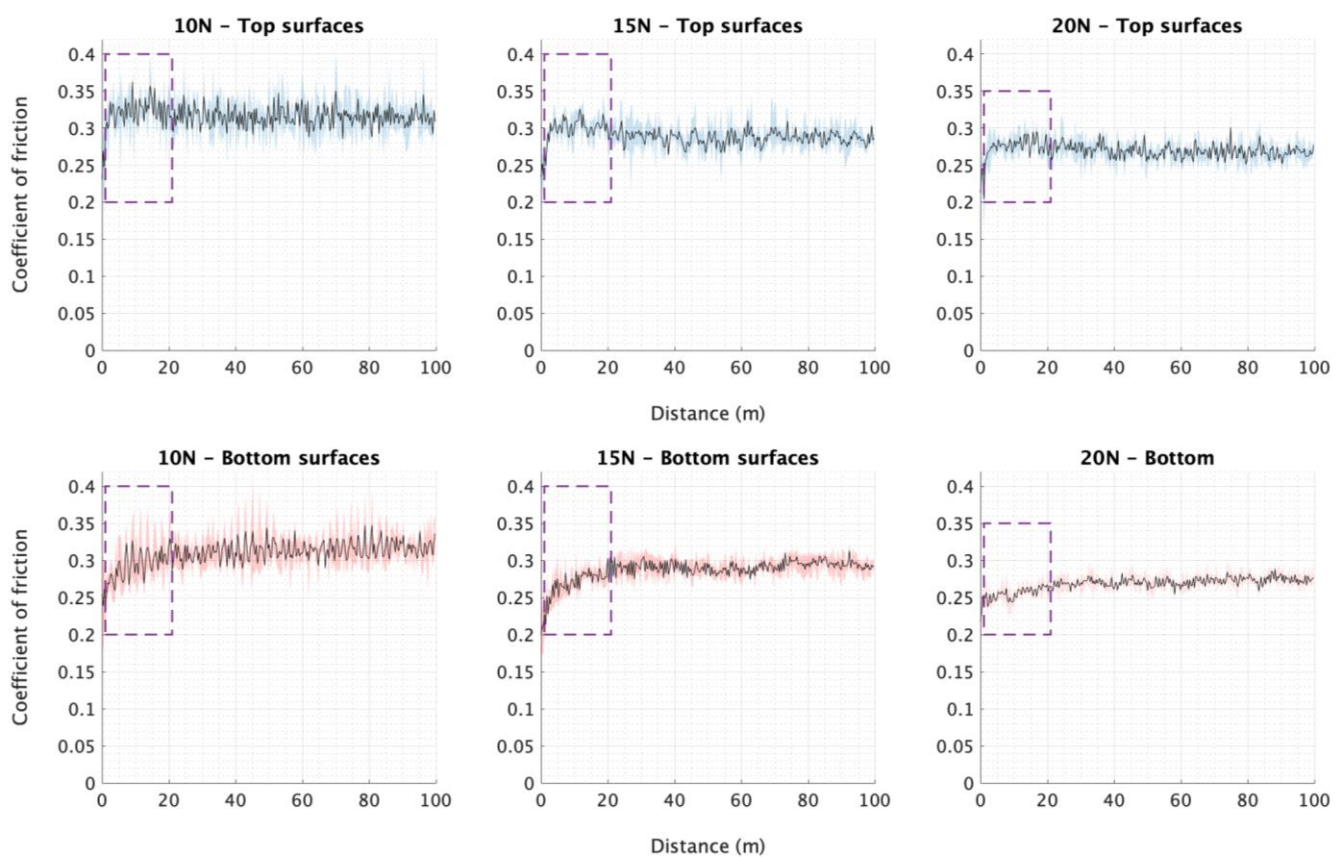


Figure 7.2 – The mean COF responses recorded during 10N, 15N and 20N sliding on the top and bottom surfaces of each of the three laser sintered 50/50-PA12 samples evaluated. The highlighted regions within each mean response plot represents the maximum and minimum values recorded. The areas within each dashed purple sector draw attention to the distances and magnitudes over which COF differed as a result of surface orientation specifically.

As shown in **Figure 7.2**, laser sintered PA12 bottom surfaces were found to experience relatively conventional running-in periods [157,194,195], as indicated by the plateauing increases in COF incurred during the first 20m of sliding. These transient increases in friction will have been concomitant with the penetration depth of the pin. More

specifically, greater magnitudes of friction will have been induced as the pin ploughed deeper into each bottom surface region, as illustrated in **Figure 7.3**. Accordingly, steady-state sliding will have commenced when entirely bulk surface material constrained both the lateral and normal path of the pin.

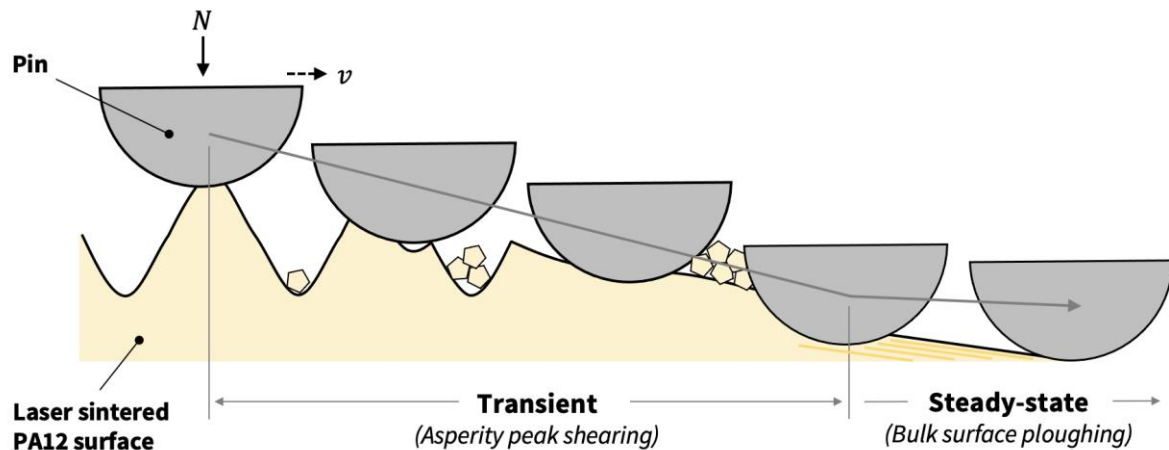


Figure 7.3 – An illustration highlighting the travel path of the pin during running-in.

Contrastingly, top surface COF responses were initially heightened during running-in, as can be seen within the dashed regions in **Figure 7.2**.

Though, as discussed in **Chapter 6**, laser sintered PA12 top surfaces are characteristically asperity peak dominated. This particular topographical attribute serves as a potential explanation as to why these surfaces encountered comparatively augmented levels of friction during the first 20m of sliding. It is likely that the presence of these asperity peaks will have initially increased the friction force incurred by the pin prior to them yielding / fracturing and subsequently being removed from the contact / the commencement of sub-surface ploughing.

Furthermore, it can be seen in **Figure 7.2** that both top and bottom laser sintered PA12 surfaces exhibited their transient frictional behaviours over similar running-in lengths – from test commencement to approximately 20m of continuous sliding. This further

supplements the proposed hypothesis that steady-state sliding ensued upon the onset of sub-surface ploughing.

7.3.1.1 Scratch Testing

The results from the scratch tests performed on the top and bottom surfaces of different laser sintered PA12 samples can be seen in **Figure 7.4**.

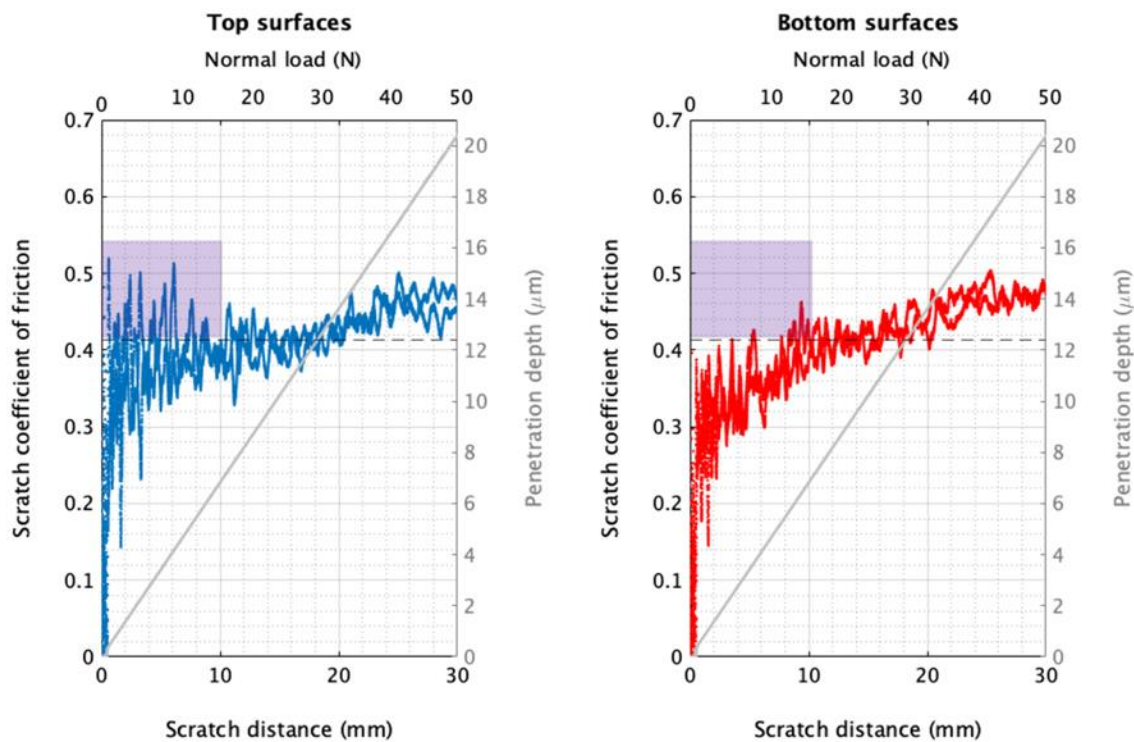


Figure 7.4 – Scratch coefficient of friction (SCOF) and indenter penetration depth data as a function of scratch distance and applied normal load for each top and bottom laser sintered PA12 surface evaluated. Highlighted regions denote the distances and magnitudes over which top and bottom surface SCOF responses varied.

It can be seen in **Figure 7.4** that both top and bottom surfaces supported the progressively applied normal loads relatively identically, as indicated by their alike penetration depth responses relative to N . This suggests that the differences in initial COF response observed in **Figure 7.2** were not induced as a result of any potential differences in sub-surface microstructure. This also supports the hypothesis that steady-state sliding

ensued upon the onset of sub-surface ploughing, and that this behaviour occurred at a similar sliding distance for both top and bottom laser sintered PA12 surfaces.

In agreement with the COF results presented in **Figure 7.2**, top and bottom laser sintered PA12 surfaces exhibited different initial scratch coefficient of friction (SCOF) responses, as can be seen in the highlighted regions in **Figure 7.4**. This reaffirms that laser sintered PA12 top surfaces incurred higher levels of friction during running-in due to the increased presence of asperity peaks ($S_{sk} > 0$).

Furthermore, at penetration depths greater than $12.5\mu\text{m}$ ($d_p > |12.5\mu\text{m}|$), both top and bottom surfaces began to exhibit relatively similar SCOF responses. In concurrence with the S_q roughness data presented in **Table 7.1**, this critical penetration depth marked the onset of sub-surface ploughing, when $d_p \geq S_q/2$, and ultimately the transition from transient to steady-state sliding.

7.3.2 Wear

Figure 7.5 and **Figure 7.6** show the results obtained from each interrupted sliding test. Typical running-in regimes can be seen, as indicated by plateauing wear rate and volume loss curves. During this regime, asperity peak shearing dominated, resulting in greater initial wear magnitudes prior to the onset of steady-state sliding and subsequent bulk surface ploughing.

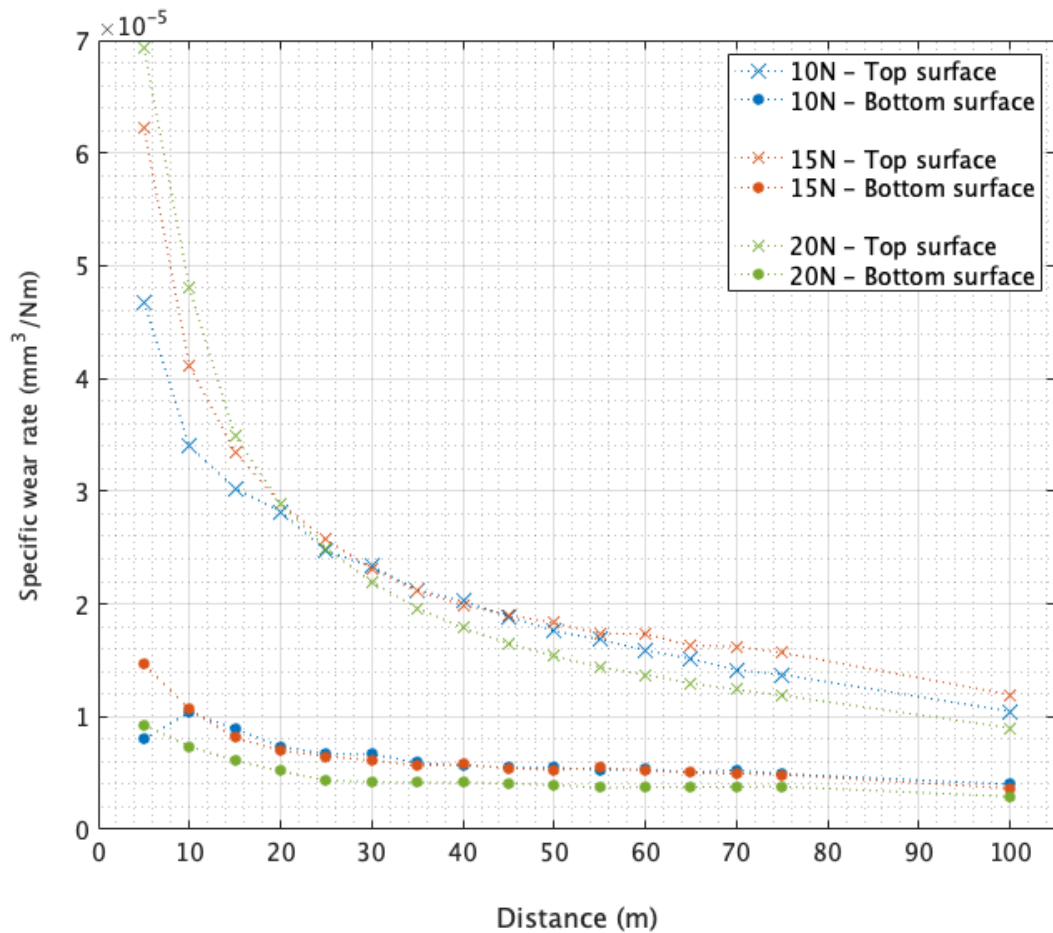


Figure 7.5 – The changes in specific wear rate of top and bottom laser sintered PA12 surfaces during running-in.

In accordance with the results presented in **Section 7.3.1**, asperity peak prevalence was also found to influence wear. More specifically, laser sintered PA12 top surfaces generated comparatively greater amounts of wear debris, and thus had larger resultant wear rates, than bottom surfaces from the same samples.

It was ascertained previously in **Chapter 6** that finish layer powder particle adhesion is the mechanism by which asperity peaks are formed within laser sintered PA12 top surfaces. This adhesion is not an intended requisite of the LS build process; therefore, these asperity peaks are likely to have intrinsically weak cohesive strengths and readily fracture during sliding.

Correspondingly, it is important to consider surface orientation when implementing laser sintered PA12 components within real-world tribosystems. For example, within highly conformal contacts (in which resultant wear debris may not be able to escape), it may be more apt to use bottom, rather than top, surfaces at the sliding interface to reduce the occurrence of 3rd body abrasion and /or adhesive wear [196].

7.3.2.1 Predicting Wear

As discussed in **Chapter 3**, specifically **Section 2.5.3.2**, the Ratner-Lancaster expression was derived to model the abrasive wear rate of polymers⁸.

Accordingly, **Figure 7.6** compares measured wear volume data with model approximations. More specifically, the original Ratner-Lancaster expression was used to calculate laser sintered PA12 bottom surface approximations, whereas a modified version was used to predict equivalent values for laser sintered PA12 top surfaces. The latter included a Skewness term to account for the aforementioned augmented magnitudes of asperity peak fracture incurred during running-in. This modified Ratner-Lancaster expression is detailed in **Equation 7.1** below:

$$V_{abr(mod)} = \frac{\mu \cdot N \cdot x}{H_{Shore D} (\sigma_b \cdot \varepsilon_b) S_{sk}}$$

Equation 7.1

The specific values used when calculating abrasive wear volume approximations via the original and modified Ratner-Lancaster expression are given in **Table 7.2**.

⁸ For reference, this expression is detailed in **Equation 2.15**.

Table 7.2

The specific values used to compute abrasive wear volume approximations via original and modified Ratner-Lancaster expressions, as well as their sources of ascertainment.

Variable		Value	Source of ascertainment
Symbol	Description		
μ	Coefficient of friction	Incrementally determined during each sliding test	Section 7.3.1
N	Normal load (N)	10N, 15N and 20N	Predetermined
x	Sliding distance (m)	5m – 75m (every 5m increment) + 100m (test completion)	Predetermined
$H_{Shore D}$	Shore D hardness	75	Material manufacturer data sheet [171]
σ_b	Break stress (MPa)	40.2	Chapter 6
ε_b	Elongation at break (%)	27.6	Chapter 6
S_{sk}	Skewness	0.414 (Mean top surface S_{sk})	Table 7.1

The scratch testing data presented in **Figure 7.4** showed that top and bottom laser sintered PA12 surfaces exhibited alike penetration depth responses relative to N , which reaffirms that it was apt to use the same hardness value for both surface orientations. Despite the majority of asperity peaks being removed relatively quickly during testing (as shown in **Figure 7.7** and **Figure 7.8**), their increased presence on laser sintered PA12 top surfaces still impacted mass loss measurements as their wear scar widths increased.

As shown in **Figure 7.6**, a strong congruency was observed when comparing measured wear volume data with approximations calculated using the original and modified Ratner-Lancaster expression. Though, this correlation was discerned to be stronger for Gaussian bottom surfaces than peak dominated top surfaces. The linearity of both Ratner-Lancaster expressions does not account for the change in material removal as wear transitioned from occurring primarily by asperity peak shearing (transient) to bulk surface ploughing (steady-state). The former will have induced greater amounts of wear debris initially, in agreement with the plateauing measured volume loss responses exhibited by laser sintered PA12 top surfaces in **Figure 7.6a**.

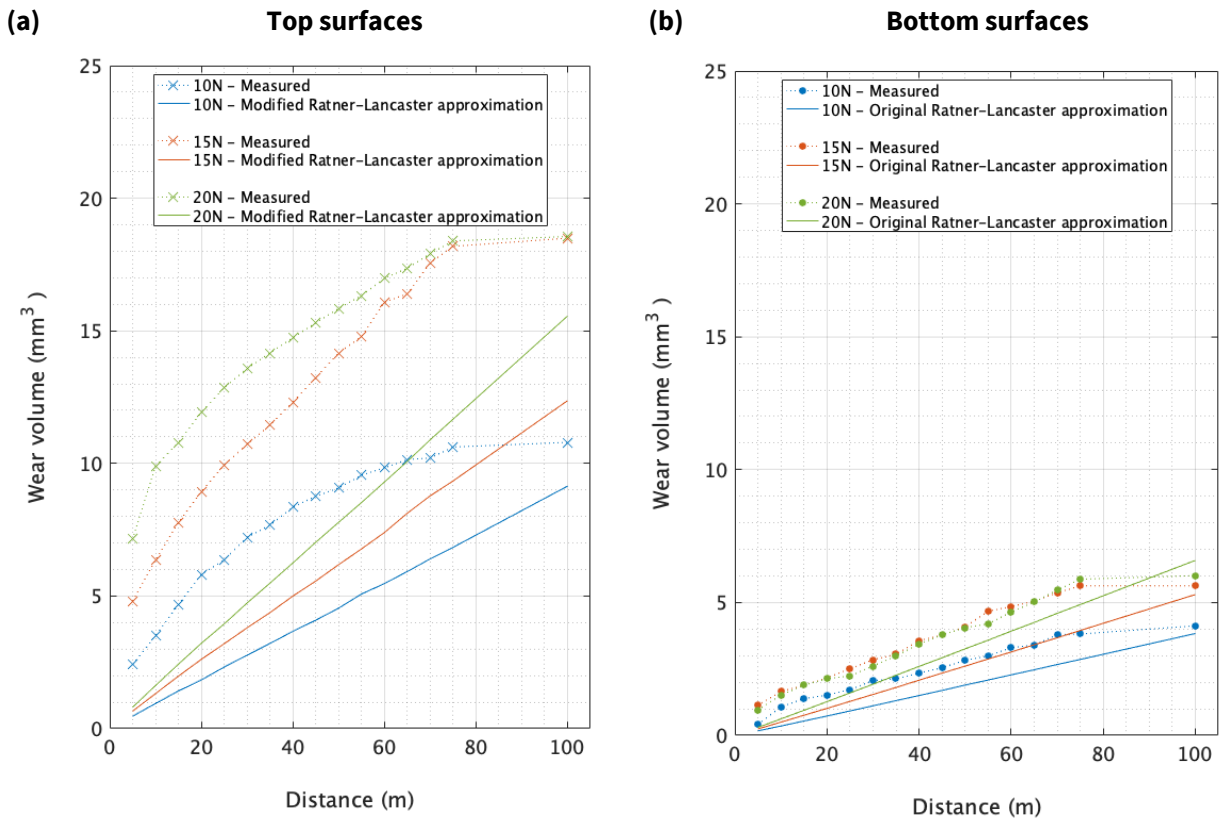


Figure 7.6 – Empirically determined wear volume data and corresponding V_{abr} approximations (calculated via the aforementioned modified and original Ratner-Lancaster expressions) for each laser sintered PA12 **(a)** top and **(b)** bottom surface evaluated. V_{abr} approximations are plotted at the same distance intervals as the measured data.

7.3.2.2 Material Transfer

As mentioned in **Section 7.2.2.2**, each contacts progression through the transient regime was characterised by FV microscopy. Scan images of pin and disk top and bottom surfaces during each 15N sliding test can be seen in **Figure 7.7** and **Figure 7.8**, respectively. Additionally, scan images recorded during every other configuration of sliding test are given in **Appendix B**.

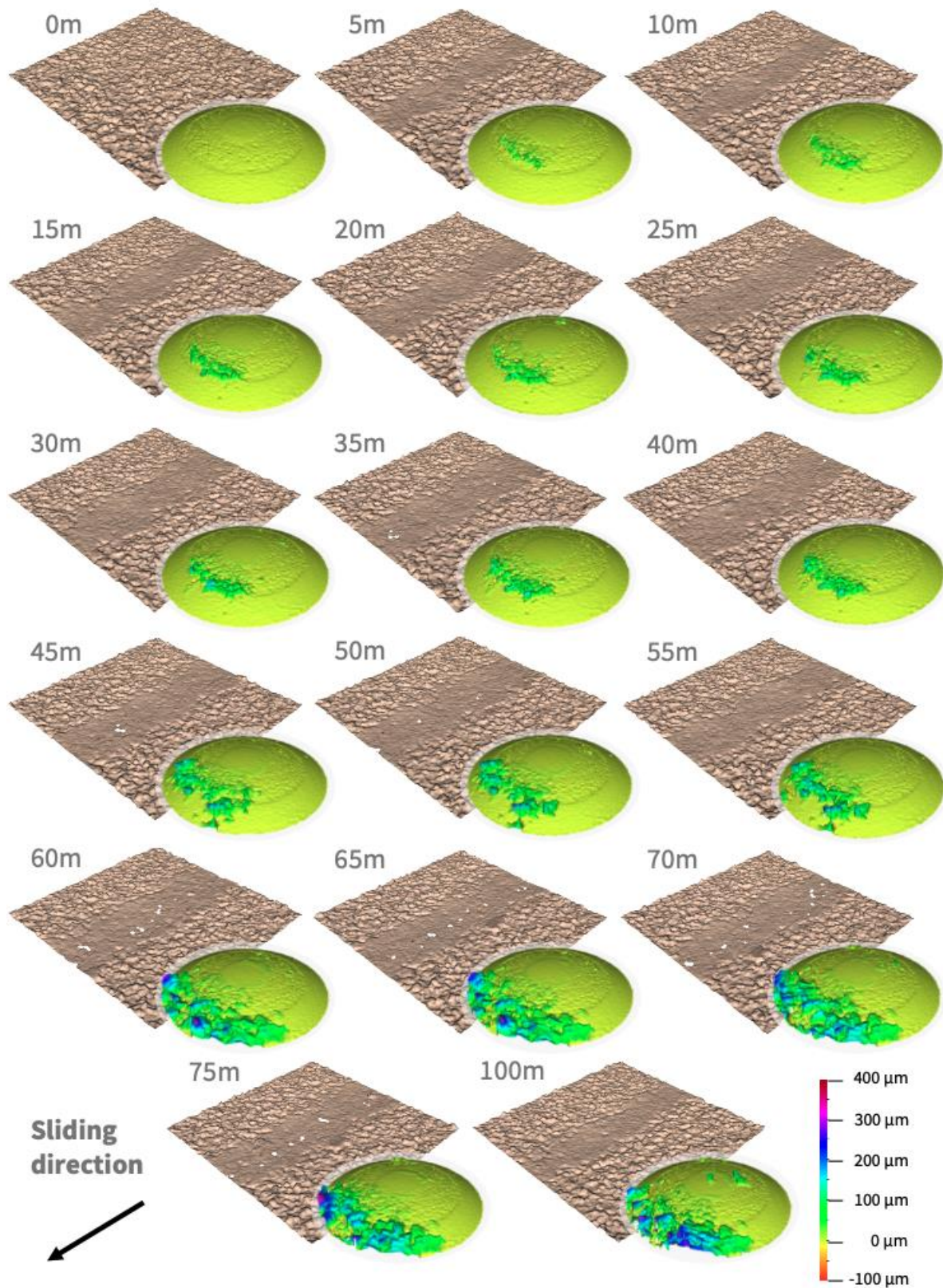


Figure 7.7 – Resultant pin and disk top surfaces at each interval during 15N sliding.

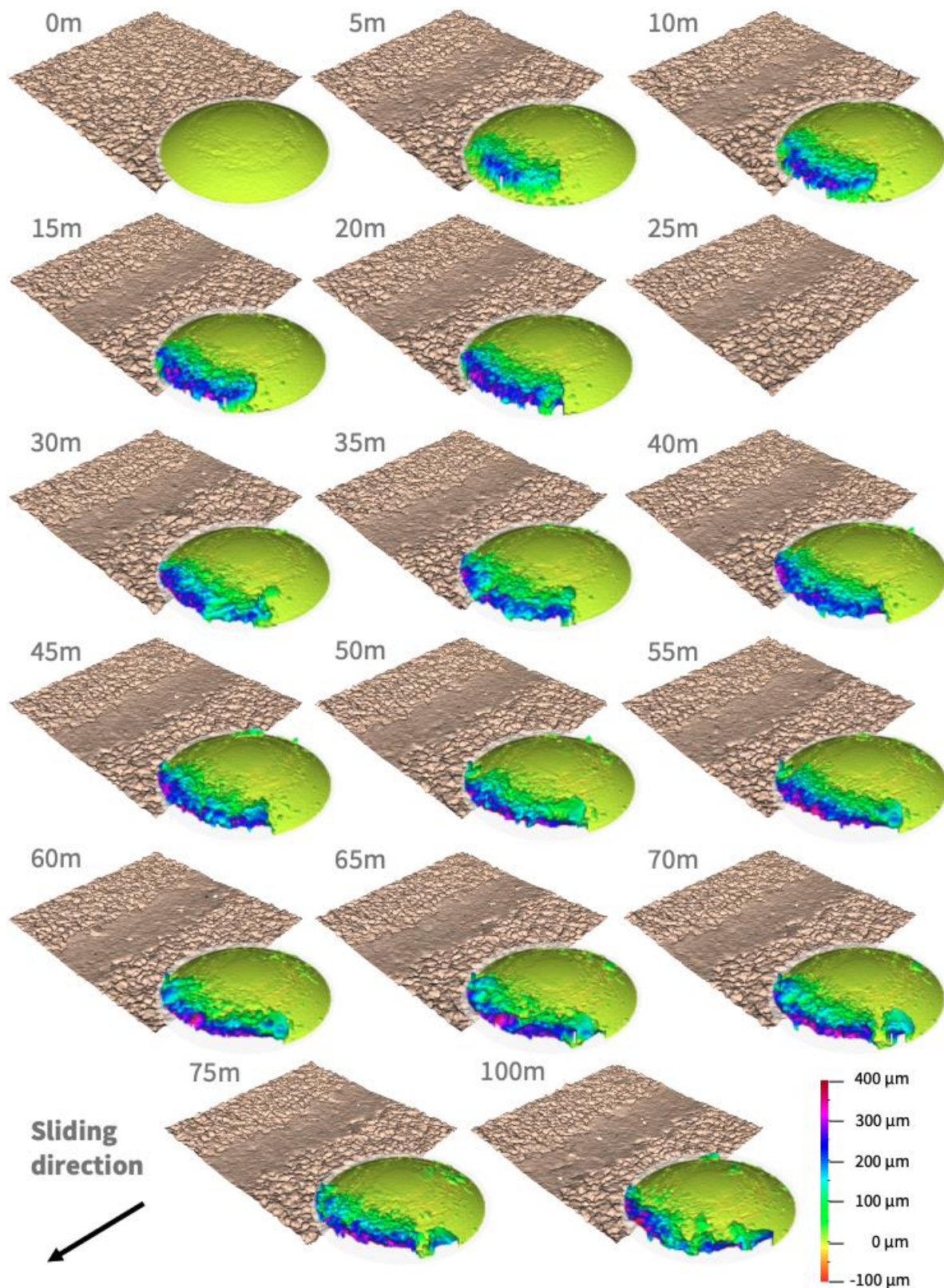


Figure 7.8 – Resultant pin and disk bottom surfaces at each interval during 15N sliding. Please note that the 25m pin sample surface could not be accurately characterised due to an unfamiliar software-related misalignment error when executing the difference measurement.

Qualitatively, it can be seen in both **Figure 7.7** and **Figure 7.8**, as well as in **Appendix B**, that polymer wear debris did transfer to the surface of the pin during running-in. More generally, the magnitude and morphology of this transferred polymer material was analogous, and no apparent correlations between applied normal load and counterface surface orientation could be discerned. However, no transfer film was formed, as there was no wear debris present within the contact areas of each pin surface during sliding. In practice, wear debris was found to adhere tentatively to the leading edge of the pin, as indicated by the loose, grain-like morphologies visible in **Figure 7.7** and **Figure 7.8**.

However, the incremental nature of this test method did not permit frictional heating to be considered, which may have been prerequisite to transfer film formation. Therefore, both of these aspects were investigated further in **Chapter 8** and **Chapter 9**.

7.4 Conclusions

In this chapter, sliding and scratch tests were performed to characterise the friction and wear behaviours of top and bottom laser sintered PA12 surfaces during running-in.

When analysing friction, bottom surfaces incurred conventional running-in periods concomitant with the penetration depth of the pin, whereas top surfaces were found to initially experience relatively heightened magnitudes of friction during the first 20m of sliding. Subsequent scratch testing validated that these orientation-dependent variations in friction were due to differences in surface topography, specifically Skewness. Additionally, it was ascertained that the onset of sub-surface ploughing marked the transition from transient to steady-state sliding.

Skewness was also found to influence wear. More specifically, laser sintered PA12 top surfaces incurred comparatively greater magnitudes of wear than bottom surfaces from the same samples. Furthermore, original and modified Ratner-Lancaster expressions were discerned to approximate these abrasive wear volume losses with a reasonable degree of accuracy.

Transfer film formation was not observed at any point during this study. Though, this may have been due to the lack of consideration for frictional heating as a result of the test methodology adopted.

Chapter 8

The Influence of Normal Load, Sliding Speed and Contact Configuration on the Friction and Wear Properties of Laser Sintered Polyamide-12 Components

Chapter Summary

This chapter investigated how the sliding behaviours of laser sintered PA12 components were affected by varying operating conditions. More specifically, sliding tests were performed in accordance with a Design of Experiments (DoE) to ascertain the extent by which normal load, sliding speed and contact configuration influenced the friction and wear properties of parts produced. Results were characterised both quantitatively and qualitatively, which enabled statistically significant effects and corresponding sliding phenomena to be identified, respectively.

8.1 Introduction

It is well recognised that the friction and wear properties of contacting bodies are dependent on the operating conditions employed during sliding. More specifically, pertinent operating conditions include normal load; sliding speed; contact configuration; sliding distance; sliding motion; and the environment (i.e. dry or lubricated) / atmosphere (i.e. temperature and humidity) in which sliding occurs.

Existing research [135,147,148] indicates that laser sintered PA12 components are also sensitive to the operating conditions employed during sliding. However, the specific mechanisms that determine these behaviours, particularly those pertaining to wear, have yet to be comprehensively reported in the literature.

Furthermore, as previously discussed in **Chapter 1**, the adoption of laser sintered polymer components for end-use applications remains hindered due to concerns regarding their in-service capabilities.

Accordingly, this work investigated the extent by which normal load, sliding speed and contact configuration (specifically the configuration in which samples were loaded against one another) affected the friction and wear properties of laser sintered PA12 components.

8.2 Materials and Methods

8.2.1 Materials

To best emulate conventional practice, 50/50 – PA12 was employed throughout this study. All samples were manufactured from the same batch of powder, which was blended for approximately 20 minutes by rotary tumbling prior to processing by LS.

8.2.2 Specimens

Specimens comprised of pin- and disk- type geometries, with the same dimensions as those previously detailed in **Chapter 4**, specifically **Figure 4.9a**. These included both laser sintered 50/50 – PA12 and steel / stainless steel samples, as shown in **Table 8.1**.

Table 8.1

An overview of the pin and disk specimens used within this study.

Sample properties	Pin samples		Disk samples	
	Lasers sintered 50/50 – PA12	Stainless steel	Lasers sintered 50/50 – PA12	Steel
Major dimensions	SØ = 6.75mm	SØ = 6.75mm	Diameter = 80mm, Thickness = 5mm	Diameter = 80mm, Thickness = 5mm
Number of Samples	67	12	4	2
Surface preparation Method	None	Polishing	None	Surface grinding

Laser sintered polymer samples were manufactured in a single build, using standard PA12 parameters (detailed in **Table 4.3**), and once fully cooled were post-processed with compressed air to dislodge any loose powder particles from their surfaces.

Sliding tests were performed on the top surfaces of polymer disk samples. Resultant topographies had mean S_q and S_{sk} roughness values of $16.65\mu\text{m}$ ($SD = \pm 1.25\mu\text{m}$) and 0.410 ($SD = \pm 0.079$), respectively. These values were congruous with the laser sintered 50/50 – PA12 top surfaces analysed in **Chapter 6**.

Information pertinent to the material and preparation details of the steel disk samples used in this study is outlined in **Section 4.2.2.6**.

Due to their spherical geometries, the surfaces of both the polymer and stainless steel pin samples could not be quantitatively characterised. Though, it is expected that the

topographies of the former will have been similar to the top surfaces of the 50/50 – PA12 disk samples, as they were produced in the same build. Contrastingly, polished stainless-steel pins will have likely had isotropic surface roughness' with an R_a value of $<1\mu\text{m}$, in agreement with related topographies reported within the literature [197].

Furthermore, polymer and metal pin samples were only used once, whereas both sets of disk samples were reused during testing. Though, it should be noted that polymer wear tracks were concentrically well-spaced, and each steel disk was reground prior to testing to remove any contaminants, such as oxide formations and previously transferred polymer material.

For improved readability, laser sintered 50/50 – PA12, and both stainless steel and steel specimens, will hereinafter be referred to as polymer and metal samples, respectively.

8.2.3 Experimental Procedure

A 2^3 full factorial DoE was performed to ascertain the extent to which the friction and wear properties of resultant samples were affected by varying operating conditions. Accordingly, low and high factors for normal load, sliding speed and contact configuration were employed, as detailed in **Table 8.2**. These operating conditions either ranged by an order of magnitude or were the opposite of one another. More specifically, values for normal load and sliding speed were selected based on the upper and lower limits previously employed within existing literature (outlined in **Table 8.3**), and converse contact configurations, as specified in **Figure 8.1**, were evaluated so that the effects of frictional heating could be investigated.

Table 8.2

The varying operating conditions employed as part of the DoE.

Operating condition	Low value (-1)	High value (1)
Normal load (N)	3	30
Sliding speed (ms^{-1})	0.05	0.5
Contact configuration	Metal pin / Polymer disk	Polymer pin / Metal disk

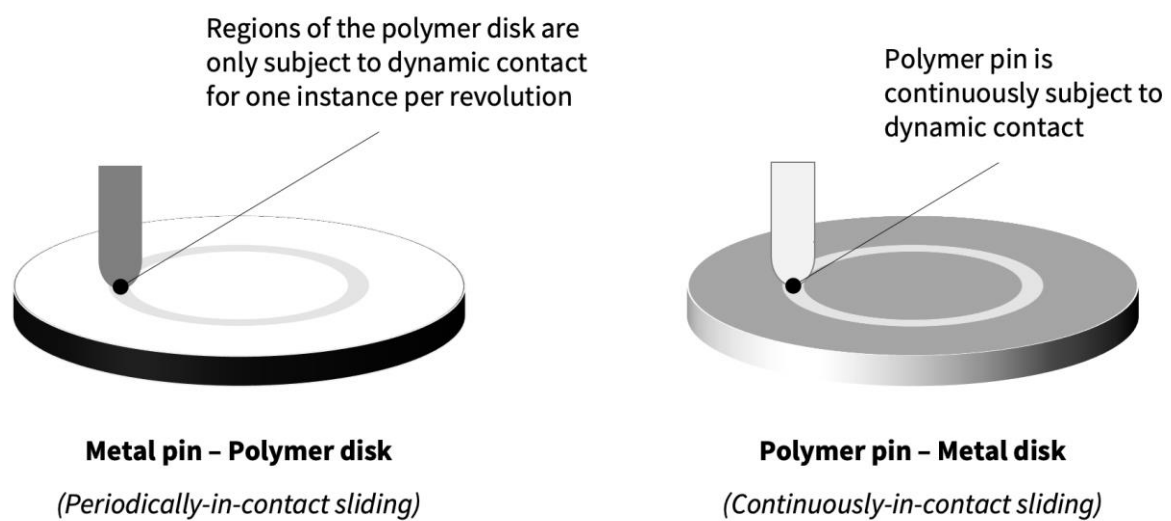


Figure 8.1 – The variations in polymer sliding intrinsically induced by the different contact configurations employed during testing.

A total of 24 sliding tests, each covering a distance of 1000m, were performed as part of the DoE. This involved repeatedly evaluating the eight different sliding conditions outlined in **Table 8.3** three times.

Table 8.3

The different sliding conditions evaluated as part of the DoE.

Test configuration	A – Normal load	B – Sliding speed	C – Contact configuration
1	-1	-1	-1
2	-1	-1	1
3	-1	1	-1
4	-1	1	1
5	1	-1	-1
6	1	-1	1
7	1	1	-1
8	1	1	1

The statistical software package ‘Minitab’ was used to analyse the data obtained from the DoE. Results were deemed to be statistically significant when their p-values were less than a significance level (α) of 0.05.

8.2.4 Surface Analysis

Both SEM and FV microscopy were used to analyse pin and disk sample surfaces. These microscopy methods were executed in accordance with the procedures outlined in **Section 4.2.2.2**.

Though, in addition to the standard operating procedures previously defined in **Chapter 4**, disk surfaces were evaluated at north, east, south and west locations, as shown in **Figure 8.2**. Furthermore, when the resultant polymer pin worn areas were larger than the evaluation region of the SEM (at $\times 50$ magnification), the former were scanned at four locations (as outlined in **Figure 8.3**) and manually merged to form complete captures.

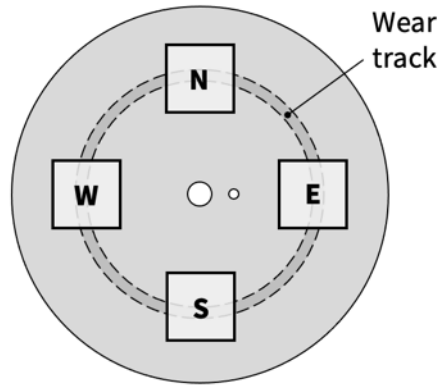


Figure 8.2 – The north, east, south and west locations evaluated on each disk surface post-testing.

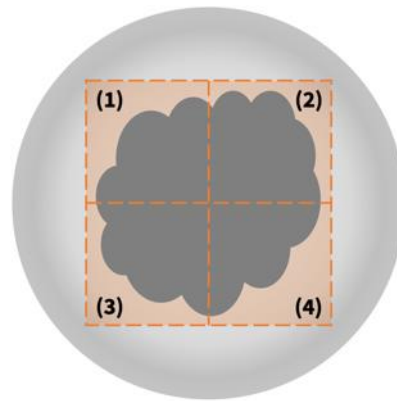


Figure 8.3 – The four quadrants scanned when polymer pin worn areas were larger than the evaluation region of the SEM (at $\times 50$ magnification).

8.2.5 Friction and Wear Testing

Following the procedure discussed in **Section 4.2.2.6**, ball-on-flat, pin-on-disk, uni-directional sliding tests were performed. These tests were carried out in accordance with the varying operating conditions outlined in **Table 8.3**.

As previously mentioned in **Section 8.1**, friction and wear were the dependent variables of interest within this study. Friction was characterised by friction force (F_f) and coefficient of friction (COF), which were both outputted directly from the ‘CETR’ UMT software post-testing. Wear, on the other hand, was described by wear rate (W), obtaining which first involved using FV microscopy or SEM to determine the widths / diameters of the wear

scars produced. With this information, volume loss values were then calculated via the corresponding methods outlined in **Table 4.6**, which subsequently enabled wear rate data to be computed using **Equation 4.1** and **Equation 4.2**.

8.3 Results and Discussion

8.3.1 Friction

As previously mentioned in **Section 8.2.5**, resultant friction responses were described by both F_f and COF. More specifically, F_f was utilised when explicitly analysing the extent to which normal load, sliding speed and contact configuration influenced friction, as its determination was not dependent on any of the operating conditions employed. COF, on the other hand, was adopted when characterising friction-related phenomena, such as frictional heating and variation in sliding, to facilitate the direct comparison of results obtained within this study with data reported in related literature.

The mean F_f and COF results determined for each of the eight different sliding conditions evaluated as part of the DoE are detailed in **Table 8.4** and **Table 8.5**, respectively. These values were calculated between the onset of steady-state sliding and test completion, as specified within each of the mean response plots presented throughout **Section 8.3.1.1**.

Table 8.4

The mean F_f results, and corresponding standard deviation values, determined for each of the sliding conditions evaluated as part of the DoE. Standard deviation values indicate the variation between repeat tests.

Contact configuration	Friction force (N)			
	3N – 0.05ms ⁻¹	3N – 0.5ms ⁻¹	30N – 0.05ms ⁻¹	30N – 0.5ms ⁻¹
Metal pin – Polymer disk	0.810 ± 0.039	1.040 ± 0.067	7.423 ± 0.031	7.752 ± 0.457
Polymer pin – Metal disk	0.948 ± 0.212	1.009 ± 0.040	10.024 ± 0.256	11.112 ± 0.260

Table 8.5

The mean COF results, and corresponding standard deviation values, determined for each of the sliding conditions evaluated as part of the DoE. Standard deviation values indicate the variation between repeat tests.

Contact configuration	Coefficient of friction			
	3N – 0.05ms ⁻¹	3N – 0.5ms ⁻¹	30N – 0.05ms ⁻¹	30N – 0.5ms ⁻¹
Metal pin – Polymer disk	0.288 ± 0.020	0.352 ± 0.022	0.248 ± 0.002	0.261 ± 0.016
Polymer pin – Metal disk	0.316 ± 0.071	0.336 ± 0.012	0.334 ± 0.009	0.371 ± 0.009

As shown in **Figure 8.4**, the mean COF values presented in **Table 8.5** are in good agreement with data collated in **Table 3.3** – In which the COF results from related literature were summarised. Additionally, the variations in COF results between repeat tests were found to be relatively small, particularly when compared with the in-laboratory variation values intrinsically expected during tribological testing [198].

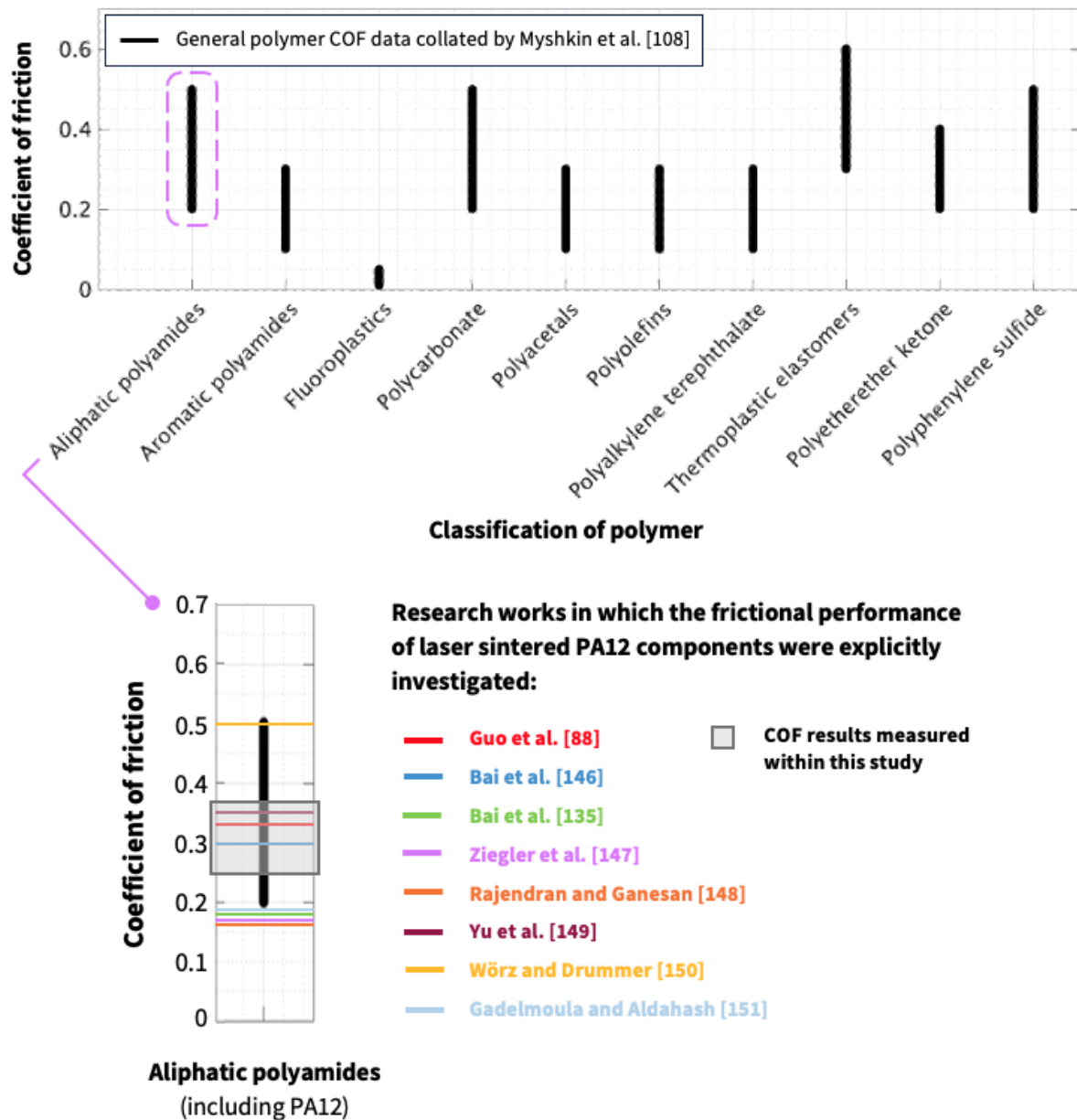


Figure 8.4 – A comparison between the COF results determined within this study with those collated from literature and previously presented in **Chapter 3**, specifically **Table 3.3**

8.3.1.1 Friction Responses

This section includes the mean COF and F_f responses recorded during each of the sliding conditions evaluated as part of the DoE. The individual responses recorded when conducting each repeat test can be seen in **Appendix C**.

During metal pin on polymer disk sliding, regions of the latter were subject to dynamic contact for only one instance per revolution, as illustrated in **Figure 8.1**.

$3\text{N} - 0.05\text{ms}^{-1}$ / Low Load – Low Speed

Figure 8.5 shows the mean COF and F_f responses recorded during $3\text{N} - 0.05\text{ms}^{-1}$, metal pin on polymer disk sliding.

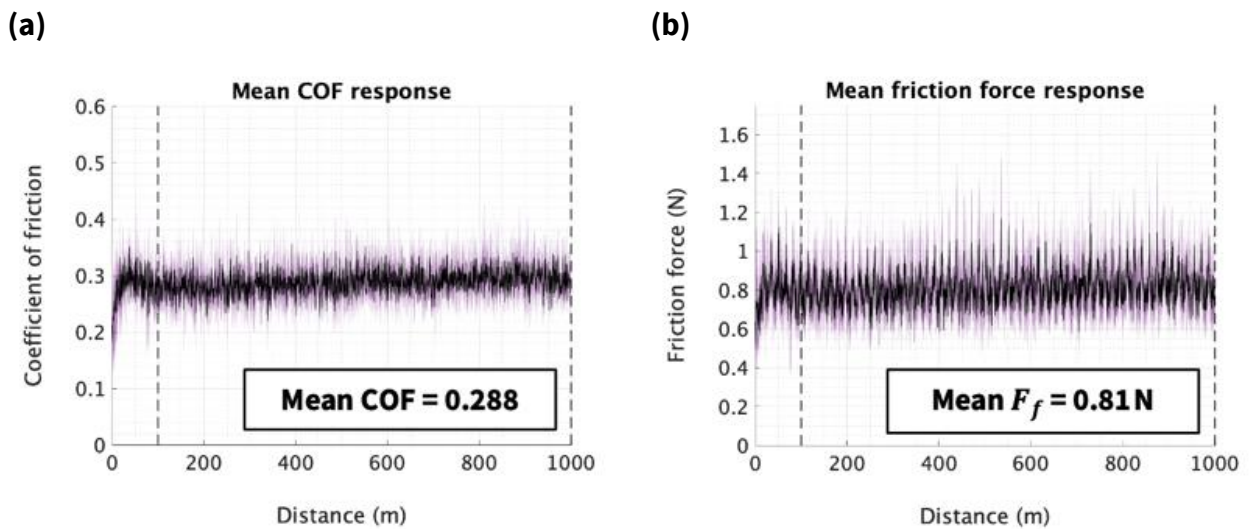


Figure 8.5 – The mean (a) COF and (b) friction force responses recorded during $3\text{N} - 0.05\text{ms}^{-1}$ (low load / low speed), metal pin on polymer disk sliding. The highlighted regions within each response plot represents the maximum and minimum values recorded. The distance between dashed vertical lines within the former indicates the period over which mean COF and F_f values were calculated.

As shown in **Figure 8.5**, low load / low speed sliding induced relatively large variations in COF. These fluctuations were concomitant with the method by which the 3N normal loads were supported during sliding, which is discussed in greater detail, with accompanying SEM micrographs, in **Section 8.3.2.2**.

This sliding condition also exhibited a parabolic running-in response over the first 100m of sliding, as elucidated in **Figure 8.6**. These transient COF responses were in good

agreement with the friction behaviours observed in **Chapter 7**, in which it was ascertained that extreme asperity peaks impede sliding prior to them yielding and /or fracturing, thus resulting in relatively heightened COF responses during running-in.

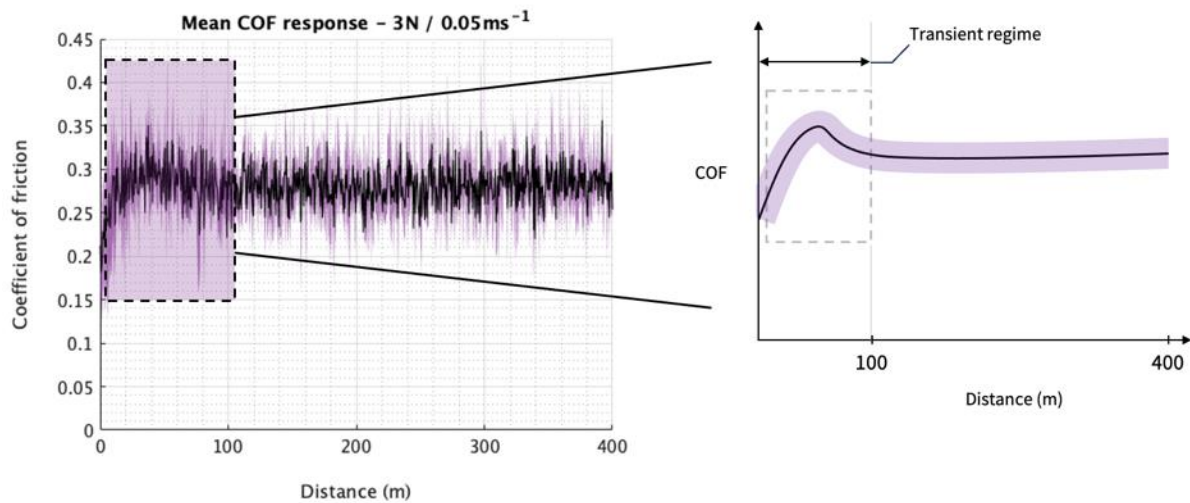
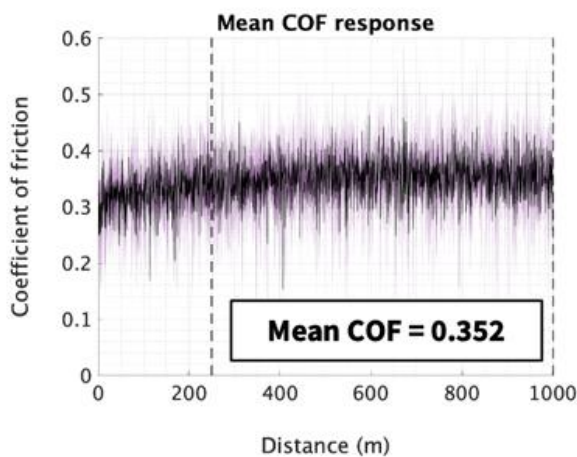


Figure 8.6 – The mean transient COF response recorded during $3\text{N} - 0.05\text{ms}^{-1}$ (low load / low speed), metal pin on polymer disk sliding.

$3\text{N} - 0.5\text{ms}^{-1}$ / Low Load – High Speed

Figure 8.7 shows the mean COF and F_f responses recorded during $3\text{N} - 0.5\text{ms}^{-1}$, metal pin on polymer disk sliding.

(a)



(b)

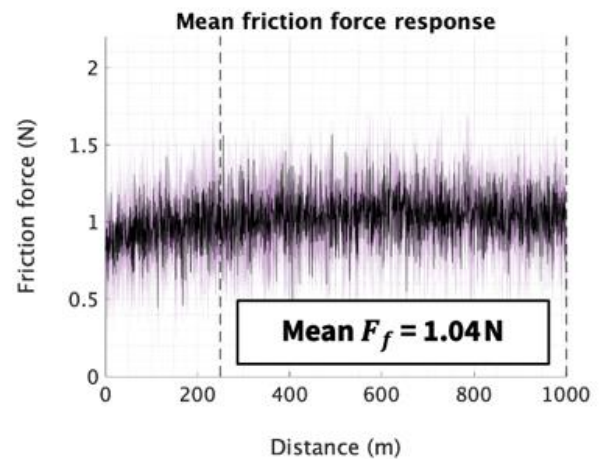


Figure 8.7 – The mean (a) COF and (b) friction force responses recorded during $3\text{N} - 0.5\text{ms}^{-1}$ (low load / high speed), metal pin on polymer disk sliding. The highlighted regions within each response plot represents the maximum and minimum values recorded. The distance between dashed vertical lines within the former indicates the period over which mean COF and F_f values were calculated.

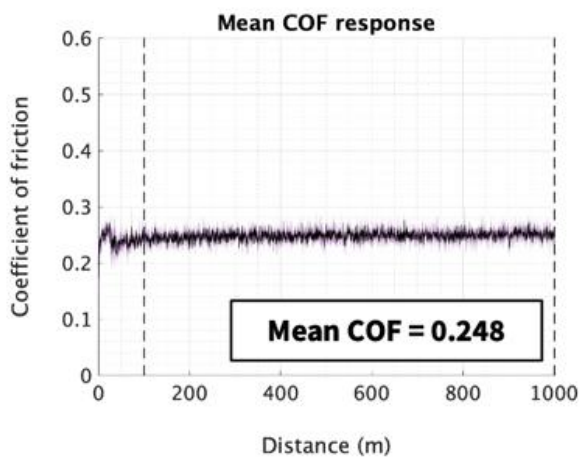
This sliding condition ($3\text{N} - 0.5\text{ms}^{-1}$) induced the largest metal pin on polymer disk COF response, both in terms of mean value and standard deviation recorded during sliding. The latter will have intrinsically varied in accordance with the frequency at which asperity peak fracture occurred, which as discussed in greater detail in **Section 8.3.2.2**, was found to occur more readily during this low load / high speed test configuration than during $3\text{N} - 0.05\text{ms}^{-1}$ (low load / low speed) sliding.

No prolonged running-in behaviours were exhibited during $3\text{N} - 0.5\text{ms}^{-1}$ sliding. Though, plateauing increases in COF were observed during the first $\sim 250\text{m}$ of testing.

$30\text{N} - 0.05\text{ms}^{-1}$ / High Load – Low Speed

Figure 8.8 shows the mean COF and F_f responses recorded during $30\text{N} - 0.05\text{ms}^{-1}$, metal pin on polymer disk sliding.

(a)



(b)

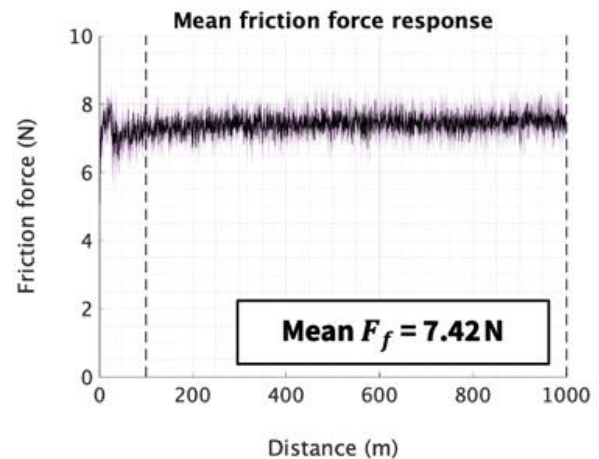


Figure 8.8 – The mean (a) COF and (b) friction force responses recorded during $30\text{N} - 0.05\text{ms}^{-1}$ (high load / low speed), metal pin on polymer disk sliding. The highlighted regions within each response plot represents the maximum and minimum values recorded. The distance between dashed vertical lines within the former indicates the period over which mean COF and F_f values were calculated.

As detailed in **Figure 8.8a**, this sliding condition ($30\text{N} - 0.05\text{ms}^{-1}$) induced a mean COF response of 0.248, which was the smallest value recorded during metal pin on polymer disk sliding.

Furthermore, as shown in **Figure 8.9**, the transient COF responses exhibited during the first $\sim 100\text{m}$ of sliding were akin to the behaviours characterised during $3\text{N} - 0.05\text{ms}^{-1}$ sliding, as well as those previously discussed in **Chapter 7**. This suggests that these parabolic surges in COF were a function of sliding speed rather than normal load.

Additionally, a shallow dip in COF can be seen in **Figure 8.9**. It is likely that COF momentarily decreased upon the complete shearing and removal of asperity peaks, before subsequently increasing as bulk surface ploughing ensued. Moreover, it is expected that this phenomena was particularly apparent and discernible due to the relatively low sliding speed and high normal load applied during this test condition.

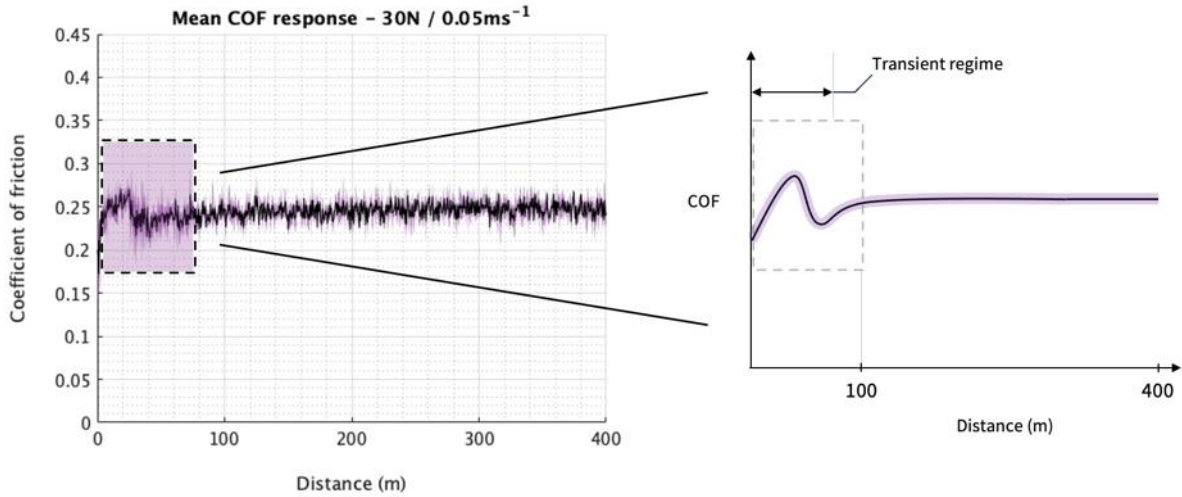


Figure 8.9 – The mean transient COF response recorded during 30N – 0.05ms⁻¹ (high load / low speed), metal pin on polymer disk sliding.

30N – 0.5ms⁻¹ / High Load – High Speed

Figure 8.10 shows the mean COF and F_f responses recorded during 30N – 0.5ms⁻¹, metal pin on polymer disk sliding.

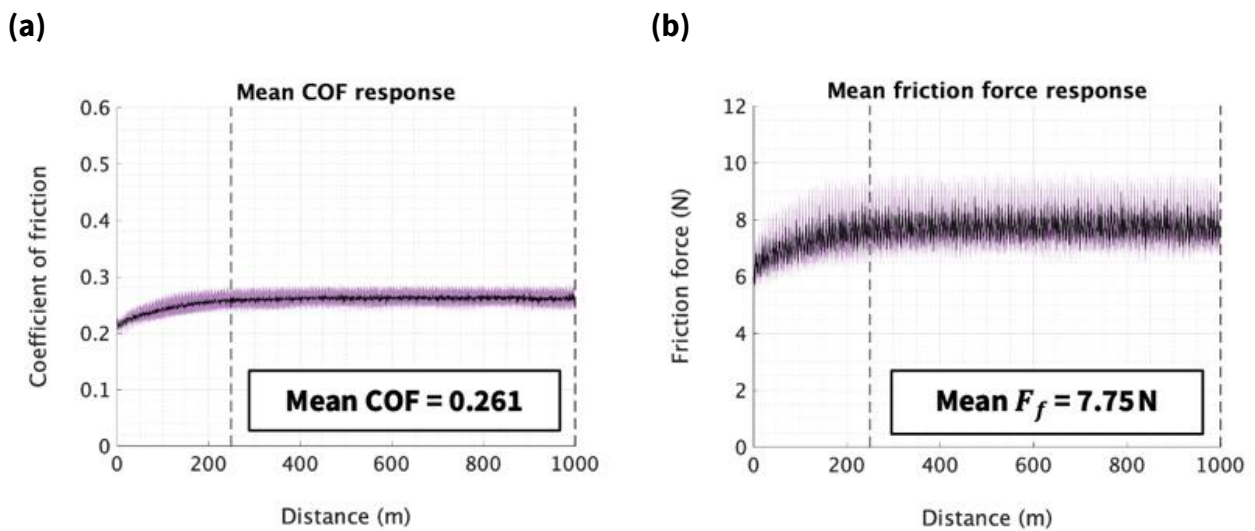


Figure 8.10 – The mean (a) COF and (b) friction force responses recorded during 30N – 0.5ms⁻¹ (high load / high speed), metal pin on polymer disk sliding. The highlighted regions within each response plot represents the maximum and minimum values recorded. The distance between dashed vertical lines within the former indicates the period over which mean COF and F_f values were calculated.

This sliding condition ($30\text{N} - 0.5\text{ms}^{-1}$) induced the lowest variation in COF. Moreover, no distinct transient behaviours, other than plateauing increases in COF, could be discerned in **Figure 8.10a**. This further suggests that the previously observed parabolic surges in COF were primarily influenced by sliding speed, rather than normal load, during metal pin on polymer disk sliding.

Polymer Pin on Metal Disk Sliding

During polymer pin on metal disk sliding, the former was continuously subject to dynamic contact, as illustrated in **Figure 8.1**.

$3\text{N} - 0.05\text{ms}^{-1}$ / Low Load – Low Speed

Figure 8.11 shows the mean COF and F_f responses recorded during $3\text{N} - 0.05\text{ms}^{-1}$, polymer pin on metal disk sliding.

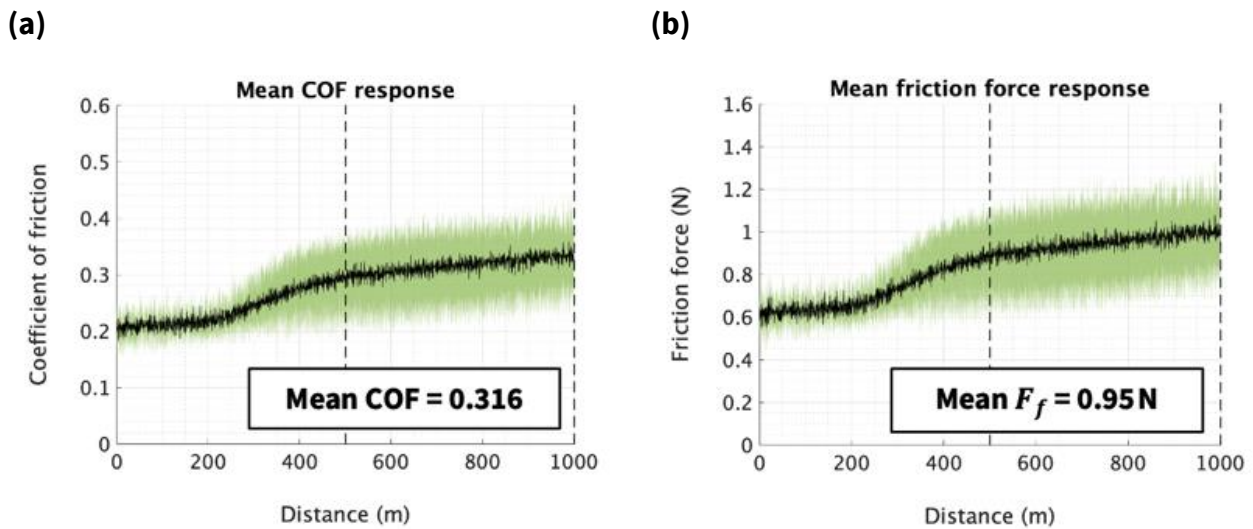


Figure 8.11 – The mean (a) COF and (b) friction force responses recorded during $3\text{N} - 0.05\text{ms}^{-1}$ (low load / low speed), polymer pin on metal disk sliding. The highlighted regions within each mean response plot represents the maximum and minimum values recorded. The distance between dashed vertical lines within the former indicates the period over which mean COF and F_f values were calculated.

As detailed in **Figure 8.11a**, this sliding condition ($3\text{N} - 0.05\text{ms}^{-1}$) induced a mean COF response of 0.316, which was the smallest value recorded during polymer pin on metal disk sliding. Though, it should be noted that this mean COF value was calculated between the onset of steady-state sliding and test completion, which as shown in **Figure 8.12**, only occurred during the last 500m of testing. Since this value was calculated over a considerably shorter steady-state sliding distance than any of the other polymer pin on metal disk sliding conditions evaluated, frictional heating will have had less of an effect on its determination.

Furthermore, the transition from transient to steady-state sliding was marked by a sharp change in COF (~ 0.125). It is expected that this sudden increase in friction corresponded with a change in how the 3N normal loads were supported during sliding. More specifically, the applied 3N normal loads will have initially been supported by asperity peaks prior to them yielding and / or fracturing. Whereby commencement of the latter will have initiated a transformation in contact geometry from ball-on-flat to flat-on-flat, as elucidated in **Figure 8.12**. Consequently, the resultant enlargements in A_R that ensued will have given rise to larger friction forces.

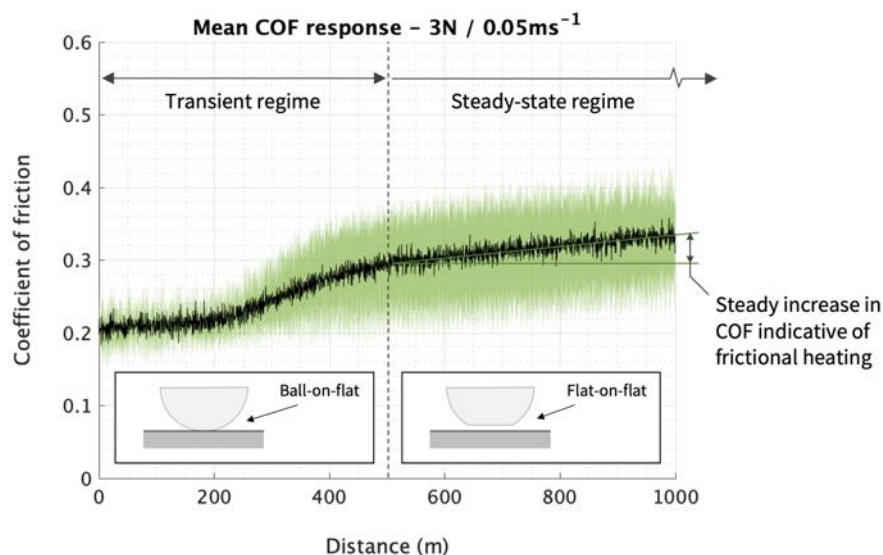


Figure 8.12 – A detailed overview of the main friction-related features that occurred during $3\text{N} - 0.05\text{ms}^{-1}$ (low load / low speed) polymer pin on metal disk sliding.

Upon steady-state sliding being attained, COF increased linearly due to frictional heating, which was intrinsically generated as a result of the continuously-in-contact nature of this polymer pin on metal disk test set-up. This is discussed in greater detail in **Section 8.3.1.2**.

3N – 0.5ms⁻¹ / Low Load – High Speed

Figure 8.13 shows the mean COF and F_f responses recorded during 3N – 0.5ms⁻¹, polymer pin on metal disk sliding.

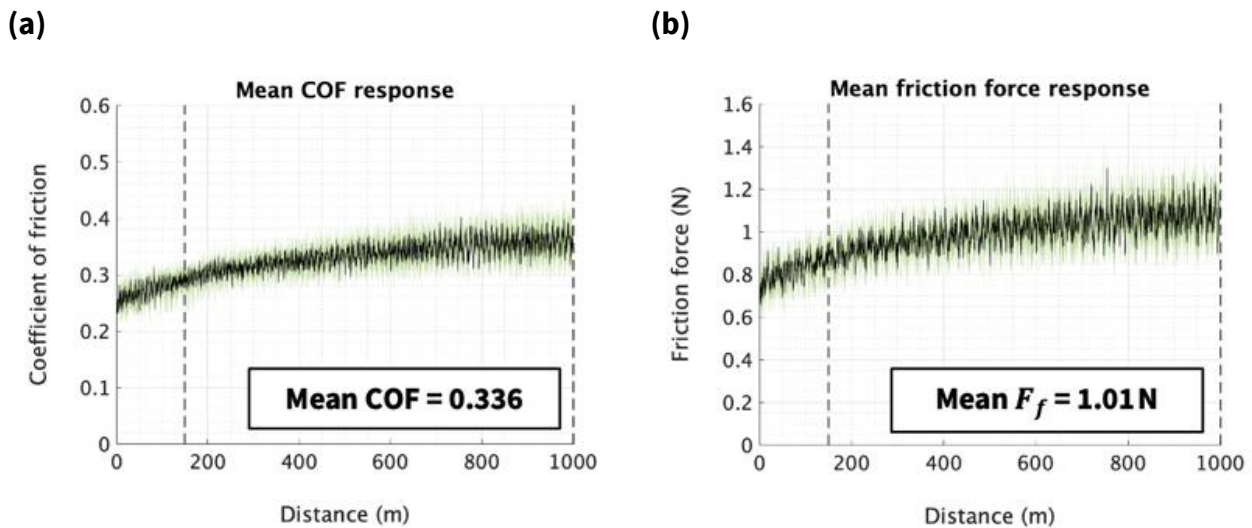


Figure 8.13 – The mean (a) COF and (b) friction force responses recorded during 3N – 0.5ms⁻¹ (low load / high speed), polymer pin on metal disk sliding. The highlighted regions within each mean response plot represents the maximum and minimum values recorded. The distance between dashed vertical lines within the former indicates the period over which mean COF and F_f values were calculated.

As shown in **Figure 8.13**, COF increased steadily, both in terms of linear regression and variation in sliding, throughout each repeat test. Though, the former can be seen to have increased at a greater rate over the first 150m of sliding, particularly within ‘Test 1’ (shown in **Appendix C**), prior to the commencement of steady-state sliding.

Furthermore, it is expected that the additional momentum incurred during this high speed (0.5ms⁻¹) sliding condition, coupled with the ground topography of each metal disk

surface, prompted the early-onset formation of flat-on-flat contact geometries during initial dynamic contact.

$30\text{N} - 0.05\text{ms}^{-1}$ / High Load – Low Speed

Figure 8.14 shows the mean COF and F_f responses recorded during $30\text{N} - 0.05\text{ms}^{-1}$, polymer pin on metal disk sliding.

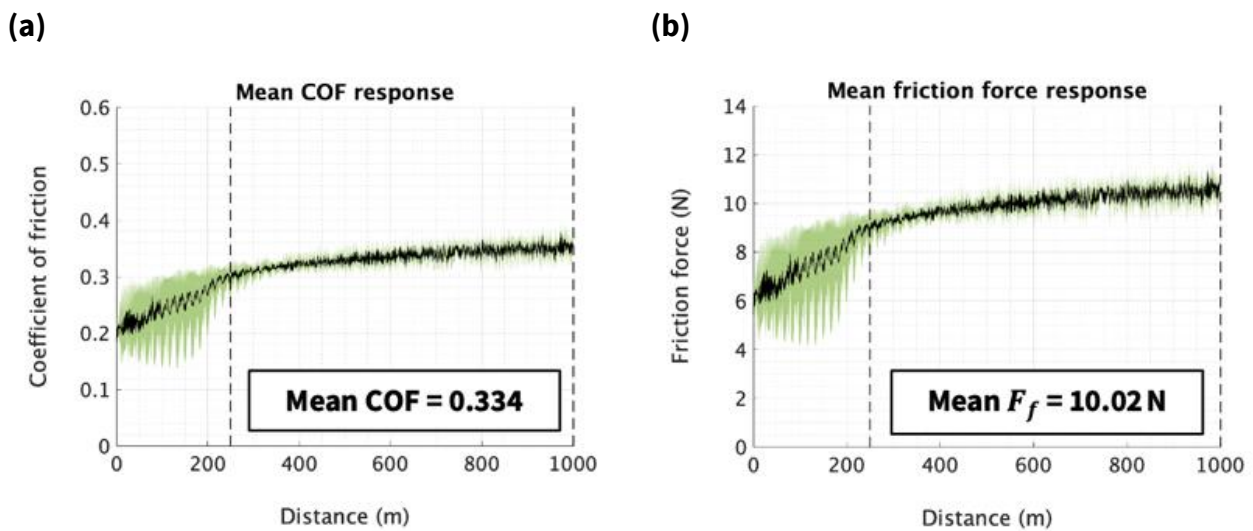


Figure 8.14 – The mean (a) COF and (b) friction force responses recorded during $30\text{N} - 0.05\text{ms}^{-1}$ (high load / low speed), polymer pin on metal disk sliding. The highlighted regions within each mean response plot represents the maximum and minimum values recorded. The distance between dashed vertical lines within the former indicates the period over which mean COF and F_f values were calculated.

In accordance with the COF behaviours previously analysed during low load / low speed sliding, the transition from transient to steady-state $30\text{N} - 0.05\text{ms}^{-1}$ (high load / low speed) sliding was again characterised by a sharp increase in COF. As shown in **Figure 8.15**, the magnitude by which COF increased was consistent across all three repeat tests, as well as with the ΔCOF values exhibited during $3\text{N} - 0.05\text{ms}^{-1}$ sliding.

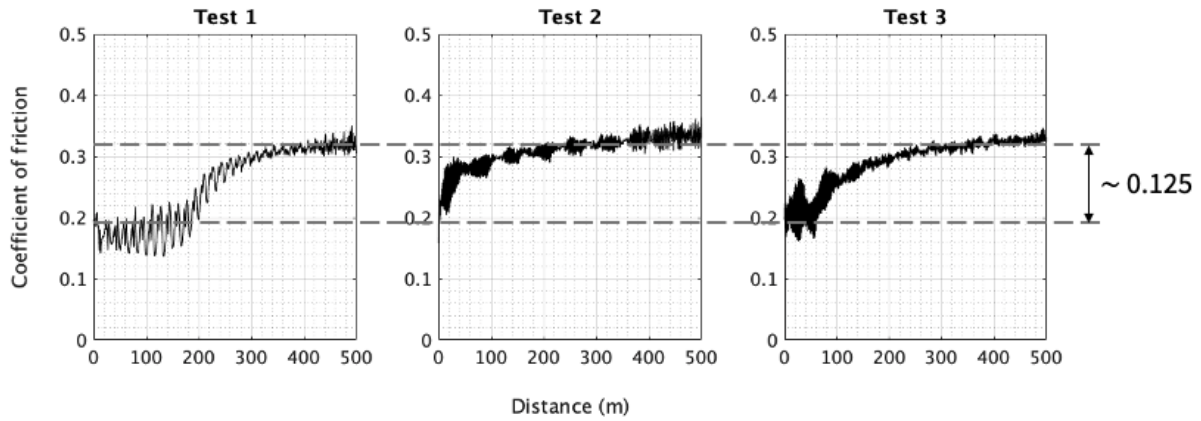


Figure 8.15 – The transient COF responses recorded during $30\text{N} - 0.05\text{ms}^{-1}$ (high load / low speed), polymer pin on metal disk sliding.

The alike magnitudes by which COF surged further suggests that this event marked the transition from transient (elastic, ball-on-flat) to steady-state (plastic, flat-on-flat) sliding.

$30\text{N} - 0.5\text{ms}^{-1}$ / High Load – High Speed

Figure 8.16 shows the mean COF and F_f responses recorded during $30\text{N} - 0.5\text{ms}^{-1}$, polymer pin on metal disk sliding.

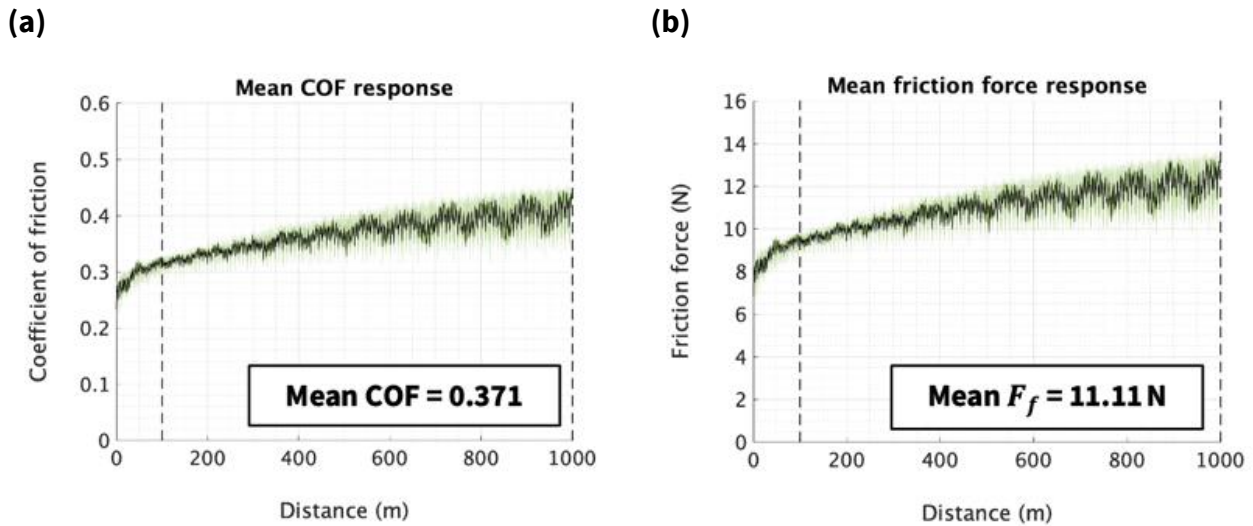


Figure 8.16 – The mean (a) COF and (b) friction force responses recorded during $30\text{N} - 0.5\text{ms}^{-1}$ (high load / high speed), polymer pin on metal disk sliding. The highlighted regions within each mean response plot represents the maximum and minimum values recorded. The distance between dashed vertical lines within the former indicates the period over which mean COF and F_f values were calculated.

30N – 0.5ms⁻¹ (high load / high speed) sliding induced a mean COF response of 0.371, which was the largest value recorded during metal pin on polymer disk sliding. This particular sliding condition was also found to be the most affected by frictional heating, which impacted both the magnitude by which COF increased, and also the extent by which it varied from the mean, during steady-state sliding. This is discussed in greater detail in **Section 8.3.1.2** and **Section 8.3.1.3**, respectively.

As can be seen in **Figure 8.16a**, 30N – 0.5ms⁻¹ running-in responses comprised of plateauing increases in COF, specifically between sliding distances of 0m and 150m. These transient behaviours were similar to those exhibited during every other high speed (0.5ms⁻¹) sliding condition evaluated, including those recorded during metal pin on polymer disk sliding. Ultimately, this confirmed that sliding speed, rather than normal load, preponderantly influenced the friction incurred during running-in.

8.3.1.2 Frictional Heating

As mentioned in **Section 8.2.3**, varying the contact configuration employed during testing intrinsically enabled both periodically-in-contact and continuously-in-contact polymer sliding to be evaluated.

Upon analysing the COF response plots presented throughout **Section 8.3.1.1**, no apparent increases in COF were discerned during steady-state, metal pin on polymer disk sliding, independent of the operating conditions employed. Ultimately, this confirmed that contacting polymer regions were able to sufficiently cool between consecutive interactions, thus preventing the accumulation of frictional heat.

Contrastingly, gradual increases in COF were observed during steady-state, polymer pin on metal disk sliding. Though, as previously mentioned, the nature of this test configuration ensured that interfacing polymer pin surfaces remained continuously-in-contact during sliding. Consequently, frictional heat will have been generated at the sliding interface, leading to the thermal softening and subsequent

enlargement of each polymer pin's apparent area of contact. The exact increases in COF ascertained during polymer pin on metal disk sliding, specifically between sliding distances of 300m and 995m, are detailed in **Table 8.6**. These distances were selected because they encompassed the majority of each corresponding steady-state sliding regime evaluated.

Table 8.6

The increases in COF, as well as their corresponding standard deviation values, measured between sliding distances of 300m and 995m during polymer pin on metal disk sliding. In order to calculate the difference between COF values at 300m and 995m, mean values for each were first computed between 295m – 305m and 990m – 1000m, respectively.

Polymer pin – metal disk sliding conditions	Test number	Increase in COF	Mean increase in COF	Mean percentage increase in COF
3N – 0.05ms ⁻¹	<i>Extended running-in periods of up to approximately 500m meant that changes in COF due to frictional heating could not be characterised over the same distances as the other sliding test conditions.</i>			
3N – 0.5ms ⁻¹	1	0.0518	0.0471 (± 0.0041)	13.02 (± 0.96)
	2	0.0453		
	3	0.0442		
30N – 0.05ms ⁻¹	1	0.0467	0.0420 (± 0.0044)	11.94 (± 1.47)
	2	0.0413		
	3	0.0379		
30N – 0.5ms ⁻¹	1	0.0638	0.0617 (± 0.0018)	15.13 (± 0.26)
	2	0.0606		
	3	0.0606		

As shown in **Table 8.6**, relatively similar mean percentage increases in COF (%ΔCOF) were determined for each sliding condition evaluated. Additionally, there was good agreement between repeat tests, as indicated by %ΔCOF values having relatively small corresponding standard deviations. Ultimately, this demonstrated that prioritising contact configuration, over normal load and / or sliding speed, is the best practice when wanting to minimise the effect of frictional heating in analogous real-world tribosystems.

8.3.1.3 Variations in COF

COF fluctuated by varying magnitudes during sliding, as shown in the response plots presented throughout **Section 8.3.1.1**. Similar variations in sliding were also observed by Bai et al. [146] and Gadelmoula and Aldahash [195], who referred to the former as being indicative of sliding smoothness and stability, respectively.

Furthermore, these variations in COF differed depending on the operating conditions employed. Though generally, fluctuating COF amplitudes remained relatively constant during metal pin on polymer disk sliding, but gradually increased during steady-state, polymer pin on metal disk interactions, as illustrated schematically in **Figure 8.17**.

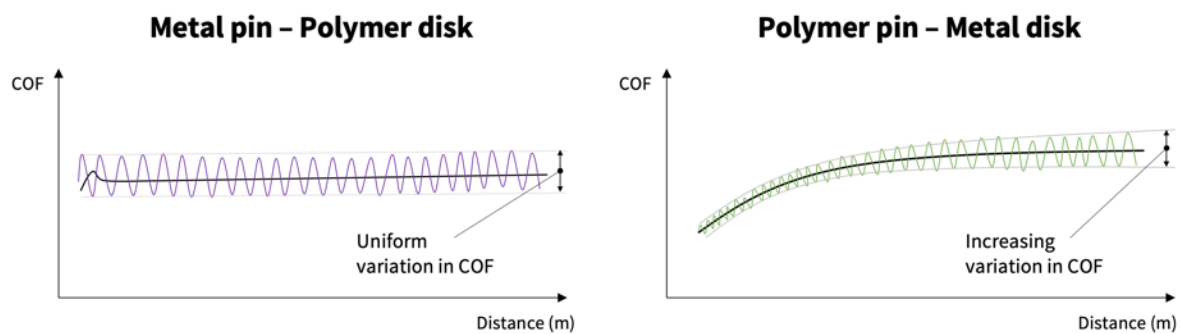


Figure 8.17 – Schematic plots highlighting the typical variations in COF observed when converse contact configurations were employed during testing.

Figure 8.19 quantitatively describes the magnitudes by which COF varied during each sliding condition. These values were determined by calculating the standard deviation (SD) of COF results recorded between consecutive 50m increments during each sliding test, as shown in **Figure 8.18**.

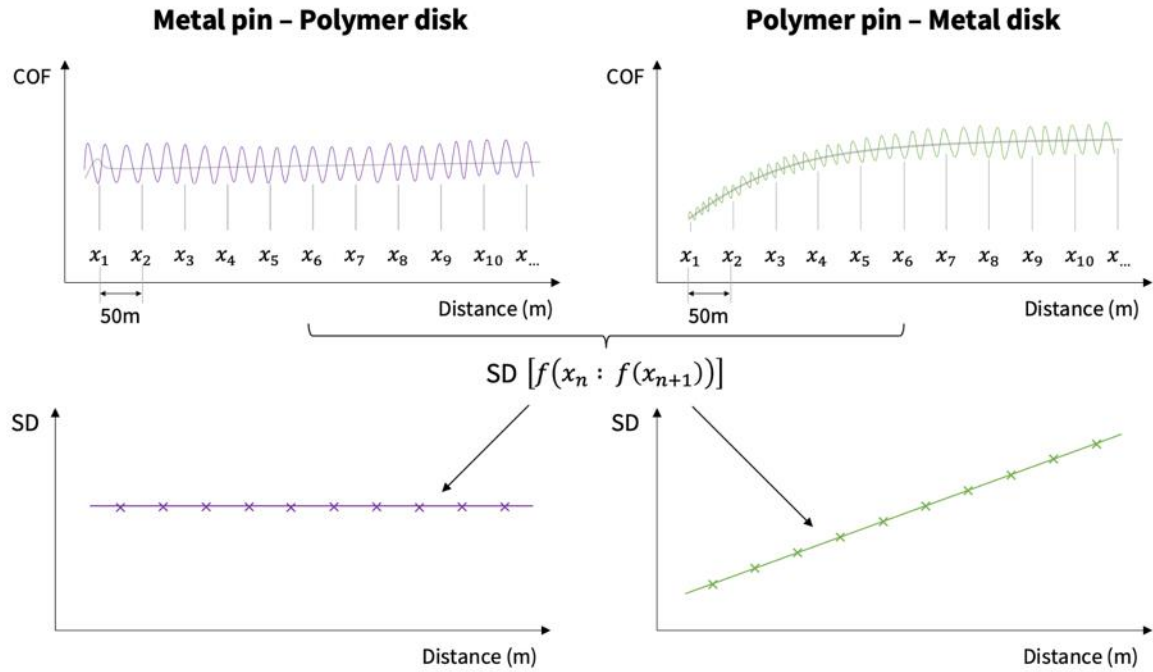


Figure 8.18 – A schematic illustrating how the variation in COF values in **Figure 8.19** were calculated.

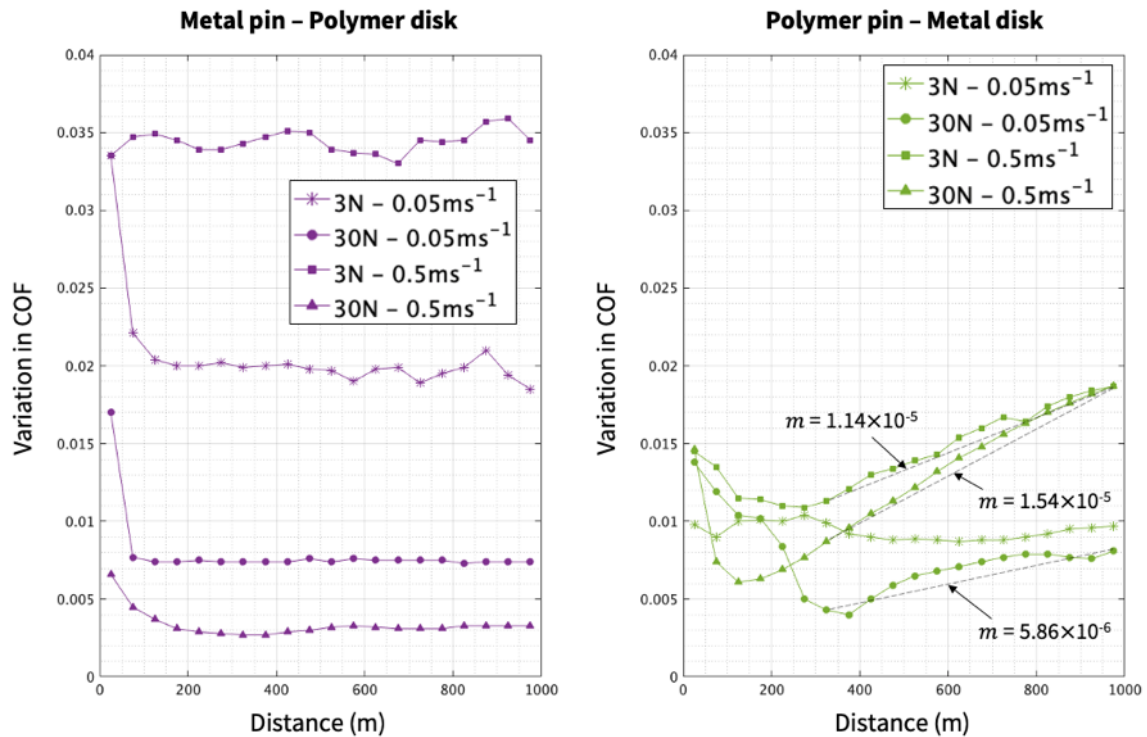


Figure 8.19 – The magnitudes by which COF fluctuated during each sliding condition. More specifically, variation in sliding values were determined by calculating the standard deviation of COF results recorded between consecutive 50m increments during each sliding test, as shown in **Figure 8.18**.

Figure 8.19 confirms that COF varied relatively uniformly during metal pin on polymer disk sliding, independent of normal load and sliding speed. Additionally, it can also be seen that COF became increasingly varied during steady-state polymer pin on metal disk sliding⁹. Moreover, the gradient magnitudes which evidence the latter also correspond with the mean percentage increases in COF (% Δ COF) detailed in **Table 8.6**. Ultimately, this suggests that frictional heating was proportional to the magnitudes by which COF fluctuated during sliding.

Furthermore, significantly different variations in COF were discerned during 3N and 30N metal pin on polymer disk sliding. This is discussed in greater detail in **Section 8.3.2.2**, though to summarise, these differences were determined by how each normal load was supported during sliding. More specifically, 3N normal loads were jointly supported by polymer surface asperities and partially yielded peaks, whereas 30N normal loads led to the plastic deformation of bulk surface material.

8.3.1.4 Statistical Analysis of Friction Results

Figure 8.20 includes contour plots that visually elucidate the relationship between friction force, normal load and sliding speed for both contact configurations evaluated.

⁹ Excluding 3N – 0.05ms⁻¹ (low load / low speed) results, though this test configuration only exhibited evidence of frictional heating over the latter half of the entire test duration.

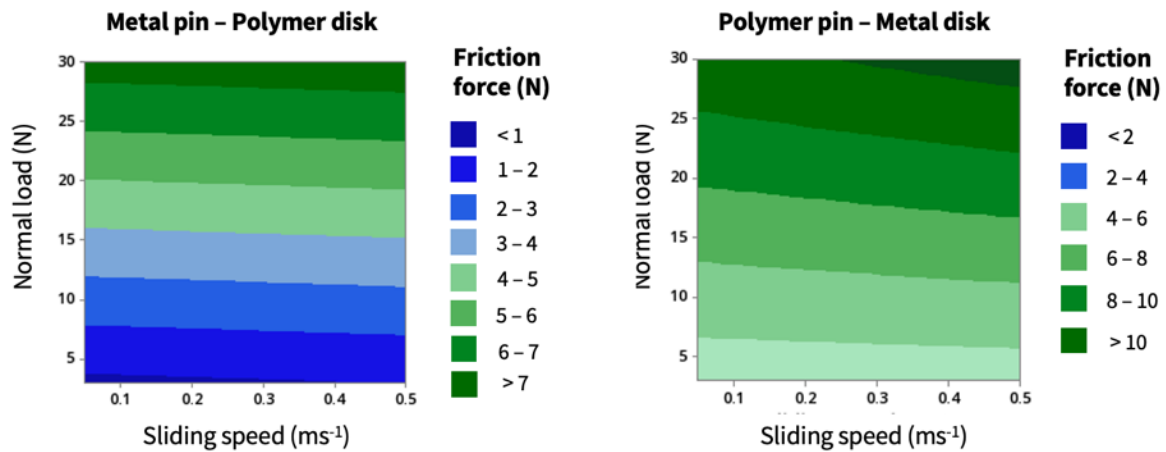


Figure 8.20 – Contour plots showing the relationship between COF, normal load and sliding speed for both contact configurations evaluated.

Additionally, **Figure 8.21** outlines the main and interaction effects each operating condition had on friction force in ascending / descending order of influence. Terms that had a standardised effect greater than 2.120 were deemed to be statistically significant. This reference value for statistical significance is displayed at point t , where t is the $(1 - \alpha/2)$ quantile of the resultant t -distribution in which its degrees of freedom are equal to the degrees of freedom of its error term [187].

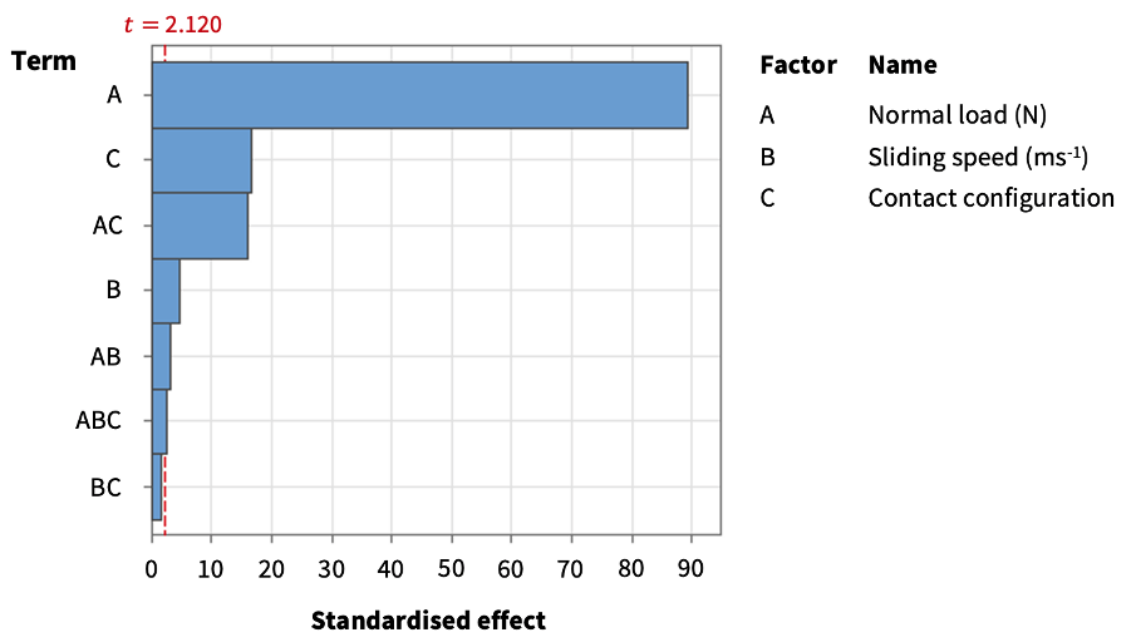


Figure 8.21 – A Pareto chart showing the extent to which normal load, sliding speed and contact configuration influenced friction force.

F_f was extremely sensitive to the operating conditions employed during sliding. Every term, besides from the interaction between sliding speed x contact configuration (BC), was found to have a statistically significant effect on friction force.

As shown in **Figure 8.21**, normal load had by far the most significant impact on F_f . In general, increasing normal loads will have given rise to larger contact areas (A_R), which will have resulted in greater F_f values.

Contact configuration, as well as its interaction with normal load, also impacted F_f . As discussed in **Section 8.3.1.2**, the former was deemed to have preponderantly influenced frictional heating, resulting in percentage increases in COF of up to 15% over the sliding distances evaluated.

Additionally, it can be seen in **Figure 8.21** that sliding speed had a statistically significant effect on F_f , despite this being discordant with Coulomb's Law of Friction. Moreover, the steepness of the contour band gradients within **Figure 8.20** indicate that sliding speed had the greatest influence on F_f during high load, polymer pin on metal disk sliding.

8.3.2 Wear

Table 8.7 details the mean wear rate results determined for each of the eight different sliding configurations evaluated as part of the DoE.

Table 8.7

Mean wear rate results, and corresponding standard deviation values, for each of the sliding conditions evaluated as part of the DoE. Standard deviation values indicate the variation between repeat tests.

Contact configuration	Mean wear rate ($\times 10^{-3}$ (mm ³) m ⁻¹)			
	3N – 0.05ms ⁻¹	3N – 0.5ms ⁻¹	30N – 0.05ms ⁻¹	30N – 0.5ms ⁻¹
Metal pin on polymer disk	0.650 ± 0.110	1.270 ± 0.240	7.044 ± 0.623	8.589 ± 1.480
Polymer pin on metal disk	0.098 ± 0.010	0.156 ± 0.045	0.902 ± 0.191	0.487 ± 0.111

8.3.2.1 Congruency with Literature

In order to assess the congruency of the wear results ascertained within this study with those documented within literature, the wear rate results detailed in **Table 8.7** were normalised by N , so that specific wear rate values could be compared. Correspondingly, **Table 8.8** details the specific wear rate values determined for each of the eight different sliding conditions evaluated as part of the DoE.

Table 8.8

Mean specific wear rate results, and corresponding standard deviation values, for each of the sliding conditions evaluated as part of the DoE. Standard deviation values indicate the variation between repeat tests.

Contact configuration	Mean specific wear rate ($\times 10^{-4}$ (mm ³) Nm ⁻¹)			
	3N – 0.05ms ⁻¹	3N – 0.5ms ⁻¹	30N – 0.05ms ⁻¹	30N – 0.5ms ⁻¹
Metal pin on polymer disk	2.166 \pm 0.366	4.235 \pm 0.799	2.348 \pm 0.208	2.863 \pm 0.493
Polymer pin on metal disk	0.326 \pm 0.034	0.519 \pm 0.149	0.301 \pm 0.064	0.162 \pm 0.037

The measured results detailed in **Table 8.8** are in good agreement with data reported in related literature, as indicated by their exact values being of the same order of magnitude. More specifically, metal pin on polymer disk wear rate results were concordant with data obtained by Bai et al. [135,146] and Guo et al. [88], who characterised wear via linear reciprocating, ball-on-flat, pin-on-block (steel pin – laser sintered PA12 block) testing. Similarly, polymer pin on metal disk wear rate values were congruous with results collected by Gadelmoula and Aldahash [151], who performed analogous rotating, ball-on-flat, pin-on-disk (laser sintered PA12 pin – steel disk) sliding tests.

8.3.2.2 Wear Responses

This section includes microscopy images which provide indications of the magnitudes and types of wear incurred during each of sliding conditions evaluated as part of the DoE.

Additional SEM and FV microscopy images of pin and disk surfaces obtained after repeat testing can be seen in **Appendix C**.

Metal Pin on Polymer Disk Sliding

During metal pin on polymer disk sliding, discrete regions of the latter were subject to dynamic contact for only one instance per revolution, as illustrated in **Figure 8.1**.

3N – 0.05ms⁻¹ / Low Load – Low Speed

Figure 8.22 includes microscopy images of the wear scars produced during 3N – 0.05ms⁻¹, metal pin on polymer disk sliding.

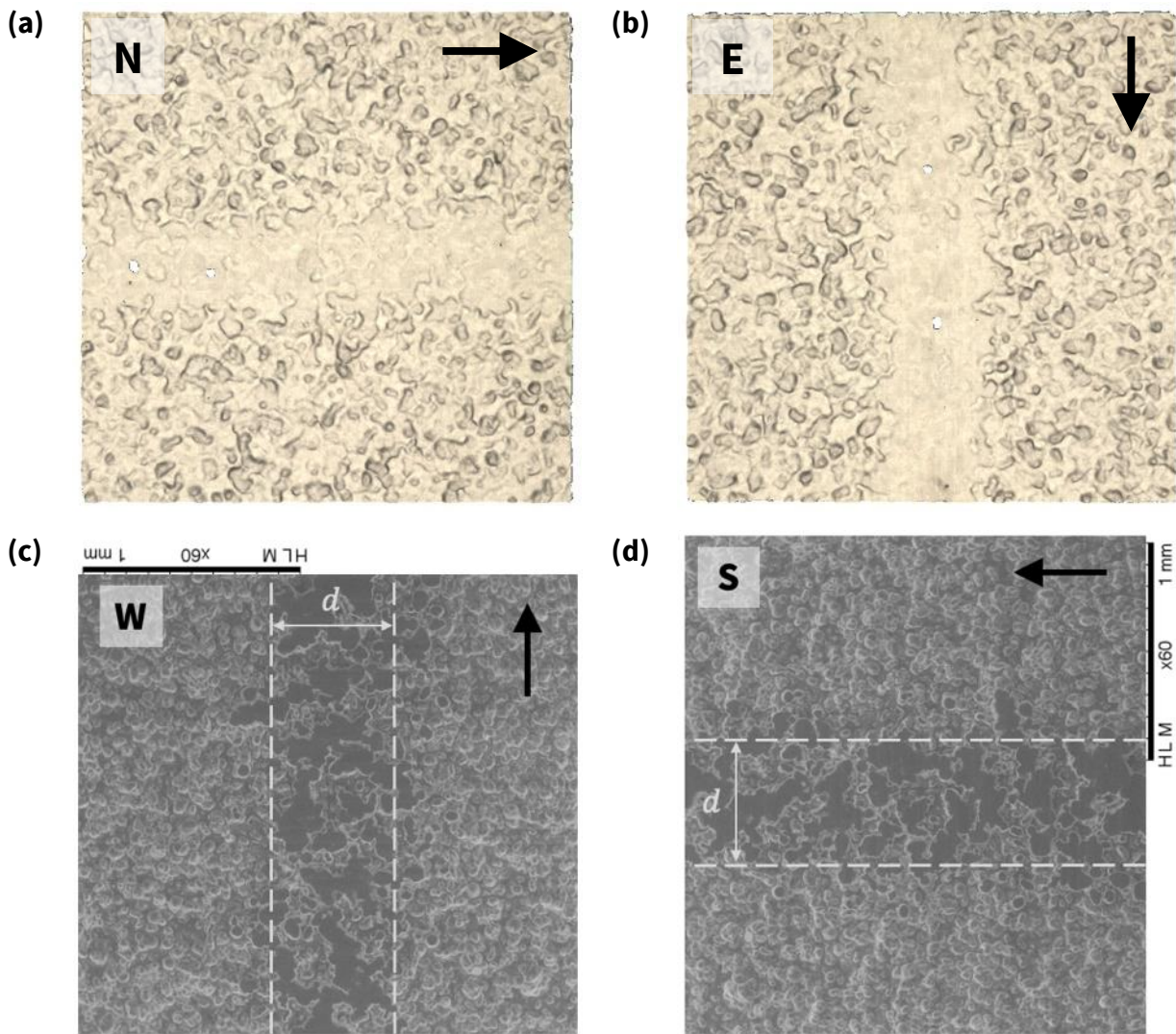


Figure 8.22 – Microscopy images captured after the second repeat $3\text{N} - 0.05\text{ms}^{-1}$ (low load / low speed) sliding test. These include wear scars obtained by FV microscopy at **(a)** north and **(b)** east locations, as well as SEM images obtained at **(c)** west and **(d)** south locations. The orientation of each arrow denotes the instantaneous direction of rotation of each disk region relative to the metal pin, and dashed lines signify the mean wear track width determined for this sliding condition.

This low load / low speed sliding condition was determined to have a mean wear rate of $0.650 \times 10^{-3} \text{ mm}^3 \text{ m}^{-1}$, which was the lowest W_{mean} value recorded during metal pin on polymer disk sliding.

As shown in **Figure 8.22**, the applied 3N normal loads were jointly supported by bulk surface material and clusters of asperity peaks. This indicates that during $3\text{N} - 0.05\text{ms}^{-1}$ sliding, polymer disk samples were subject to both elastic and plastic deformation. This

was in good agreement with findings made by Kragelski [153], who proposed the general relationship outlined below:

$$\text{Elastic deformation} \leftarrow 1\text{N} < N < 5\text{N} \rightarrow \text{Plastic deformation}$$

Furthermore, upon analysing the tensile test curves of the laser sintered 50/50 – PA12 samples evaluated in **Chapter 6**, which were processed identically to those investigated within this study, it was determined that they had a mean offset yield strength of 35.1 MPa (SD = ± 1.20 MPa). Ultimately, this σ_{yield} value was just less than the 38.5 MPa Hertzian contact stress approximation detailed in **Table 8.11**, which reaffirms that the applied 3N normal loads will have likely been supported elastically by polymer asperity peaks during sliding.

$$3\text{N} - 0.5\text{ms}^{-1} / \text{Low Load} - \text{High Speed}$$

Figure 8.23 includes microscopy images of the wear scars produced during 3N – 0.5ms⁻¹, metal pin on polymer disk sliding.

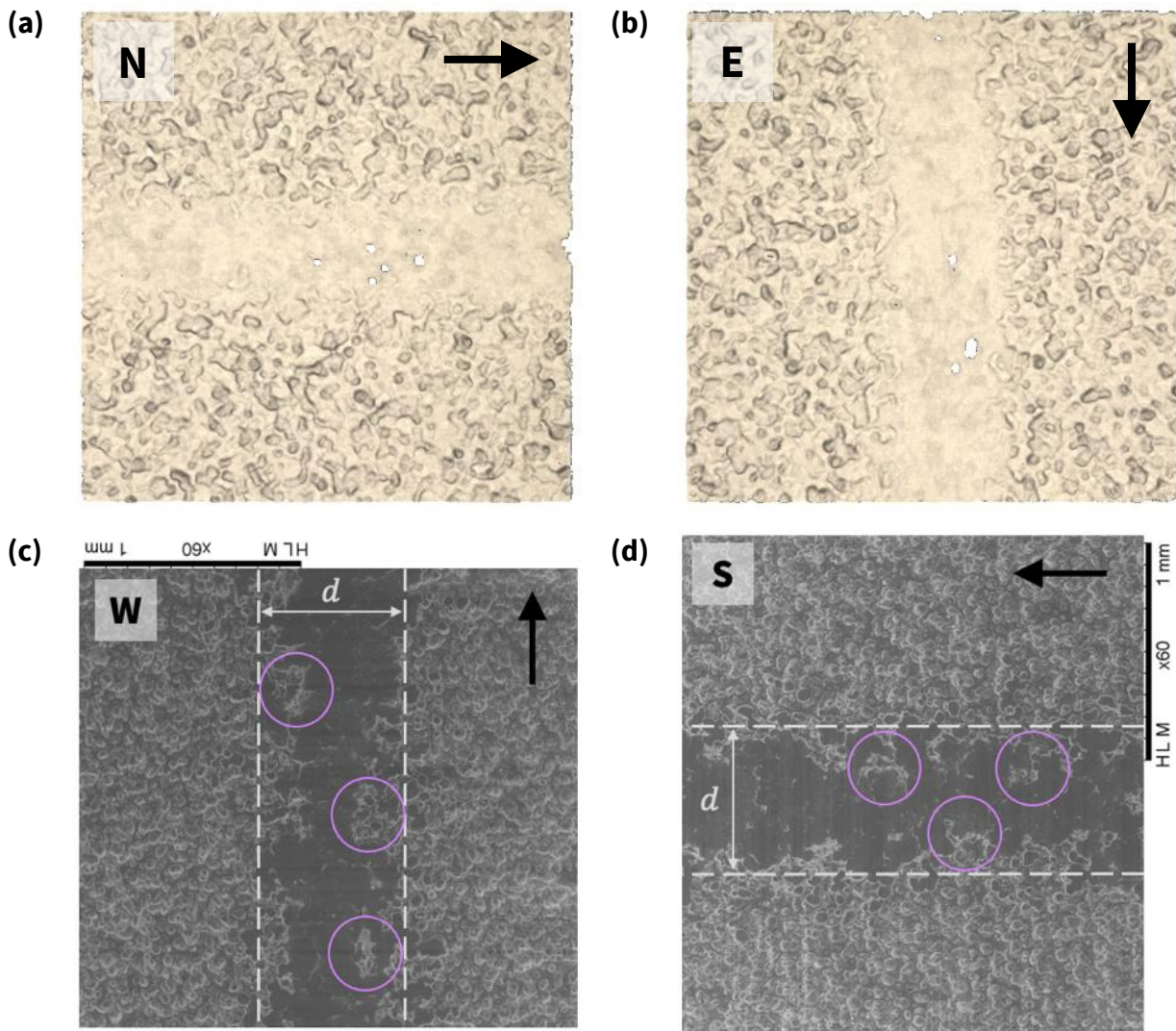


Figure 8.23 – Microscopy images captured after the second repeat $3\text{N} - 0.5\text{ms}^{-1}$ (low load / high speed) sliding test. These include wear scars obtained by FV microscopy at **(a)** north and **(b)** east locations, as well as SEM images obtained at **(c)** west and **(d)** south locations. The orientation of each arrow denotes the instantaneous direction of rotation of each disk region relative to the metal pin. Each circled location highlights a region in which the 3N normal load was supported by a cluster of asperity peaks within the mean wear scar width determined for this sliding condition, as signified by the distance between parallel dashed lines.

As shown in **Figure 8.23**, the applied 3N normal loads were again supported by both asperity peak clusters and bulk surface material. Though, the additional momentum incurred during this sliding condition resulted in greater amounts of asperity peak fracture and subsequent ploughing, which meant that plastic, rather than elastic, deformation dominated.

$30\text{N} - 0.05\text{ms}^{-1}$ / High Load – Low Speed

Figure 8.24 includes microscopy images of the wear scars produced during $30\text{N} - 0.05\text{ms}^{-1}$, metal pin on polymer disk sliding.

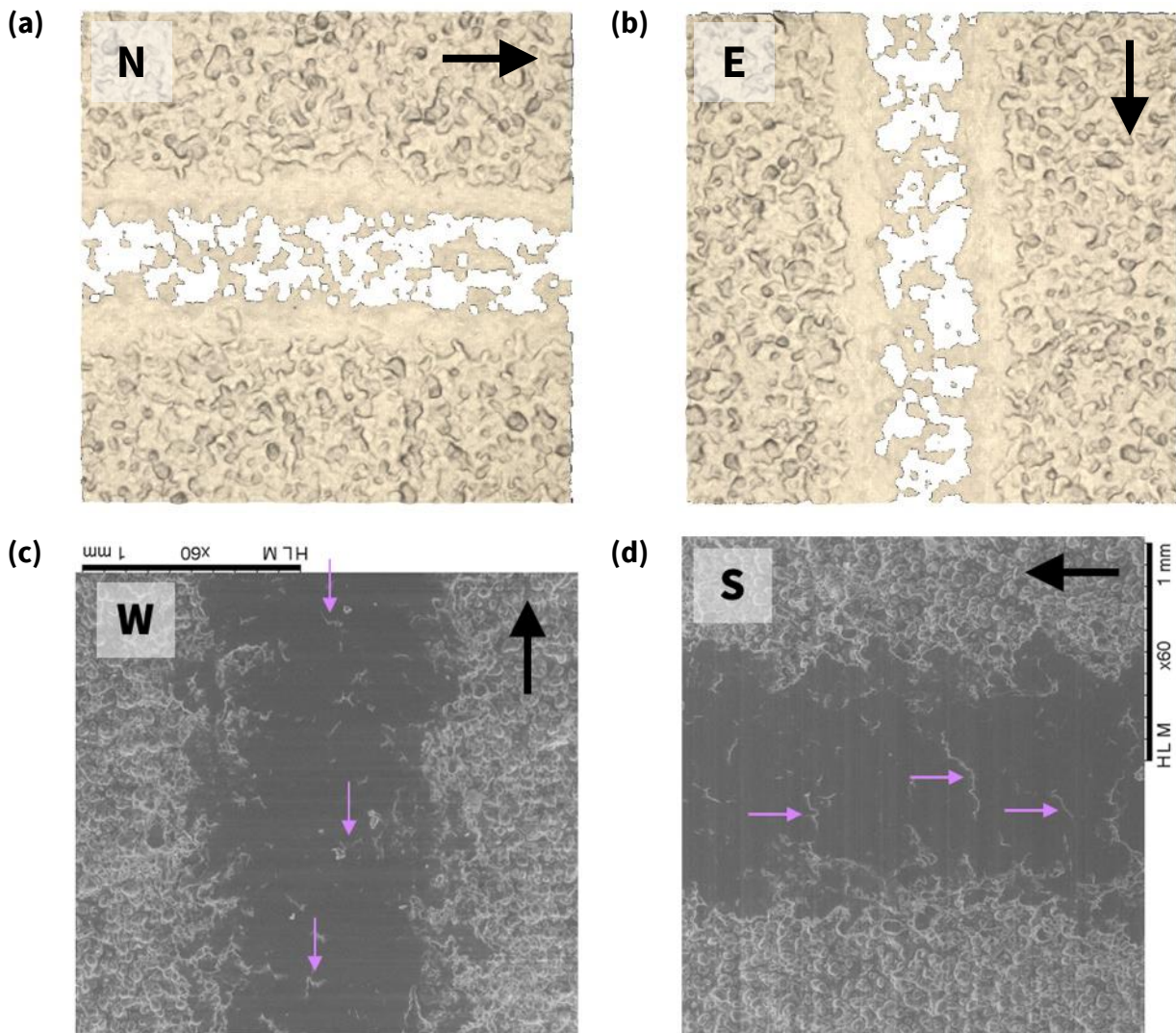


Figure 8.24 – Microscopy images captured after the second repeat $30\text{N} - 0.05\text{ms}^{-1}$ (high load / low speed) sliding test. These include wear scars obtained by FV microscopy at **(a)** north and **(b)** east locations, as well as SEM images obtained at **(c)** west and **(d)** south locations. The orientation of each arrow denotes the instantaneous direction of rotation of each disk region relative to the metal pin. Purple arrows specify the locations where evidence of plastic flow can be seen.

The missing information within each wear scar shown in **Figure 8.24a** and **Figure 8.24b** was due to their worn surfaces becoming highly reflective which inhibited light from being received by the microscope's detector. This indicates that sufficient amounts of frictional

heat was generated at the contacting interface to prompt the subsequent thermal softening and spreading of localised polymer material, as shown in **Figure 8.24c** and **Figure 8.24d**, thus resulting in a highly reflective surface. Ultimately, these heightened flash temperatures will have been generated due to the considerable plastic deformation and prolonged contact durations incurred during this high load / low speed sliding condition, respectively [126].

Additionally, the high reflectivity of the wear scars produced indicates that they were also intrinsically very smooth. This will have likely facilitated $30\text{N} - 0.05\text{ms}^{-1}$ sliding and serves as an explanation as to why this test condition resulted in the smallest COF values being recorded during metal pin on polymer disk sliding.

$30\text{N} - 0.5\text{ms}^{-1}$ / High Load – High Speed

Figure 8.25 includes microscopy images of the wear scars produced during $30\text{N} - 0.5\text{ms}^{-1}$, metal pin on polymer disk sliding.

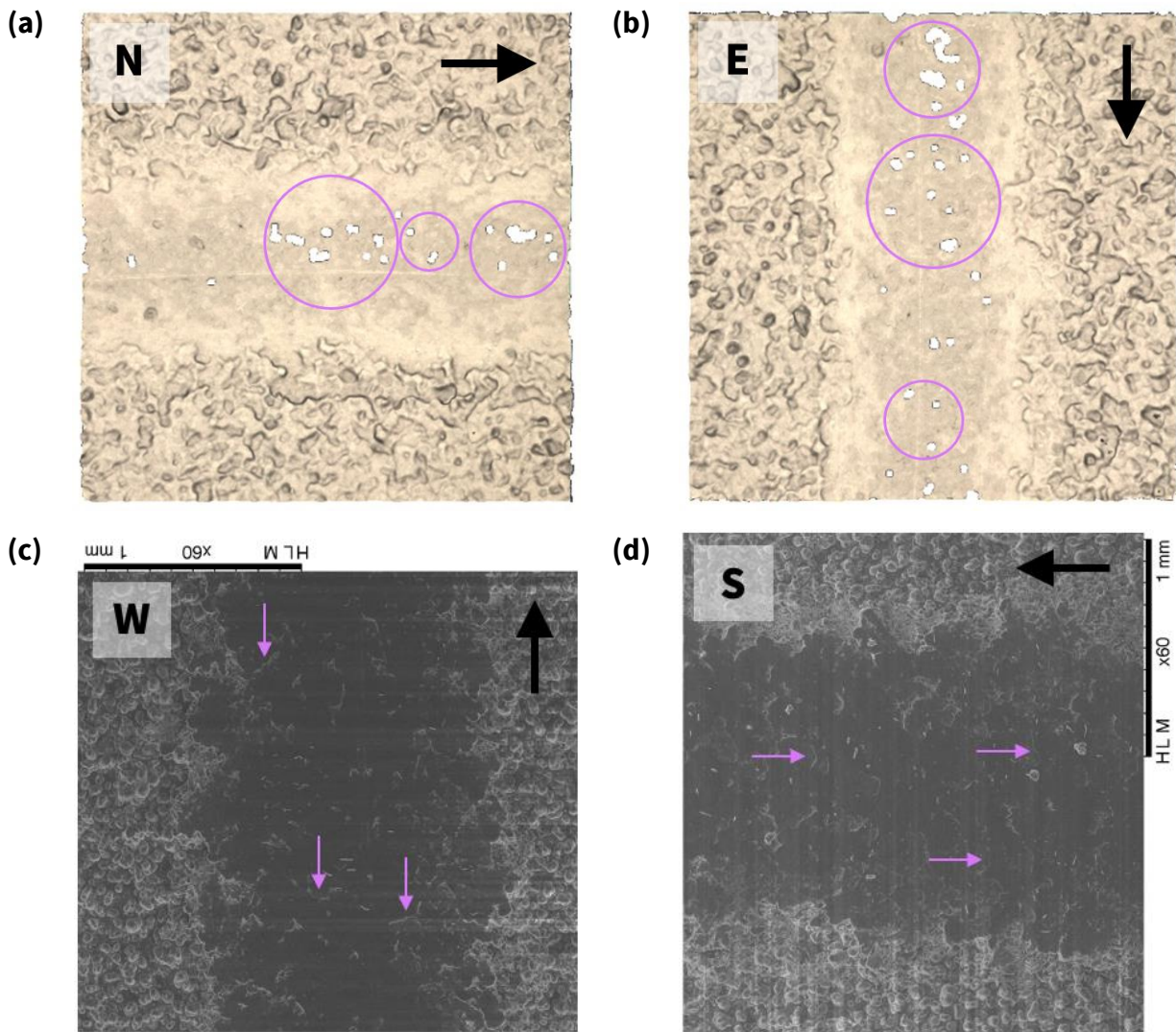


Figure 8.25 – Microscopy images captured after the second repeat $30\text{N} - 0.5\text{ms}^{-1}$ (high load / high speed) sliding test. These include wear scars obtained by FV microscopy at **(a)** north and **(b)** east locations, as well as SEM images obtained at **(c)** west and **(d)** south locations. The orientation of each arrow denotes the instantaneous direction of rotation of each disk region relative to the metal pin. Purple circled regions and arrow icons specify the locations where evidence of surface melting and plastic flow can be seen, respectively.

This high load / high speed sliding condition was determined to have a mean wear rate of $8.589 \times 10^{-3} \text{ mm}^3 \text{ m}^{-1}$, which was the largest W_{mean} value recorded during metal pin on polymer disk sliding.

Upon analysing the wear scars produced after $30\text{N} - 0.5\text{ms}^{-1}$ sliding, it was discerned that ploughing was the dominant mechanism by which wear occurred. More specifically,

evidence of plastic flow and surface melting (though very limited in comparison to the magnitude observed during to $30\text{N} - 0.05\text{ms}^{-1}$ sliding) can be seen in **Figure 8.25**.

Polymer Pin on Metal Disk Sliding

During polymer pin on metal disk sliding, the former was continuously subject to dynamic contact, as illustrated in **Figure 8.1**.

$3\text{N} - 0.05\text{ms}^{-1}$ / Low Load – Low Speed

Figure 8.26 includes SEM micrographs of a polymer pin worn surface and corresponding metal disk sample captured after $3\text{N} - 0.05\text{ms}^{-1}$ testing.

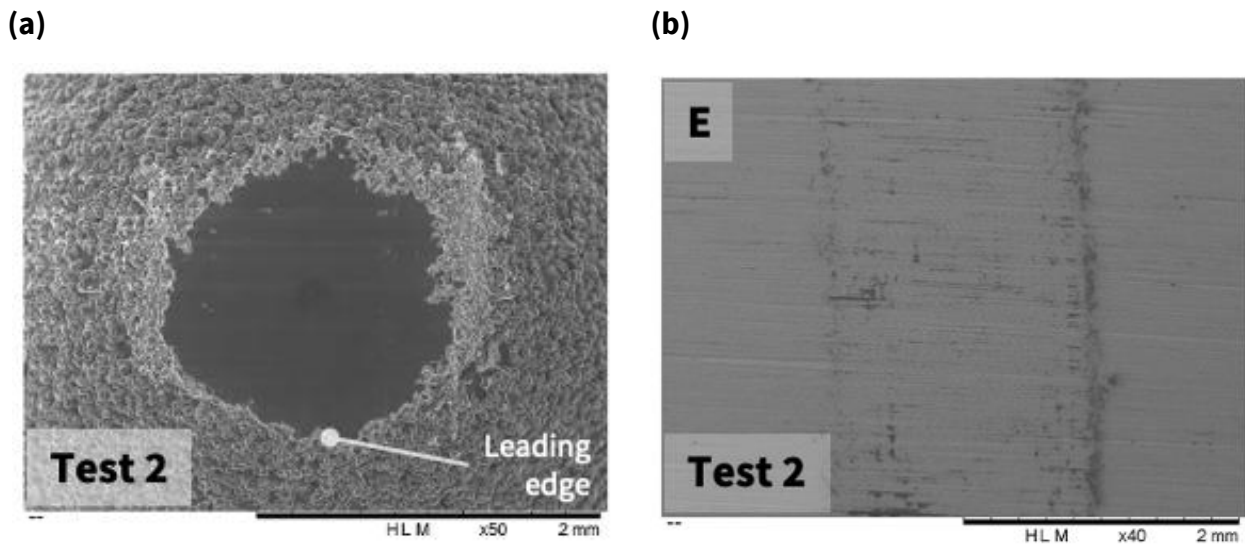


Figure 8.26 – SEM scan images of a **(a)** polymer pin worn surface and **(b)** metal disk sample (east location) captured after $3\text{N} - 0.05\text{ms}^{-1}$ (low load / low speed) sliding, specifically from test 2.

This low load / low speed sliding condition was determined to have a mean wear rate of $0.098 \times 10^{-3} \text{ mm}^3 \text{ m}^{-1}$, which was the lowest W_{mean} value recorded during polymer pin on metal disk sliding.

All of the worn polymer pin surfaces evaluated within this study were too reflective to be analysed by FV microscopy, independent of the normal loads or sliding speeds employed. An example of a nullified FV obtained scan can be seen in **Figure 8.27**.

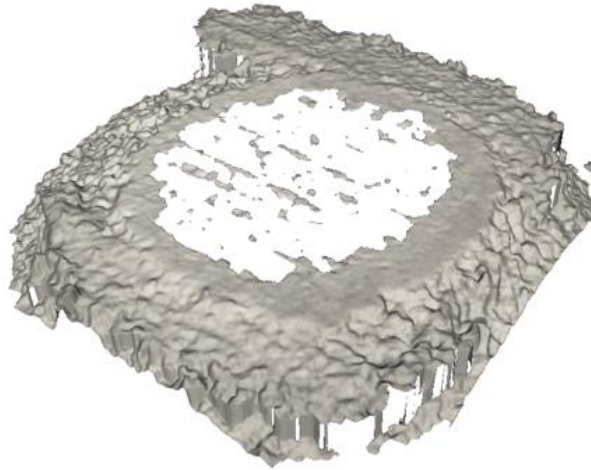


Figure 8.27 – An example of a worn polymer pin surface that was too reflective to be successfully scanned by FV microscopy.

The high reflectivity of each worn polymer pin surface indicates that frictional heating induced surface melting ensued during sliding. Moreover, concomitant thermal softening will have facilitated the yielding of asperity peaks, which explains why only plastic deformation was evident within the A_N of each polymer pin surface post-testing.

Furthermore, it can be seen in **Figure 8.26a** that material which resembles flash (within the context of polymer moulding) was displaced outwards, away from the leading edge of the polymer pin during sliding. The drawn-out nature of this polymer material was indicative of abrasive wear by plastic shear flow [199].

Additionally, relatively minor amounts of polymer material can be seen to have transferred and accumulated within the scratches on each metal disk surface presented in **Figure 8.26b**.

$3N - 0.5ms^{-1}$ / Low Load – High Speed

Figure 8.28 includes SEM micrographs of a polymer pin worn surface and corresponding metal disk sample captured after $3N - 0.5ms^{-1}$ testing.

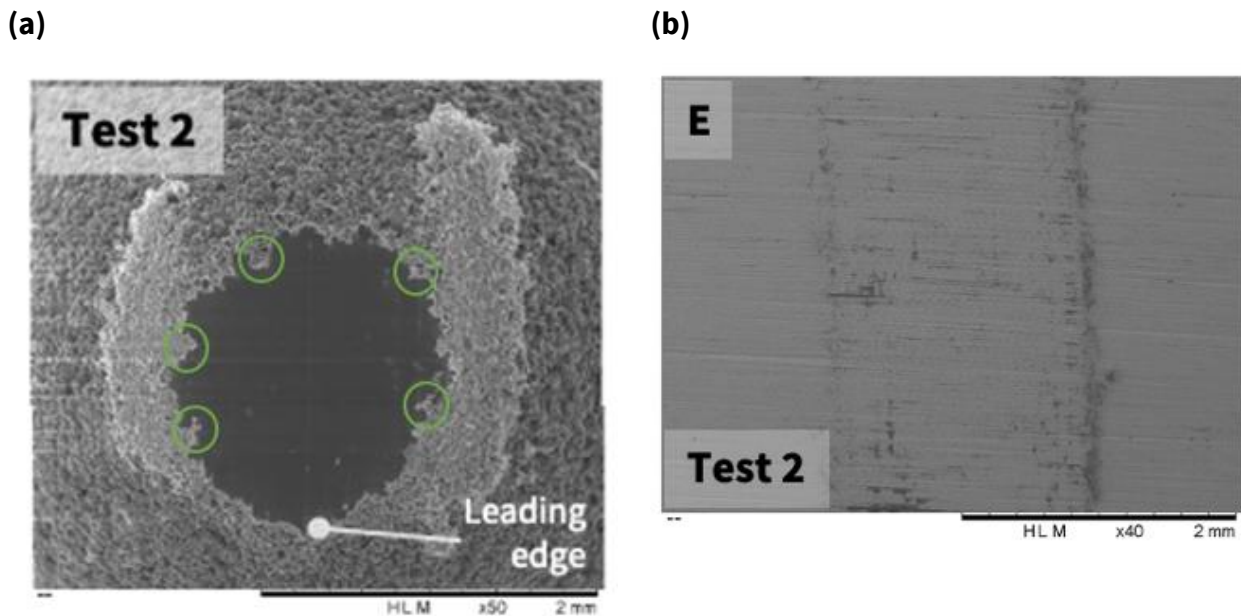


Figure 8.28 – SEM scan images of a **(a)** polymer pin worn surface and **(b)** metal disk sample (east location) captured after $3N - 0.5ms^{-1}$ (low load / high speed) sliding, specifically from test 2. Each circled location highlights a region in which clusters of asperity peaks can be seen.

In general, alike wear mechanisms to those previously examined (when analysing $3N - 0.05ms^{-1}$, polymer pin on metal disk sliding) were found to dominate during this low load / high speed sliding condition.

Though, the edge geometries of the polymer pin worn areas shown in **Figure 8.28a** suggest that asperity peak clusters supported the $3N$ normal loads elastically prior to them shearing during sliding.

Additionally, upon comparing **Figure 8.26b** and **Figure 8.28b**, it can be seen that similar magnitudes of polymer wear debris became interposed between adjacent scratch valleys during low load ($3N$), polymer pin on metal disk sliding. This indicates that sliding speed

had a negligible impact on the magnitude of polymer material that accumulated on each metal disk surface during testing.

$30\text{N} - 0.05\text{ms}^{-1}$ / High Load – Low Speed

Figure 8.29 includes SEM micrographs of a polymer pin worn surface and corresponding metal disk sample captured after $30\text{N} - 0.05\text{ms}^{-1}$ testing.

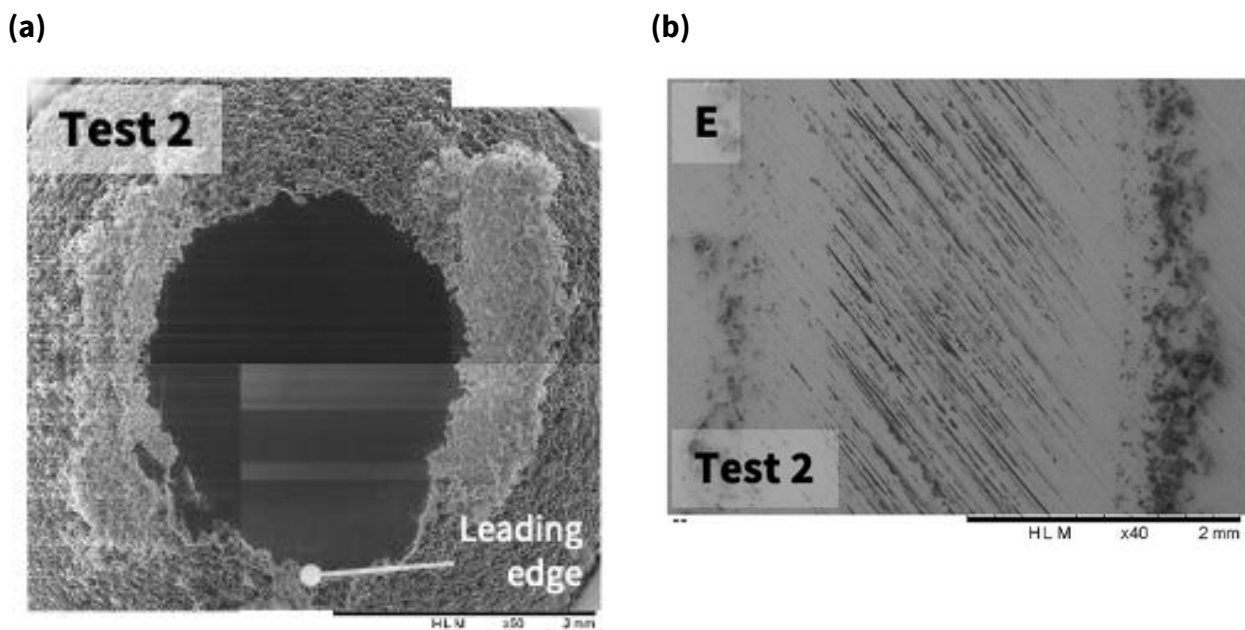


Figure 8.29 – SEM scan images of a **(a)** polymer pin worn surface and **(b)** metal disk sample (east location) captured after $30\text{N} - 0.05\text{ms}^{-1}$ (high load / low speed) sliding, specifically from test 2.

This high load / low speed sliding condition was determined to have a mean wear rate of $0.902 \times 10^{-3} \text{ mm}^3 \text{ m}^{-1}$, which was the largest W_{mean} value recorded during metal pin on polymer disk sliding.

The worn polymer pin surfaces shown in **Figure 8.29a** were akin to those presented in **Figure 8.26a** and **Figure 8.28a**, which suggests that they were also subject to frictional heating facilitated plastic shear flow during steady-state sliding.

As shown in **Figure 8.29b**, this sliding condition resulted in the largest volumes of polymer wear debris being transferred to each metal disk surface. However, this was proportional to the total amount of wear incurred during testing (as characterised by wear rate), which suggests that increased availability prompted more material transfer.

Furthermore, it can be seen in **Figure 8.29b** that the transferred polymer material accumulated within the adjacent scratch lengths within each wear track, and also at their edges. Despite this, no discernible changes in COF were evident in any of the steady-state sliding responses ($\sim 250\text{m} - 100\text{m}$) presented in **Figure 8.14a**.

30N – 0.5ms⁻¹ / High Load – High Speed

Figure 8.30 includes SEM micrographs of a polymer pin worn surface and corresponding metal disk sample captured after 30N – 0.5ms⁻¹ testing.

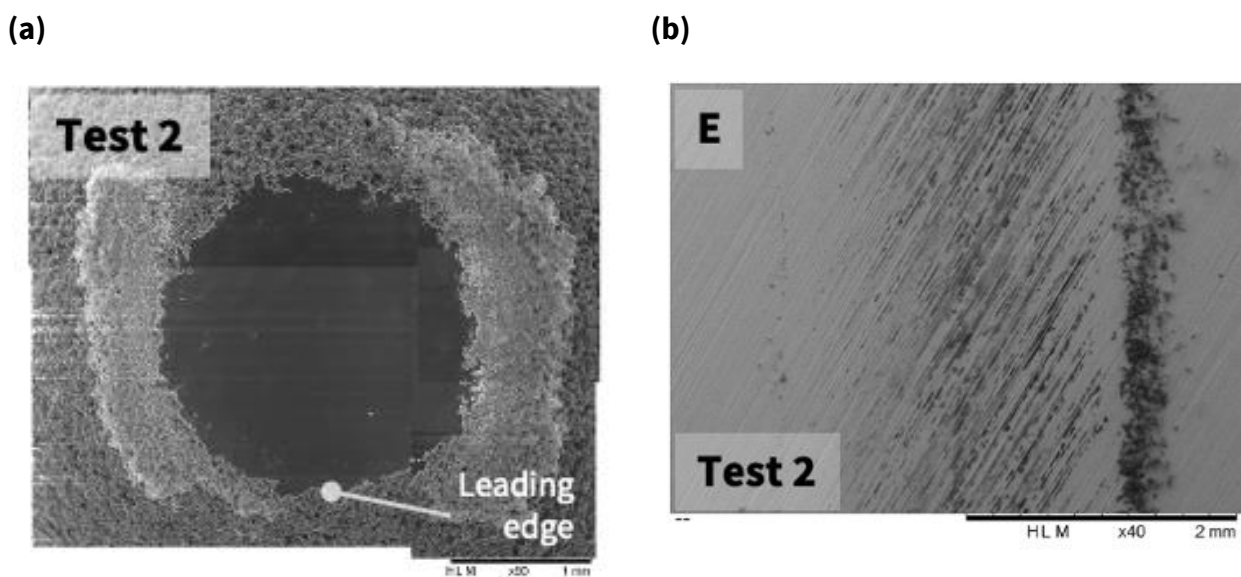


Figure 8.30 – SEM scan images of a (a) polymer pin worn surface and (b) metal disk sample (east location) captured after 30N – 0.5ms⁻¹ (high load / high speed) sliding, specifically from test 2.

As shown in **Figure 8.30a**, this 30N – 0.5ms⁻¹ (high load / high speed) sliding condition also led to the abrasive wear of each polymer pin surface, primarily via the mechanism of frictional heating facilitated plastic shear flow.

Furthermore, it can be seen in **Figure 8.30b** that transferred polymer wear debris accumulated within the scratches on each metal disk surface, as well as at the edges of each wear track. This was congruent with observations made during $30\text{N} - 0.05\text{ms}^{-1}$ (high load / low speed) sliding. Though, during this sliding condition, the latter was more prevalent at the outer edges of each wear track, which was likely due to the increased rotational forces incurred as a result of the higher sliding speeds employed (0.5ms^{-1}) during testing.

8.3.2.3 Material Transfer

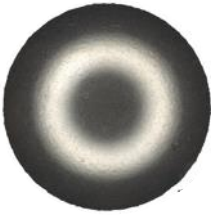
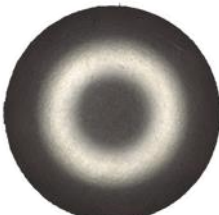
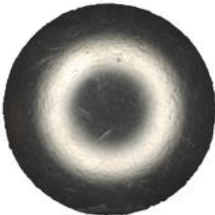
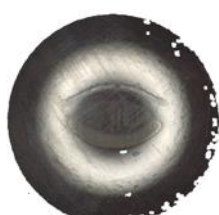
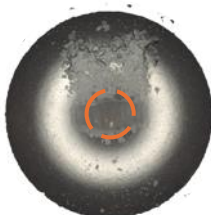
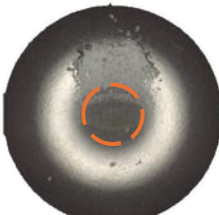
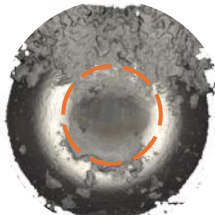
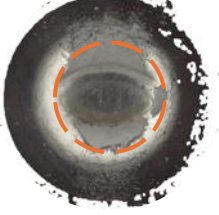
Metal Pin on Polymer Disk Sliding

Table 8.9 includes FV microscopy obtained scan images of several polymer pin surfaces before and after each sliding test. While it can be seen that polymer material did transfer to all of the pin surfaces during testing, no visible transfer film formation occurred within their respective contact areas (denoted by the regions circled in orange). The polymer wear debris that did transfer, predominantly attached itself loosely to the leading edge of each metal pin surface and adhered more securely to the rear. However, neither of these occurrences were ascertained to have had any effect on friction or wear.

Though, notably larger amounts of polymer material transfer were observed during $30\text{N} - 0.05\text{ms}^{-1}$ sliding, compared to any of the other metal pin on polymer disk sliding conditions detailed in **Table 8.9**. In agreement with the discussion in **Section 8.3.2.2**, it is likely that the higher interfacial contact temperatures incurred during $30\text{N} - 0.05\text{ms}^{-1}$ sliding prompted the increased adhesion of polymer wear debris to the leading edges of each metal pin surface during testing.

Table 8.9

FV microscopy obtained scan images of metal pin surfaces captured before and after each second repeat sliding test. Despite only one set of metal pin surfaces being presented for each sliding condition evaluated, the volume of polymer material that accumulated on each remained consistent between repeat tests. Circled orange regions represent the contact area of each metal pin surface evaluated.

Evaluated before / after testing	3N – 0.05ms ⁻¹	3N – 0.5ms ⁻¹	30N – 0.05ms ⁻¹	30N – 0.5ms ⁻¹
Before				
After	<i>Leading edge</i> 	<i>Leading edge</i> 	<i>Leading edge</i> 	<i>Leading edge</i> 

Polymer Pin on Metal Disk Sliding

As mentioned in **Section 8.2.2**, surface grinding was employed to prepare each metal disk sample prior to testing. Consequently, the surfaces produced comprised of scratch marks, in which polymer material was observed to accumulate within. More specifically, greater amounts of polymer material accumulated within the valleys of each scratch when its lay direction was perpendicular to the direction of sliding, as shown in **Figure 8.31**.

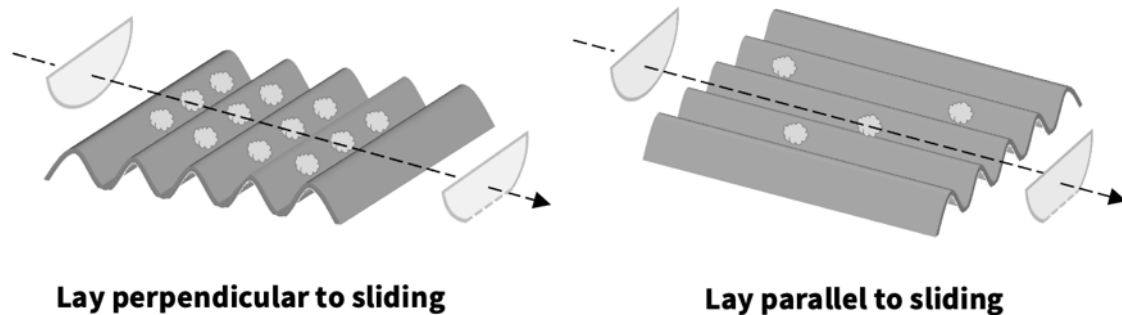


Figure 8.31 – Illustrations highlighting the impact lay direction had on the magnitude of polymer wear debris that accumulated within adjacent scratch valleys during sliding.

As can be seen throughout **Section 8.3.2.2**, transferred polymer material appeared to remain relatively separate and was localised within the scratch valleys on each metal disk surface. This suggests that resultant wear debris became interposed between adjacent scratches, rather than adhered together to form a transfer film. Ultimately, no marked changes in COF, indicative of facilitated or impeded sliding, could be identified in any of the steady-state, polymer pin on metal disk sliding responses presented throughout **Section 8.3.1.1**.

8.3.2.4 Contact Configuration

As illustrated in **Figure 8.32**, the configuration in which contacting bodies were loaded against one another intrinsically determined the contact geometries and wear mechanisms that ensued during sliding.

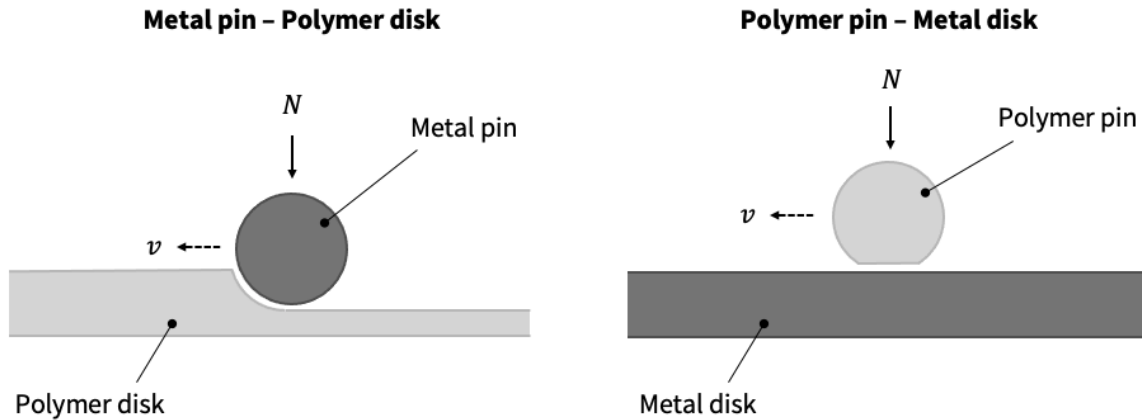


Figure 8.32 – An illustration highlighting the differences in contact geometry induced when converse contact configurations were employed.

Metal Pin on Polymer Disk Sliding

As illustrated in **Figure 8.32**, upon indenting the polymer disk, the leading edge of the metal pin, specifically the proportion that was subject to lateral dynamic contact, increased significantly during sliding. Consequently, the rate at which asperity peaks were sheared or ploughing ensued will have also increased, hence why comparatively greater magnitudes of wear occurred during this configuration of testing than during polymer pin on metal disk sliding.

Polymer Pin on Metal Disk Sliding

Polymer pin on metal disk sliding was characteristic of a change in contact geometry, such that point contacts transformed into flat-on-flat contacts, independent of the operating conditions employed. Consequently, the apparent area of contact area (A_N) of each polymer pin will have increased significantly during sliding. A comparison between initial Hertzian contact area approximations and post-testing determined polymer pin worn areas can be seen in **Table 8.10**.

Table 8.10

A comparison between initial Hertzian contact area approximations and polymer pin mean worn areas measured post-testing. Corresponding standard deviation values are also given for the latter.

Normal load (N)	Hertzian contact area approximations (mm ²)	Worn pin surface areas measured post testing (mm ²)	
		0.05ms ⁻¹	0.5ms ⁻¹
3	0.078	1.952 ± 0.099	2.442 ± 0.344
30	0.362	5.783 ± 0.581	4.283 ± 0.468

The differences between initial Hertzian contact pressure approximations and the resultant contact stresses (p) (calculated post-testing) are detailed in **Table 8.11**. More specifically, the latter were calculated via **Equation 8.1** below:

$$p = \frac{N}{A_{\emptyset}}$$

Equation 8.1

where N is the predetermined applied normal load and A_{\emptyset} is a circular approximation of the worn surface area being evaluated.

Table 8.11

A comparison between initial Hertzian contact pressure approximations and the mean resultant contact stresses (p) calculated post-testing. Corresponding standard deviation values are also given for latter.

Normal load (N)	Hertzian ball-on-flat mean contact pressure approximations (MPa)	Flat-on-flat contact stresses determined post testing (MPa)	
		0.05ms ⁻¹	0.5ms ⁻¹
3	38.5	1.54 ± 0.08	1.24 ± 0.17
30	82.9	5.22 ± 0.50	7.06 ± 0.73

As can be seen in **Table 8.11**, the transformation from a ball-on-flat to a flat-on-flat contact geometry significantly reduced the contact stresses incurred during sliding. This

suggests that the greatest amounts of wear occurred during initial sliding when contact stresses were at their maximum.

Furthermore, upon test completion, resultant worn pin surfaces were found to be fully dense, as can be seen in the SEM micrographs presented throughout **Section 8.3.2.2**. This indicates that the adjacent powder particles which comprised each contacting polymer pin interface will have further coalesced due to the compaction and frictional heating incurred as result of the applied normal loads and continuously-in-contact nature of this test configuration, respectively.

8.3.2.5 Statistical Analysis of Wear Results

Figure 8.33 includes contour plots that visually elucidate the relationship between friction force, normal load and sliding speed for both contact configurations evaluated.

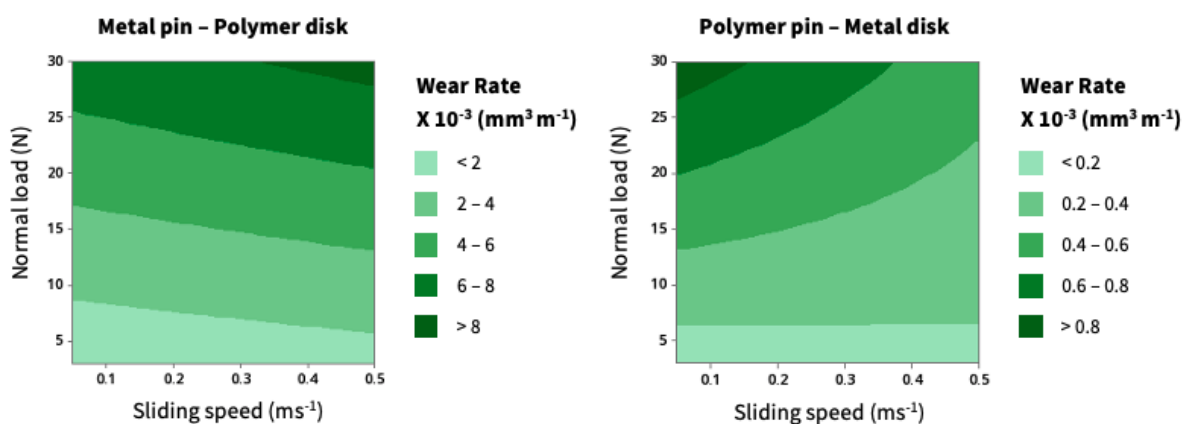


Figure 8.33 – Contour plots showing the relationship between wear rate, normal load and sliding speed for both contact configurations evaluated.

Additionally, **Figure 8.34** outlines the main and interaction effects each operating condition had on wear rate in ascending / descending order of influence. Statistically significant terms included contact configuration (C), normal load (A), as well as the interaction between normal load x contact configuration (AC), sliding speed x contact configuration (BC).

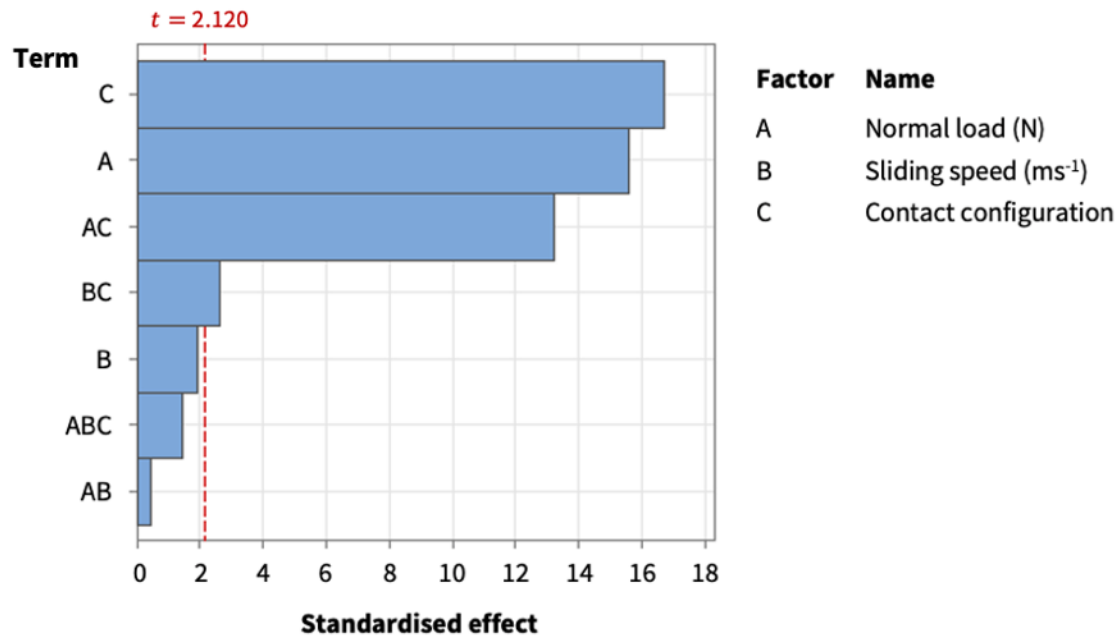


Figure 8.34 – A Pareto chart showing the extent to which normal load, sliding speed and contact configuration influenced wear rate.

Contact configuration was found to be the most statistically influential operating condition evaluated. This is congruent with previous discussion in **Section 8.3.2.4**, where it was established that contact configuration intrinsically determined the size and shape of the contact area that ensued during sliding.

Additionally, normal load, as well as its interaction with contact configuration, were both determined to impact wear. As discussed throughout **Section 8.3.2.2**, the extent to which normal load affected wear corresponded with the wear mechanisms that dominated during each sliding condition.

The interaction between sliding speed and contact configuration was also found to have an influential effect on wear rate. Though, as shown in **Figure 8.34**, the impact of this interaction effect was relatively minor when compared to the other statistically significant terms.

8.4 Conclusions

This study investigated how the sliding behaviours of laser sintered PA12 components were affected by varying operating conditions. More specifically, a Design of Experiments was executed to determine the extent by which normal load, sliding speed and contact configuration influenced the friction and wear properties of parts produced, as well as to ascertain insight into the mechanisms that ensued during each sliding condition. A summary of the key findings discerned during this study is outlined in **Table 8.12**.

Table 8.12A summary of the key findings ascertained during **Chapter 8**.

Operating conditions	Key phenomena ascertained	
	Friction	Wear
Normal load	<ul style="list-style-type: none"> - Normal load had by far the most statistically significant effect on F_f. - The interaction between normal load and contact configuration (AC), as well as sliding speed (AB), were both found to have statistically significant effects on F_f (in descending order of influence). 	<ul style="list-style-type: none"> - Normal load, as well as its interaction with contact configuration, both had a statistically significant effect on wear rate. - During metal pin on polymer disk sliding, applied 3N normal loads were jointly supported by bulk surface material and clusters of asperity peaks. - Higher normal loads (30N) resulted in larger wear rates, which prompted more material transfer during polymer pin on metal disk sliding.
	Mechanisms / impact of N : <ul style="list-style-type: none"> - Affected the fluctuations in COF recorded during sliding, as characterised by standard deviation. - Prompted frictional heating during polymer pin on metal disk sliding. - Determined whether elastic or plastic interactions occurred during metal pin polymer disk sliding. - Plastic shear flow and surface melting were both evident at higher normal loads (30N), and promoted by frictional heating during polymer pin on metal disk sliding. 	
Sliding speed	<ul style="list-style-type: none"> - Sliding speed had a statistically significant effect on F_f, despite this being discordant with Coulombs Law of Friction. - Low sliding speeds (0.05ms^{-1}) prompted heightened parabolic COF responses during initial metal pin on polymer disk sliding. - High sliding speeds (0.5ms^{-1}) resulted in plateauing increases in COF during running-in, independent of the normal load or contact configuration employed. 	<ul style="list-style-type: none"> - Higher speeds resulted in more wear during metal pin on polymer disk sliding. -

Mechanisms / impact of v :		
	<ul style="list-style-type: none"> - Running-in behaviours were primarily influenced by sliding speed. - Frictional heating affected COF by greater magnitudes at higher sliding speeds during polymer pin on metal disk sliding. 	<ul style="list-style-type: none"> - The additional momentum incurred during high speed sliding (0.5ms^{-1}) resulted in either greater asperity peak fracture, leading to an earlier onset of ploughing (metal pin – polymer disk), or an earlier transformation in contact geometry from ball-on-flat to flat-on-flat (polymer pin – metal disk).
Contact configuration	<ul style="list-style-type: none"> - Contact configuration, as well as its interaction with normal load (AC), both had a statistically significant effect on F_f. - Gradual increases in COF indicated that frictional heating was induced during polymer pin on metal disk sliding. - No apparent changes in COF could be discerned during metal pin on polymer disk sliding. - Increases in COF, due to frictional heating, were proportional to the magnitudes by which COF fluctuated during polymer pin on metal disk sliding. 	<ul style="list-style-type: none"> - Contact configuration had the most statistically significant effect on wear rate. - Specific mean wear rate values were in good agreement with those reported in the literature for both contact configurations evaluated. - Metal pin on polymer disk sliding prompted more wear than equivalent polymer pin on metal disk sliding.
Mechanisms / impact of contact configuration:		
	<ul style="list-style-type: none"> - Determined whether frictional heating was induced. 	<ul style="list-style-type: none"> - The configuration in which contacting bodies were loaded against one another intrinsically determined the contact geometries that ensued during sliding. - Frictional heating led to the thermal softening and subsequent enlargement of each polymer pin's A_N.

This work elucidated the main sliding features exhibited by laser sintered PA12 samples when subject to a wide range of operating conditions. Consequently, the insights gained could adequately inform the suitability of alike components for different end-use applications, or highlight the specific mechanisms to consider when further investigating their sliding behaviours.

Chapter 9

The Use of Solid Lubricants to Modify the Properties of Laser Sintered Polyamide-12 Components

Chapter Summary

This chapter investigated whether the tribological properties of specimens manufactured by LS could be modified through the inclusion of solid lubricants. The processability of PA12 powders containing polytetrafluoroethylene (PTFE), Graphite and Molybdenum disulphide (MoS₂) fillers were evaluated, and the surface, mechanical, friction and wear properties of the parts produced were characterised and compared with those of Virgin – PA12.

This chapter includes published work, available via the following citation:

K. Nar, C. Majewski and R. Lewis, Evaluating the effect of solid lubricant inclusion on the friction and wear properties of Laser Sintered Polyamide-12 components, *Wear*. 522 (2023) 204873. <https://doi.org/10.1016/j.wear.2023.204873>.

9.1 Introduction

In recent years, the inclusion of inorganic fillers within PA12 matrices has been explored as a way of introducing additional functionality to laser sintered polymer components, in order to improve their suitability for end-use applications [26,200].

Several additional factors must be considered to ensure filler reinforced polymeric composites are processable by LS and that their required functionalities are attained. These include the size [26], morphology [201], chemistry and percentage weight addition (% wt) [202] of filler reinforcement, as well as the interfacial adhesion between composite constituents [19,203] and the method by which they are combined [27].

As previously discussed in **Chapter 3**, specifically **Section 3.3**, Bai et al. [146] modified the tribological performance of laser sintered PA12 samples by including Molybdenum disulphide (MoS_2) within feedstock powders prior to processing. The addition of this solid lubricant reduced coefficient of friction (COF) and wear rate by 56.7% and 41.7%, respectively (during linear reciprocating, ball-on-flat sliding). The research presented in this chapter investigates a broader range of solid lubricants, in order to establish their suitability for use in LS and determine whether they also induce friction and / or wear altering responses.

9.1.1 Solid Lubricants

Bart et al. [204] highlighted that many materials qualify as solid lubricants but their intrinsic ability to reduce friction and wear arise by different mechanisms.

Structural solid lubricants have layered lattice compositions that feature weak bond strengths between layers, which enables them to shear easily when subject to loads parallel to their planar directions [205]. It is common for these sheared planes to then adhere to the contacting counterface and form a transfer film, so that facilitated sliding instead ensues between alike material [206]. Mariani [205] asserted that Graphite and

MoS₂ are the most well-established structural solid lubricants. Both have laminar crystal lattice structures that comprise of strong covalently bonded hexagonal planes separated by comparatively weaker Van der Waals forces [207].

Polytetrafluoroethylene (PTFE) is another well recognised solid lubricant. However, unlike Graphite and MoS₂, PTFE is an organic polymer that is lubricious due to its high softening point [208] and smooth macro molecular polymer chain profiles, which orient to facilitate slip [205]. Despite its exceptional efficacy as a low friction additive, PTFE is very susceptible to wear [209] and therefore rarely used for sliding applications in its neat form.

9.2 Materials and Methods

9.2.1 Materials

Virgin – PA12 was blended with the solid lubricants previously discussed in **Section 9.1.1** to create three different polymeric composites, hereinafter referred to as PTFE – PA12, Graphite – PA12 and MoS₂ – PA12.

PA12 matrices comprised of sieved virgin material that had an average particle size of 56µm [171]. Solid lubricant particle sizes, as quoted by their suppliers, are listed in **Table 9.1**. These were incorporated into each PA12 matrix in mass ratios of 1 : 100 (solid lubricant : PA12). More specifically, each batch of polymeric composite powder had a total weight of 3.03kg, which comprised of 30g of solid lubricant added to 3kg of PA12 powder. This solid lubricant loading ratio and particle size range was chosen to minimise agglomeration during dry mixing so that a uniform dispersion could be attained [26].

Table 9.1

Solid lubricant particle sizes, as quoted by their suppliers.

Solid lubricant	Size (μm)	Supplier
Graphite	Particle size distribution (PSD) = 5 – 10	Nanografi
Molybdenum disulphide	Average particle size (D_{50}) = 4.5	Lower Friction
Polytetrafluoroethylene	Average particle size (D_{50}) = 3	Lower Friction

Each polymeric composite was blended by rotary tumbling for 60 minutes upon filler inclusion, and for a further 60 minutes prior to loading each material into the LS machine.

Resultant samples were evaluated with respect to Virgin – PA12 control specimens, which were also laser sintered from the same batch of sieved virgin PA12 material.

9.2.2 Specimens

The Laser Sintering build process was performed in accordance with procedure outlined in **Section 4.2.1**. To ensure the properties of the parts produced were evaluated systematically, each material was processed identically, using the standard PA12 parameters detailed in **Table 4.3**. This was so that any changes in processability, or variations in resultant part sliding, could be attributed to the addition of each solid lubricant.

Four identical builds were performed (one for each material evaluated), with each comprising of different specimens depending on their subsequent intended analyses, as outlined in **Figure 9.1**. These included five ASTM D638 Type 1 specimens for tensile testing, three cylinders for micro-CT analysis, and six disk samples for friction and wear testing. The specific geometries of each are detailed in **Figure 4.5**, **Figure 5.2** and **Figure 4.9a**, respectively.

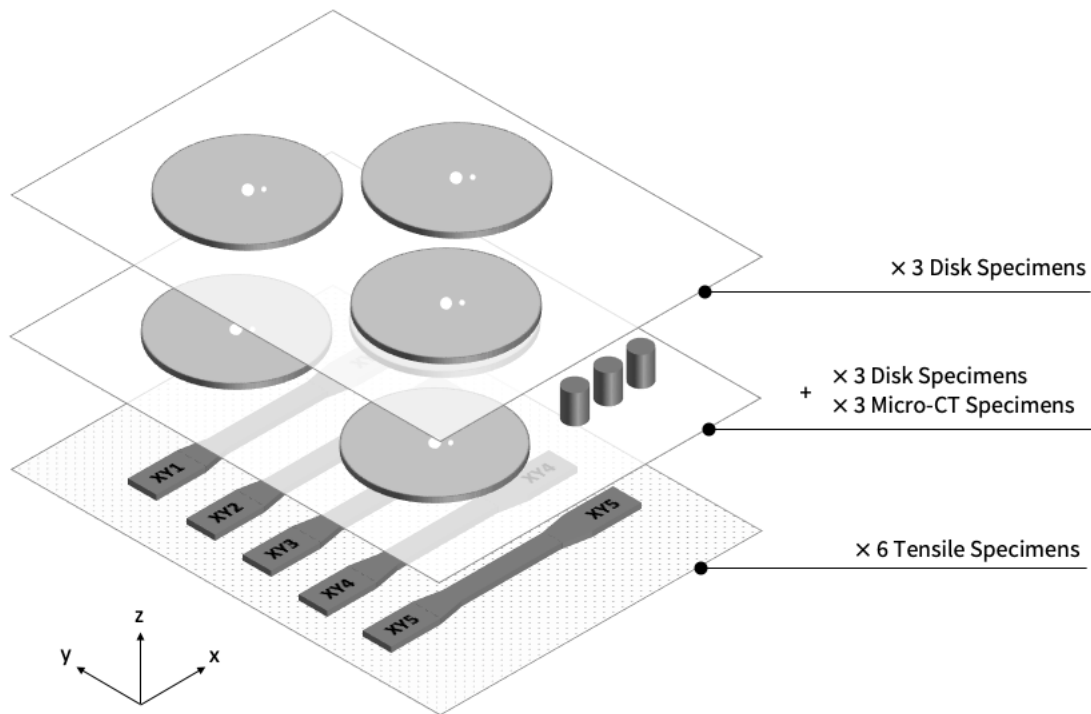


Figure 9.1 – A schematic illustrating the geometry and positioning of samples produced within this study (**Chapter 9**).

Once the LS build process was complete and the parts produced were fully cooled to room temperature, compressed air was used to remove any loose powder particles from the surfaces of Virgin – PA12, Graphite – PA12 and MoS₂ – PA12 samples. PTFE – PA12 specimens were found to have ‘harder’ powder cakes so additional glass bead blasting was required to break these samples out from their surrounding powder.

9.2.3 Characterisation

9.2.3.1 Filler Dispersion

SEM and micro-CT were utilised to identify the presence of solid lubricants within each PA12 matrix, both in powder and part form. These analyses were carried out in accordance with the procedures outlined in **Section 4.2.2.2** and **Section 4.2.2.4**, respectively.

9.2.3.2 Surface Analysis

Focus Variation (FV) microscopy was used to evaluate the top surface topographies of each laser sintered material, as well as post-testing, to characterise the widths of the wear scars produced, and any material transfer that occurred during sliding; the former were quantitatively described by their Root Mean Square (S_q) and Skewness (S_{sk}) roughness values.

All surface analysis was carried out in accordance with the procedure specified in **Section 4.2.2.2**, with roughness being characterised at three evenly distributed locations across the top surfaces of tensile test specimens.

9.2.3.3 Tensile Testing

Tensile testing was used to characterise the Young's Modulus (YM), Ultimate Tensile Strength (UTS) and Elongation at Break (EaB) of samples produced. Each test was executed via the procedure outlined in **Section 4.2.2.1**, in accordance with ASTM D638-14.

9.2.3.4 Thermal Analysis

A Perkin Elmer DSC8500 Differential Scanning Calorimeter (DSC), programmed with the procedure outlined in **Table 9.2**, was used to determine the melting and cooling behaviours of each material ¹⁰. Approximately 8mg of polymeric feedstock powder was analysed when conducting each DSC run.

¹⁰ This previously developed DSC programme is standard operating procedure within the Advanced Polymer Sintering Laboratory for characterising the thermal properties of polymers for LS.

Table 9.2

The DSC programme employed within this study.

Step number	Step details
1	Hold at 20°C for 1 minute
2	Heat from 20°C to 250°C at 10(°C) min ⁻¹
3	Hold at 250°C for 1 minute
4	Cool from 250°C to 20°C at 10(°C) min ⁻¹
5	Hold at 20°C for 1 minute

9.2.3.5 Friction and Wear Testing

Friction and wear were characterised by COF and specific wear rate, respectively, which involved performing rotating, ball-on-flat, pin-on-disk, uni-directional sliding tests, in accordance with the procedure detailed in **Section 4.2.2.6**, specifically via ‘configuration 1’ (stainless steel pin – laser sintered polymeric disk). More specifically, sliding tests were performed on the top surfaces of disk samples at a constant speed of 0.35ms⁻¹, over a sliding distance of 1000m, and at low and high applied normal loads of 10N and 30N, respectively. In congruency with **Chapter 7**, these operating conditions were chosen because they fell within the mid-range of parameters previously employed within the literature, as outlined in **Table 3.3**, whilst allowing varying loading conditions to be evaluated. Each laser sintered material was evaluated three times ¹¹ so that mean values could be obtained.

COF data was outputted directly from the UMT, and specific wear rate values were calculated using **Equation 4.2**. The latter of which, first required wear volumes to be determined from the widths of the wear scars produced, as outlined in **Table 4.6**.

¹¹ Excluding MoS₂ – PA12 samples which could only be evaluated once during 30N sliding due to resultant components curling significantly during building. This is discussed in greater detail in **Section 9.3.2**.

9.3 Results and Discussion

Each polymeric composite material was successfully processed via LS, and the properties of the parts produced are discussed in the following sections of this chapter.

9.3.1 Filler Dispersion

Particles with sizes and morphologies congruent with the solid lubricants used within this study can be seen in the SEM images presented in **Figure 9.2**. These particles were all well-dispersed within their respective matrices, and no qualitative evidence of agglomeration can be seen¹². Ultimately, solid lubricant particle size distributions within the range of 3 μ m – 10 μ m were found to be suitable for producing homogenous composite PA12 powders when combined by rotary blending.

¹² Supplementary analysis provided in **Appendix D** includes SEM images of virgin – PA12 powders containing PTFE (from the same batch used in this study) in increased mass loadings of 1 : 50 and 1 : 25 (solid lubricant : PA12). The increased presence of PTFE particles within these SEM images, proportionate to their mass loadings, reaffirms that the particles highlighted in **Figure 9.2** correspond with the addition of each solid lubricant evaluated within this study.

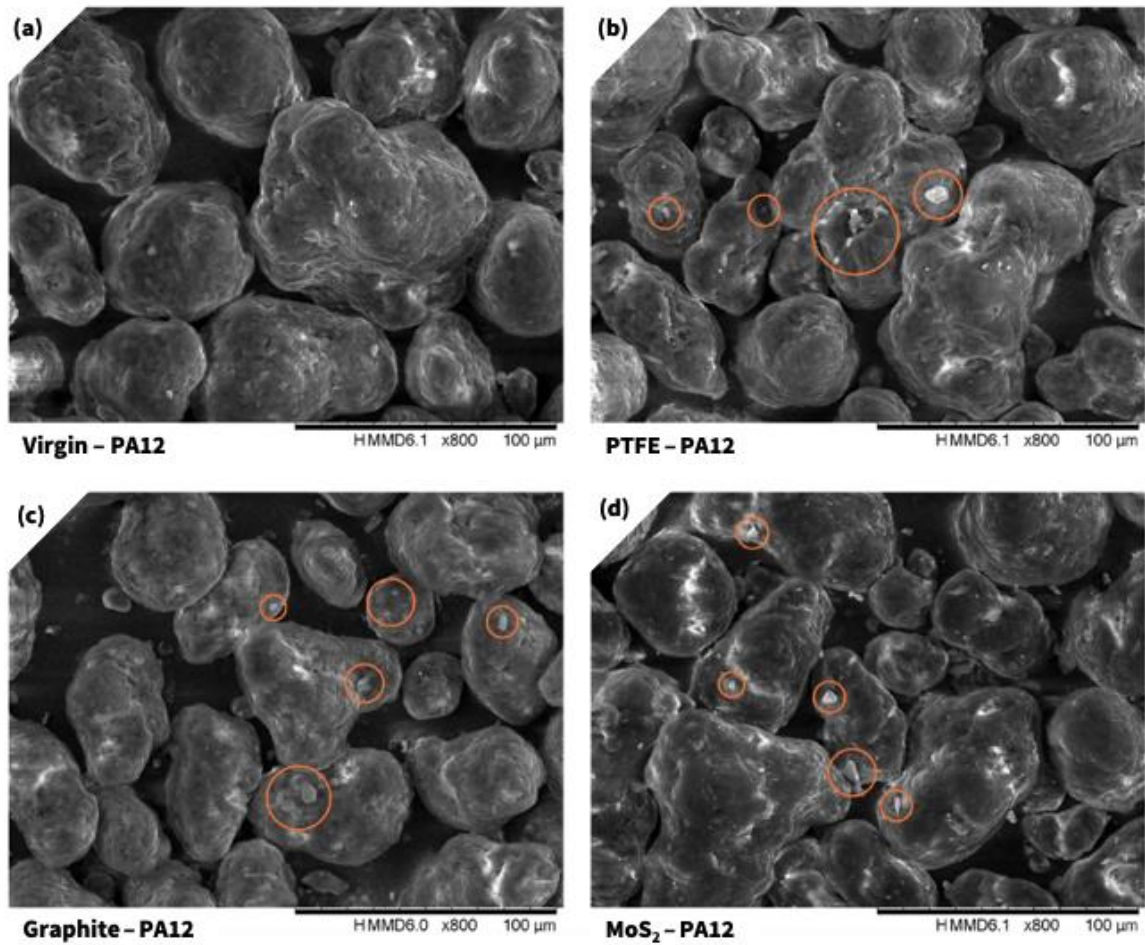


Figure 9.2 – SEM images of each feedstock material, including **(a)** Virgin – PA12, **(b)** PTFE – PA12, **(c)** Graphite – PA12 and **(d)** MoS₂ – PA12 powders. Corresponding solid lubricant particles have been circled in orange.

Figure 9.3 includes micro-CT obtained volumetric renderings of each material after they were laser sintered.

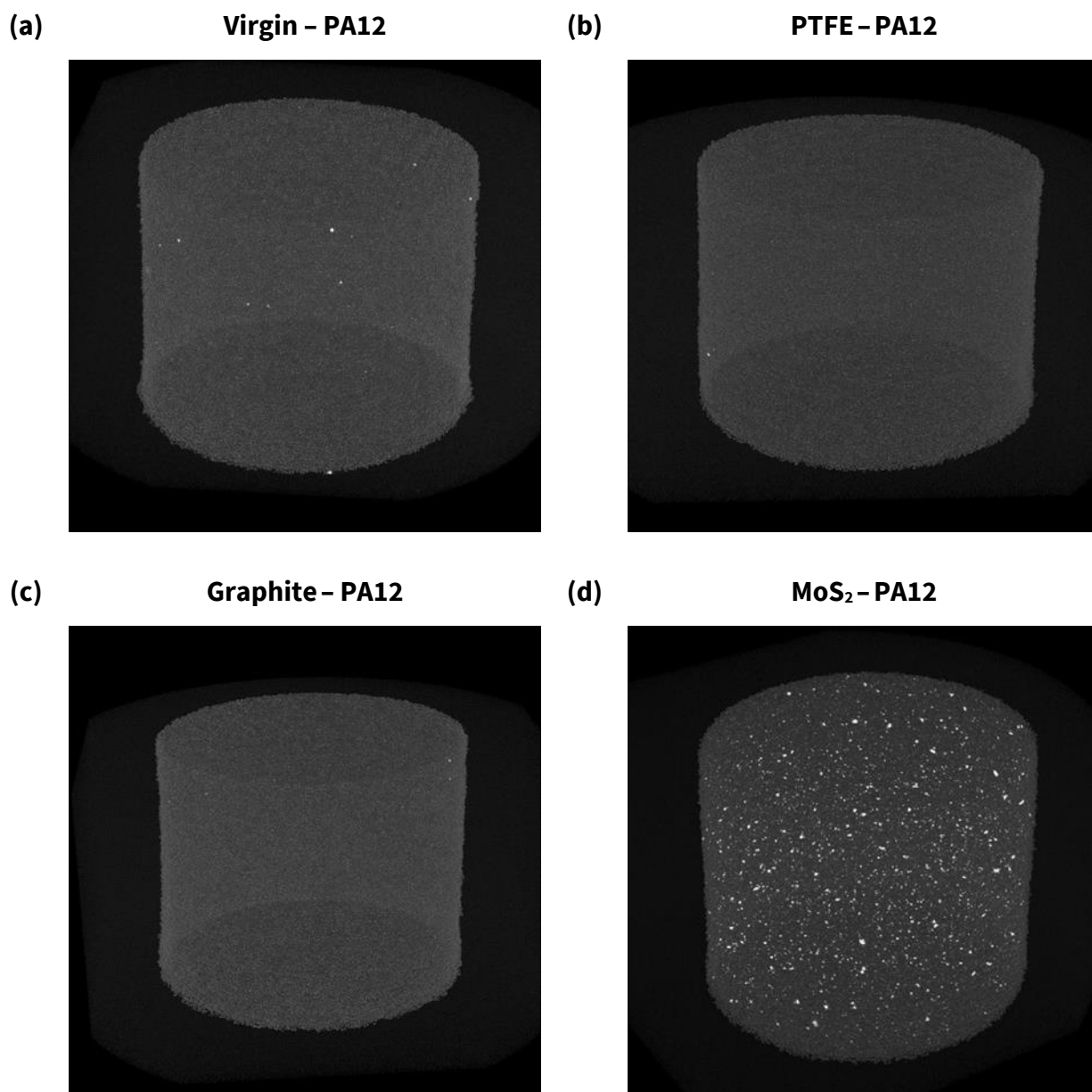


Figure 9.3 – Micro-CT rendered volumes of **(a)** Virgin – PA12, **(b)** PTFE – PA12, **(c)** Graphite – PA12 and **(d)** MoS₂ – PA12 samples. Brighter voxels represent locations in which more radiation was attenuated, and thus the presence of inclusions and / or contaminants within each laser sintered PA12 matrix.

It was not possible to distinguish PTFE from PA12 due to both polymers having similar densities, and thus alike attenuation characteristics.

MoS₂ – PA12 was the only polymeric composite within which solid lubricant material could be identified. Accordingly, comparatively brighter voxels can be seen to be well-dispersed without any qualitative evidence of apparent agglomeration.

Contrastingly, only a few Graphite particles could be seen in the corresponding scan output presented in **Figure 9.3b**. This finding contradicts the results discussed in the subsequent sections of this chapter, in which the addition of Graphite was shown to alter the mechanical and tribological properties of PA12, as well as its appearance both in powder and part form. This suggests that the micro-CT scanning parameters adopted within this study require further tuning in order to differentiate Graphite from PA12.

9.3.2 Part Warpage


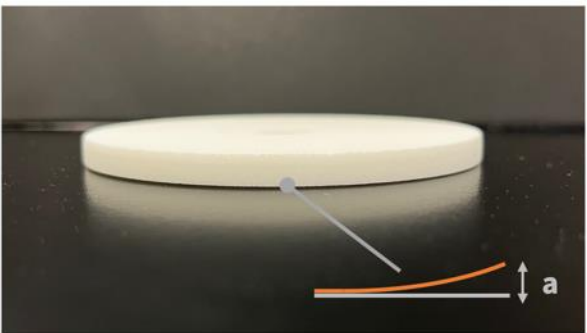

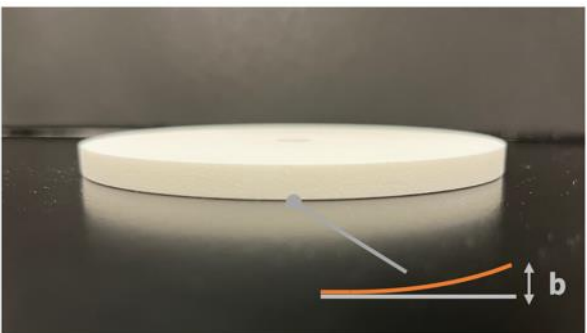

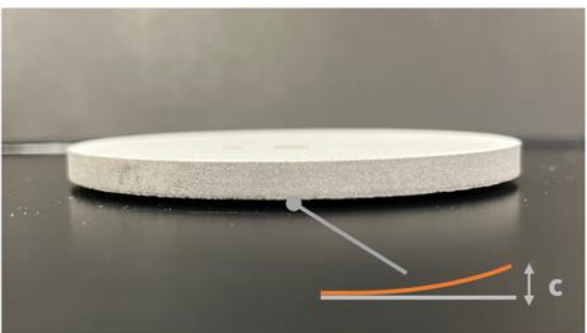
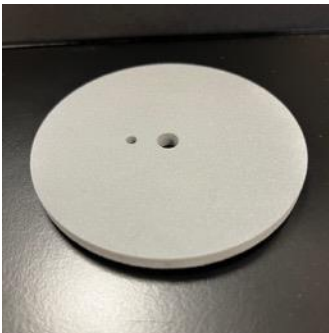
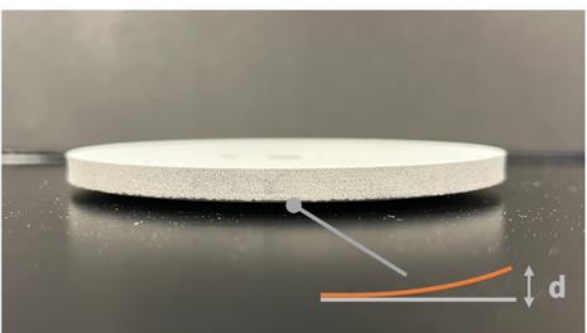
As can be seen in **Table 9.3**, Graphite – PA12 and MoS₂ – PA12 samples experienced curl localised at the perimeters of each disk specimen. Practically, this would render many parts produced as being unsuitable for end-use adoption, and in this study prevented repeat 30N sliding tests from being carried out on MoS₂ – PA12 samples.

Part warpage is intrinsic to polymer LS and typically occurs when the temperature differential between the bulk and upper surface of a part is too extreme during building. The latter will typically be lower in temperature, particularly at the edges of the part, due to being convectively cooled every time a new powder layer is deposited. Consequently, residual stresses will be induced, resulting in differential shrinkage at the edges of the parts produced. Furthermore, the disk specimens produced had large cross-sections relative to the build area, which will have prompted the occurrence of significant in-situ cooling during the scanning of each layer [210].

As shown in **Figure 9.4** and **Table 9.4**, the onset of crystallisation temperature (T_c) of each composite powder was greater than the T_c of Virgin – PA12. The magnitudes by which the former differed from the latter were also concordant with the resultant part warpages visible in **Table 9.3**. Therefore, correspondingly increasing each materials powder bed temperature (T_b) would likely minimise the curl induced during building.

Table 9.3

A qualitative description of the curl induced during the processing of each material. Resultant part warpages were as follows: $a \sim b < c < d$.

Material	Resultant part warpage	
Virgin – PA12		
PTFE – PA12		
Graphite – PA12		
MoS ₂ – PA12		

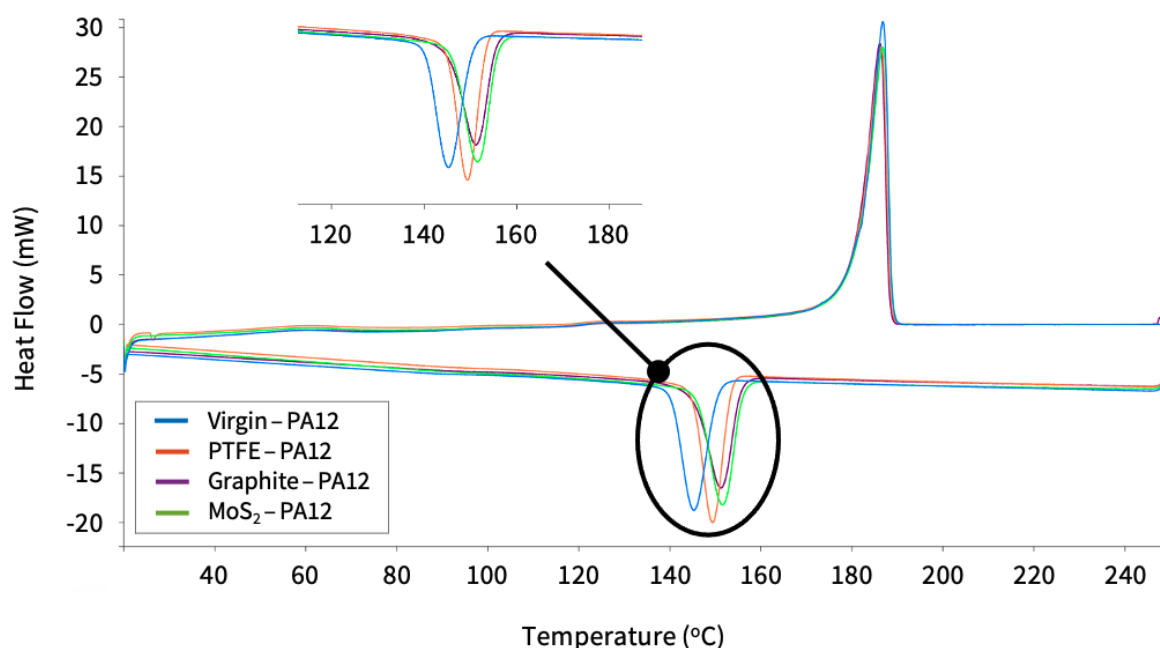


Figure 9.4 – Differential Scanning Calorimetry (DSC) obtained heating and cooling curves of each powdered material evaluated within this study.

Table 9.4

The onset of crystallisation temperatures of each powdered material. Specific values were determined from the DSC obtained cooling curves presented in **Figure 9.4**.

Material	Onset of crystallisation temperature (°C)
Virgin – PA12	150.43
PTFE – PA12	153.38
Graphite – PA12	155.52
Mos ₂ – PA12	155.94

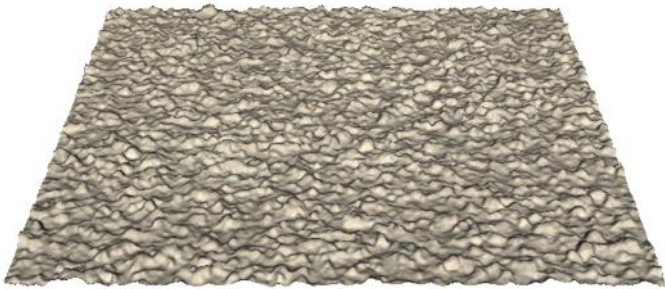
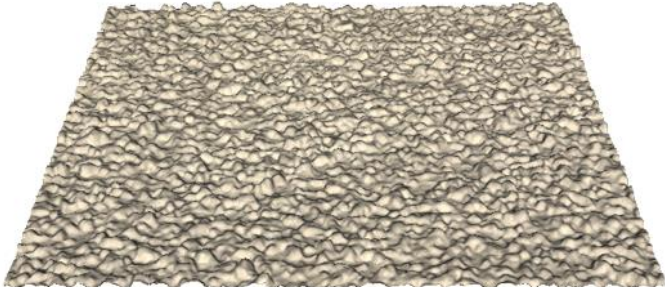
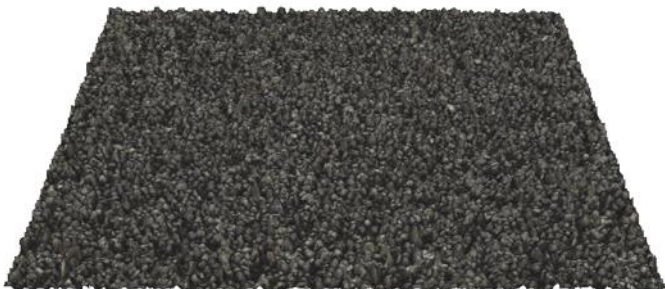

9.3.3 Surface Topographies

Table 9.5 includes both qualitative and quantitative descriptions of each materials resultant top surface topographies. As shown in **Figure 9.5a**, the addition of PTFE, Graphite and MoS₂ increased the mean top surface heights of parts produced by 2.24µm, 2.08µm and 1.91µm, relative to Virgin – PA12, respectively. Despite this, all measured top

surface S_q values were in good agreement with those discussed in **Chapter 6**, as well as those reported in related literature [93,211].

Table 9.5

Qualitative and quantitative descriptions of the top surface topographies of each laser sintered material. The evaluation areas depicted within each scan image are 3.7mm x 3.7mm in size.

Material	FV microscopy obtained scan images of each materials laser sintered top surface topography	S_q (μm)	S_{sk}
Virgin – PA12		12.82 (± 0.53)	0.76 (± 0.12)
PTFE – PA12		15.06 (± 1.17)	0.30 (± 0.06)
Graphite – PA12		14.90 (± 0.62)	0.55 (± 0.06)
MoS ₂ – PA12		14.73 (± 0.59)	0.77 (± 0.04)

Furthermore, it can be seen in **Figure 9.5b** that all sample top surfaces had positive Skewness values and were therefore all asperity peak dominated (in accordance with the

mechanism of finish layer powder particle adhesion). However, resultant PTFE – PA12 sample top surfaces were notably more Gaussian, which suggests that the inclusion of PTFE diminished the effect of finish layer powder particle adhesion by instead facilitating the mechanism of polymer melt viscous flow. Both of these mechanisms were previously discussed in detail in **Chapter 6**.

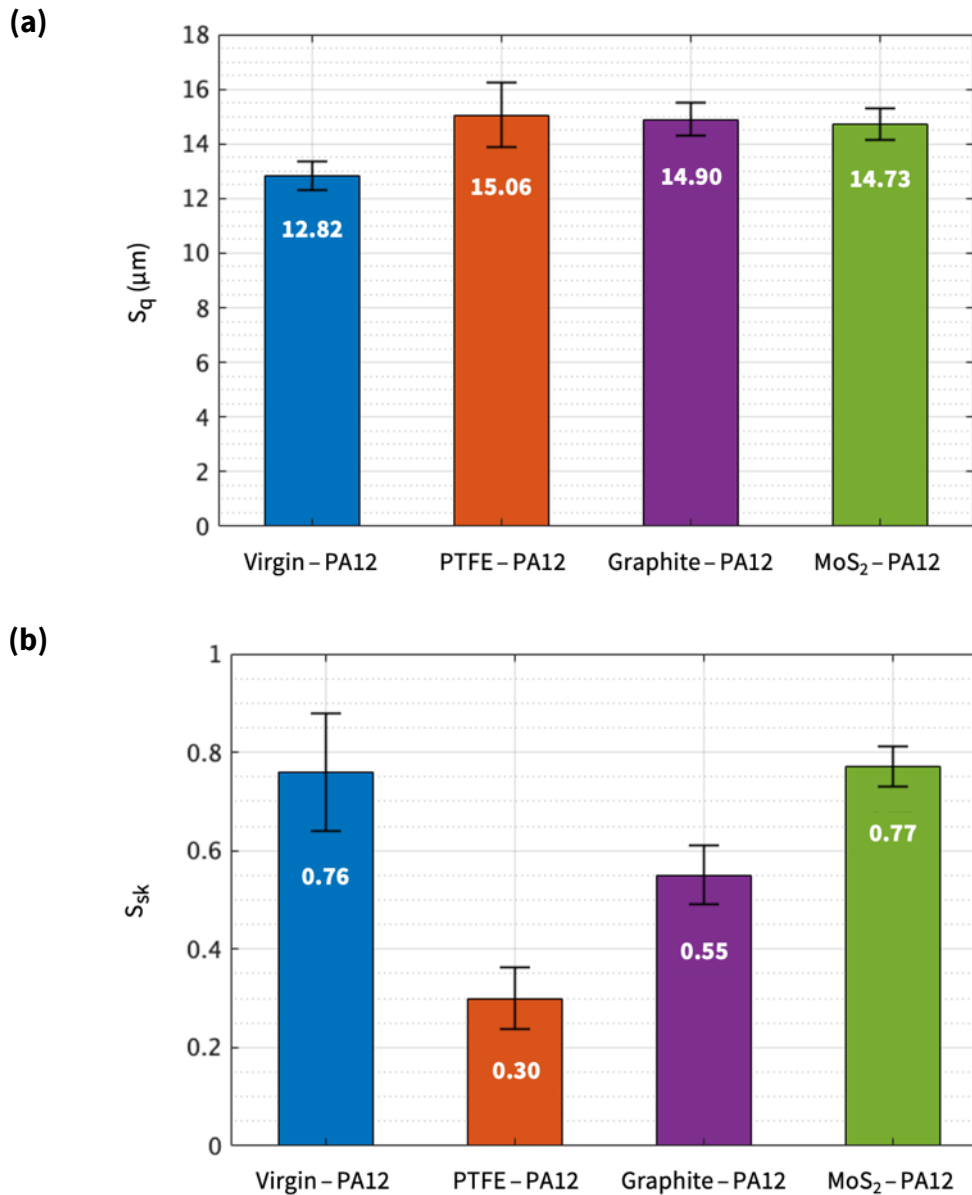


Figure 9.5 – Top surface topography information, including the mean (a) S_q and (b) S_{sk} roughness values determined for each material evaluated within this study.

9.3.4 Tensile Properties

The stress-strain curves and corresponding mean tensile properties for each material are shown in **Figure 9.6** and **Table 9.6**, respectively. In general, the mechanical performance of laser sintered PTFE – PA12, Graphite – PA12 and MoS₂ – PA12 composites were comparable with Virgin – PA12.

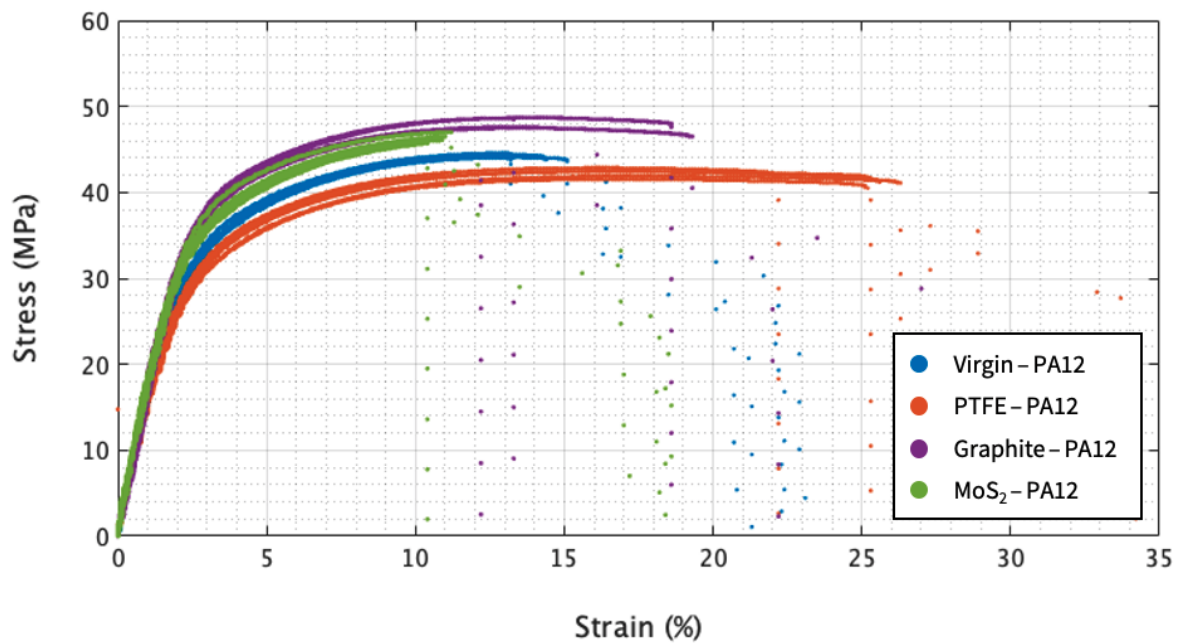


Figure 9.6 – The resultant tensile curve of each material specimen evaluated within this study.

Table 9.6

The mean tensile properties of each material, as well as their corresponding standard deviation values.

Material	Young's Modulus (MPa)	Ultimate Tensile Strength (MPa)	Elongation at Break (%)
Virgin – PA12	1464 (± 66)	44.3 (± 0.2)	14.0 (± 0.8)
PTFE – PA12	1422 (± 79)	42.2 (± 0.5)	24.9 (± 1.6)
Graphite – PA12	1754 (± 246)	46.3 (± 0.5)	10.8 (± 0.3)
MoS ₂ – PA12	1740 (± 135)	48.0 (± 0.6)	15.5 (± 3.3)

The inclusion of MoS₂ increased the stiffness, strength and ductility of PA12 parts produced. This was in good agreement with findings ascertained by Bai et al. [146], who demonstrated that the addition of 1wt% MoS₂ could increase the impact strength of PA12 by as much as 11.4% when optimised LS processing parameters were employed.

Furthermore, the addition of Graphite reduced the ductility, but increased the stiffness and strength of PA12 parts produced. It is expected that more heat will have accumulated within the Graphite – PA12 powder bed during processing, due to Graphite having a significantly larger thermal conductivity than PA12. Accordingly, greater part densification will have ensued [212], resulting in increased EaB and UTS values relative to Virgin – PA12¹³. Similarly, Kigure et al. [213] found that processing PA12 at higher powder bed temperatures resulted in parts with increased crystallinity, strength and stiffness values.

In contrast to Graphite – PA12, the addition of PTFE reduced the stiffness and strength, but increased the ductility of PA12 parts produced. Constituently, PTFE has a greater EaB than PA12 [214,215], which is likely why the resultant PTFE – PA12 compatible polymer blend was 77.8% more ductile than Virgin – PA12.

Ultimately, the inclusion of PTFE, Graphite and MoS₂ solid lubricant fillers, in accordance with the material preparation method outlined in **Section 9.2**, did not compromise the tensile properties of PA12 parts produced.

9.3.5 Friction

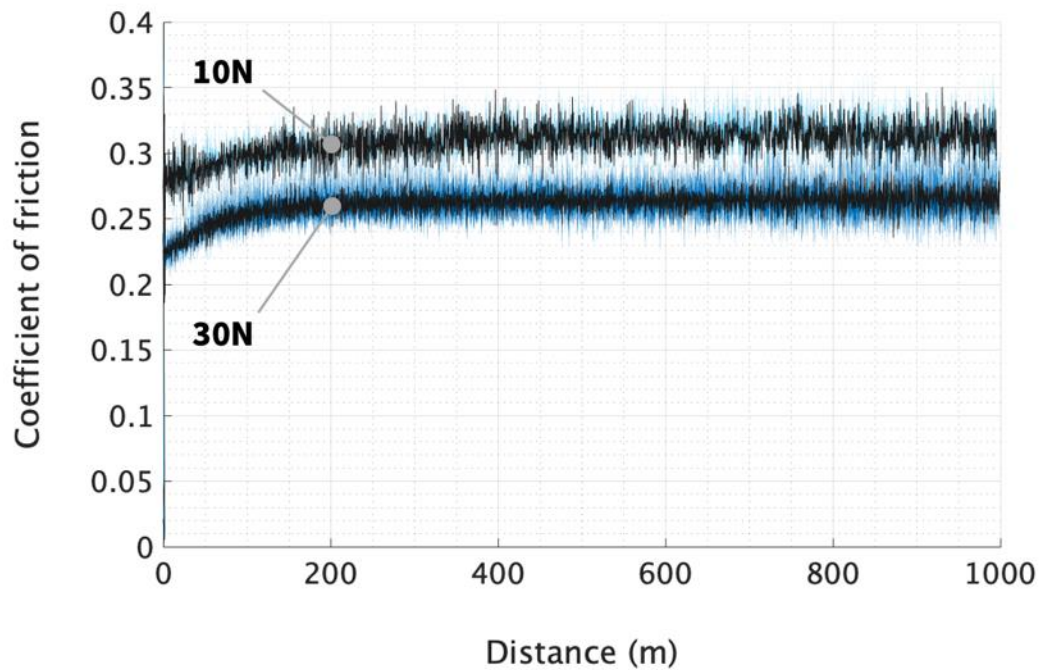
Figure 9.7 shows the friction responses exhibited by each laser sintered material during low (10N) and high (30N) load sliding. Corresponding mean COF values are detailed in **Table 9.7**, and percentage-based comparisons of the former, specifically the differences

¹³ This phenomenon will have also been pertinent to MoS₂ – PA12 during processing.

in the mean COF values determined for each solid lubricant filled polymeric composite relative to Virgin – PA12, can be seen in **Figure 9.8**.

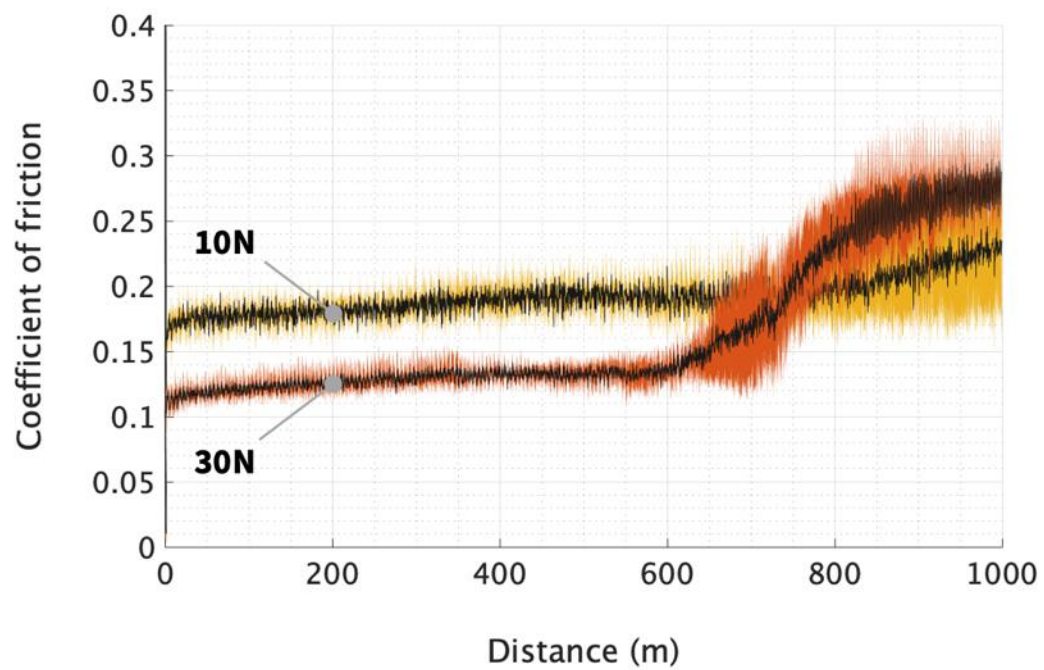
(a)

Virgin – PA12

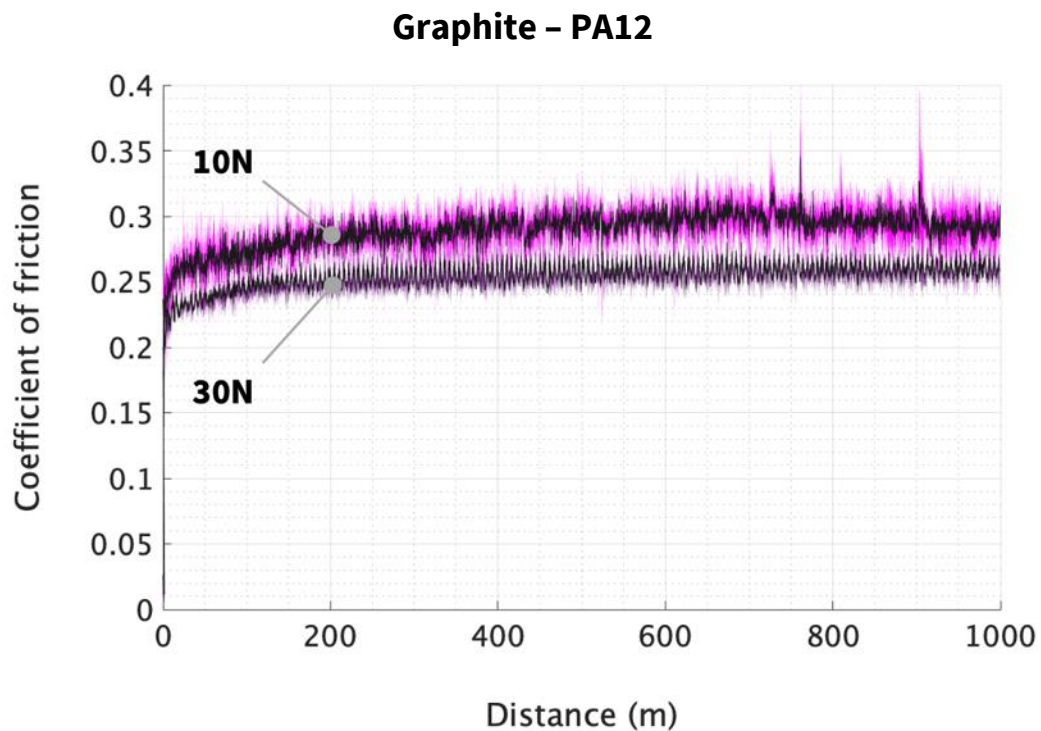


(b)

PTFE – PA12



(c)



(d)

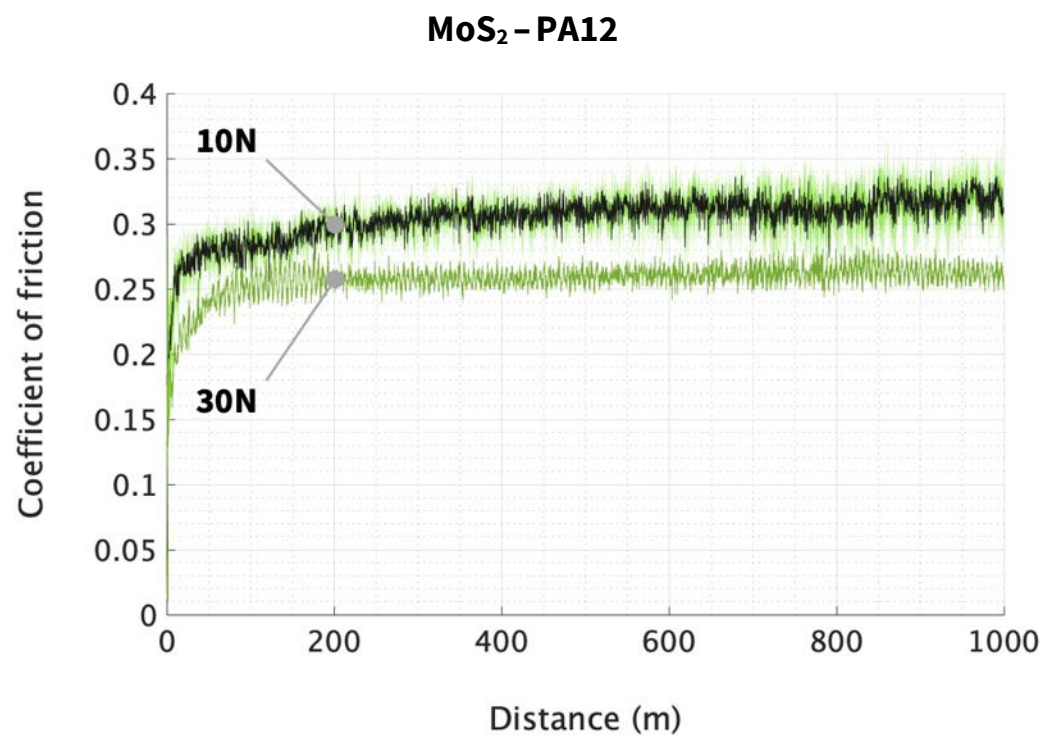


Figure 9.7 – The mean COF responses exhibited during **(a)** Virgin – PA12, **(b)** PTFE – PA12, **(c)** Graphite – PA12 and **(d)** MoS₂ – PA12 sliding. The highlighted regions within each mean response plot represents the maximum and minimum values recorded during repeat testing. It should be noted that MoS₂ – PA12 samples could only be evaluated once during 30N sliding due to them experiencing excessive magnitudes of curl during building.

Table 9.7

The mean COF values recorded for each material, as well as their corresponding standard deviation values.

Material	Coefficient of friction	
	10N	30N
Virgin – PA12	0.305 (± 0.010)	0.261 (± 0.011)
PTFE – PA12	0.192 (± 0.011)	0.128 (± 0.005) ^a
Graphite – PA12	0.289 (± 0.009)	0.246 (± 0.012)
MoS ₂ – PA12	0.304 (± 0.005)	0.257 ^b

^a Mean coefficient of friction value was computed prior to the breakdown in lubrication.

^b MoS₂ – PA12 samples could only be evaluated once during 30N sliding due to them experiencing excessive magnitudes of curl during building.

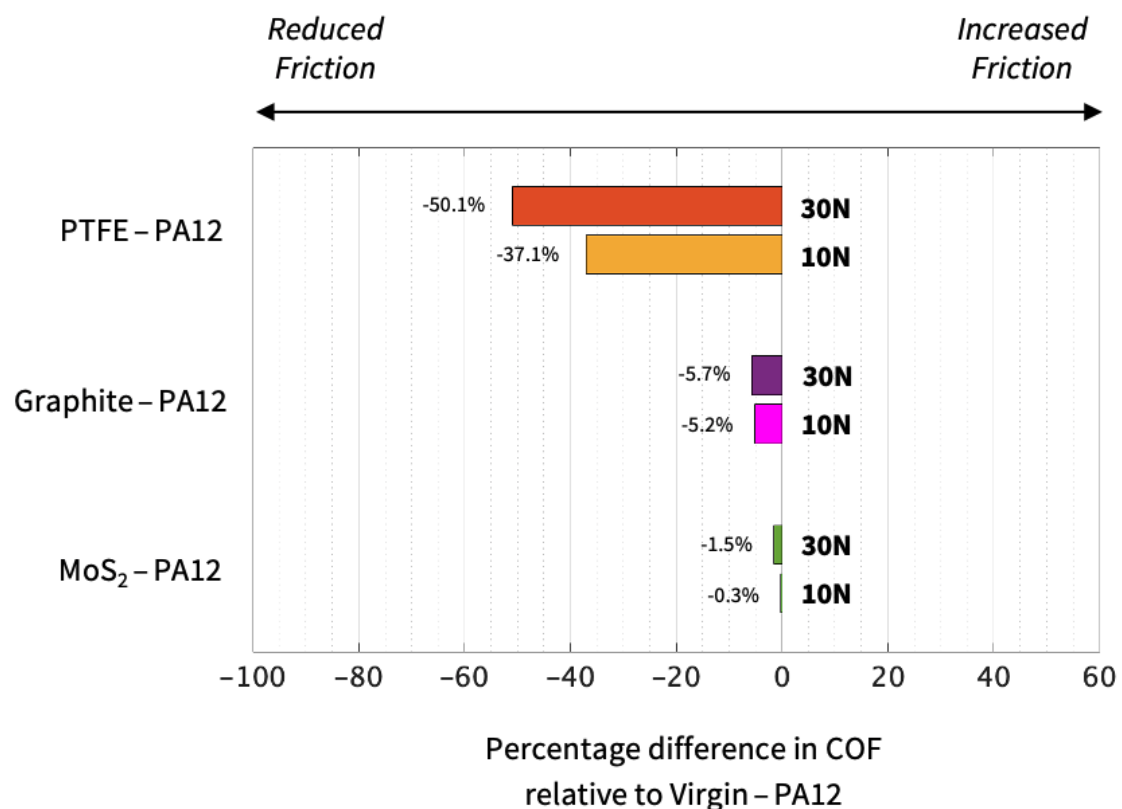


Figure 9.8 – The percentage differences in the mean COF values recorded for each solid lubricant filled polymeric composite relative to Virgin – PA12.

PTFE – PA12 was the only solid lubricant filled polymeric composite that exhibited a major frictional change relative to Virgin – PA12. As can be seen in **Figure 9.8**, a 37.1% reduction in COF was achieved during 10N sliding. This lubricating response was attributed to transfer film formation, such that a proportion of dynamic contact will have instead occurred between alike self-lubricating polymer material rather than entirely with the stainless steel pin during sliding. Material transfer, indicative of transfer film formation, can be seen within the contacting region of the corresponding stainless steel pin surface presented in **Figure 9.10b**. Furthermore, during the last 200m of 10N sliding, COF began to steadily increase in a manner which suggests that the lubricating response of PTFE – PA12 broke down due to the effects of frictional heating. This phenomenon was more pronounced during 30N sliding and is discussed in more detail below.

During high load PTFE – PA12 sliding, the friction incurred was initially reduced by an even greater magnitude. From 0m – 600m, the inclusion of PTFE resulted in a mean COF response of 0.128, which was a 50.1% reduction relative to Virgin – PA12. Smoother sliding, given by reduced fluctuations in COF, can also be seen in **Figure 9.7b**. However, at an approximate sliding distance of 600m, the lubricating response of PTFE – PA12 broke down. As shown in **Figure 9.9** this phenomenon occurred at a similar distance in every repeat test. In all instances, COF increased sharply, doubling within the following 200m, and fluctuated irregularly for the remaining duration of each 1000m sliding test. The consistency in which PTFE – PA12's lubricating response broke down, both in terms of applied normal load and moment of occurrence, is indicative of a frictional heating related failure. It is likely that frictional heating prompted interfacial contact temperatures to exceed the T_g of PTFE – PA12 ($T_{g-PA12} = 48.8^\circ$) [156], which, as discussed in **Section 3.2.3.3**, will have caused the molecular chains within the amorphous regions of each laser sintered PA12 matrix to stretch and elongate [155]. Consequently, the stiffness of PA12 will have decreased during sliding, leading to pin bodies further indenting PTFE – PA12 disk surfaces, thus resulting in larger contact areas and the sharp increases in F_f shown in **Figure 9.9**. Furthermore, it can be seen in **Figure 9.10b** that significantly less PTFE – PA12 material adhered to the stainless steel pin surface after 30N sliding. A transfer film was still present within the contact area; however, it was comparatively

discontinuous and covered a considerably reduced area fraction relative to the transfer film observed after 10N testing.

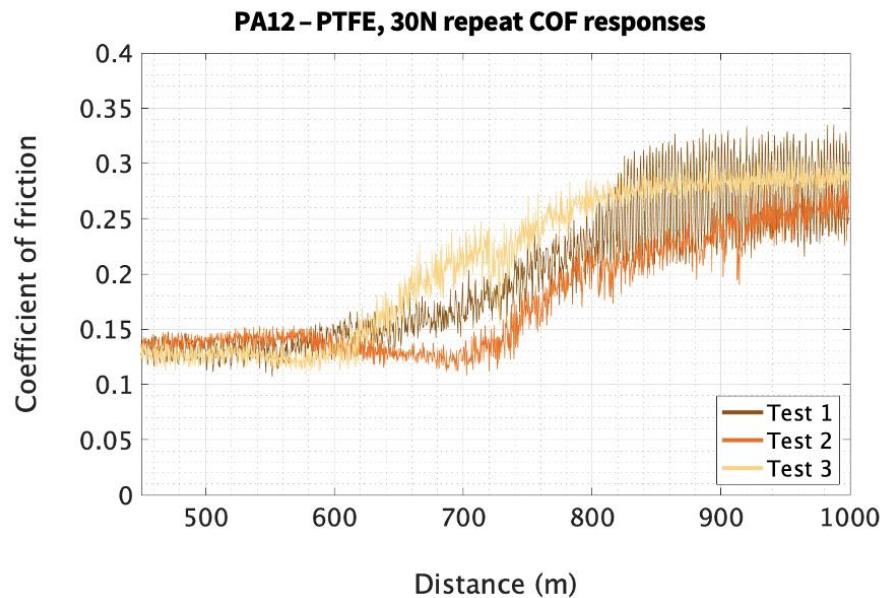


Figure 9.9 – The breakdown in lubrication observed during high load (30N) PTFE – PA12 sliding.

Upon evaluating the other pin surfaces presented in **Figure 9.10**, no evidence of transfer film facilitated sliding could be identified. This is likely why Graphite – PA12 and MoS₂ – PA12 induced relatively minor changes in friction (with respect to Virgin – PA12) compared to PTFE – PA12.

More specifically, the addition of Graphite reduced COF by 5.2% and 5.7% relative to Virgin – PA12 during 10N and 30N sliding, respectively. It is expected that increasing the percentage weight inclusion of Graphite would further facilitate sliding, as previously demonstrated by Ben Difallah et al. [216] and Sathees Kumar et al. [217]. However, it is likely that this would also prompt issues relating to LS processability, such as powder flowability.

As shown in **Figure 9.8**, there were negligible differences between the mean COF values recorded during MoS₂ – PA12 and Virgin – PA12 sliding, independent of applied normal load. Though, the inclusion of MoS₂ did notably reduce the extent by which COF fluctuated during 30N sliding. Mariani [205] identified that the lubrication performance of MoS₂ is

most effective in high load applications, where contact pressures are typically orders of magnitude greater than those incurred in this study. Therefore, insufficient applied normal loads are likely to have prevented MoS₂ enriched transfer films from forming within this work.

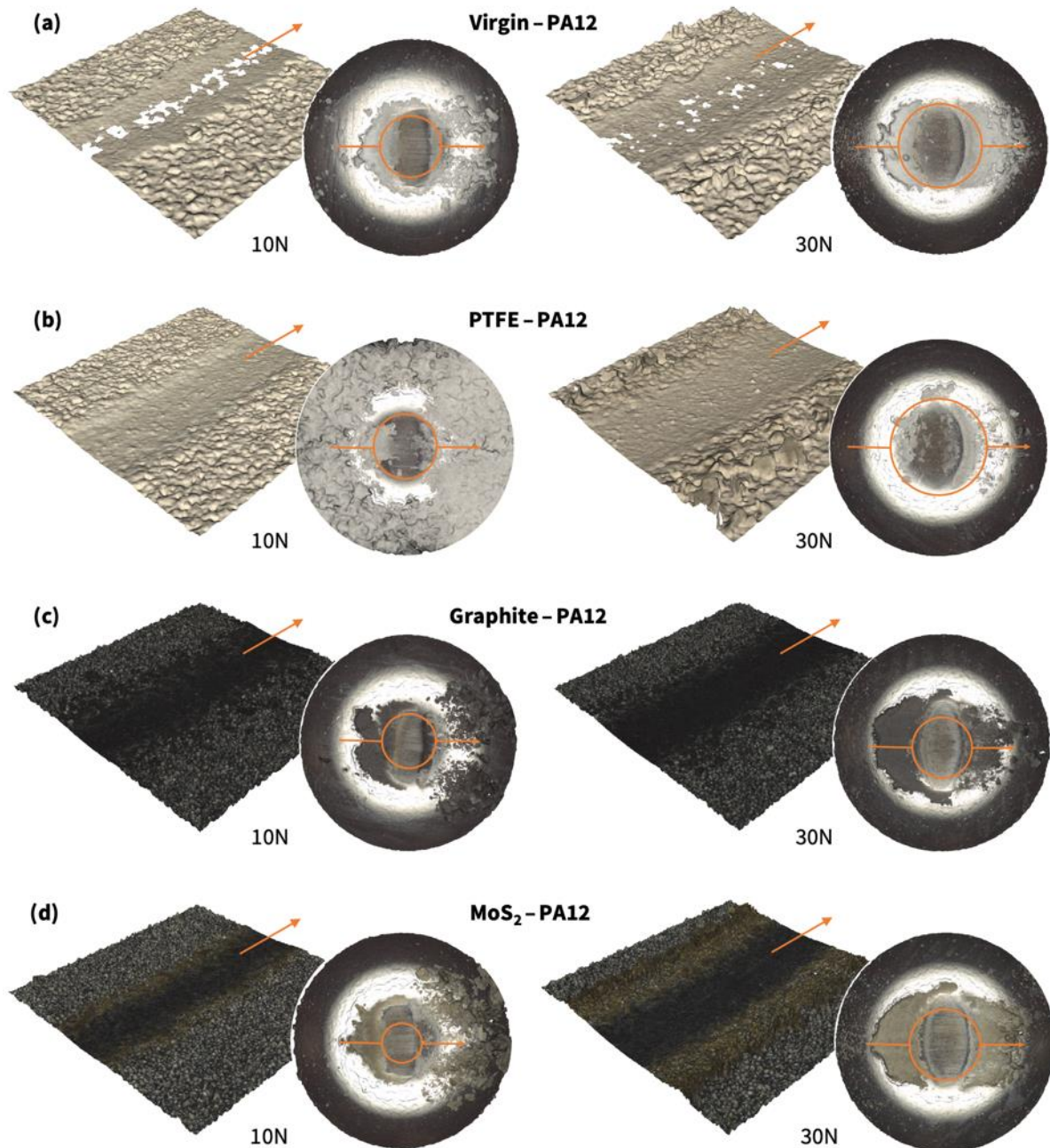


Figure 9.10 – Resultant (a) Virgin – PA12, (b) PTFE – PA12, (c) Graphite – PA12 and (d) MoS₂ – PA12 surfaces and corresponding pin counterfaces after 10N and 30N sliding. Orange annotations denote the sliding directions and contacting regions of each pin counterface. The missing information within the Virgin – PA12 wear scars are due to their worn surfaces being highly reflective which inhibited light from being received by the microscope’s detector.

9.3.6 Wear

The specific wear rate values determined for each laser sintered material are detailed in **Table 9.8**. In general, these results were in good agreement with data collected by Bai et al. [146] and Guo et al. [88], as well as the results presented in **Chapter 8**.

An inverse trend between the modified friction and wear responses of each material was discerned. More specifically, PTFE – PA12 experienced the most wear, despite sliding with the least resistance, whereas Graphite – PA12 and MoS₂ – PA12 resulted in the smallest specific wear rates, even though they incurred the most friction during testing. Moreover, wear resistance was correlated with the strengths and stiffness' of parts produced; materials with greater UTS and YM values experienced less wear, and vice versa.

Table 9.8

The mean specific wear rate values determined for each material, as well as their corresponding standard deviation values.

Material	Specific wear rate ($10^{-4} \text{ mm}^3 (\text{Nm})^{-1}$)	
	10N	30N
Virgin – PA12	4.782 (± 0.086)	3.197 (± 0.147)
PTFE – PA12	5.343 (± 0.082)	4.480 (± 0.141)
Graphite – PA12	2.782 (± 0.056)	1.139 (± 0.070)
MoS ₂ – PA12	1.033 (± 0.116)	1.465 ^a

^a MoS₂ – PA12 samples could only be evaluated once during 30N sliding due to them experiencing excessive magnitudes of curl during building.

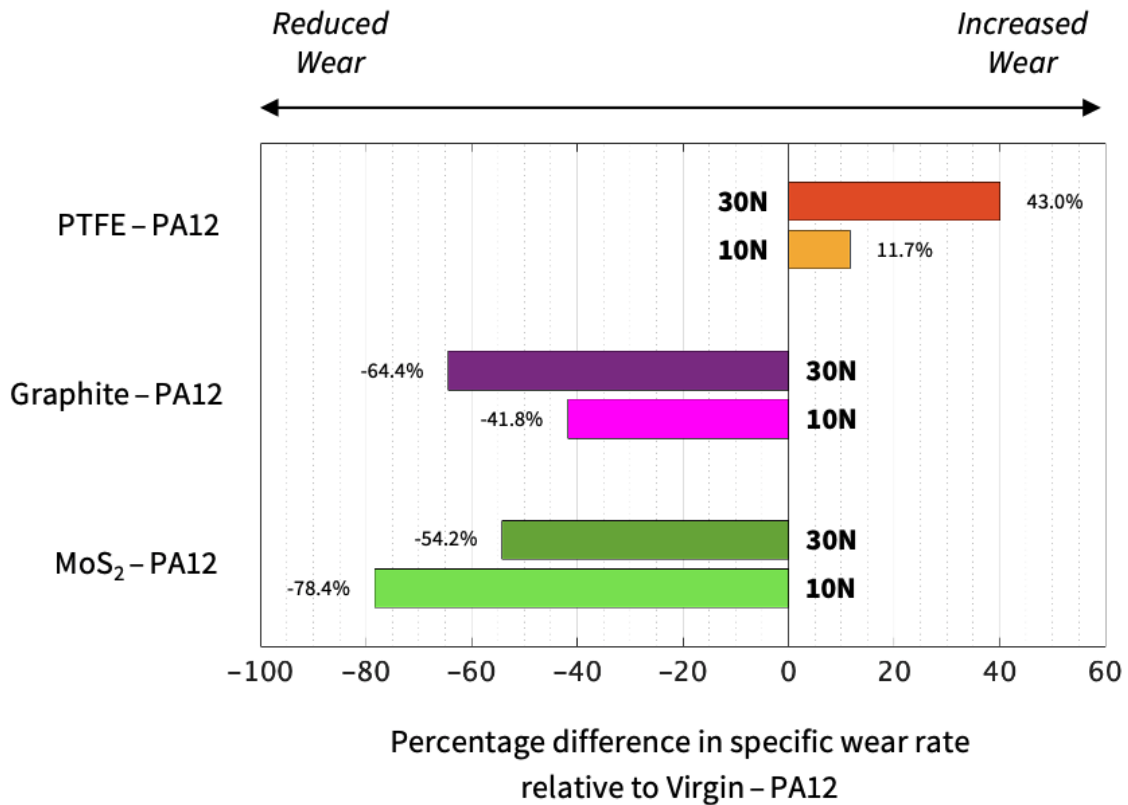


Figure 9.11 – The percentage differences in the mean specific wear rate values determined for each solid lubricant filled polymeric composite relative to Virgin – PA12.

PTFE – PA12 was the only solid lubricant filled composite that exhibited a lower wear resistance than Virgin – PA12 during testing. As can be seen in **Figure 9.11**, this was exacerbated when the normal loads employed were increased from 10N to 30N. Consequently, the magnitude by which the specific wear rate of PTFE – PA12 differed from Virgin – PA12 increased from 11.7% to 43.0%, respectively. These augmented specific wear rate values were likely attributed to PTFE – PA12 being softer and more ductile than Virgin – PA12. As previously discussed in **Section 9.3.4**, the EaB of PTFE – PA12 was 77.8% greater than the mean value measured for PA12. This coupled with virgin PTFE having a Shore D hardness of 60 [218], compared to 75 for PA12 [171], will have resulted in PTFE – PA12 being more susceptible to abrasive wear, particularly ploughing.

In agreement with observations discerned in **Chapter 8**, it can be seen in **Figure 9.10** that wear debris attached itself loosely to the leading edge, but more securely to the rear, of

each contacting pin surface during sliding¹⁴. More specifically, the latter was characteristic of adhesive wear, whereby frictional heating induced thermal softening resulted in the visibly thick, coalesced wear debris adhering to the rear edge of each pin surface.

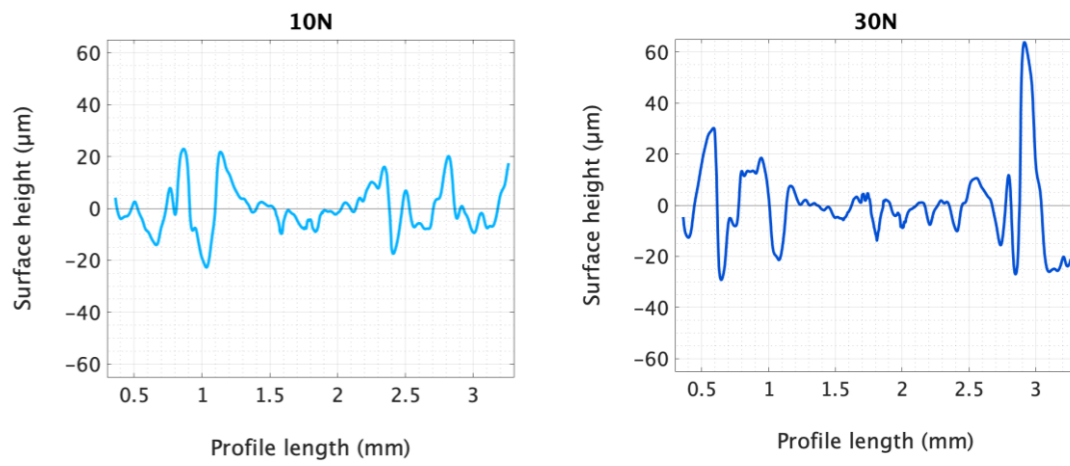
Graphite – PA12 and MoS₂ – PA12 composites exhibited significantly reduced specific wear rate values relative to Virgin – PA12. As outlined in **Figure 9.11**, MoS₂ – PA12 was the most effective polymeric material at reducing wear during 10N sliding, whereas Graphite – PA12 exhibited the greatest wear resistance during 30N sliding.

Additionally, it can be seen in **Figure 9.12** that the vertical height deviations within Graphite – PA12 and MoS₂ – PA12 wear scars were comparatively smaller than those visible within the worn profiles of Virgin – PA12 and PTFE – PA12 samples, independent of the normal load applied. Singh et al. [219] demonstrated that there was a correlation between powder bed temperature and indentation hardness when processing PA12, which in accordance with the findings discerned in **Section 9.3.4**, explains why Graphite – PA12 and MoS₂ – PA12 samples were more resistant to abrasive scratching.

¹⁴ Excluding the distinctly large amounts of PTFE – PA12 material transfer that occurred during 10N sliding.

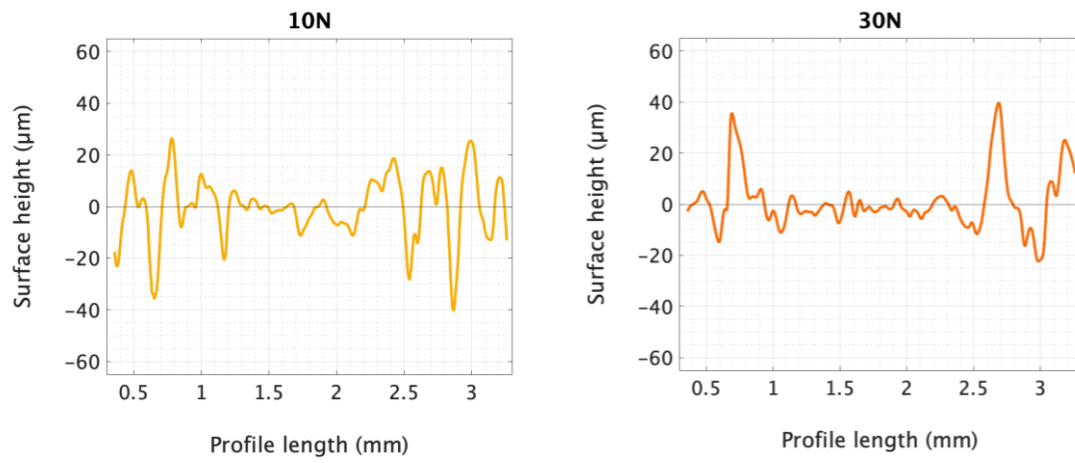
(a)

Virgin – PA12



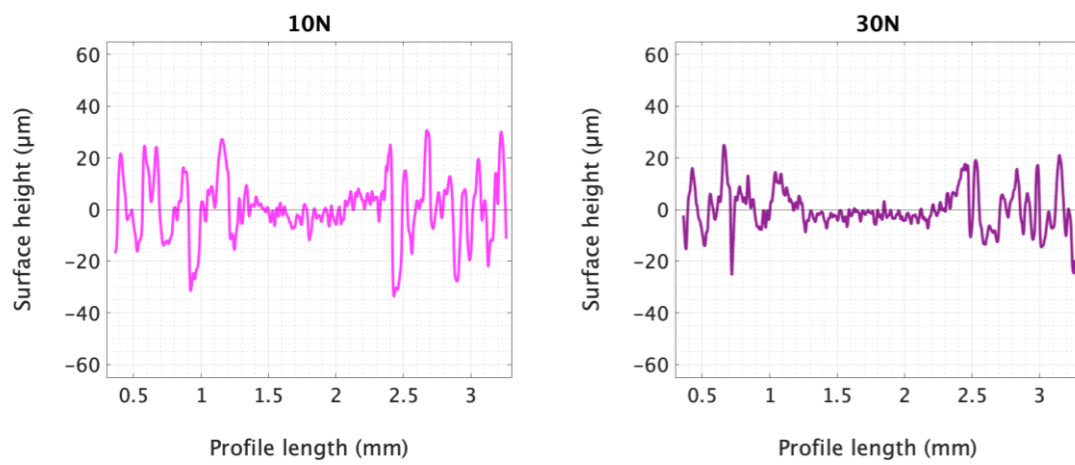
(b)

PTFE – PA12



(c)

Graphite – PA12



(d)

MoS₂ – PA12

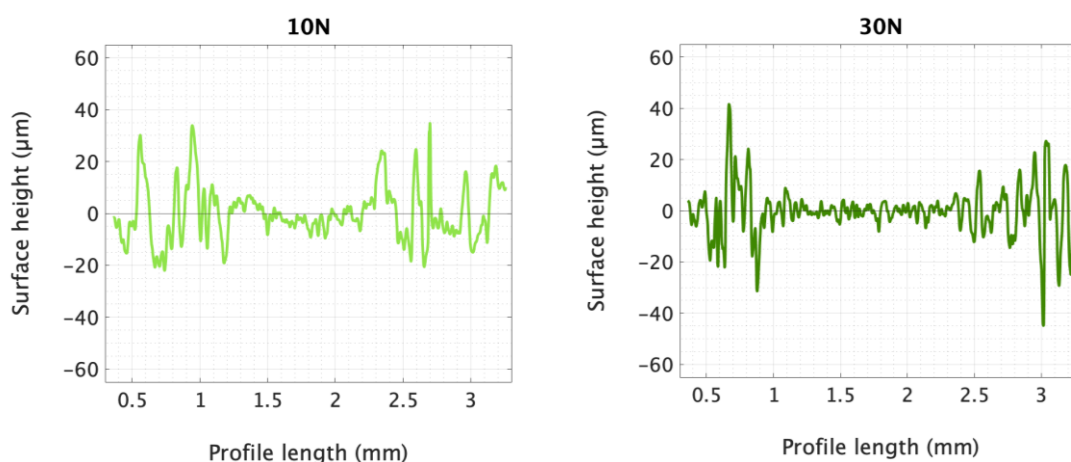


Figure 9.12 – Resultant (a) Virgin – PA12, (b) PTFE – PA12, (c) Graphite – PA12 and (d) MoS₂ – PA12 wear scar profiles.

9.4 Conclusions

This chapter investigated whether including solid lubricants, specifically PTFE, Graphite and MoS₂, within PA12 powders modified the tribological properties of specimens manufactured by LS. More specifically, the processability of each material was evaluated, and the resultant surface, mechanical, friction and wear properties of the parts produced were characterised and compared with those of Virgin – PA12.

SEM analysis showed that homogenous composite powder blends were attainable via simple mixing methods. However, micro-CT analysis could only confirm the presence of MoS₂ filler particles within the parts produced, thus highlighting the need for further refinement of the scanning parameters employed. Additionally, Graphite – PA12 and MoS₂ – PA12 samples experienced curl during building, attributed to their feedstock crystallisation temperatures. Despite this, the top surface topographies of each polymeric composite were in good agreement with Virgin – PA12, and tensile testing confirmed that solid lubricant inclusion did not compromise the mechanical performance of parts produced.

An inverse trend between the modified friction and wear responses of each solid lubricant filled laser sintered polymeric composite was discerned. More specifically, PTFE – PA12 experienced the most wear, despite sliding with the least resistance, whereas Graphite – PA12 and MoS₂ – PA12 resulted in the smallest specific wear rates, even though they incurred the most friction during testing. Wear resistance was also found to be correlated with the strengths and stiffness' of parts produced. Ultimately, it was demonstrated that the individual additions of PTFE and MoS₂ (in 1 : 100 mass ratios) reduced the friction and wear properties of laser sintered PA12 components by as much as 50.1% and 78.4%, respectively.

This work realised the possibility of creating specific powdered-material compositions that once laser sintered exhibit modified friction and wear responses. Consequently, it highlighted the potential to develop tailored LS materials optimised for specific sliding applications.

Chapter 10

Conclusions and Further Work

Chapter Summary

This chapter discusses how the aim of this project was achieved by summarising the key conclusions attained from each of the experimental studies that comprised this thesis. Additionally, the scope for further work is highlighted, and several areas of potential future research are outlined.

10.1 Conclusions

This work investigated the surface, friction and wear properties of laser sintered Polyamide-12 components. Upon comprehensively reviewing related literature in **Chapter 3**, it was discerned that this thesis should focus on:

- Further characterising laser sintered PA12 surfaces, with a particular focus on identifying any recurring surface features that may affect their sliding behaviours.
- Investigating the friction and wear behaviours of laser sintered PA12 components during both transient and steady-state wear regimes, including the effects of different surface orientations and varying operating conditions.
- Exploring whether the COF and / or wear rate of laser sintered PA12 surfaces can be reduced by including solid lubricant fillers within PA12 powders prior to LS.

Specific programs of work were executed so that each of these research themes could be studied in detail, enabling a comprehensive understanding of the following surface and sliding phenomena:

Surfaces

Chapter 5 comprised of work that comprehensively characterised the surfaces of different laser sintered 50/50 – PA12 components. Results showed that their top and bottom surfaces comprised of similar surface heights but different surface symmetries, as characterised by S_q and S_{sk} , respectively. The latter was attributed to finish layer deposition, specifically the mechanism of finish layer powder particle adhesion, which was subsequently demonstrated to be the reason why laser sintered polymer top surfaces tend to be asperity peak dominated.

Additionally, a Design of Experiments (DoE) was performed in **Chapter 6** to understand the relationship between applied laser parameters and resultant top surface S_q and S_{sk}

roughness responses. Ultimately, employing optimised laser parameters and building without finish layers was found to reduce the top surface heights of 50/50 – PA12 components by as much as 56% compared to those built conventionally.

Friction and Wear

Chapter 7 evaluated the extent by which the previously identified anisotropies in surface Skewness influenced transient sliding. It was discerned that laser sintered 50/50 – PA12 top surfaces exhibited notably heightened friction responses during running-in, which was attributed to augmented peak fracturing and / or yielding, as also confirmed by scratch testing analysis. Correspondingly, top surfaces were subject to greater magnitudes of wear than bottom surfaces during initial sliding, with resultant volume loss measurements being in good agreement with Ratner-Lancaster approximations.

Chapter 8 investigated how the sliding behaviours of laser sintered PA12 components were affected by varying operating conditions, specifically normal load, sliding speed and contact configuration. Accordingly, a DoE was performed, which enabled both statistically significant effects and pertinent sliding phenomena to be identified. Analysis of the former elucidated that friction force and wear rate were preponderantly influenced by applied normal load and contact configuration, respectively. Contact configuration, in particular, was ascertained to have intrinsically determined the dominant wear mechanisms and the extent by which frictional heat accumulated during sliding. Additionally, no transfer film formation was observed during any of the PA12 sliding tests performed throughout this thesis.

Modifying tribological performance

Chapter 9 explored the potential of including solid lubricants within virgin – PA12 powders (prior to processing via LS) as a means of modifying the friction and wear properties of parts produced. Each material evaluated was successfully processed, and the individual additions of PTFE and MoS₂ led to reductions in coefficient of friction and specific wear

rate of up to 50% and 78%, respectively. Moreover, these reductions were achieved without compromising the mechanical properties of each laser sintered PA12 composite material.

Ultimately, the work presented in this thesis comprehensively consolidated knowledge between polymer Laser Sintering and tribology for the first time, and in doing so, enabled new correlations between material, process and resultant surface and sliding phenomena to be established.

10.2 Further Work

Based on the insights gained from this thesis, the following areas of research have been identified as potential worthwhile avenues for further investigation:

Application-Specific Analysis

As outlined in **Chapter 1**, work presented in this thesis aimed to holistically investigate the friction and wear behaviours of polymer laser sintered components. To transition towards a more applied research direction, future work should focus on characterising application-specific interactions to explicitly determine the suitability of adopting different laser sintered polymer components for their intended end-use functions. This would be best achieved by collaborating with industry partners to identify the conditions in which they expect laser sintered polymer components to operate within, as well as to establish the validation criteria required for their implementation.

Characterising Other LS Polymers

As previously mentioned in **Chapter 2**, PA12 currently dominates the LS materials market. However, other compatible LS polymers are increasingly becoming more widely adopted due to their growing commercial availability. These include, but are not limited to, PEKK's, PEEK's, PP's and various TPU's. Therefore, further work should focus on characterising the

surface, friction and wear properties of parts produced from these LS polymers also. The results of which, may even promote their future adoption, particularly for sliding-related applications.

Investigating the Tribological Performance of Parts Produced Via Other Powder Bed Fusion Processes

As briefly discussed in **Chapter 3**, other well-established and industrially adopted polymer-PBF techniques include High Speed Sintering (HSS) and Multi Jet Fusion (MJF). These processes consolidate powdered-polymer materials by different methods to LS, though both utilise infrared radiation to fuse together ink-jetted regions of the powder bed. Several existing research works [95,220,221] demonstrated that the surface, friction and wear properties of parts produced via HSS and MJF differ to those characterised with this thesis. Therefore, dedicated programs of work should be designed and executed to additionally elucidate the surface and sliding properties pertinent to both HSS and MJF.

Further Exploring Additive Inclusion as a Means of Modifying the Friction and Wear Properties of Laser Sintered Polymer Components

The work presented in **Chapter 9** demonstrated the potential to modify the friction and wear properties of laser sintered polymer components by incorporating functional additives within their feedstock powders prior to processing. Based on this research, future studies should investigate the effects of including the previously analysed solid lubricants (PTFE, Graphite and MoS₂), as well as other filler materials, in different loading ratios. Additionally, the tribological properties of parts produced should be characterised over a greater range of operating conditions than those performed in **Chapter 9**, and their LS processing parameters should be optimised to mitigate component curl.

References

- [1] M. Attaran, The rise of 3-D printing: The advantages of additive manufacturing over traditional manufacturing, *Bus Horiz* 60 (2017) 677–688. <https://doi.org/10.1016/j.bushor.2017.05.011>.
- [2] T. Wohlers, I. Campbell, O. Diegel, J. Kowen, N. Mostow, Wohlers Report 2022: 3D Printing and Additive Manufacturing, Global State of the Industry, Washington DC, 2022.
- [3] G. Reinhard, J. Wunderlin, J. Lehr, The future of spare parts is 3D - A look at the challenges and opportunities of 3D printing, 2017.
- [4] Sculpteo, The state of 3D Printing - 2020 Edition, 2020.
- [5] Sculpteo, The state of 3D Printing - 2021 Edition, 2021.
- [6] Ernst & Young Global Limited, 3D printing: hype or game changer? - A Global EY Report, 2019.
- [7] Stratasys, Looking Forward: Additive Manufacturing in 2020, 2020.
- [8] BS EN ISO-ASTM 52900:2021 - Additive Manufacturing, General principles, Fundamentals and vocabulary, (2021) 1–38.
- [9] A. Averardi, C. Cola, S.E. Zeltmann, N. Gupta, Effect of particle size distribution on the packing of powder beds: A critical discussion relevant to additive manufacturing, *Mater Today Commun* 24 (2020). <https://doi.org/10.1016/j.mtcomm.2020.100964>.
- [10] Y. Wang, Z. Xu, D. Wu, J. Bai, Current status and prospects of polymer powder 3D printing technologies, *Materials* 13 (2020). <https://doi.org/10.3390/ma13102406>.
- [11] ASTM International, ASTM F2792-12a - Standard Terminology for Additive Manufacturing Technologies, (2013) 10–12. <https://doi.org/10.1520/F2792-12A.2>.
- [12] J. Wingham, Antimicrobial efficacy of laser sintered polyamide 12 / silver microcomposites, University of Sheffield, 2022.
- [13] AMFG, The Evolution of SLS: New Technologies, Materials and Applications, (2020). <https://amfg.ai/2020/01/21/the-evolution-of-sls-new-technologies-materials-and-applications/> (accessed March 6, 2023).
- [14] H. Wu, W.P. Fahy, S. Kim, H. Kim, N. Zhao, L. Pilato, A. Kafi, S. Bateman, J.H. Koo, Recent developments in polymers/polymer nanocomposites for additive manufacturing, *Prog Mater Sci* 111 (2020). <https://doi.org/10.1016/j.pmatsci.2020.100638>.
- [15] D.T. Pham, K.D. Dotchev, W.A.Y. Yusoff, Deterioration of polyamide powder properties in the laser sintering process, *Proc Inst Mech Eng C J Mech Eng Sci* 222 (2008) 2163–2176. <https://doi.org/10.1243/09544062JMES839>.
- [16] I. Gibson, D. Shi, Material properties and fabrication parameters in selective laser sinter process, *Rapid Prototyp J* 3 (1997) 129–136. <https://doi.org/10.1108/13552549710191836>.
- [17] W. Han, L. Kong, M. Xu, Advances in selective laser sintering of polymers, *International Journal of Extreme Manufacturing* 4 (2022). <https://doi.org/10.1088/2631-7990/ac9096>.
- [18] F. Lupone, E. Padovano, F. Casamento, C. Badini, Process phenomena and material properties in selective laser sintering of polymers: A review, *Materials* 15 (2022). <https://doi.org/10.3390/ma15010183>.
- [19] R.D. Goodridge, C.J. Tuck, R.J.M. Hague, Laser sintering of polyamides and other polymers, *Prog Mater Sci* 57 (2012) 229–267. <https://doi.org/10.1016/j.pmatsci.2011.04.001>.

- [20] A.F.A. Becker, Characterization and prediction of SLS processability of polymer powders with respect to powder flow and part warpage, ETH Zurich, 2016. <https://doi.org/https://doi.org/10.3929/ethz-a-010657585>.
- [21] M. Zhao, D. Drummer, K. Wudy, M. Drexler, Sintering Study of Polyamide 12 Particles for Selective Laser Melting, *International Journal of Recent Contributions from Engineering, Science & IT (IJES)* 3 (2015) 28. <https://doi.org/10.3991/ijes.v3i1.4290>.
- [22] M. Asgarpour, F. Bakir, S. Khelladi, A. Khavandi, A. Tcharkhtchi, Characterization and modeling of sintering of polymer particles, *J Appl Polym Sci* 119 (2011) 2784–2792. <https://doi.org/10.1002/app.32924>.
- [23] T.L. Starr, T.J. Gornet, J.S. Usher, The effect of process conditions on mechanical properties of laser-sintered nylon, *Rapid Prototyp J* 17 (2011) 418–423. <https://doi.org/10.1108/13552541111184143>.
- [24] R.D. Goodridge, R.J.M. Hague, C.J. Tuck, An empirical study into laser sintering of ultra-high molecular weight polyethylene (UHMWPE), *J Mater Process Technol* 210 (2010) 72–80. <https://doi.org/10.1016/j.jmatprotec.2009.08.016>.
- [25] A. Wegner, G. Witt, Laser Sintered Parts with Reduced Anisotropy of Mechanical Properties, in: *Proceedings of the RAPID 2012, Society of Manufacturing Engineers, Atlanta, GA, 2012*.
- [26] L.J. Tan, W. Zhu, K. Zhou, Recent Progress on Polymer Materials for Additive Manufacturing, *Adv Funct Mater* 2003062 (2020) 1–54. <https://doi.org/10.1002/adfm.202003062>.
- [27] S. Yuan, F. Shen, C.K. Chua, K. Zhou, Polymeric composites for powder-based additive manufacturing: Materials and applications, *Prog Polym Sci* 91 (2019) 141–168. <https://doi.org/10.1016/j.progpolymsci.2018.11.001>.
- [28] Q.G. Chen, J.C. Zhang, Experimental Study on Sintering Parameters in Selective Laser Sintering for ABS, *Adv Mat Res* 314–316 (2011) 738–741. <https://doi.org/10.4028/www.scientific.net/AMR.314-316.738>.
- [29] J. Lisi Leite, G.V. Salmoria, R.A. Paggi, C.H. Ahrens, A.S. Pouzada, Microstructural characterization and mechanical properties of functionally graded PA12/HDPE parts by selective laser sintering, *International Journal of Advanced Manufacturing Technology* 59 (2012) 583–591. <https://doi.org/10.1007/s00170-011-3538-5>.
- [30] G. V. Salmoria, J.L. Leite, R.A. Paggi, A. Lago, A.T.N. Pires, Selective laser sintering of PA12/HDPE blends: Effect of components on elastic/plastic behavior, *Polym Test* 27 (2008) 654–659. <https://doi.org/10.1016/j.polymertesting.2008.04.007>.
- [31] S.H. Diermann, M. Lu, Y. Zhao, L.J. Vandi, M. Dargusch, H. Huang, Synthesis, microstructure, and mechanical behaviour of a unique porous PHBV scaffold manufactured using selective laser sintering, *J Mech Behav Biomed Mater* 84 (2018) 151–160. <https://doi.org/10.1016/j.jmbbm.2018.05.007>.
- [32] L. Verbelen, S. Dadbakhsh, M. Van Den Eynde, J.P. Kruth, B. Goderis, P. Van Puyvelde, Characterization of polyamide powders for determination of laser sintering processability, *Eur Polym J* 75 (2016) 163–174. <https://doi.org/10.1016/j.eurpolymj.2015.12.014>.
- [33] K. Nar, C. Majewski, R. Lewis, A comprehensive characterisation of Laser Sintered Polyamide-12 surfaces, *Polym Test* 106 (2021) 107450. <https://doi.org/10.1016/j.polymertesting.2021.107450>.
- [34] G. V. Salmoria, J.L. Leite, L.F. Vieira, A.T.N. Pires, C.R.M. Roesler, Mechanical properties of PA6/PA12 blend specimens prepared by selective laser sintering, *Polym Test* 31 (2012) 411–416. <https://doi.org/10.1016/j.polymertesting.2011.12.006>.
- [35] Y. Shi, J. Chen, Y. Wang, Z. Li, S. Huang, Study of the selective laser sintering of polycarbonate and postprocess for parts reinforcement, in: *Proceedings of the Institution of*

- Mechanical Engineers, Part L: Journal of Materials: Design and Applications, 2007: pp. 37–42. <https://doi.org/10.1243/14644207JMDA65>.
- [36] W.Y. Yeong, N. Sudarmadji, H.Y. Yu, C.K. Chua, K.F. Leong, S.S. Venkatraman, Y.C.F. Boey, L.P. Tan, Porous polycaprolactone scaffold for cardiac tissue engineering fabricated by selective laser sintering, *Acta Biomater* 6 (2010) 2028–2034. <https://doi.org/10.1016/j.actbio.2009.12.033>.
 - [37] S. Berretta, K.E. Evans, O. Ghita, Processability of PEEK, a new polymer for high temperature laser sintering (HT-LS), *Eur Polym J* 68 (2015) 243–266. <https://doi.org/10.1016/j.eurpolymj.2015.04.003>.
 - [38] S. Berretta, Y. Wang, R. Davies, O.R. Ghita, Polymer viscosity, particle coalescence and mechanical performance in high-temperature laser sintering, *J Mater Sci* 51 (2016) 4778–4794. <https://doi.org/10.1007/s10853-016-9761-6>.
 - [39] P. Peyre, Y. Rouchausse, D. Defauchy, G. Régnier, Experimental and numerical analysis of the selective laser sintering (SLS) of PA12 and PEKK semi-crystalline polymers, *J Mater Process Technol* 225 (2015) 326–336. <https://doi.org/10.1016/j.jmatprotec.2015.04.030>.
 - [40] K.C. Chuang, T. Gornet, H. Koerner, Challenges in laser sintering of melt-processable thermoset imide resin, in: *CAMX 2016 - Composites and Advanced Materials Expo*, 2016.
 - [41] E.N. Antonov, V.N. Bagratashvili, S.M. Howdle, A.N. Konovalov, V.K. Popov, V.Ya. Panchenko, Fabrication of polymer scaffolds for tissue engineering using surface selective laser sintering, *Laser Phys* 16 (2006) 774–787. <https://doi.org/10.1134/s1054660x06050070>.
 - [42] E.N. Antonov, A.G. Dunaev, A.N. Konovalov, S.A. Minaeva, V.K. Popov, Temperature field distribution in polymer particles during surface-selective laser sintering, *Laser Phys* 30 (2020). <https://doi.org/10.1088/1555-6611/ab7be3>.
 - [43] W.Y. Zhou, S.H. Lee, M. Wang, W.L. Cheung, W.Y. Ip, Selective laser sintering of porous tissue engineering scaffolds from poly(L-lactide)/carbonated hydroxyapatite nanocomposite microspheres, *J Mater Sci Mater Med* 19 (2008) 2535–2540. <https://doi.org/10.1007/s10856-007-3089-3>.
 - [44] R. Velu, S. Singamneni, Evaluation of the influences of process parameters while selective laser sintering PMMA powders, *Proc Inst Mech Eng C J Mech Eng Sci* 229 (2015) 603–613. <https://doi.org/10.1177/0954406214538012>.
 - [45] D. Drummer, D. Rietzel, F. Kühnlein, Development of a characterization approach for the sintering behavior of new thermoplastics for selective laser sintering, *Phys Procedia* 5 (2010) 533–542. <https://doi.org/10.1016/j.phpro.2010.08.081>.
 - [46] W. Zhu, C. Yan, Y. Shi, S. Wen, J. Liu, Y. Shi, Investigation into mechanical and microstructural properties of polypropylene manufactured by selective laser sintering in comparison with injection molding counterparts, *Mater Des* 82 (2015) 37–45. <https://doi.org/10.1016/j.matdes.2015.05.043>.
 - [47] D. Strobbe, S. Dadbakhsh, L. Verbelen, P. Van Puyvelde, J.P. Kruth, Selective laser sintering of polystyrene: a single-layer approach, *Plastics, Rubber and Composites* 47 (2018) 2–8. <https://doi.org/10.1080/14658011.2017.1399532>.
 - [48] S. Sun, X. Gan, Z. Wang, D. Fu, W. Pu, H. Xia, Dynamic healable polyurethane for selective laser sintering, *Addit Manuf* 33 (2020) 101176. <https://doi.org/10.1016/j.addma.2020.101176>.
 - [49] C. Shuai, Z. Mao, H. Lu, Y. Nie, H. Hu, S. Peng, Fabrication of porous polyvinyl alcohol scaffold for bone tissue engineering via selective laser sintering, *Biofabrication* 5 (2013). <https://doi.org/10.1088/1758-5082/5/1/015014>.

- [50] J.L. Brito Guaricela, C.H. Ahrens, G.M. de Oliveira Barra, C. Merlini, Evaluation of poly(vinylidene fluoride)/carbon black composites, manufactured by selective laser sintering, *Polym Compos* 42 (2021) 2457–2468. <https://doi.org/10.1002/pc.25991>.
- [51] C. Yan, Y. Shi, J. Yang, J. Liu, Investigation into the selective laser sintering of styrene-acrylonitrile copolymer and postprocessing, *International Journal of Advanced Manufacturing Technology* 51 (2010) 973–982. <https://doi.org/10.1007/s00170-010-2681-8>.
- [52] S. Ziegelmeier, P. Christou, F. Wöllecke, C. Tuck, R. Goodridge, R. Hague, E. Krampe, E. Wintermantel, An experimental study into the effects of bulk and flow behaviour of laser sintering polymer powders on resulting part properties, *J Mater Process Technol* 215 (2015) 239–250. <https://doi.org/10.1016/j.jmatprotec.2014.07.029>.
- [53] D. Drummer, M. Medina-Hernández, M. Drexler, K. Wudy, Polymer powder production for laser melting through immiscible blends, in: *The 7th World Congress on Particle Technology (WCPT7)*, Elsevier B.V., 2015: pp. 1918–1925. <https://doi.org/10.1016/j.proeng.2015.01.332>.
- [54] M. Schmid, K. Wegener, Additive Manufacturing: Polymers applicable for laser sintering (LS), in: *International Conference on Manufacturing Engineering and Materials, ICMEM 2016*, The Author(s), 2016: pp. 457–464. <https://doi.org/10.1016/j.proeng.2016.06.692>.
- [55] S. Dadbakhsh, L. Verbelen, O. Verkinderen, D. Strobbe, P. Van Puyvelde, J.P. Kruth, Effect of PA12 powder reuse on coalescence behaviour and microstructure of SLS parts, *Eur Polym J* 92 (2017) 250–262. <https://doi.org/10.1016/j.eurpolymj.2017.05.014>.
- [56] K. Dotchev, W. Yusoff, Recycling of polyamide 12 based powders in the laser sintering process, *Rapid Prototyp J* 15 (2009) 192–203. <https://doi.org/10.1108/13552540910960299>.
- [57] T. Wohlers, I. Campbell, O. Diegel, R. Huff, J. Kowen, Wohler Report 2019: 3D Printing and Additive Manufacturing, State of the Industry, Wohlers Associates, Fort Collins, 2019.
- [58] L. Verbelen, S. Dadbakhsh, M. Van Den Eynde, J.P. Kruth, B. Goderis, P. Van Puyvelde, Characterization of polyamide powders for determination of laser sintering processability, *Eur Polym J* 75 (2016) 163–174. <https://doi.org/10.1016/j.eurpolymj.2015.12.014>.
- [59] W.A.Y. Yusoff, S.A. Nasir, W.M.H. Ahmad, Investigation of the effect of Orange Peel surface texture on the laser sintered part, in: *ISBEIA 2011 - 2011 IEEE Symposium on Business, Engineering and Industrial Applications*, IEEE, 2011: pp. 43–48. <https://doi.org/10.1109/ISBEIA.2011.6088854>.
- [60] A. Amado, M. Schmid, K. Wegener, Flowability of SLS Powders at Elevated Temperature, (2014) 1–7. <https://doi.org/10.3929/ETHZ-A-010057815>.
- [61] J.K. Prescott, R.A. Barnum, On powder flowability, *Pharmaceutical Technology* 24 (2000) 60–84+236.
- [62] S. Vock, B. Klöden, A. Kirchner, T. Weißgärber, B. Kieback, Powders for powder bed fusion: a review, *Progress in Additive Manufacturing* 4 (2019) 383–397. <https://doi.org/10.1007/s40964-019-00078-6>.
- [63] S. Berretta, O. Ghita, K.E. Evans, A. Anderson, C. Newman, Size, shape and flow of powders for use in Selective Laser Sintering (SLS), *High Value Manufacturing: Advanced Research in Virtual and Rapid Prototyping - Proceedings of the 6th International Conference on Advanced Research and Rapid Prototyping, VR@P 2013* (2014) 49–54. <https://doi.org/10.1201/b15961-11>.
- [64] S. Dupin, O. Lame, C. Barrès, J.Y. Charneau, Microstructural origin of physical and mechanical properties of polyamide 12 processed by laser sintering, *Eur Polym J* 48 (2012) 1611–1621. <https://doi.org/10.1016/j.eurpolymj.2012.06.007>.
- [65] C.H. Clausen, D.J. Mickish, W.J. Nebe, S.R. Vaidya, Laser Sinterable Thermoplastic Powder, 6,110,411, 2000.

- [66] M.M. Lexow, D. Drummer, New Materials for SLS: The Use of Antistatic and Flow Agents, *Journal of Powder Technology* 2016 (2016) 1–9. <https://doi.org/10.1155/2016/4101089>.
- [67] T. Laumer, T. Stichel, K. Nagulin, M. Schmidt, Optical analysis of polymer powder materials for Selective Laser Sintering, *Polym Test* 56 (2016) 207–213. <https://doi.org/10.1016/j.polymertesting.2016.10.010>.
- [68] X. Cui, D. Yan, Preparation, characterization and crystalline transitions of odd-even polyamides 11,12 and 11,10, *Eur Polym J* 41 (2005) 863–870. <https://doi.org/10.1016/j.eurpolymj.2004.10.045>.
- [69] S. Xi, P. Zhang, Y. Huang, M. Kong, Q. Yang, G. Li, Laser sintering of cryogenically ground polymer powders into high-performance parts: The role of dry particle coating with a conductive flow agent, *Polymer (Guildf)* 186 (2020) 122044. <https://doi.org/10.1016/j.polymer.2019.122044>.
- [70] M. Schmid, A. Amado, K. Wegener, Materials perspective of polymers for additive manufacturing with selective laser sintering, *J Mater Res* 29 (2014) 1824–1832. <https://doi.org/10.1557/jmr.2014.138>.
- [71] J.P. Kruth, G. Levy, F. Klocke, T.H.C. Childs, Consolidation phenomena in laser and powder-bed based layered manufacturing, *CIRP Ann Manuf Technol* 56 (2007) 730–759. <https://doi.org/10.1016/j.cirp.2007.10.004>.
- [72] H. Zarringhalam, N. Hopkinson, N.F. Kamperman, J.J. de Vlieger, Effects of processing on microstructure and properties of SLS Nylon 12, *Materials Science and Engineering A* 435–436 (2006) 172–180. <https://doi.org/10.1016/j.msea.2006.07.084>.
- [73] H. Zarringhalam, Investigation into Crystallinity and Degree of Particle Melt in Selective Laser Sintering, 2007.
- [74] C. Majewski, H. Zarringhalam, N. Hopkinson, Effect of the degree of particle melt on mechanical properties in selective laser-sintered Nylon-12 parts, *Proc Inst Mech Eng B J Eng Manuf* 222 (2008) 1055–1064. <https://doi.org/10.1243/09544054JEM1122>.
- [75] B. Haworth, N. Hopkinson, D. Hitt, X. Zhong, Shear viscosity measurements on Polyamide-12 polymers for laser sintering, *Rapid Prototyp J* 19 (2013) 28–36. <https://doi.org/10.1108/13552541311292709>.
- [76] M. Vetterli, Powder Optimization for Laser Sintering: An insight in powder intrinsic and extrinsic properties, ETH Zurich, 2019.
- [77] B. Yao, Z. Li, F. Zhu, Effect of powder recycling on anisotropic tensile properties of selective laser sintered PA2200 polyamide, *Eur Polym J* 141 (2020) 110093. <https://doi.org/10.1016/j.eurpolymj.2020.110093>.
- [78] A. Almansoori, R. Masters, K. Abrams, J. Schäfer, T. Gerling, C. Majewski, C. Rodenburg, Surface modification of the laser sintering standard powder polyamide 12 by plasma treatments, *Plasma Processes and Polymers* 15 (2018). <https://doi.org/10.1002/ppap.201800032>.
- [79] G. Stachowiak, A.W. Batchelor, *Engineering Tribology*, 4th ed., Elsevier, 2014. <https://doi.org/10.1016/C2011-0-07515-4>.
- [80] P. Jost, *Lubrication (Tribology)–A report on the present position and industry’s needs*, HM Stationary Office, London, UK, 1966.
- [81] N.K. Myshkin, M.I. Petrokovets, A. V. Kovalev, Tribology of polymers: Adhesion, friction, wear, and mass-transfer, *Tribol Int* 38 (2005) 910–921. <https://doi.org/10.1016/j.triboint.2005.07.016>.
- [82] S.K. Sinha, B.J. Briscoe, *Polymer Tribology*, World Scientific Publishing Company, 2009.

- [83] D. Scott, Introduction to Tribology, in: *Fundamentals of Tribology*, WORLD SCIENTIFIC (EUROPE), 2018: pp. 1–9. https://doi.org/10.1142/9781786345189_0001.
- [84] T.V. Vorburger, Methods for Characterizing Surface Topography, in: D.T. Moore (Ed.), *Tutorials in Optics*, Gaithersburg, 1992: pp. 137–151.
- [85] E.S. Gadelmawla, M.M. Koura, T.M.A. Maksoud, I.M. Elewa, H.H. Soliman, Roughness parameters, *J Mater Process Technol* 123 (2002) 133–145. [https://doi.org/10.1016/S0924-0136\(02\)00060-2](https://doi.org/10.1016/S0924-0136(02)00060-2).
- [86] C. Kundera, T. Kozior, Evaluation of the influence of selected parameters of Selective Laser Sintering technology on surface topography, *J Phys Conf Ser* 1183 (2019). <https://doi.org/10.1088/1742-6596/1183/1/012002>.
- [87] S. Beitz, R. Uerlich, T. Bokelmann, A. Diener, T. Vietor, A. Kwade, Influence of powder deposition on powder bed and specimen properties, *Materials* 12 (2019). <https://doi.org/10.3390/ma12020297>.
- [88] J. Guo, J. Bai, K. Liu, J. Wei, Surface quality improvement of selective laser sintered polyamide 12 by precision grinding and magnetic field-assisted finishing, *Mater Des* 138 (2017) 39–45. <https://doi.org/10.1016/j.matdes.2017.10.048>.
- [89] A. Sachdeva, S. Singh, V.S. Sharma, Investigating surface roughness of parts produced by SLS process, *International Journal of Advanced Manufacturing Technology* 64 (2013) 1505–1516. <https://doi.org/10.1007/s00170-012-4118-z>.
- [90] F. Blateyron, The Areal Field Parameters, in: R. Leach (Ed.), *Characterisation of Areal Surface Texture*, Springer Berlin Heidelberg, Berlin, Heidelberg, 2013: pp. 15–43. https://doi.org/10.1007/978-3-642-36458-7_2.
- [91] M. Launhardt, A. Wörz, A. Loderer, T. Laumer, D. Drummer, T. Hausotte, M. Schmidt, Detecting surface roughness on SLS parts with various measuring techniques, *Polym Test* 53 (2016) 217–226. <https://doi.org/10.1016/j.polymertesting.2016.05.022>.
- [92] A. Townsend, N. Senin, L. Blunt, R.K. Leach, J.S. Taylor, Surface texture metrology for metal additive manufacturing: a review, *Precis Eng* 46 (2016) 34–47. <https://doi.org/10.1016/j.precisioneng.2016.06.001>.
- [93] S. Petzold, J. Klett, A. Schauer, T.A. Osswald, Surface roughness of polyamide 12 parts manufactured using selective laser sintering, *Polym Test* 80 (2019) 106094. <https://doi.org/10.1016/j.polymertesting.2019.106094>.
- [94] S. Jaturunruangsri, *Evaluation of Material Surface Profiling Methods: Contact versus Non-contact*, Brunel University London, 2014.
- [95] Z. Zhu, S. Lou, C. Majewski, Characterisation and correlation of areal surface texture with processing parameters and porosity of High Speed Sintered parts, *Addit Manuf* 36 (2020). <https://doi.org/10.1016/j.addma.2020.101402>.
- [96] R. Danzl, F. Helml, S. Scherer, Focus Variation – a Robust Technology for High Resolution Optical 3D Surface Metrology, *Strojniški Vestnik – Journal of Mechanical Engineering* 2011 (2011) 245–256. <https://doi.org/10.5545/sv-jme.2010.175>.
- [97] L. Newton, N. Senin, C. Gomez, R. Danzl, F. Helml, L. Blunt, R. Leach, Areal topography measurement of metal additive surfaces using focus variation microscopy, *Addit Manuf* 25 (2019) 365–389. <https://doi.org/10.1016/j.addma.2018.11.013>.
- [98] T. Grimm, G. Wiora, G. Witt, Characterization of typical surface effects in additive manufacturing with confocal microscopy, *Surf Topogr* 3 (2015). <https://doi.org/10.1088/2051-672X/3/1/014001>.

- [99] J. Gockel, L. Sheridan, B. Koerper, B. Whip, The influence of additive manufacturing processing parameters on surface roughness and fatigue life, *Int J Fatigue* 124 (2019) 380–388. <https://doi.org/10.1016/j.ijfatigue.2019.03.025>.
- [100] M.A. De Pastre, A. Thompson, Y. Quinsat, J.A. Albajez García, N. Senin, R. Leach, Polymer powder bed fusion surface texture measurement, *Meas Sci Technol* 31 (2020). <https://doi.org/10.1088/1361-6501/ab63b1>.
- [101] G. Guan, M. Hirsch, Z.H. Lu, D.T.D. Childs, S.J. Matcher, R. Goodridge, K.M. Groom, A.T. Clare, Evaluation of selective laser sintering processes by optical coherence tomography, *Mater Des* 88 (2015) 837–846. <https://doi.org/10.1016/j.matdes.2015.09.084>.
- [102] W. Zhou, R.P. Apkarian, Z.L. Wang, D. Joy, Fundamentals of Scanning Electron Microscopy, in: W. Zhou, Z.L. Wang (Eds.), *Scanning Microscopy for Nanotechnology*, Springer New York, New York, NY, 2007: pp. 1–40. <https://doi.org/10.1007/978-0-387-39620-0>.
- [103] A. Ul-Hamid, *A Beginners' Guide to Scanning Electron Microscopy*, Springer International Publishing, Cham, 2018. <https://doi.org/10.1007/978-3-319-98482-7>.
- [104] A. Townsend, L. Pagani, L. Blunt, P.J. Scott, X. Jiang, Factors affecting the accuracy of areal surface texture data extraction from X-ray CT, *CIRP Ann Manuf Technol* 66 (2017) 547–550. <https://doi.org/10.1016/j.cirp.2017.04.074>.
- [105] M. Vetterli, M. Schmid, W. Knapp, K. Wegener, New horizons in selective laser sintering surface roughness characterization, *Surf Topogr* 5 (2017) 045007. <https://doi.org/10.1088/2051-672x/aa88ee>.
- [106] J. Williams, The friction of solids, in: *Engineering Tribology*, Cambridge University Press, 2005: pp. 132–165. <https://doi.org/10.1017/CBO9780511805905>.
- [107] F.P. Bowden, D. Tabor, *The Friction and Lubrication of Solids. Part I*, in: Second, Oxford University Press, Oxford, 1954.
- [108] N.K. Myshkin, S.S. Pesetskii, A.Y. Grigoriev, Polymer tribology: Current state and applications, *Tribology in Industry* 37 (2015) 284–290.
- [109] N. Myshkin, A. Kovalev, Adhesion and surface forces in polymer tribology—A review, *Friction* 6 (2018) 143–155. <https://doi.org/10.1007/s40544-018-0203-0>.
- [110] K.R. Shull, Contact mechanics and the adhesion of soft solids, *Materials Science and Engineering* 36 (2002) 1–45.
- [111] N.K. Myshkin, A. Kovalev, Polymer mechanics and tribology, *Industrial Lubrication and Tribology* 70 (2018) 764–772. <https://doi.org/10.1108/ILT-06-2017-0162>.
- [112] N.K. Myshkin, A. V. Kovalev, Adhesion and Friction of Polymers, in: *Polymer Tribology*, IMPERIAL COLLEGE PRESS, 2009: pp. 3–37. https://doi.org/10.1142/9781848162044_0001.
- [113] J. A. Greenwood and J. B. P. Williamson, Contact of Nominally Flat Surfaces, *Proc. Roy. Soc. (London)*, 5 (1967) 1967.
- [114] P.D. Evans, *The Hardness and Abrasion of Polymers*, University of London, 1987.
- [115] R.L. Jackson, I. Green, A statistical model of elasto-plastic asperity contact between rough surfaces, *Tribol Int* 39 (2006) 906–914. <https://doi.org/10.1016/j.triboint.2005.09.001>.
- [116] J. Williams, Wear and surface damage, in: *Engineering Tribology*, Cambridge University Press, Cambridge, 2013: pp. 166–199. <https://doi.org/10.1017/cbo9780511805905.006>.
- [117] I.M. Hutchings, The Challenge of Wear, in: G.W. Stachowiak (Ed.), *Wear – Materials, Mechanisms and Practice*, Wiley, 2005: pp. 1–7. <https://doi.org/10.1002/9780470017029.ch1>.
- [118] Standard Guide for Developing and Selecting Wear Tests - G190, (2015) 1–5. <https://doi.org/10.1520/G0190-15.2>.

- [119] ASTM-International, Standard Test Method for Wear Testing with a Pin-on-Disk Apparatus - ASTM G99, (2017) 1–6. <https://doi.org/10.1520/G0099-17.Copyright>.
- [120] Standard Test Method for Linearly Reciprocating Ball-on-Flat Sliding Wear - G133, ASTM Standard G133 (2016) 1–10. <https://doi.org/10.1520/G0133-05R16.2>.
- [121] Standard Test Method for Ranking Resistance of Materials to Sliding Wear Using Block-on-Ring Wear Test - G77, ASTM Standard G77 (2017) 1–11. <https://doi.org/10.1520/G0077-17.2>.
- [122] I. Hutchings, P. Shipway, Sliding Wear, in: *Tribology: Friction and Wear of Engineering Materials*, 2nd ed., Elsevier Science & Technology, Oxford, UNITED KINGDOM, 2017: pp. 106–164.
- [123] Y.R. Jeng, Z.W. Lin, S.H. Shyu, Changes of surface topography during running-in process, *J Tribol* 126 (2004) 620–625. <https://doi.org/10.1115/1.1759344>.
- [124] A. International, Standard Terminology Relating to Wear and Erosion, ASTM Standards (2016) 1–9. <https://doi.org/10.1520/G0040-17.2>.
- [125] V.A. Belyi, A.I. Sviridyonok, V.A. Smurugov, V. V Nevzorov, Adhesive Wear of Polymers, *Journal of Lubrication Technology* 4 (1977) 396–400.
- [126] A. Abdelbary, Polymer tribology, in: *Wear of Polymers and Composites*, Elsevier, Cambridge, 2014: pp. 1–36. <https://doi.org/10.1533/9781782421788.1>.
- [127] S. Bahadur, C. Schwartz, The effect of nanoparticle fillers on transfer film formation and the tribological behavior of polymers, in: K. Friedrich, A.K. Schlarb (Eds.), *Tribology of Polymeric Nanocomposites. Friction and Wear of Bulk Materials and Coatings*, second, 2013: pp. 23–46.
- [128] S.K. Sinha, W.L.M. Chong, S.C. Lim, Scratching of polymers-Modeling abrasive wear, *Wear* 262 (2007) 1038–1047. <https://doi.org/10.1016/j.wear.2006.10.017>.
- [129] J.K. Lancaster, Abrasive wear of polymers, *Wear* 14 (1969) 223–239. [https://doi.org/10.1016/0043-1648\(69\)90047-7](https://doi.org/10.1016/0043-1648(69)90047-7).
- [130] K. Herrmann, *Hardness testing: principles and applications*, ASM International, Materials Park, Ohio, 2011.
- [131] B.J. Briscoe, P.D. Evans, E. Pelillo, S.K. Sinha, Scratching maps for polymers, *Wear* 200 (1996) 137–147. [https://doi.org/10.1016/S0043-1648\(96\)07314-0](https://doi.org/10.1016/S0043-1648(96)07314-0).
- [132] B.J. Briscoe, E. Pelillo, S.K. Sinha, Scratch Hardness and Deformation Maps for Polycarbonate and Polyethylene, *Polym Eng Sci* 36 (1996) 2996–3005.
- [133] K.G. Budinski, Resistance to particle abrasion of selected plastics, *Wear* 203–204 (1997) 302–309. [https://doi.org/10.1016/S0043-1648\(96\)07346-2](https://doi.org/10.1016/S0043-1648(96)07346-2).
- [134] R.S. Dwyer-Joyce, R.S. Sayles, E. Ioannides, An investigation into the mechanisms of closed three-body abrasive wear, *Wear* 175 (1994) 133–142. [https://doi.org/10.1016/0043-1648\(94\)90176-7](https://doi.org/10.1016/0043-1648(94)90176-7).
- [135] J. Bai, S. Yuan, W. Chow, C.K. Chua, K. Zhou, J. Wei, Effect of surface orientation on the tribological properties of laser sintered polyamide 12, *Polym Test* 48 (2015) 111–114. <https://doi.org/10.1016/j.polymertesting.2015.09.017>.
- [136] M. Schmid, R. Kleijnen, M. Vetterli, K. Wegener, Influence of the origin of polyamide 12 powder on the laser sintering process and laser sintered parts, *Applied Sciences* 7 (2017). <https://doi.org/10.3390/app7050462>.
- [137] N.K. Mavoori, S. Vekatesh, M. Manzoor Hussain, Investigation on surface roughness of sintered PA2200 prototypes using Taguchi method, *Rapid Prototyp J* 25 (2019) 454–461. <https://doi.org/10.1108/RPJ-10-2017-0201>.

- [138] P.B. Bacchewar, S.K. Singhal, P.M. Pandey, Statistical modelling and optimization of surface roughness in the selective laser sintering process, *Proc Inst Mech Eng B J Eng Manuf* 221 (2007) 35–52. <https://doi.org/10.1243/09544054JEM670>.
- [139] F. Sillani, R.G. Kleijnen, M. Vetterli, M. Schmid, K. Wegener, Selective laser sintering and multi jet fusion: Process-induced modification of the raw materials and analyses of parts performance, *Addit Manuf* 27 (2019) 32–41. <https://doi.org/10.1016/j.addma.2019.02.004>.
- [140] C.E. Majewski, D. Oduye, H.R. Thomas, N. Hopkinson, Effect of infra-red power level on the sintering behaviour in the high speed sintering process, *Rapid Prototyp J* 14 (2008) 155–160. <https://doi.org/10.1108/13552540810878012>.
- [141] H.R. Thomas, N. Hopkinson, P. Erasenthiran, High speed sintering - Continuing research into a new rapid manufacturing process, in: *17th Solid Freeform Fabrication Symposium*, 2006: pp. 682–691.
- [142] Z. Zhu, S. Lou, C. Majewski, Characterisation and correlation of areal surface texture with processing parameters and porosity of High Speed Sintered parts, *Addit Manuf* 36 (2020). <https://doi.org/10.1016/j.addma.2020.101402>.
- [143] C. Cai, W.S. Tey, J. Chen, W. Zhu, X. Liu, T. Liu, L. Zhao, K. Zhou, Comparative study on 3D printing of polyamide 12 by selective laser sintering and multi jet fusion, *J Mater Process Technol* 288 (2021). <https://doi.org/10.1016/j.jmatprotec.2020.116882>.
- [144] Z. Xu, Y. Wang, D. Wu, K.P. Ananth, J. Bai, The process and performance comparison of polyamide 12 manufactured by multi jet fusion and selective laser sintering, *J Manuf Process* 47 (2019) 419–426. <https://doi.org/10.1016/j.jmapro.2019.07.014>.
- [145] S. Rosso, R. Meneghello, L. Biasetto, L. Grigolato, G. Concheri, G. Savio, In-depth comparison of polyamide 12 parts manufactured by Multi Jet Fusion and Selective Laser Sintering, *Addit Manuf* 36 (2020). <https://doi.org/10.1016/j.addma.2020.101713>.
- [146] J. Bai, J. Song, J. Wei, Tribological and mechanical properties of MoS₂ enhanced polyamide 12 for selective laser sintering, *J Mater Process Technol* 264 (2019) 382–388. <https://doi.org/10.1016/j.jmatprotec.2018.09.026>.
- [147] T. Ziegler, J.H. Marquez, R. Jaeger, S. Phommahavong, Wear mechanisms and abrasion rates in selective laser sintering materials, *Polym Test* 67 (2018) 545–550. <https://doi.org/10.1016/j.polymertesting.2018.03.026>.
- [148] P. Rajendran, A. Ganesan, Experimental Investigation on Friction Behavior of Selective Laser Sintering Processed Parts, *3D Print Addit Manuf* 00 (2023) 1–10. <https://doi.org/10.1089/3dp.2022.0249>.
- [149] G. Yu, J. Ma, J. Li, J. Wu, J. Yu, X. Wang, Mechanical and Tribological Properties of 3D Printed Polyamide 12 and SiC/PA12 Composite by Selective Laser Sintering, *Polymers (Basel)* 14 (2022). <https://doi.org/10.3390/polym14112167>.
- [150] A. Wörz, D. Drummer, Tribological anisotropy of selective laser sintered PA12 parts, *Polym Test* 70 (2018) 117–126. <https://doi.org/10.1016/j.polymertesting.2018.06.028>.
- [151] A. Gadelmoula, S.A. Aldahash, Effect of Reinforcement with Short Carbon Fibers on the Friction and Wear Resistance of Additively Manufactured PA12, *Polymers (Basel)* 15 (2023) 3187. <https://doi.org/10.3390/polym15153187>.
- [152] K. Friedrich, Polymer composites for tribological applications, *Advanced Industrial and Engineering Polymer Research* 1 (2018) 3–39. <https://doi.org/10.1016/j.aiepr.2018.05.001>.
- [153] I. V. Kragelsky, M.N. Dobychin, V.S. Kambalov, *Friction and wear: calculation methods.*, Pergamon Press, 1982.
- [154] K. V. Shooter, D. Tabor, Frictional properties of plastics, *Proceedings of the Physical Society. Section B* 65 (1952) 661–671. <https://doi.org/10.1088/0370-1301/65/9/302>.

- [155] B. Van Hooreweder, D. Moens, R. Boonen, J.P. Kruth, P. Sas, On the difference in material structure and fatigue properties of nylon specimens produced by injection molding and selective laser sintering, *Polym Test* 32 (2013) 972–981. <https://doi.org/10.1016/j.polymertesting.2013.04.014>.
- [156] G. V. Salmoria, J.L. Leite, L.F. Vieira, A.T.N. Pires, C.R.M. Roesler, Mechanical properties of PA6/PA12 blend specimens prepared by selective laser sintering, *Polym Test* 31 (2012) 411–416. <https://doi.org/10.1016/j.polymertesting.2011.12.006>.
- [157] H. Unal, U. Sen, A. Mimaroglu, Dry sliding wear characteristics of some industrial polymers against steel counterface, *Tribol Int* 37 (2004) 727–732. <https://doi.org/10.1016/j.triboint.2004.03.002>.
- [158] R.T. Steinbuch, Nylon 6 as a bearing material, *Wear* 5 (1962) 458–466. [https://doi.org/10.1016/0043-1648\(62\)90062-5](https://doi.org/10.1016/0043-1648(62)90062-5).
- [159] L. Weimin, H. Chunxiang, G. Ling, W. Jianmin, D. Hongxin, Study of the friction and wear properties of MoS₂-filled Nylon 6, *Wear* 151 (1991) 111–118. [https://doi.org/10.1016/0043-1648\(91\)90350-4](https://doi.org/10.1016/0043-1648(91)90350-4).
- [160] N. Ma, W. Liu, L. Ma, S. He, H. Liu, Z. Zhang, A. Sun, M. Huang, C. Zhu, Crystal transition and thermal behavior of Nylon 12, *E-Polymers* 20 (2020) 346–352. <https://doi.org/10.1515/epoly-2020-0039>.
- [161] J. Bijwe, V. Naidu, N. Bhatnagar, M. Fahim, Optimum concentration of reinforcement and solid lubricant in polyamide 12 composites for best tribo-performance in two wear modes, *Tribol Lett* 21 (2006) 57–64. <https://doi.org/10.1007/s11249-005-9010-7>.
- [162] D. Rouholamin, N. Hopkinson, Understanding the efficacy of micro-CT to analyse high speed sintering parts, 1 (2016) 152–161. <https://doi.org/10.1108/RPJ-03-2014-0030>.
- [163] H. Unal, U. Sen, A. Mimaroglu, Abrasive wear behaviour of polymeric materials, *Mater Des* 26 (2005) 705–710. <https://doi.org/10.1016/j.matdes.2004.09.004>.
- [164] H. Unal, U. Sen, A. Mimaroglu, Dry sliding wear characteristics of some industrial polymers against steel counterface, *Tribol Int* 37 (2004) 727–732. <https://doi.org/10.1016/j.triboint.2004.03.002>.
- [165] S. Bahadur, G. Deli, The transfer and wear of nylon and CuS-nylon composites: Filler proportion and counterface characteristics, *Wear* 162–164 (1993) 397–406. [https://doi.org/10.1016/0043-1648\(93\)90523-O](https://doi.org/10.1016/0043-1648(93)90523-O).
- [166] S. Bahadur, D. Gong, J.W. Anderegg, The role of copper compounds as fillers in transfer film formation and wear of nylon, *Wear* 154 (1992) 207–223. [https://doi.org/10.1016/0043-1648\(92\)90155-2](https://doi.org/10.1016/0043-1648(92)90155-2).
- [167] Y. Xing, G. Zhang, K. Ma, T. Chen, X. Zhao, Study on the friction and wear behaviors of modified PA66 composites, *Polymer - Plastics Technology and Engineering* 48 (2009) 633–638. <https://doi.org/10.1080/03602550902824481>.
- [168] S. Bahadur, A. Kapoor, The effect of ZnF₂, ZnS and PbS fillers on the tribological behavior of nylon 11, *Wear* 155 (1992) 49–61. [https://doi.org/10.1016/0043-1648\(92\)90108-K](https://doi.org/10.1016/0043-1648(92)90108-K).
- [169] A. Kapoor, S. Bahadur, Transfer film bonding and wear studies on CuS-nylon composite sliding against steel, *Tribol Int* 27 (1994) 323–329. [https://doi.org/10.1016/0301-679X\(94\)90026-4](https://doi.org/10.1016/0301-679X(94)90026-4).
- [170] L. xin Zhao, L. yun Zheng, S. guo Zhao, Tribological performance of nano-Al₂O₃ reinforced polyamide 6 composites, *Mater Lett* 60 (2006) 2590–2593. <https://doi.org/10.1016/j.matlet.2006.01.042>.
- [171] EOS GmbH - Electro Optical Systems, PA2200 Material Data Sheet, 2017.

- [172] B. Van Hooreweder, J.P. Kruth, High cycle fatigue properties of selective laser sintered parts in polyamide 12, *CIRP Ann Manuf Technol* 63 (2014) 241–244. <https://doi.org/10.1016/j.cirp.2014.03.060>.
- [173] B. Chen, R. Davies, Y. Liu, N. Yi, D. Qiang, Y. Zhu, O. Ghita, Laser sintering of graphene nanoplatelets encapsulated polyamide powders, *Addit Manuf* 35 (2020) 101363. <https://doi.org/10.1016/j.addma.2020.101363>.
- [174] T.J. Gornet, K.R. Davis, T.L. Starr, K.M. Mulloy, Characterisation of Selective Laser Sintering materials to determine process stability, 2002.
- [175] ASTM International, Standard Test Method for Tensile Properties of Plastics - D638–14, ASTM International, 2015. <https://doi.org/10.1520/D0638-14.1>.
- [176] British Standards, BS EN ISO 25178-3. Geometrical product specifications (GPS) — Surface texture: Areal Part 3: Specification operators, (2012).
- [177] S. Petzold, J. Klett, T.A. Osswald, A statistical study of surface roughness for polyamide 12 parts produced using selective laser sintering, *International Polymer Processing* 35 (2020) 126–138. <https://doi.org/10.3139/217.3900>.
- [178] BSI-Standards, Geometric product specifications (GPS). Surface texture: Profile method. Surfaces having stratified functional properties. Part 1: Filtering and general measurement conditions - BS EN ISO 13565-1:1998, (1998).
- [179] J.R. Wingham, R. Turner, J. Shepherd, C. Majewski, Micro-CT for analysis of laser sintered micro-composites, *Rapid Prototyp J* 26 (2020) 649–657. <https://doi.org/10.1108/RPJ-08-2019-0211>.
- [180] C.-R. Yang, R.T. Lee, Y.C. Chiou, Study on slip displacement and stick-slip characteristics in reciprocating friction drive system, *Tribol Int* 32 (1999) 97–106. [https://doi.org/10.1016/S0301-679X\(99\)00016-X](https://doi.org/10.1016/S0301-679X(99)00016-X).
- [181] T. Palma, M. Munther, P. Damasus, S. Salari, A. Beheshti, K. Davami, Multiscale mechanical and tribological characterizations of additively manufactured polyamide 12 parts with different print orientations, *J Manuf Process* 40 (2019) 76–83. <https://doi.org/10.1016/j.jmapro.2019.03.004>.
- [182] E. Ciulli, A. Betti, P. Forte, The Applicability of the Hertzian Formulas to Point Contacts of Spheres and Spherical Caps, *Lubricants* 10 (2022). <https://doi.org/10.3390/lubricants10100233>.
- [183] K. Senthilkumaran, P.M. Pandey, P.V.M. Rao, Influence of building strategies on the accuracy of parts in selective laser sintering, *Mater Des* 30 (2009) 2946–2954. <https://doi.org/10.1016/j.matdes.2009.01.009>.
- [184] N.A. Feidenhans’L, P.E. Hansen, L. Pilný, M.H. Madsen, G. Bissacco, J.C. Petersen, R. Taboryski, Comparison of optical methods for surface roughness characterization, *Meas Sci Technol* 26 (2015). <https://doi.org/10.1088/0957-0233/26/8/085208>.
- [185] B. Bhushan, Surface roughness analysis and measurement techniques, *Modern Tribology Handbook: Volume One: Principles of Tribology* (2000) 49–119. <https://doi.org/10.1201/9780849377877.ch2>.
- [186] D.C. Montgomery, Design and analysis of experiments, 5th ed., Wiley, New York; Chichester, 2001.
- [187] Pareto chart - Minitab, Minitab Support (2023). <https://support.minitab.com/en-us/minitab/21/help-and-how-to/statistical-modeling/regression/how-to/fit-regression-model/methods-and-formulas/pareto-chart/> (accessed July 20, 2023).

- [188] S. Ruesenberg, H.J. Schmid, Advanced characterization method of nylon 12 materials for application in laser sinter processing, *AIP Conf Proc* 1593 (2014) 713–718. <https://doi.org/10.1063/1.4873877>.
- [189] Formlabs, Nylon 12 Powder, (n.d.). <https://formlabs.com/uk/store/materials/nylon-12-powder/> (accessed March 12, 2022).
- [190] D. Dowson, C.M. Taylor, M. Godet, *The Running-In Process in Tribology*, Lyon, France, 1981.
- [191] T. Mang, K. Bobzin, T. Bartels, *Industrial Tribology*, 2011. [https://doi.org/10.1016/0301-679x\(83\)90075-0](https://doi.org/10.1016/0301-679x(83)90075-0).
- [192] S.E. Franklin, Wear experiments with selected engineering polymers and polymer composites under dry reciprocating sliding conditions, *Wear* 250–251 (2001) 1591–1598. [https://doi.org/10.1016/s0043-1648\(01\)00795-5](https://doi.org/10.1016/s0043-1648(01)00795-5).
- [193] S. Bahadur, The development of transfer layers and their role in polymer tribology, *Wear* 245 (2000) 92–99. [https://doi.org/10.1016/S0043-1648\(00\)00469-5](https://doi.org/10.1016/S0043-1648(00)00469-5).
- [194] V. Rodriguez, J. Sukumaran, A.K. Schlarb, P. De Baets, Influence of solid lubricants on tribological properties of polyetheretherketone (PEEK), *Tribol Int* 103 (2016) 45–57. <https://doi.org/10.1016/j.triboint.2016.06.037>.
- [195] A. Gadelmoula, S.A. Aldahash, Tribological Properties of Glass Bead-Filled Polyamide 12 Composite Manufactured by Selective Laser Sintering, *Polymers (Basel)* 15 (2023) 1–15. <https://doi.org/10.3390/polym15051268>.
- [196] B. Briscoe, Wear of polymers: an essay on fundamental aspects, *Tribol Int* 14 (1981) 231–243. [https://doi.org/10.1016/0301-679X\(81\)90050-5](https://doi.org/10.1016/0301-679X(81)90050-5).
- [197] J.F. Frank, R. Chmielewski, Influence of surface finish on the cleanability of stainless steel, *J Food Prot* 64 (2001) 1178–1182. <https://doi.org/10.4315/0362-028X-64.8.1178>.
- [198] M. Watson, P. Christoforou, P. Herrera, D. Preece, J. Carrell, M. Harmon, P. Krier, S. Lewis, R. Maiti, W. Skipper, E. Taylor, J. Walsh, M. Zalzal, L. Alhadeff, R. Kempka, J. Lanigan, Z.S. Lee, B. White, K. Ishizaka, R. Lewis, T. Slatter, R. Dwyer-Joyce, M. Marshall, An analysis of the quality of experimental design and reliability of results in tribology research, *Wear* 426–427 (2019) 1712–1718. <https://doi.org/10.1016/j.wear.2018.12.028>.
- [199] N. Gao, C.T. Wang, R.J.K. Wood, T.G. Langdon, Tribological properties of ultrafine-grained materials processed by severe plastic deformation, *J Mater Sci* 47 (2012) 4779–4797. <https://doi.org/10.1007/s10853-011-6231-z>.
- [200] S. Yuan, F. Shen, C.K. Chua, K. Zhou, Polymeric composites for powder-based additive manufacturing: Materials and applications, *Prog Polym Sci* 91 (2019) 141–168. <https://doi.org/10.1016/j.progpolymsci.2018.11.001>.
- [201] C. Yan, L. Hao, L. Xu, Y. Shi, Preparation, characterisation and processing of carbon fibre/polyamide-12 composites for selective laser sintering, *Compos Sci Technol* 71 (2011) 1834–1841. <https://doi.org/10.1016/j.compscitech.2011.08.013>.
- [202] H. Chung, S. Das, Functionally graded Nylon-11/silica nanocomposites produced by selective laser sintering, *Materials Science and Engineering A* 487 (2008) 251–257. <https://doi.org/10.1016/j.msea.2007.10.082>.
- [203] A. Mousah, Effects of filler content and coupling agents on the mechanical properties and geometrical accuracy of selective laser sintered parts in glass bead-filled polyamide 12 composites, Cardiff University, 2011.
- [204] J.C.J. Bart, E. Gucciardi, S. Cavallaro, Lubricants: properties and characteristics, in: *Biolubricants*, 2013: pp. 24–73. <https://doi.org/10.1533/9780857096326.24>.

- [205] G. Mariani, Selection and Application of Solid Lubricants as Friction Modifiers, in: *Lubricant Additives: Chemistry and Applications*, Third, 2015: pp. 249–249. <https://doi.org/10.1201/b19209-17>.
- [206] J. Ye, H.S. Khare, D.L. Burris, Quantitative characterization of solid lubricant transfer film quality, *Wear* 316 (2014) 133–143. <https://doi.org/10.1016/j.wear.2014.04.017>.
- [207] R. Kumar, H. Kumar Banga, H. Singh, S. Kundal, An outline on modern day applications of solid lubricants, *Mater Today Proc* 28 (2020) 1962–1967. <https://doi.org/10.1016/j.matpr.2020.05.558>.
- [208] K. Bashandeh, P. Lan, J.L. Meyer, A.A. Polycarpou, Tribological Performance of Graphene and PTFE Solid Lubricants for Polymer Coatings at Elevated Temperatures, *Tribol Lett* 67 (2019) 1–14. <https://doi.org/10.1007/s11249-019-1212-5>.
- [209] S. Bahadur, D. Tabor, The wear of filled polytetrafluoroethylene, *Wear* 98 (1984) 1–13. [https://doi.org/10.1016/0043-1648\(84\)90213-8](https://doi.org/10.1016/0043-1648(84)90213-8).
- [210] S.P. Soe, Quantitative analysis on SLS part curling using EOS P700 machine, *J Mater Process Technol* 212 (2012) 2433–2442. <https://doi.org/10.1016/j.jmatprotec.2012.06.012>.
- [211] M. Vetterli, M. Schmid, K. Wegener, *Comprehensive Investigation of Surface Characterization Methods for Laser Sintered Parts*, (2018).
- [212] A.E. Tontowi, T.H.C. Childs, Density prediction of crystalline polymer sintered parts at various powder bed temperatures, *Rapid Prototyp J* 7 (2001) 180–184. <https://doi.org/10.1108/13552540110395637>.
- [213] T. Kigure, Y. Yamauchi, T. Niino, Relationship between powder bed temperature and microstructure of laser sintered PA12 parts, in: *Solid Freeform Fabrication 2019: Proceedings of the 30th Annual International Solid Freeform Fabrication Symposium - An Additive Manufacturing Conference, SFF 2019*, 2019: pp. 827–834.
- [214] X. Lua, Y. Jin, Structure and properties of Nylon 12/SiC nanocomposites, *Mater Res Express* 6 (2019). <https://doi.org/10.1088/2053-1591/ab0874>.
- [215] W. Brostow, D. Zhang, Tensile elongation at break for polymers related to Vickers hardness, *Mater Lett* 276 (2020) 128179. <https://doi.org/10.1016/j.matlet.2020.128179>.
- [216] B. Ben Difallah, M. Kharrat, M. Dammak, G. Monteil, Mechanical and tribological response of ABS polymer matrix filled with graphite powder, *Mater Des* 34 (2012) 782–787. <https://doi.org/10.1016/j.matdes.2011.07.001>.
- [217] S. g Sathees Kumar, G. Kanagaraj, Investigation on Mechanical and Tribological Behaviors of PA6 and Graphite-Reinforced PA6 Polymer Composites, *Arab J Sci Eng* 41 (2016) 4347–4357. <https://doi.org/10.1007/s13369-016-2126-2>.
- [218] P.M.F. Wani, Tribological Behaviour of Virgin Ptfе and Glass Filled Ptfе under Dry Sliding Conditions, in: *Innovative Approaches In Mechanical Engineering*, n.d.: pp. 5–11.
- [219] S. Singh, A. Sachdeva, V.S. Sharma, Optimization of selective laser sintering process parameters to achieve the maximum density and hardness in polyamide parts, *Progress in Additive Manufacturing* 2 (2017) 19–30. <https://doi.org/10.1007/s40964-017-0020-4>.
- [220] T. Palma, M. Munther, P. Damasus, S. Salari, A. Beheshti, K. Davami, Multiscale mechanical and tribological characterizations of additively manufactured polyamide 12 parts with different print orientations, *J Manuf Process* 40 (2019) 76–83. <https://doi.org/10.1016/j.jmapro.2019.03.004>.
- [221] W.S. Tey, C. Cai, K. Zhou, A Comprehensive Investigation on 3D Printing of Polyamide 11 and Thermoplastic Polyurethane via Multi Jet Fusion, *Polymers (Basel)* 13 (2021) 2139. <https://doi.org/10.3390/polym13132139>.

Appendices

A. Additive Manufacturing Technologies

The figures presented within this appendix outline the general build processes intrinsic to each of the seven primary categories of AM technologies, as define by ASTM International [11].

Binder Jetting

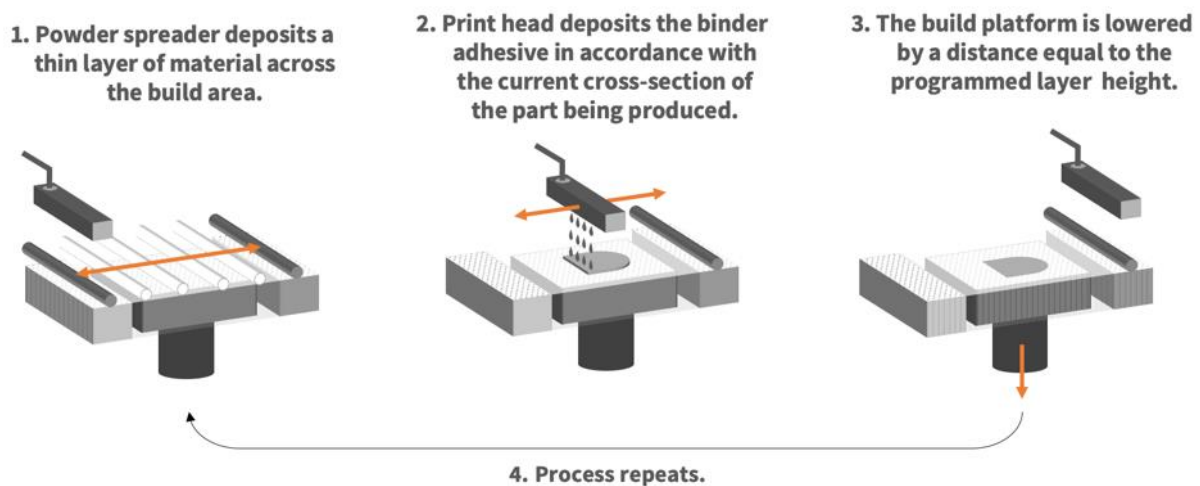


Figure A.1 – An overview of the Binder Jetting AM build process.

Directed Energy Deposition

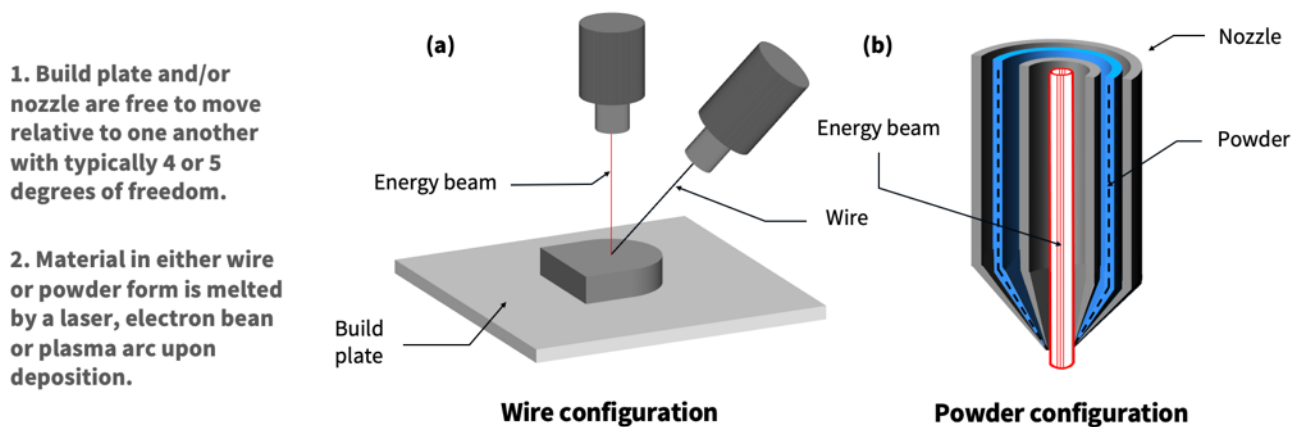


Figure A.2 – An overview of the Directed Energy Deposition AM build process in both **(a)** wire and **(b)** powder configurations.

Material Extrusion

1. Material in filament form is heated and extruded through a nozzle.

2. Layer-by-layer material is deposited in accordance with the current cross-section of the part being produced.

Support structure is typically included when overhanging features need to be manufactured.

Figure A.3 – An overview of the Material Extrusion AM build process.

Material Jetting

1. Droplets of material are deposited in accordance with the current cross-section of the part by print heads actuated either thermally or by piezoelectrics.

2. Once solidified, the layer is cured by ultraviolet light.

3. Post processing includes the removal of supporting material.

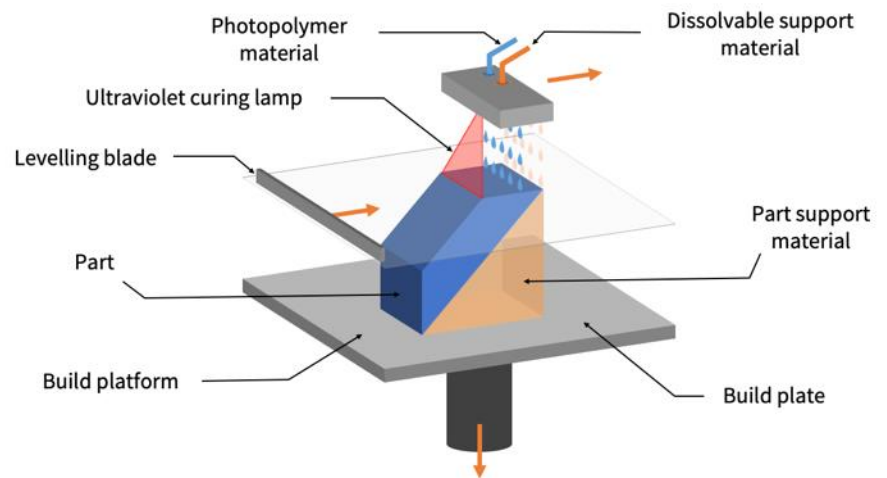


Figure A.4 – An overview of the Material Jetting AM build process.

Sheet Lamination

1. Heated roller flattens the sheet material in preparation for cutting.

2. The current cross-section of the part being produced is cut using a laser or a cutting tool.

3. Rollers move the sheet material along, and the build platform is lowered by a distance equal to the thickness of the sheet material.

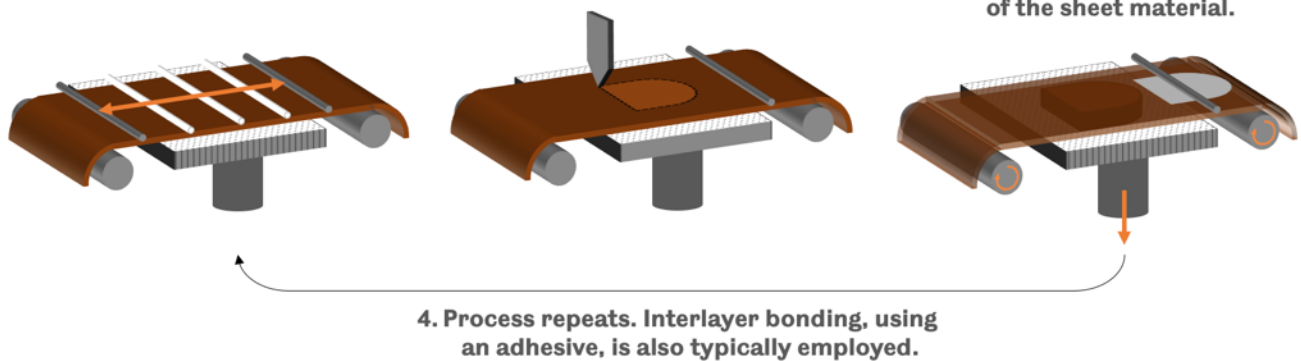


Figure A.5 – An overview of the Sheet Lamination AM build process.

Vat Photopolymerisation

1. In the current configuration, the build plate is lowered into the vat of photopolymer resin.

2. Ultraviolet light selectively cures the current cross-section of the part being produced.

3. The build plate is raised by a distance equal to the programmed layer height.

4. Stages 2 and 3 repeat until the build is complete.

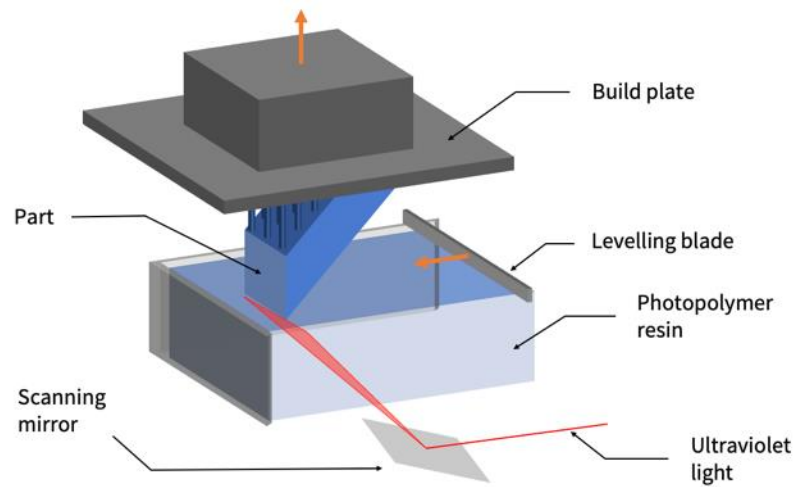


Figure A.6 – An overview of the Vat Photopolymerisation AM build process.

B. *Transient Sliding Microscopy Scan Images*

This appendix includes scan images of the pin and disk top and bottom surfaces captured during 10N and 20N sliding tests performed in work presented in **Chapter 7**.

10N Top Surface Sliding

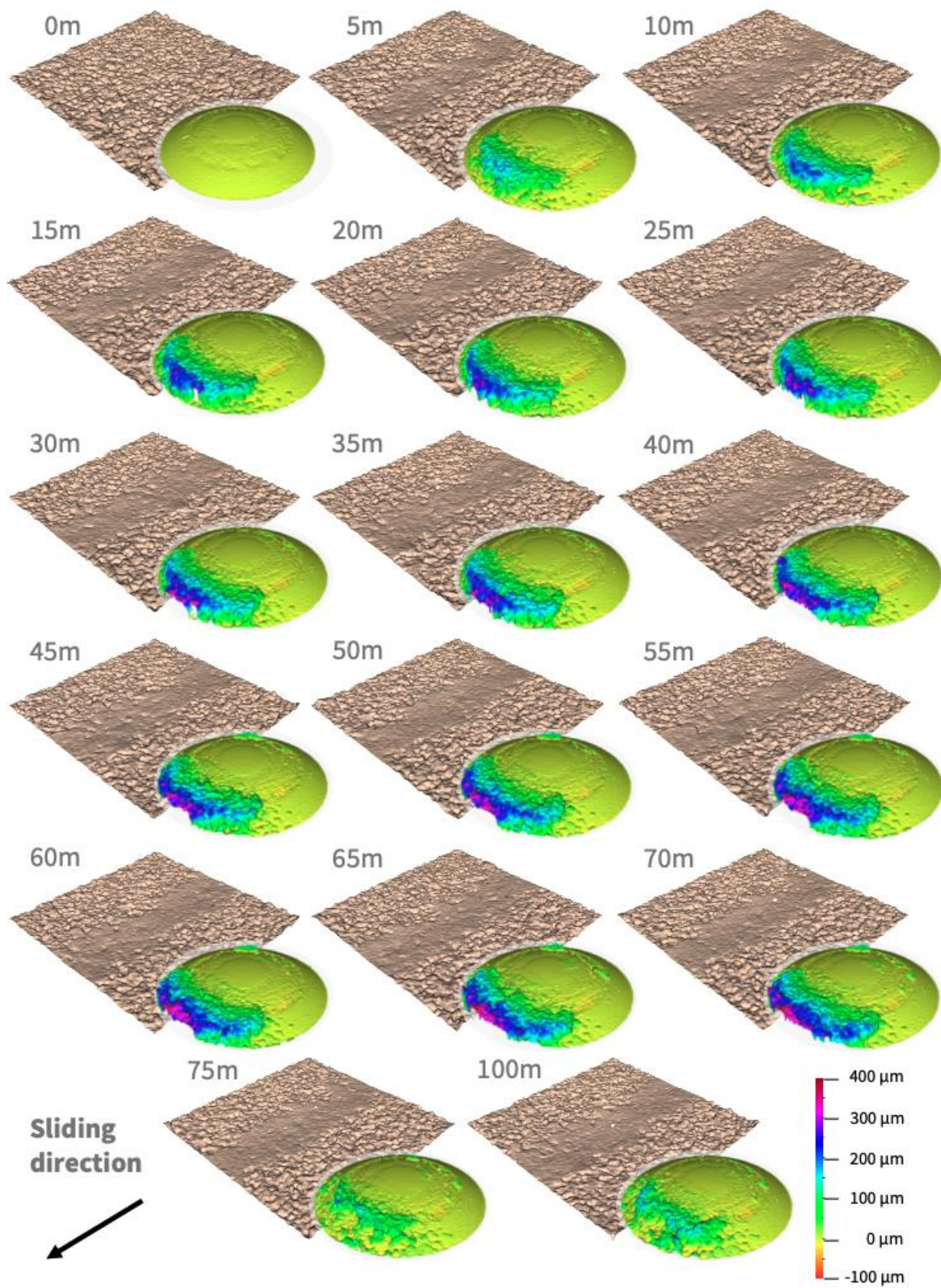


Figure B.1 – Resultant pin and disk top surfaces at each interval during 10N sliding.

10N Bottom Surface Sliding

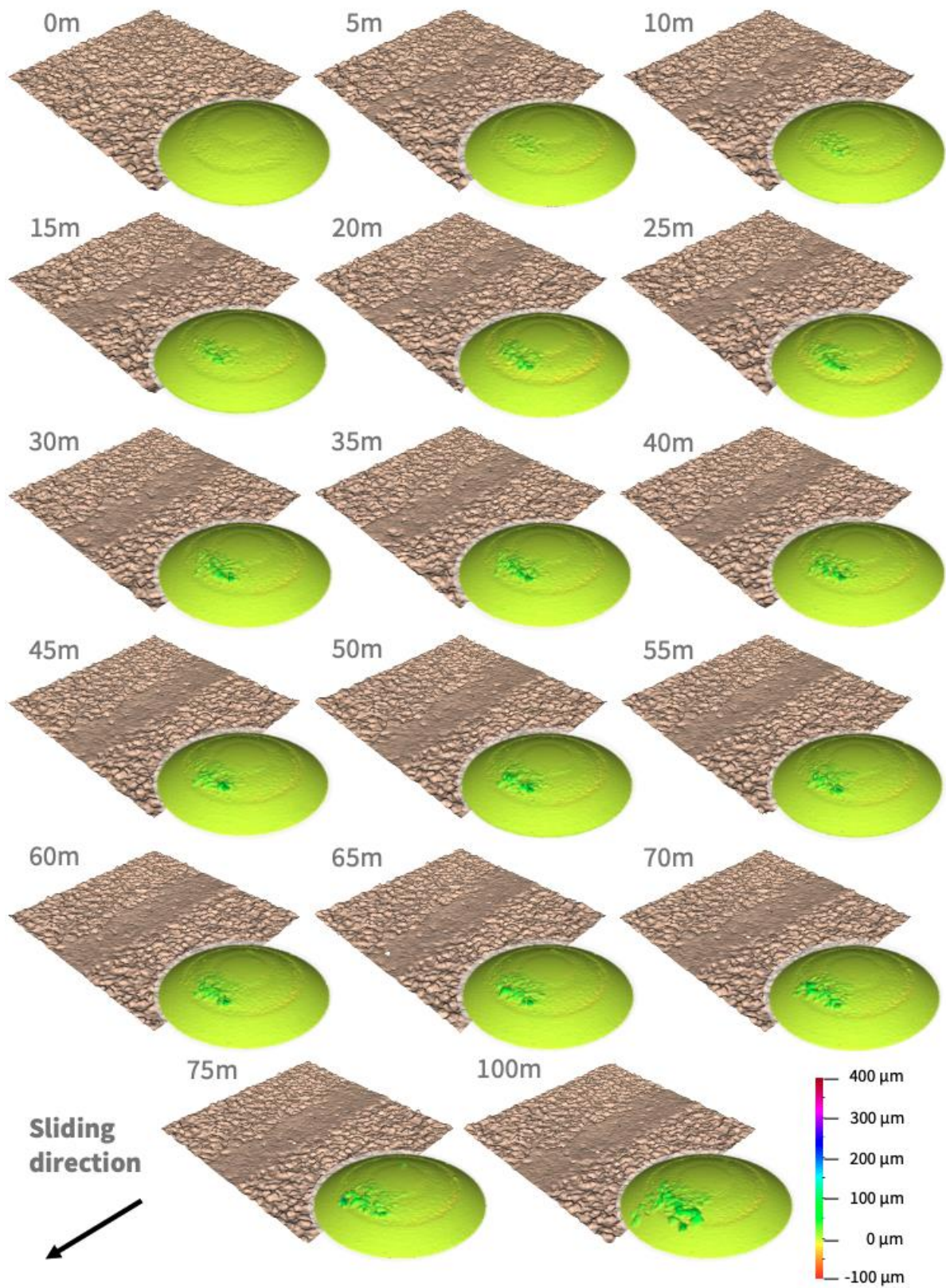


Figure B.2 – Resultant pin and disk bottom surfaces at each interval during 10N sliding.

20N Top Surface Sliding

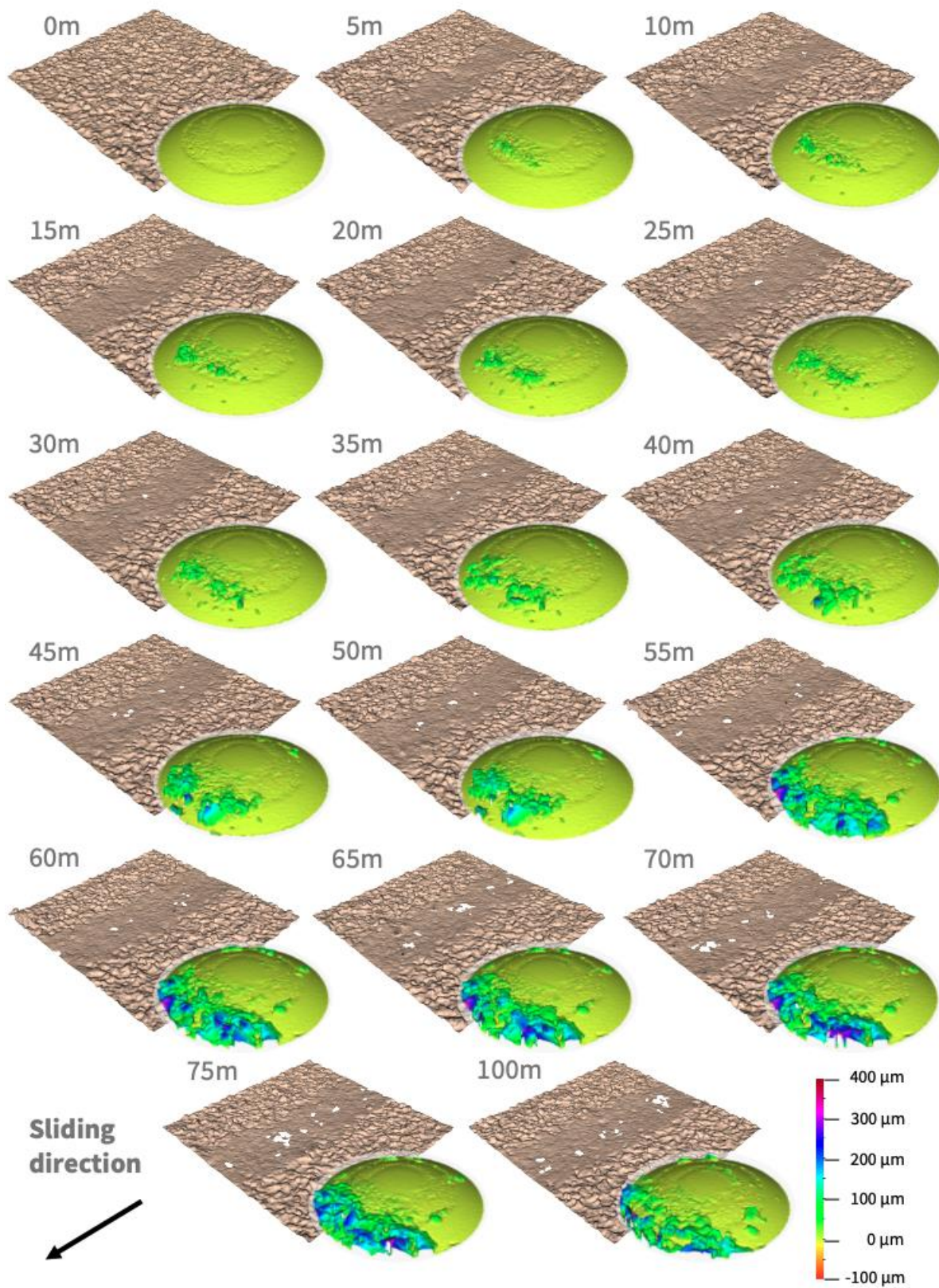


Figure B.3 – Resultant pin and disk top surfaces at each interval during 20N sliding.

20N Bottom Surface Sliding

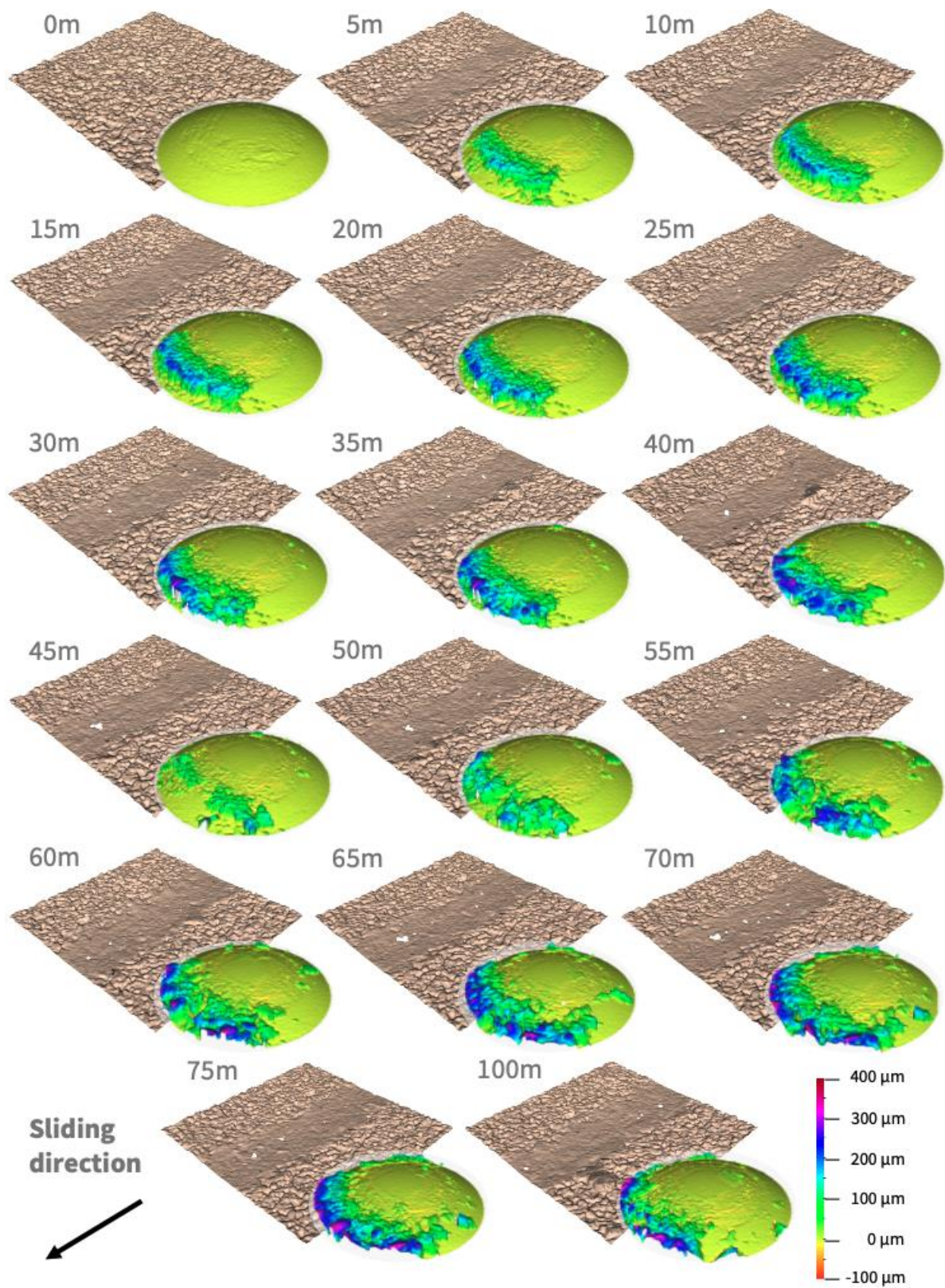


Figure B.4 – Resultant pin and disk bottom surfaces at each interval during 20N sliding.

C. Auxiliary Friction and Wear Results

This appendix includes the individual friction and wear responses recorded when conducting each repeat sliding test as part of work carried out in **Chapter 8**.

C.1 Friction Results

Metal Pin on Polymer Disk Sliding

$3N - 0.05ms^{-1}$ / Low Load – Low Speed

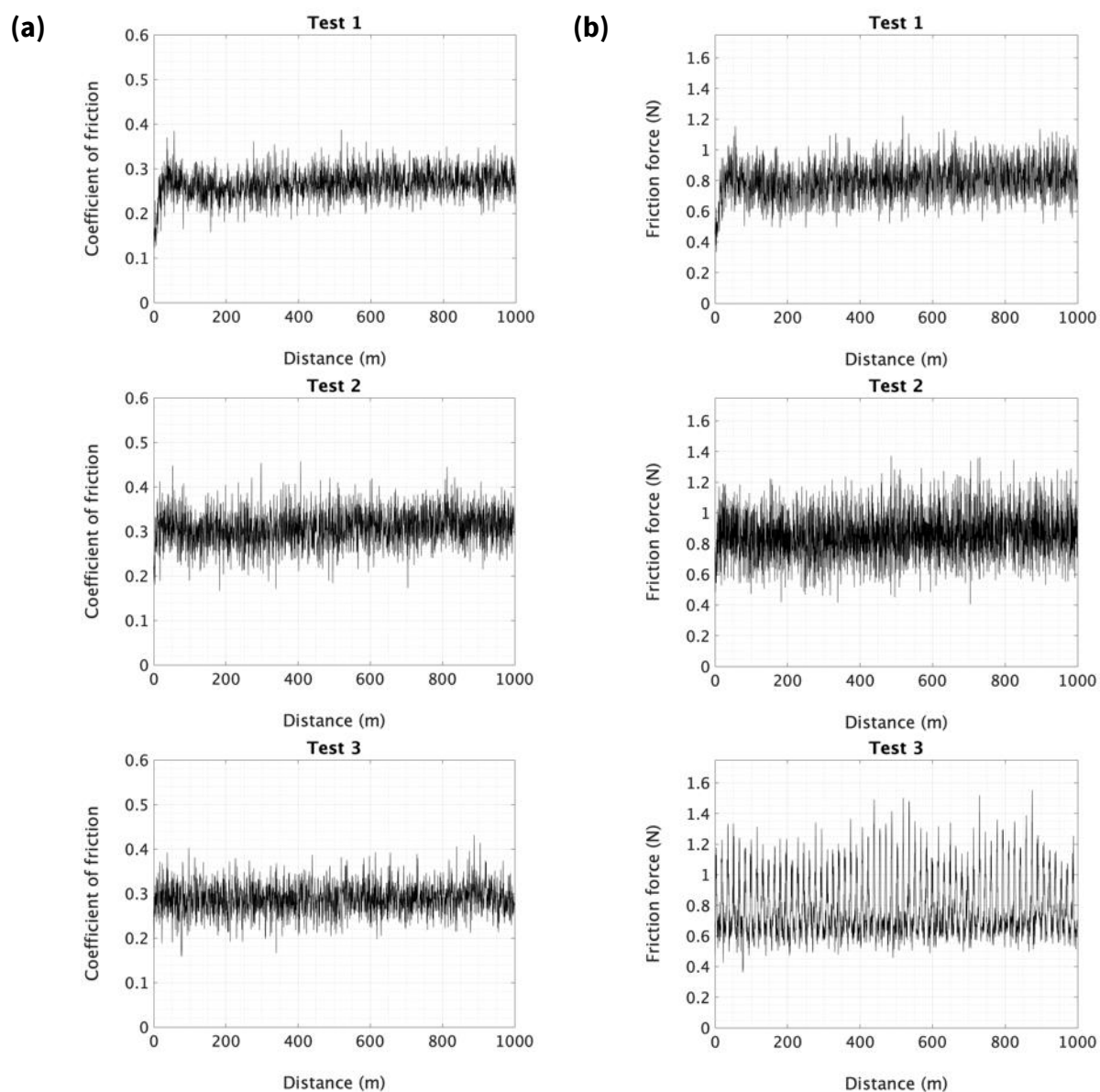


Figure C.1 – The individual **(a)** COF and **(b)** friction force responses recorded during each metal pin on polymer disk, $3N - 0.05ms^{-1}$ (low load / low speed) sliding test.

$3N - 0.5ms^{-1}$ / Low Load – High Speed

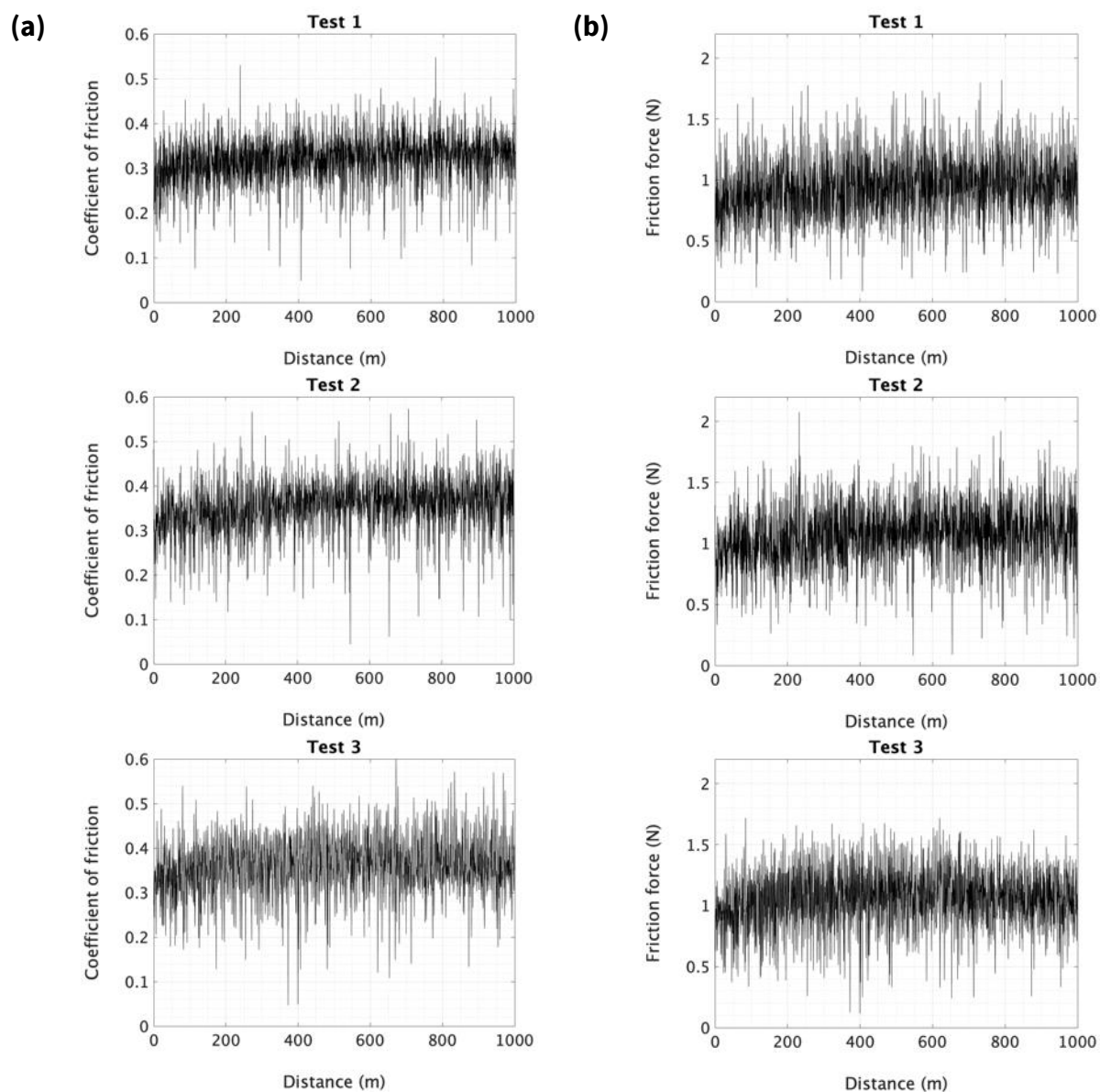


Figure C.2 – The individual (a) COF and (b) friction force responses recorded during each metal pin on polymer disk, $3N - 0.5ms^{-1}$ (low load / high speed) sliding test.

30N – 0.05ms⁻¹ / High Load – Low Speed

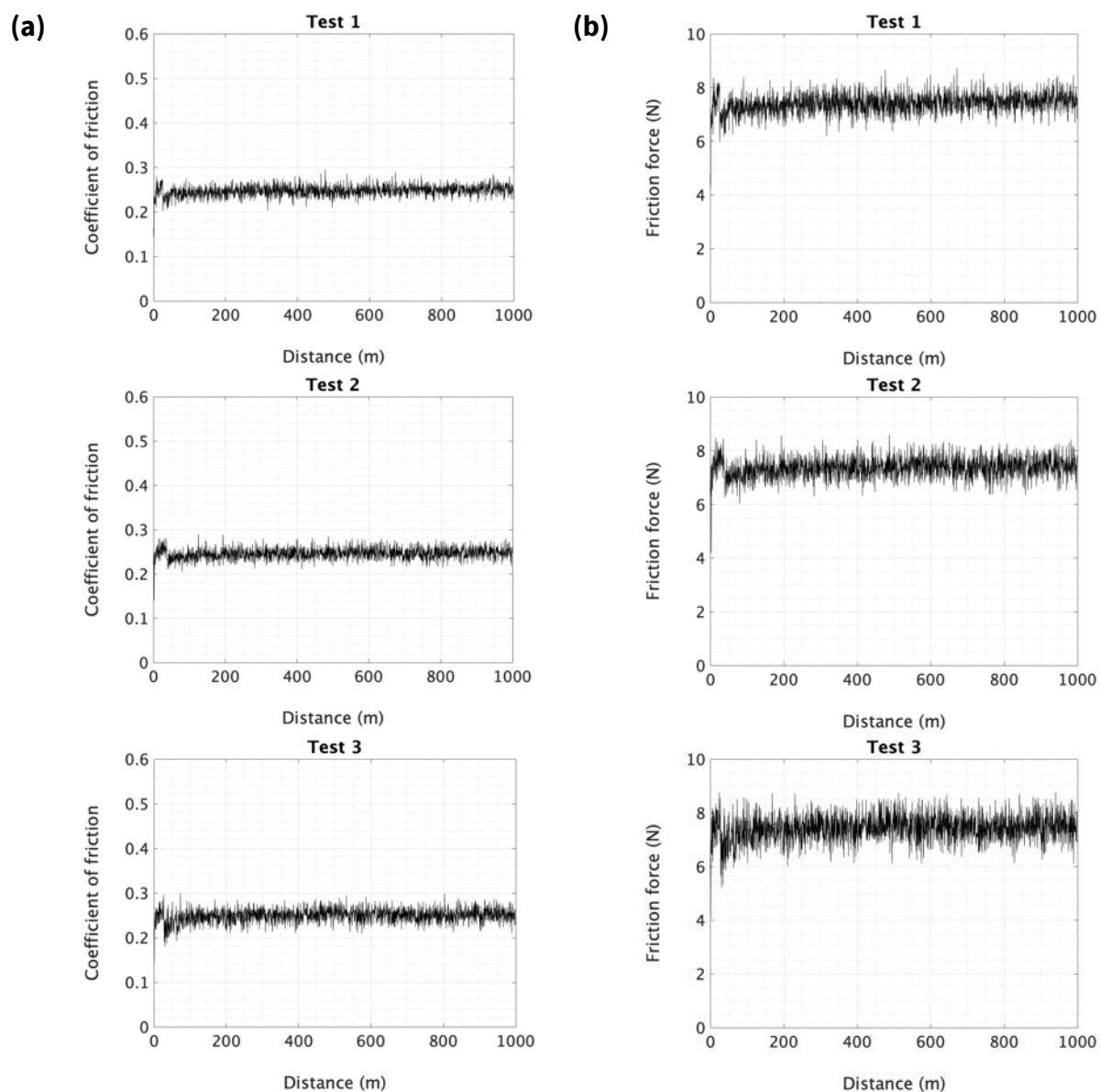


Figure C.3 – The individual **(a)** COF and **(b)** friction force responses recorded during each metal pin on polymer disk, 30N – 0.05ms⁻¹ (high load / low speed) sliding test.

$30\text{N} - 0.5\text{ms}^{-1}$ / High Load – High Speed

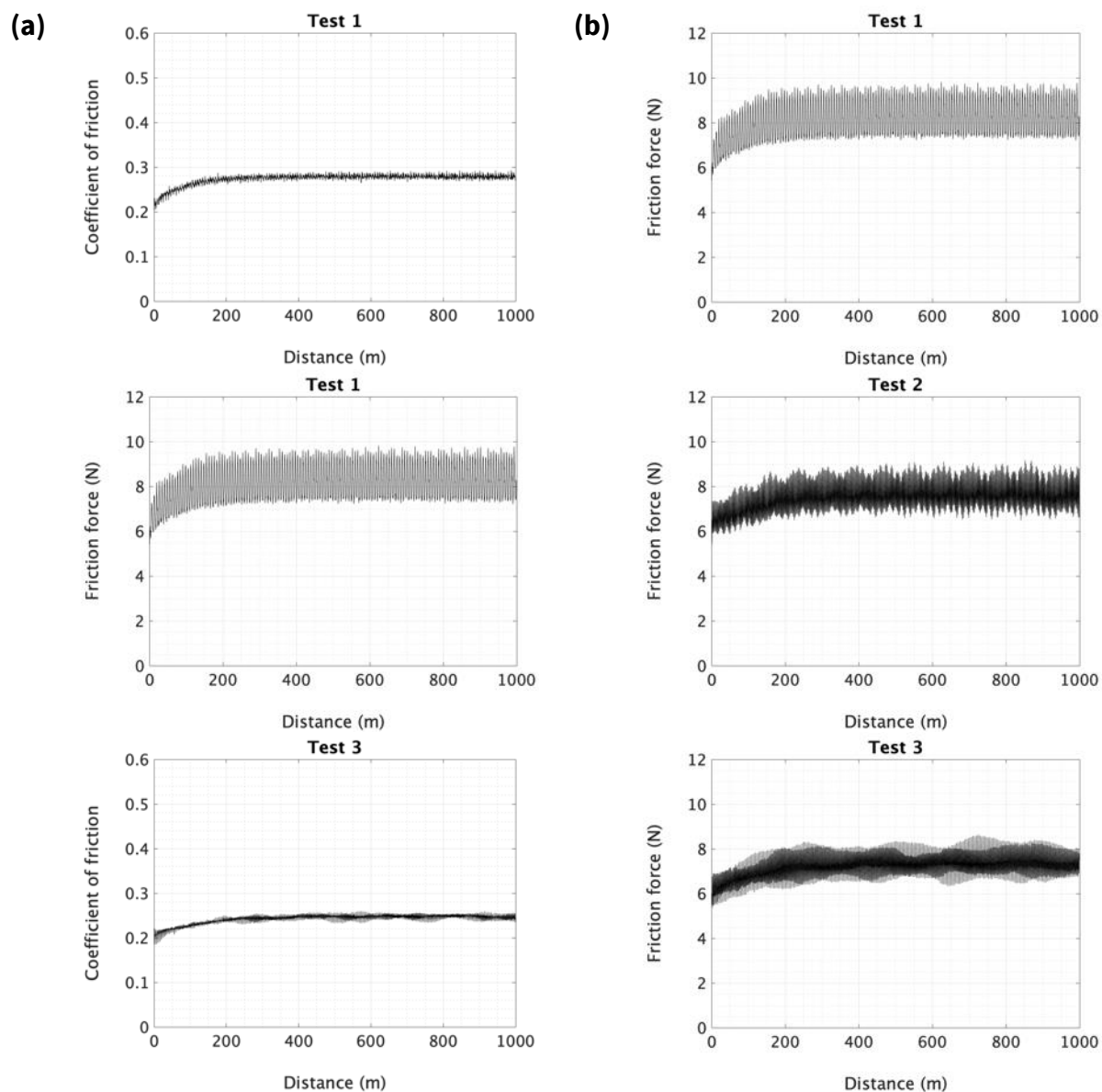


Figure C.4 – The individual (a) COF and (b) friction force responses recorded during each metal pin on polymer disk, $30\text{N} - 0.5\text{ms}^{-1}$ (high load / high speed) sliding test.

Polymer Pin on Metal Disk Sliding

$3\text{N} - 0.05\text{ms}^{-1}$ / Low Load – Low Speed

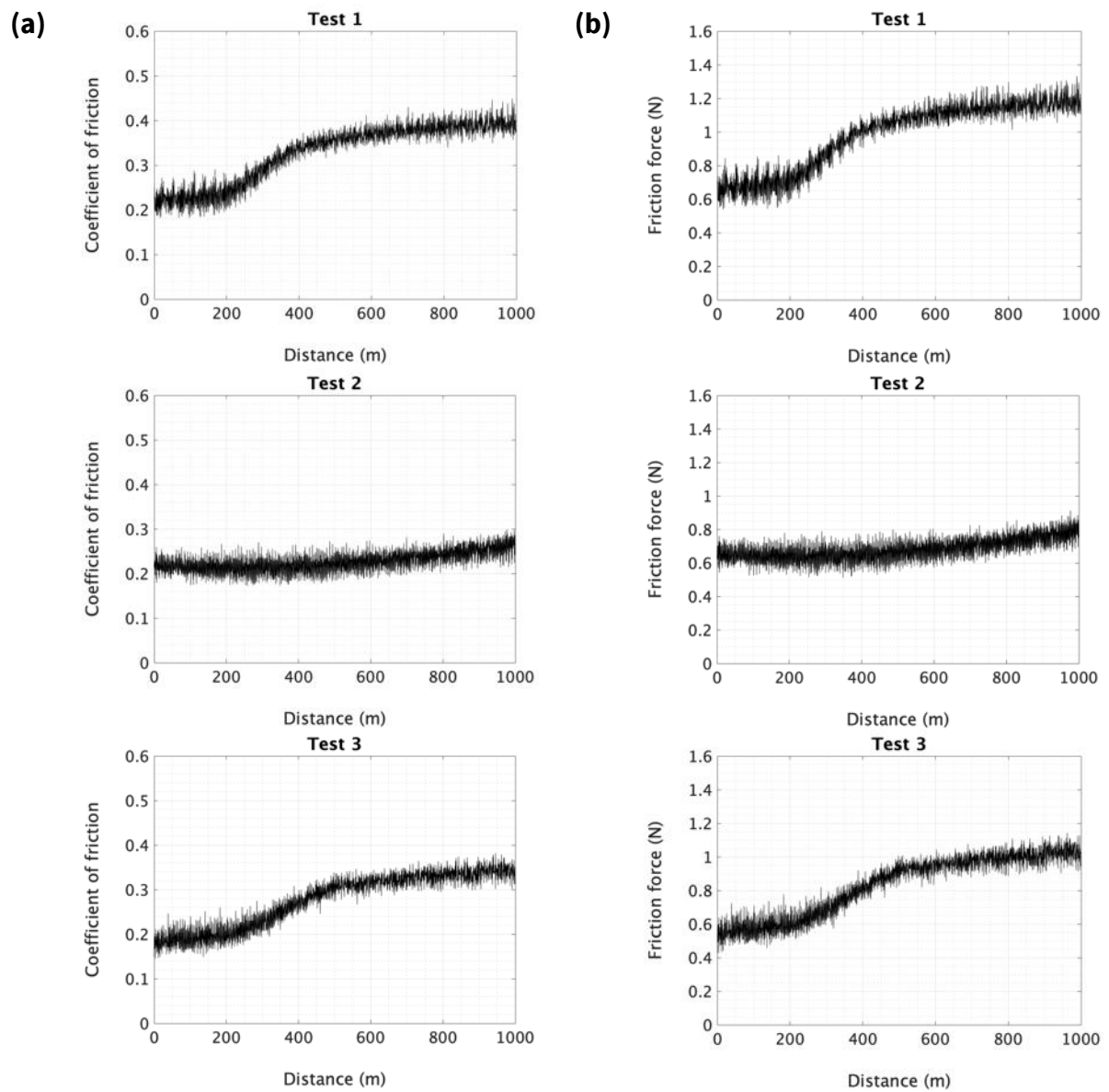


Figure C.5 – The individual (a) COF and (b) friction force responses recorded during each polymer pin on metal disk, $3\text{N} - 0.05\text{ms}^{-1}$ (low load / low speed) sliding test.

$3N - 0.5ms^{-1}$ / Low Load – High Speed

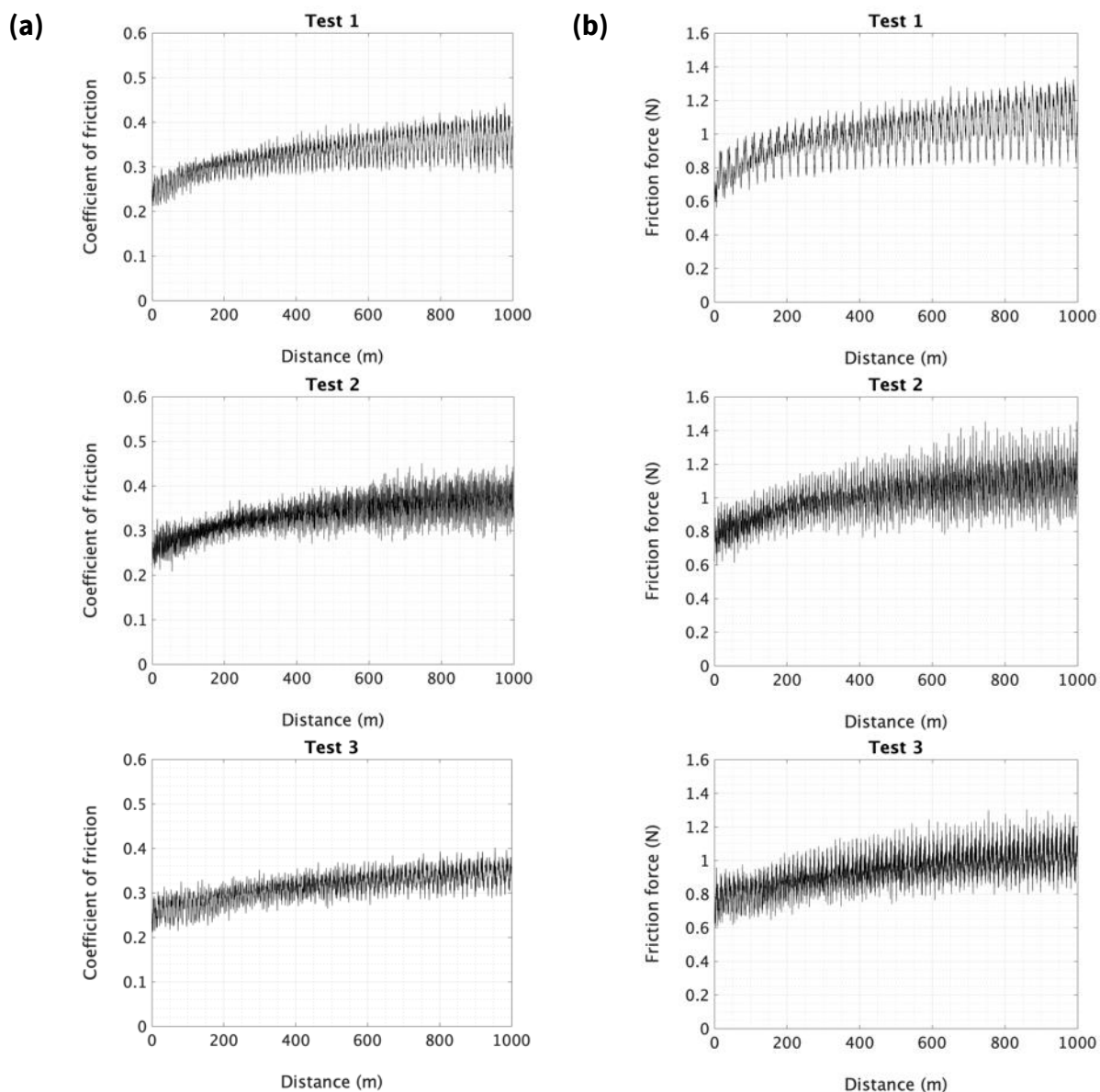


Figure C.6 – The individual (a) COF and (b) friction force responses recorded during each polymer pin on metal disk, $3N - 0.5ms^{-1}$ (low load / high speed) sliding test.

30N – 0.05ms⁻¹ / High Load – Low Speed

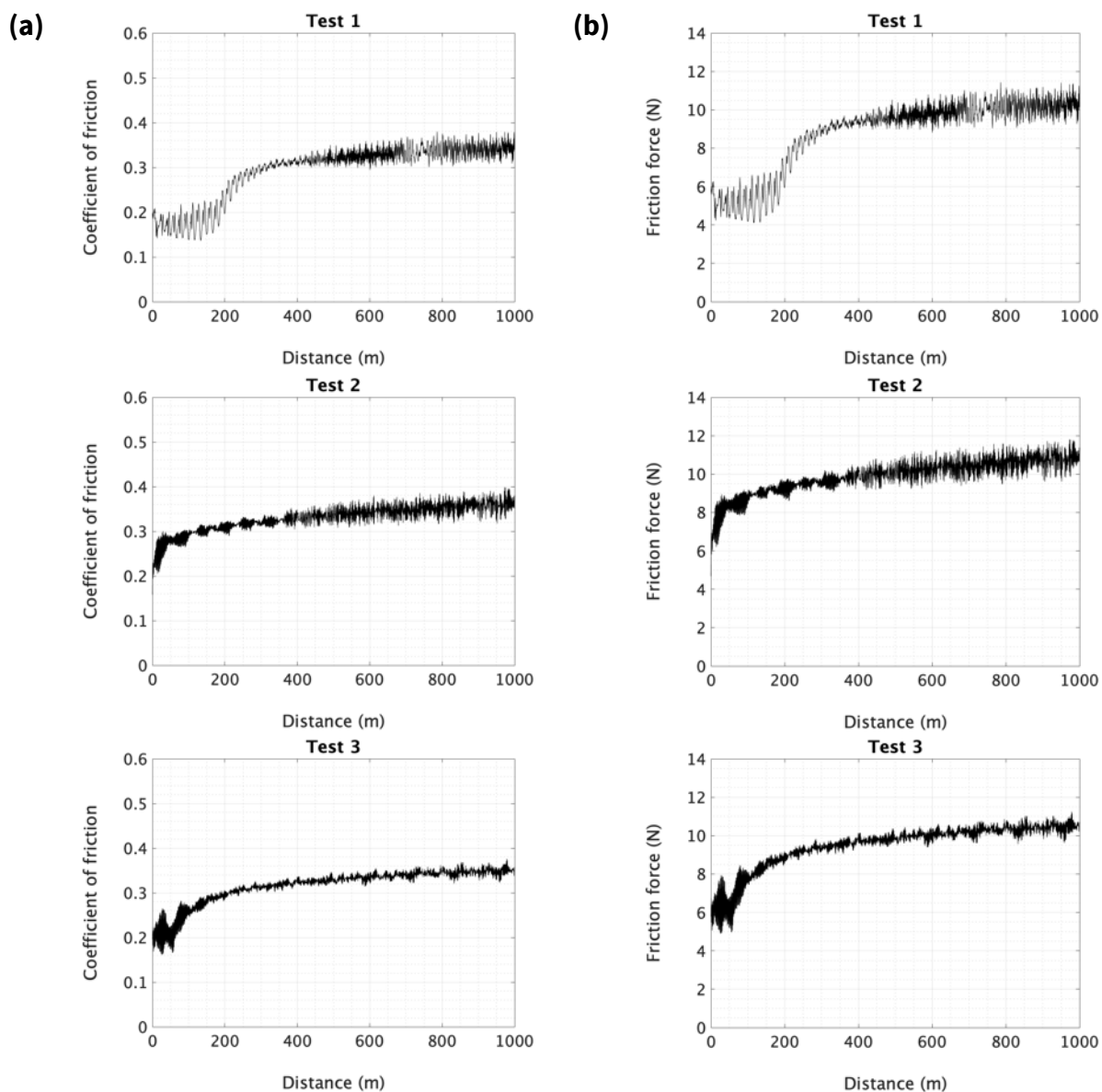


Figure C.7 – The individual (a) COF and (b) friction force responses recorded during each polymer pin on metal disk, 30N – 0.05ms⁻¹ (high load / low speed) sliding test.

$30\text{N} - 0.5\text{ms}^{-1}$ / High Load – High Speed

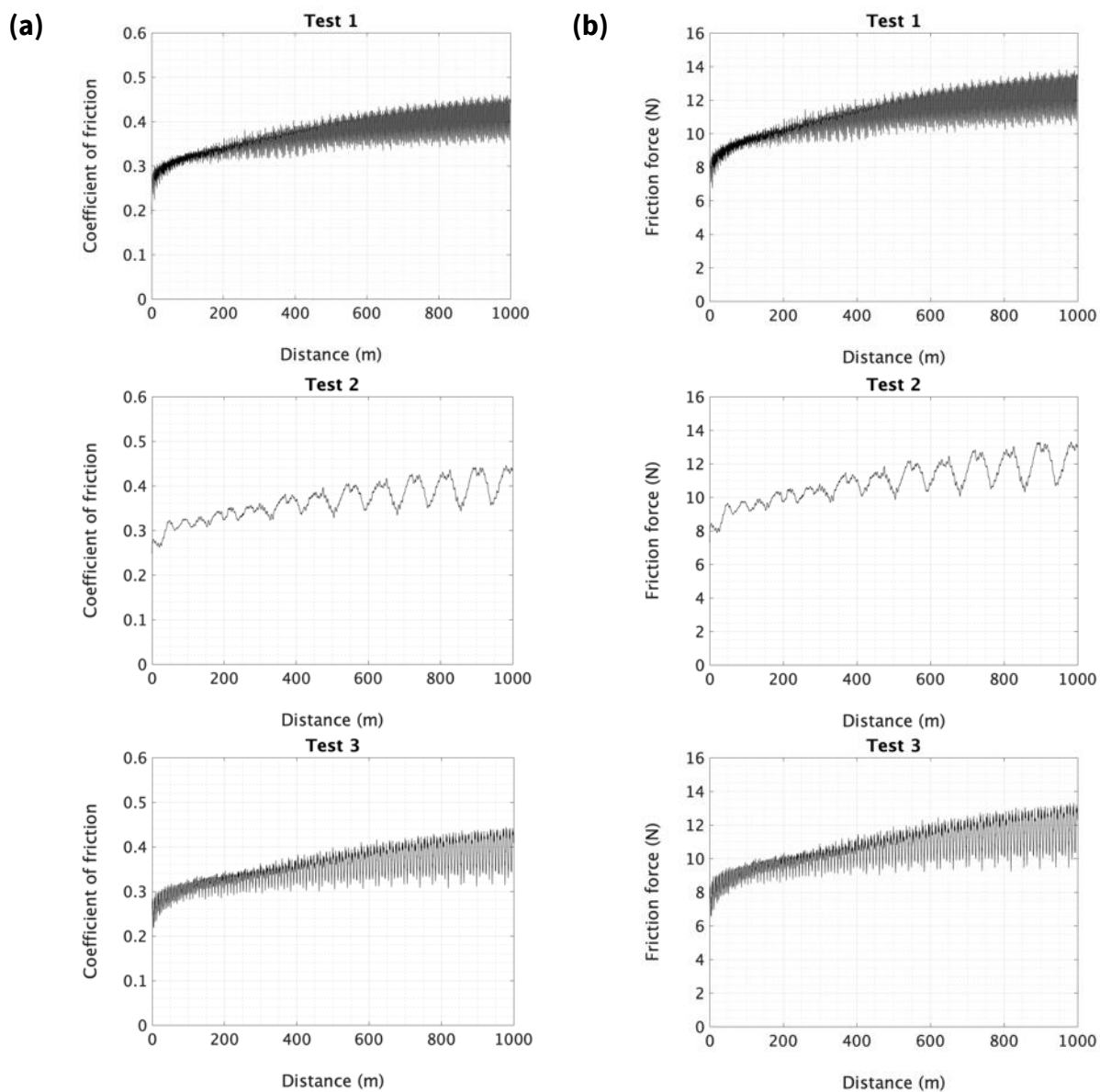


Figure C.8 – The individual (a) COF and (b) friction force responses recorded during each polymer pin on metal disk, $30\text{N} - 0.5\text{ms}^{-1}$ (high load / high speed) sliding test.

C.2 Wear Results

Metal Pin on Polymer Disk Sliding

$3N - 0.05ms^{-1}$ / Low Load – Low Speed

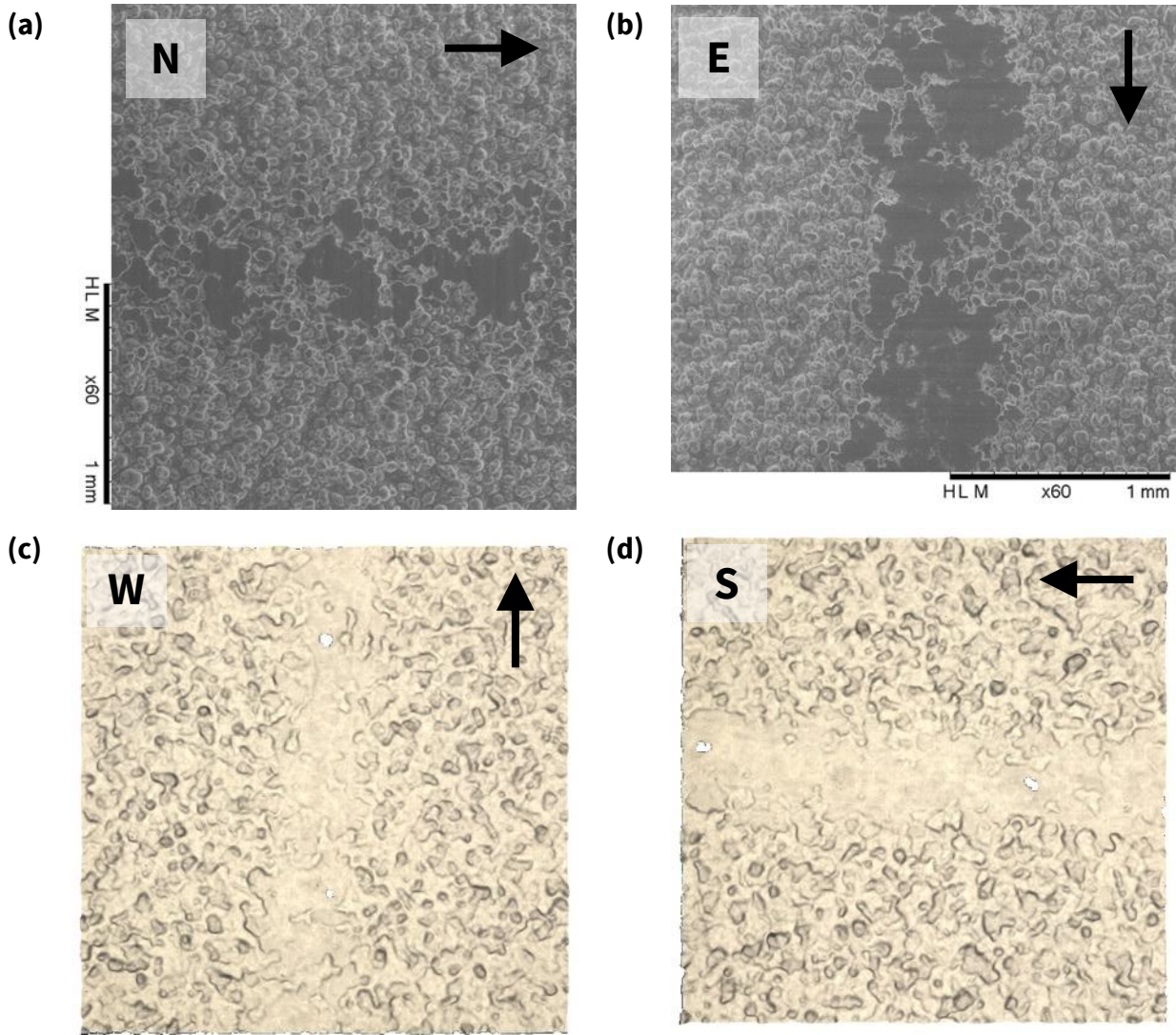


Figure C.9 – Microscopy images captured after the second repeat $3N - 0.05ms^{-1}$ (low load / low speed) sliding test. These include wear scars obtained by SEM at **(a)** north and **(b)** east locations, as well as FV microscopy images captured at **(c)** west and **(d)** south locations. The orientation of each arrow denotes the instantaneous direction of rotation of each disk region relative to the metal pin.

$3N - 0.5ms^{-1}$ / Low Load – High Speed

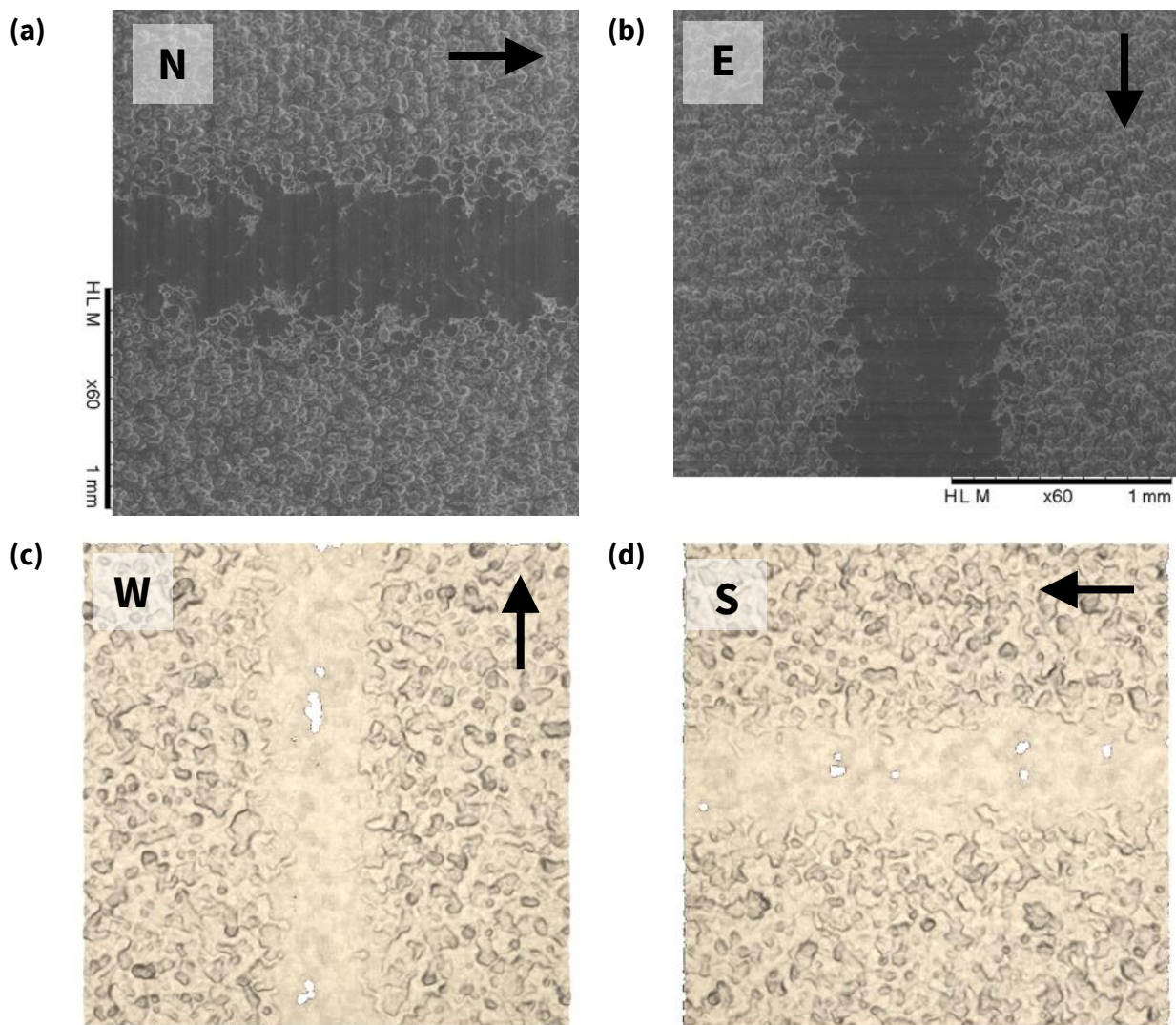


Figure C.10 – Microscopy images captured after the second repeat $3N - 0.5ms^{-1}$ (low load / high speed) sliding test. These include wear scars obtained by SEM at **(a)** north and **(b)** east locations, as well as FV microscopy images captured at **(c)** west and **(d)** south locations. The orientation of each arrow denotes the instantaneous direction of rotation of each disk region relative to the metal pin.

$30N - 0.05ms^{-1}$ / High Load – Low Speed

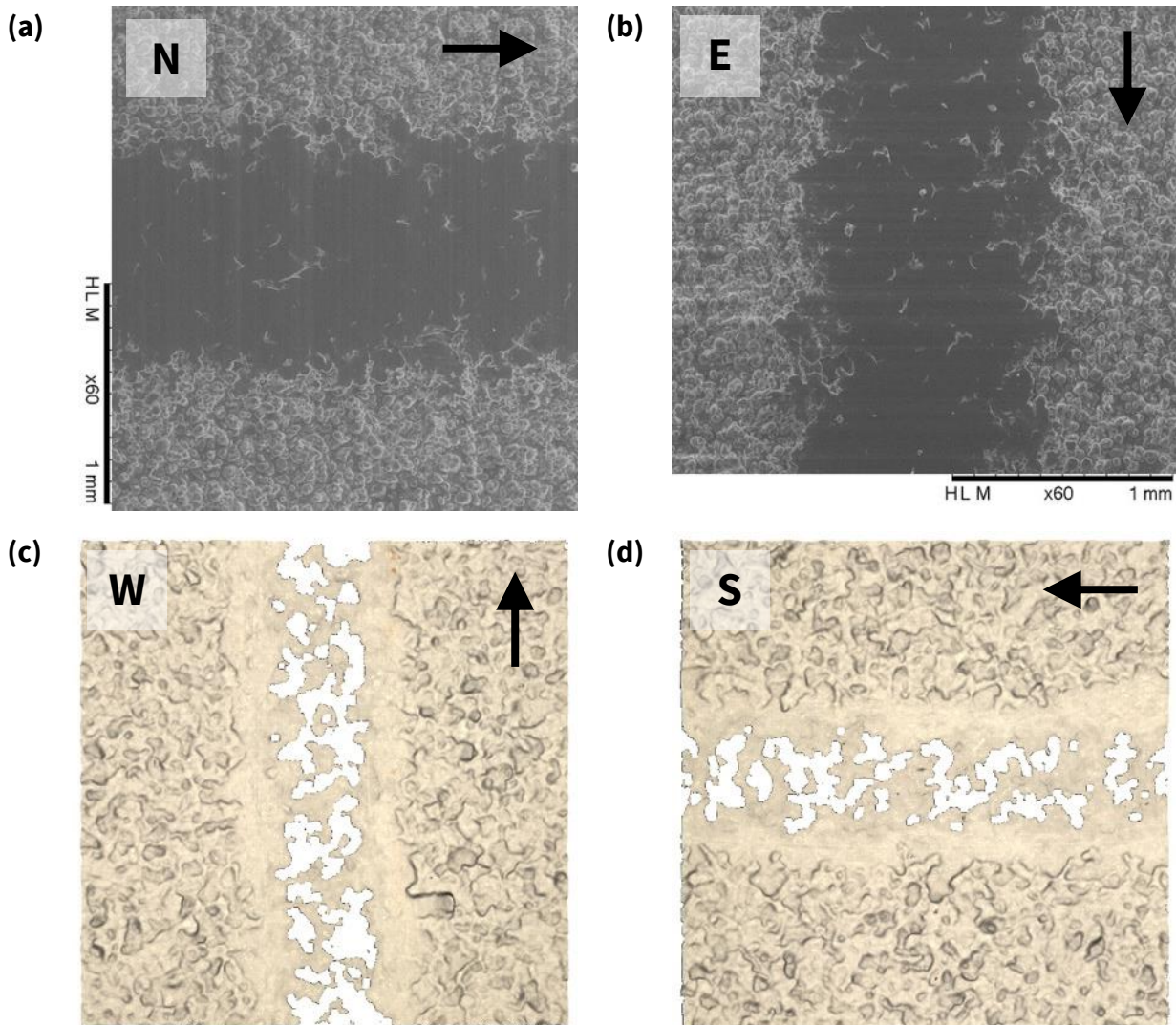


Figure C.11 – Microscopy images captured after the second repeat $30N - 0.05ms^{-1}$ (high load / low speed) sliding test. These include wear scars obtained by SEM at (a) north and (b) east locations, as well as FV microscopy images captured at (c) west and (d) south locations. The orientation of each arrow denotes the instantaneous direction of rotation of each disk region relative to the metal pin.

$30\text{N} - 0.5\text{ms}^{-1}$ / High Load – High Speed

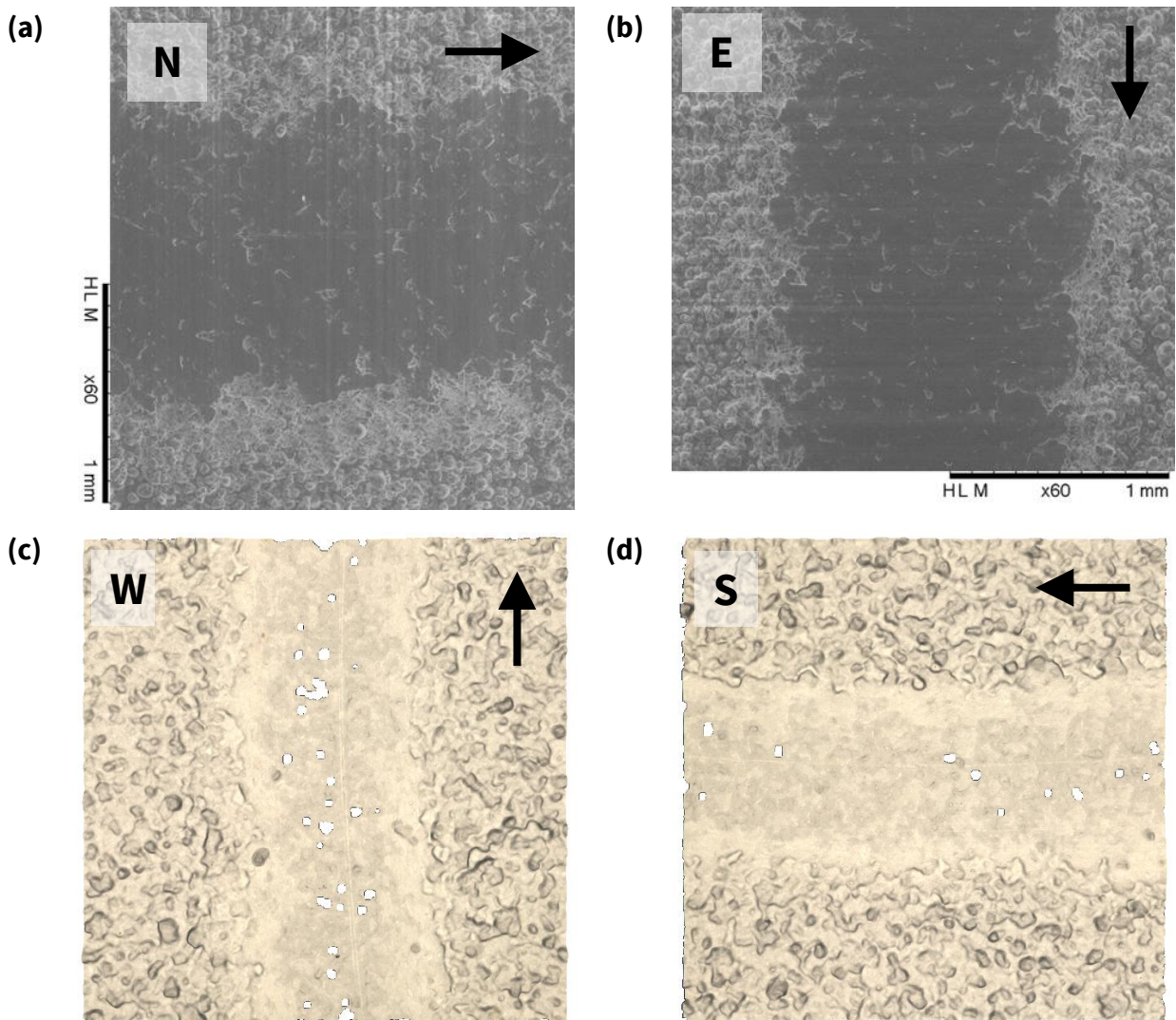
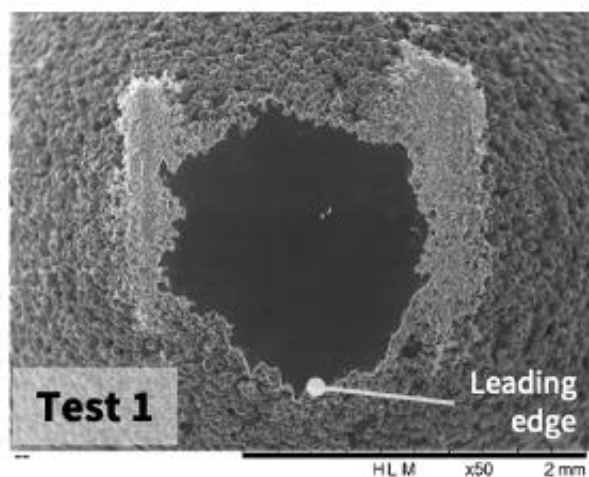


Figure C.12 – Microscopy images captured after the second repeat $30\text{N} - 0.5\text{ms}^{-1}$ (high load / high speed) sliding test. These include wear scars obtained by SEM at **(a)** north and **(b)** east locations, as well as FV microscopy images captured at **(c)** west and **(d)** south locations. The orientation of each arrow denotes the instantaneous direction of rotation of each disk region relative to the metal pin.

Polymer Pin on Metal Disk Sliding

$3N - 0.05ms^{-1}$ / Low Load – Low Speed

(a)



(b)

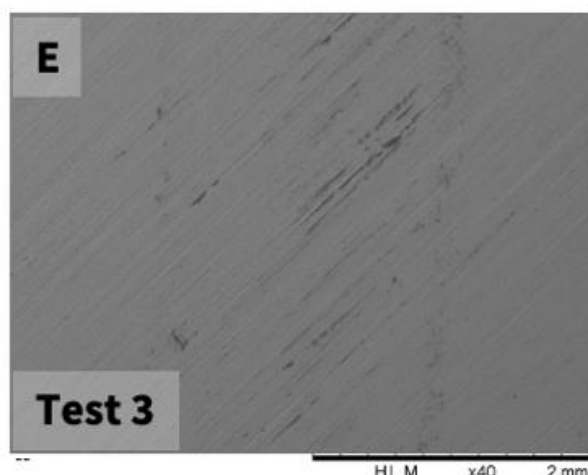
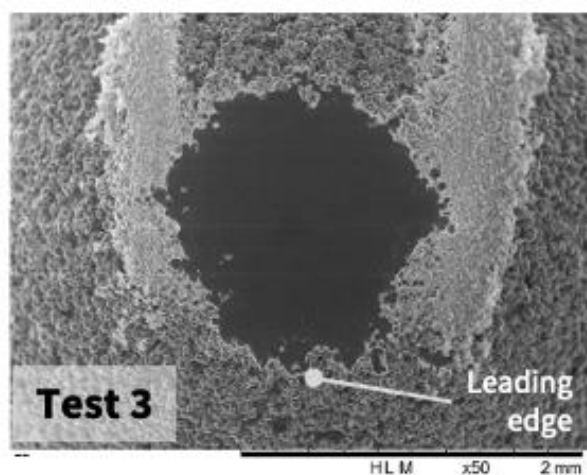
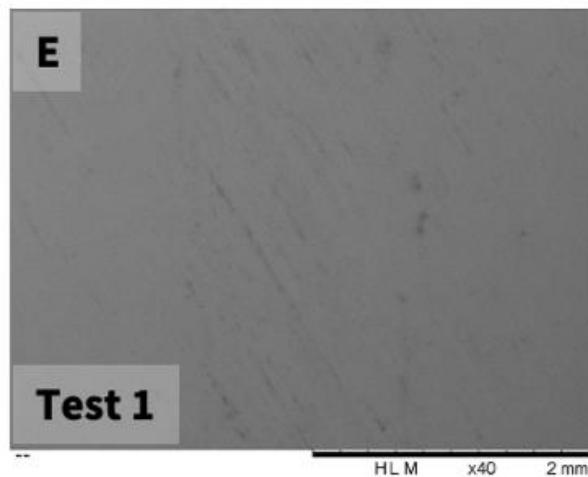
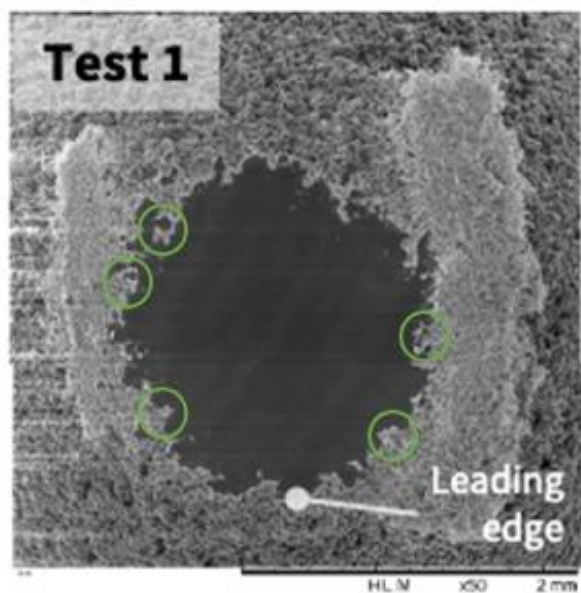


Figure C.13 – SEM scan images of (a) polymer pin worn surfaces and (b) metal disk samples (east location) captured after $3N - 0.05ms^{-1}$ (low load / low speed) sliding, specifically from tests 1 and 3.

$3N - 0.5ms^{-1}$ / Low Load – High Speed

(a)



(b)

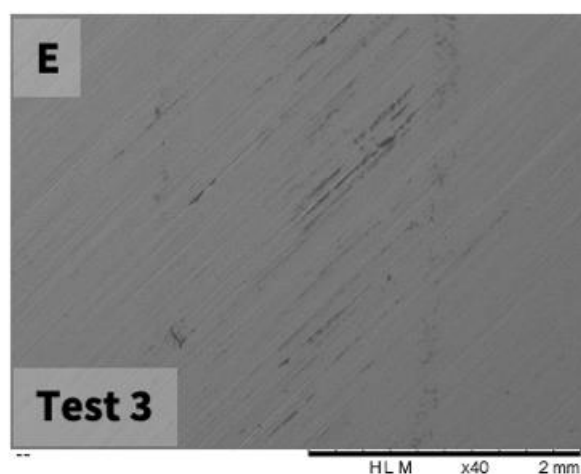
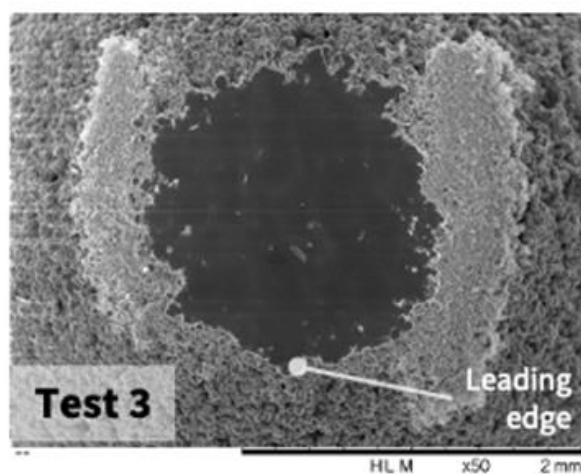
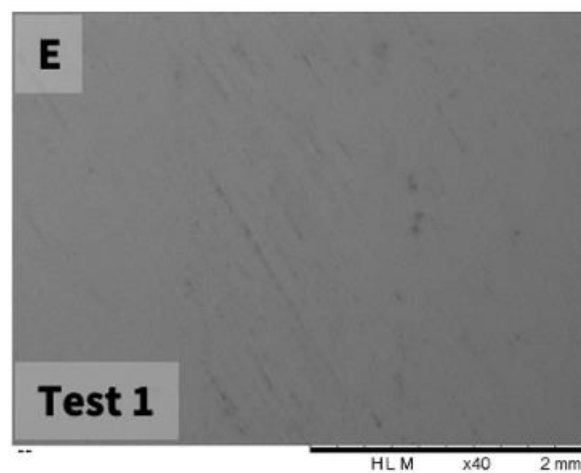
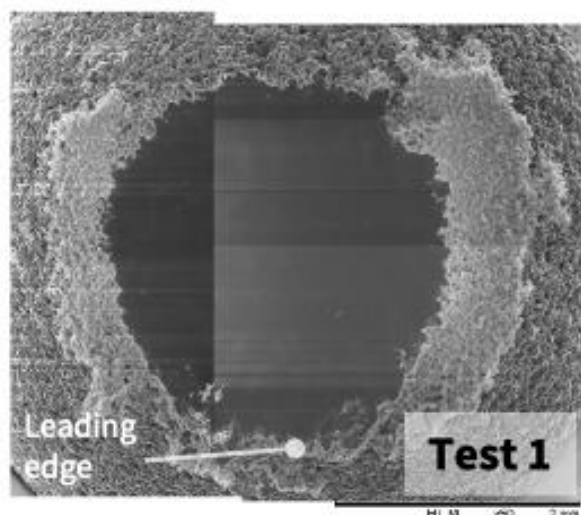


Figure C.14 – SEM scan images of (a) polymer pin worn surfaces and (b) metal disk samples (east location) captured after $3N - 0.5ms^{-1}$ (low load / high speed) sliding, specifically from tests 1 and 3. Each circled region highlights a region in which clusters of asperity peaks can be seen.

$30\text{N} - 0.05\text{ms}^{-1}$ / High Load – Low Speed

(a)



(b)

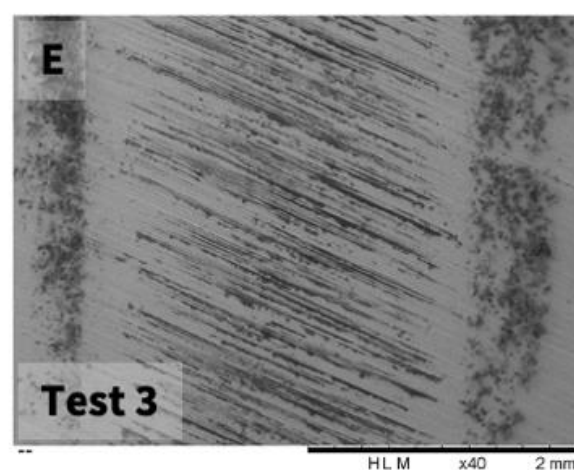
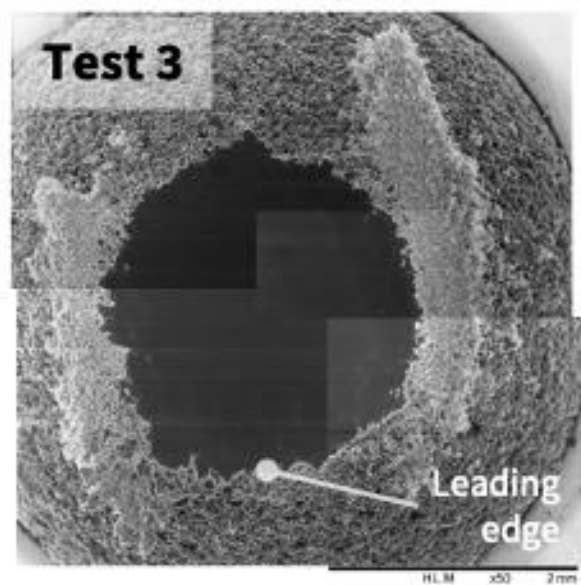
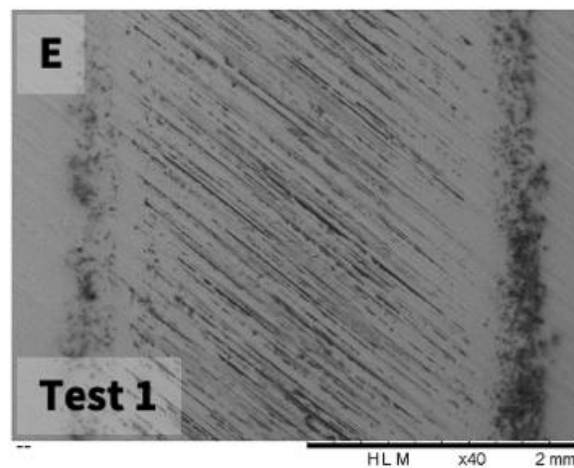
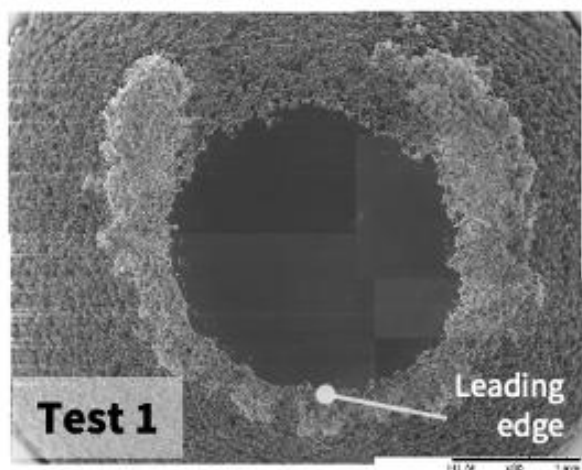


Figure C.15 – SEM scan images of (a) polymer pin worn surfaces and (b) metal disk samples (east location) captured after $30\text{N} - 0.05\text{ms}^{-1}$ (high load / low speed) sliding, specifically from tests 1 and 3.

$30\text{N} - 0.5\text{ms}^{-1}$ / High Load – High Speed

(a)



(b)

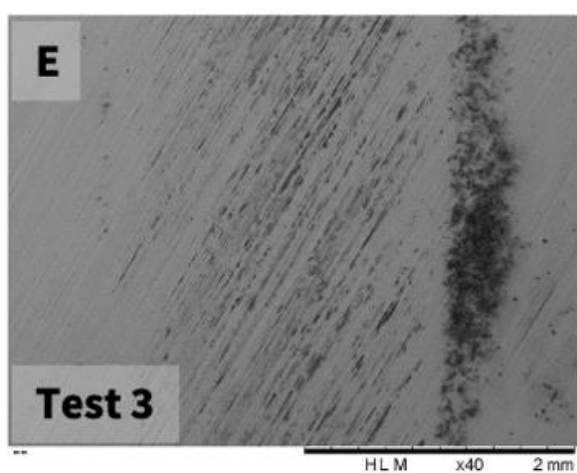
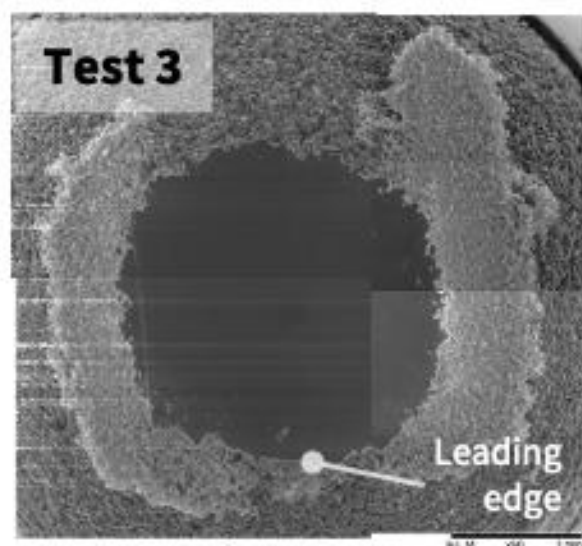
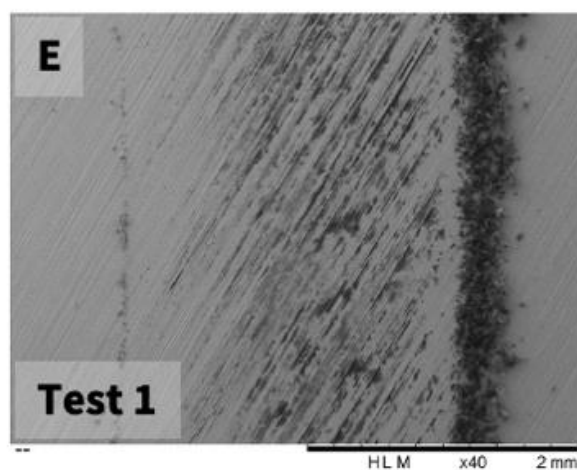


Figure C.16 – SEM scan images of (a) polymer pin worn surfaces and (b) metal disk samples (east location) captured after $30\text{N} - 0.5\text{ms}^{-1}$ (high load / high speed) sliding, specifically from tests 1 and 3.

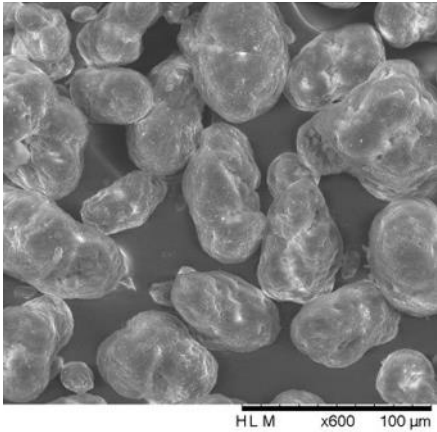
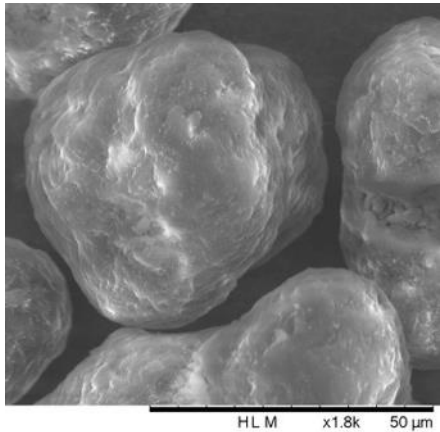
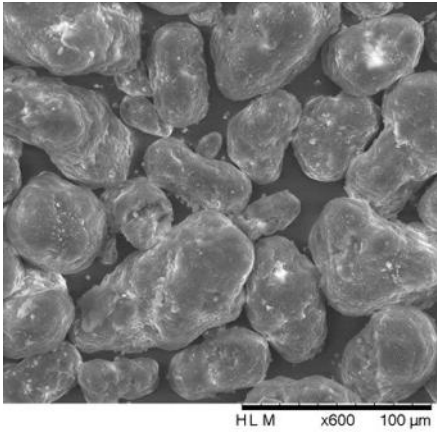
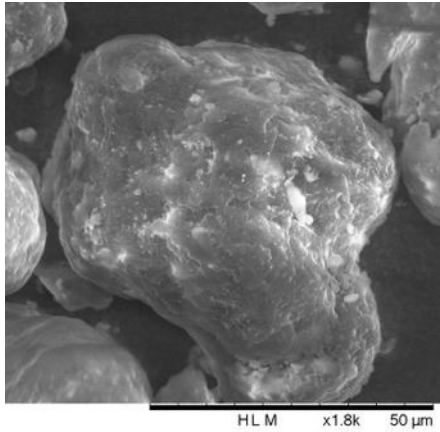
D. Auxiliary SEM Filler Inclusion Analysis

This appendix includes SEM micrographs of virgin – PA12 powders containing PTFE (from the same batch used in **Chapter 9**) in mass loadings of 1 : 50 and 1 : 25 (solid lubricant : PA12).

Accordingly, the proportionality between PTFE presence and its inclusion ratio, as shown in **Table D.1**, reaffirms that the particles highlighted in **Figure 9.2** correspond with the addition of each solid lubricant evaluated within **Chapter 9**.

Table D.1

SEM images of virgin – PA12 powders containing PTFE (from the same batch used in **Chapter 9**) in increased mass loadings of 1 : 50 and 1 : 25 (solid lubricant : PA12). With increasing mass loading ratios, greater amounts of PTFE, as indicated by white speckles or flecks (approximately 3µm in diameter), can be seen to be dispersed within each corresponding x600 and x1800 scan image.

Material configuration (including mass loading ratio)	Magnification	
	x600	x1800
Virgin – PA12		
Virgin – PA12 + PTFE (1 : 50)		
Virgin – PA12 + PTFE (1 : 25)	